UNIVERSITY OF CALIFORNIA,
IRVINE

# Galaxy Formation in the Local Group

DISSERTATION

submitted in partial satisfaction of the requirements
for the degree of

DOCTOR OF PHILOSOPHY

in Physics

by

Shea Cyrus Garrison-Kimmel

Dissertation Committee:
Professor James S. Bullock, Chair
Assistant Professor Michael Cooper
Professor Manoj Kaplinghat

2015

# DEDICATION

*For anyone whose has ever*
*supported me,*
*believed in me,*
*and especially,*
*challenged me.*

# TABLE OF CONTENTS

# LIST OF FIGURES

# LIST OF TABLES

# ACKNOWLEDGMENTS

Without the support of everyone surrounding me, neither I nor this thesis would have ever made it this far. However, there are a number of individuals to whom I owe a particularly large debt of gratitude, and I would be remiss to not thank them directly.

To my thesis advisor James Bullock, thank you for being the best advisor that I could have hoped for. You have always placed your students first by working tirelessly to enrich their lives and to direct them onto a path towards success, and for that I will be eternally grateful.

I am also grateful to the many postdoctoral scholars that guided my academic and intellectual development during my time at UC Irvine. I am especially thankful to Michael Boylan-Kolchin, without whom the ELVIS suite, and much of my subsequent work, would not exist. I am also indebted to Jose Oñorbe, who was crucial to my early development as a researcher, and to Michael Cooper, Sarah Miller, Shunsaku Horiuchi, and Annika Peter, all of whom helped to guide me along the path to this point. I would also like to acknowledge the Southern California Center for Galaxy Evolution, which helped to bring many of these individuals to UCI.

Of course, I would have never reached UC Irvine without the dedicated support of the faculty at Haverford College. In particular, I owe my interest in astronomy to Steve Boughn, who not only shaped my love for science, but also my future career plans. I would also like to thank the rest of the Haverford Physics department, including Walter Smith for setting a standard for teaching excellence that I can only hope to measure up to, Peter Love for demonstrating to me the joy of computational physics, Scott Shelley for always making labs fun, Beth Willman for supporting me at Haverford and beyond, and Bruce Partridge for the opportunity to understand that I far prefer theoretical astronomy. I am also grateful to Bret Mulligan, who demonstrated a passion for teaching that I have never seen matched.

However, my academic career would have floundered early without the steadfast support of my peers along the way. These include friends at Haverford, particularly Sean, who has not only been my closest friend but has also been instrumental to my professional success thanks to his skills as a writer and teacher; Tina, my oldest, most driven, and quite possibly smartest friend; everyone in 11; the old 8000 crew; and the entirety of my customs group, including my UCA Justin Cantley, without whom I may never have taken an astronomy course. I would also never have made it through grad school without my friends at UCI as well, including Steve, Bass (thanks for the Russian lesson), Kurt, Tyler, Jack, Amber, and many others – more than I could possibly list here. My success is also thanks to the aid of my classmates at both institutions, including Byron, Anna, Joe, Anna, Bryan, and Matt, and my research colleagues at UCI: Miguel, Coral, John, Oliver, Andrew, and especially Erik Tollerud, whose mentoring turned me from a naive first-year into a competent programmer and theoretical astronomer. I also owe my sanity to Hermes, even if he sometimes drives me crazy.

Finally, none of this would have been possible without the love and support of my family,

all of whom stood behind me every step of the way. To Mom, Dad, Cassidy and Ryan, Grandma and Grandpa, Mara and Joe, Donna and Marc, Linda, and Michael, Bryan, and Caitlin, thank you from the bottom of my heart for, well, everything.

I also want to acknowledge and thank my many other collaborators, all of whom were hugely important in making this work possible. Specifically, Kyle Lee was instrumental in the work presented in Chapter 2 with his aid in selecting the isolated analogues in the ELVIS suite and his help simulating the boxes that the Local Groups were selected from. For Chapter 3, I thank Evan Kirby, who helped provide the necessary observational data, as well as the expertise required to understand its limitations. I thank Jaspreet Lally for her help in exploring the problem tackled in Chapter 4, and I am very grateful to Kevork Abazajian and Manoj Kaplinghat for their assistance in the rapid publication of Chapter 5. I am further indebted to the many individuals that have made code publicly available, without whom this thesis could not have been completed. I would therefore like to thank Volker Springel, Phil Hopkins, Peter Behroozi, Oliver Hahn, and Alexander Knebe.

The research reported here was supported by NASA through a Hubble Space Telescope theory grant (program AR-12836) from the Space Telescope Science Institute (STScI), which is operated by the Association of Universities for Research in Astronomy (AURA), Inc., under NASA contract NAS5-26555, and a UC Irvine Chancellor's Club Fund for Excellence Fellowship. This work was also funded in part by NSF grants AST-1009999, AST-1009973, and NASA grant NNX09AD09G and was partially supported by an equipment matching grant from UC-HiPACC. I also gratefully acknowledge the computational support of XSEDE, the NASA Advanced Supercomputing Division, the NASA Center for Climate Simulation, and the *Greenplanet* cluster at UCI.

Portions of this dissertation (Chapters 2, 3, 4, and 5) are pre-copyedited, author-produced versions of articles accepted for publication in the Monthly Notices of the Royal Astronomy Society following peer review. Chapter 2 (Garrison-Kimmel et al., 2014a) is available online at `http://mnras.oxfordjournals.org/content/438/3/2578`, Chapter 3 (Garrison-Kimmel et al., 2014b) is available online at `http://mnras.oxfordjournals.org/content/444/1/222`, Chapter 4 (Garrison-Kimmel et al., 2013) is available online at `http://mnras.oxfordjournals.org/content/433/4/3539`, and Chapter 5 (Garrison-Kimmel et al., 2014c) is available online at `http://mnras.oxfordjournals.org/content/444/1/961`. The co-authors listed in those publications directed and supervised research which forms the basis for this dissertation.

CURRICULUM VITAE

# Shea C. Garrison-Kimmel

Department of Physics and Astronomy
University of California, Irvine
2152 Frederick Reines Hall
Irvine, CA 92697

Homepage: localgroup.ps.uci.edu/shea

## Education

- Ph.D. in Physics and Astronomy, University of California, Irvine *Sept 2009 - June 2015*
- M.S. in Physics and Astronomy, University of California, Irvine *Awarded Dec 2010*
- B.S. in Physics and Astronomy, concentration in Computer Science, Haverford College *Awarded May 2009*

## Fellowships and Awards

- Chancellor's Club Dissertation Fellowship, University of California, Irvine *Awarded Dec 2014*
- Price Prize, Ohio State University *Awarded July 2014*
- Chancellor's Fellowship, University of California, Irvine *Awarded Feb 2009*
- Summer Research Fellowship, University of California, Irvine *Awarded Feb 2009*

## Research Interests

Dwarf galaxy formation and theoretical cosmology, such as:

- Placing the Milky Way in its proper cosmological context as a member of the Local Group
- The impact of environment on dwarf galaxy evolution
- Numerical simulations of structure formation on both large and small scales
- The formation and evolution of the smallest galaxies in the Universe
- Comparing theoretical predictions with observational data to constrain baryonic processes

## Teaching and Mentoring

### *Teaching experience*

- University of California, Irvine, Teaching Assistant *Sept 2009 - June 2010 and March 2014 - June 2014*
- California State Summer School for Mathematics and Science, Teaching Assistant *July 2010, 2011, and 2012*
- Haverford College, Physics Clinic Tutor *Feb 2007 - May 2009*

### *Mentoring Experience*

- Mentored Jaspreet Lally, at the time an undergraduate at University of California, Irvine, on how to run and analyze simulations of dwarf galaxies in isolation with a time varying potential to search for core formation, resulting in an authorship on Garrison-Kimmel et al., 2013.
- Mentored Kyle Lee, currently an undergraduate at Chapman University, on how to set up, simulate, and analyze cosmological simulations, including selecting isolated Milky Way hosts for zoom-in simulations, resulting in an authorship on Garrison-Kimmel et al., 2014.
- Currently mentoring Emma Bardwell, an undergraduate at Case Western University, on a project exploring the relationship between halo mass and galaxy stellar mass, and the impact of scatter in that relation, resulting in an authorship on a paper in preparation.
- Currently mentoring Kris Burke, an undergraduate at University of California, Irvine, on simulating the cosmological evolution of galaxies with a central potential to explore the impact of the Milky Way disk on the substructure population with minimal CPU cost.

## Peer-Reviewed Publications

### *First Author Publications*

1. **Garrison-Kimmel, S.**, Horiuchi, S., Abazajian, K., Bullock, J., Kaplinghat, M. (2014), Running with BICEP2: Implications for Small-Scale Problems in CDM. *MNRAS*, 444, 961-970.
2. **Garrison-Kimmel, S.**, Boylan-Kolchin, M., Bullock, J., Kirby, E. (2014), Too Big to Fail in the Local Group. *MNRAS*, 444, 222-236.
3. **Garrison-Kimmel, S.**, Boylan-Kolchin, M., Bullock, J., Lee, K. (2014), ELVIS: Exploring the Local Volume in Simulations. *MNRAS* 438, 2578-2596.
4. **Garrison-Kimmel, S.**, Rocha, M., Boylan-Kolchin, M., Bullock, J., Lally, J. (2013), Can feedback solve the Too Big To Fail problem?. *MNRAS* 433, 3539–3546.

### *Nth Author Publications*

1. Wetzel, A., Deason, A., **Garrison-Kimmel, S.** (2014), Satellite Dwarf Galaxies in a Hierarchical Universe: Infall Histories, Group Preprocessing, and Reionization. Accepted into *ApJ*.
2. Deason, A., Wetzel, A., **Garrison-Kimmel, S.** (2014), Satellite Dwarf Galaxies in a Hierarchical Universe: The Prevalence of Dwarf-Dwarf Major Mergers. *ApJ*, 794, 115-123.
3. Wang, M., Peter, A. H. G., Strigari, L. E., Zentner, A. R., Arant, B., **Garrison-Kimmel, S.**, Rocha, M., (2014) Cosmological Simulations of Decaying Dark Matter: Implications for Small-scale Structure of Dark Matter Halos. *MNRAS*, 445, 614-629.
4. Boylan-Kolchin, M., Bullock, J., **Garrison-Kimmel, S.** (2014), Near-Field Limits on the Role of Faint Galaxies in Cosmic Reionization. *MNRAS Letters*, 443, L44 - L48.
5. Brook, C., Di Cintio, A., Knebe, A., Gottlöber, S., Hoffman, Y., Yepes, G., **Garrison-Kimmel, S.** (2014), The stellar-to-halo mass relation for Local Group galaxies. *APJL*, 784, L14.
6. Horiuchi, S., Humphrey, P., Oñorbe, J., Abazajian, K., Kaplinghat, M. (2014), **Garrison-Kimmel, S.**, Sterile neutrino dark matter bounds from galaxies of the Local Group. *PRD*, 89, 025017.
7. Yniguez, B., **Garrison-Kimmel, S.**, Boylan-Kolchin, M., Bullock, J. (2014), On the stark difference in satellite distributions around the Milky Way and Andromeda. *MNRAS*, 439, 73-82.

8. Oñorbe, J., **Garrison-Kimmel, S.**, Maller, A. H., Bullock, J., Rocha, M., Hahn, O. (2014), How to Zoom: Bias, Contamination, and Lagrange Volumes in Multimass Cosmological Simulations. *MNRAS* 437, 1894-1908.

9. Rocha, M., Peter, A. H. G., Bullock, J., Kaplinghat, M., **Garrison-Kimmel, S.**, Oñorbe, J., Moustakas, L. A. (2013), Cosmological simulations with self-interacting dark matter - I. Constant-density cores and substructure. *MNRAS* 430, 81–104.

## Papers Under Review

### *Nth Author Publications*

1. Elbert, O., Bullock, J., **Garrison-Kimmel, S.**, Rocha, M., Oñorbe, J., Peter, A.H.G. (2014), Core Formation in Dwarf Halos with Self Interacting Dark Matter: No Fine-Tuning Necessary. Submitted to *MNRAS*.

2. Fillingham, S., Cooper, M., Wheeler, C., **Garrison-Kimmel, S.**, Boylan-Kolchin, M., Bullock, J. (2015), Taking Care of Business in a Flash: Constraining the Timescale for Low-Mass Satellite Quenching with ELVIS. Submitted to *MNRAS*.

3. Wheeler, C., Oñorbe, J., Bullock, J., Boylan-Kolchin, M., Elbert, O., Garrison-Kimmel, S., Hopkins, P., Keres, D (2015), Sweating the small stuff: simulating dwarf galaxies, ultra-faint dwarf galaxies, and their own tiny satellites. Submitted to *MNRAS*.

4. Deason, A., Wetzel, A., **Garrison-Kimmel, S.**, Belokurov, V. (2014), Satellites of LMCs: Close Friendships Ruined by Milky Way Mass Halos. Submitted to *MNRAS*.

## Conference Proceedings

1. Rocha, M., Peter, A. H. G., Bullock, J., Kaplinghat, M., **Garrison-Kimmel, S.**, Oñorbe, J., Moustakas, L. A. (2013), Cosmological simulations with self-interacting dark matter. *Proceedings of AAS Topical Conference Series Vol. 1*, July 14-19, 2013, Monterey, CA.

2. Pancoast, A., **Garrison-Kimmel, S.**, Love, P., Gaps and Tails: The restricted N-body problem in colliding galaxies and the asteriod belt. *Proceedings of APS March Meeting 2009*, March 16-20, 2009, Pittsburgh, USA.

# ABSTRACT OF THE DISSERTATION

Galaxy Formation in the Local Group

By

Shea Cyrus Garrison-Kimmel

Doctor of Philosophy in Physics

University of California, Irvine, 2015

Professor James S. Bullock, Chair

Dwarf galaxies are among the most numerous objects in the Universe, and also appear to be the most dark matter (DM) dominated; consequently, they provide strong tests on the standard paradigm of hierarchical galaxy formation: cold dark matter with a cosmological constant ($\Lambda$CDM). Due to their low luminosities, however, observational studies of dwarfs have remained limited to the nearby Universe, with a primary focus on the satellites of the Milky Way (MW). Upcoming surveys will relax the observational constraints, allowing for studies of dwarf galaxies well beyond the virial radius ($R_{\rm v}$) of the MW, where the presence of the Andromeda (M31) galaxy may have a measurable impact. In this thesis, I introduce the ELVIS (Exploring the Local Volume in Simulations) suite, which resolves the formation and evolution of Local Group (LG)-like pairs of galaxies, chosen to resemble the MW and M31 host halos, along with thousands of dwarf halos that surround them. Using ELVIS, I demonstrate that simulations of isolated MW-size hosts do not correctly predict dwarf counts and kinematics beyond $R_{\rm v}$ of the MW, and also explore the faint-end relationship between stellar mass ($M_\star$) and halo mass ($M_{\rm halo}$). I then use ELVIS to explore the "too-big-to-fail" (TBTF) problem, a challenge for $\Lambda$CDM that points out the overabundance of large (maximum circular velocity $V_{\rm max} \gtrsim 30$ km s$^{-1}$) dwarf halos relative to observations, finding TBTF to be ubiquitous to MW-size hosts *and* the fields around them. Finally, I explore two possible explanations for TBTF in depth: fluctuations in the baryonic mass in the center of

a dwarf halo, driven by supernovae feedback, which I find lacks the energy to solve TBTF, and a "running" initial power spectrum, as motivated by the BICEP-2 measurement of primordial gravitational waves, which significantly alleviates the problem and may enhance the impact of other processes, including baryonic feedback.

# Chapter 1

# Introduction

Throughout recorded history, cultures and individuals have looked at the heavens in wonder. For example, ancient Chinese records (circa 150 CE) include accounts of nearby supernovae, though its origin and significance were not understood. Attempts to understand the skies, including both these transient events and the motion of bright objects, have lead to a better understanding of not just the Universe, but of terrestrial physics as well.

The quantification of the skies may have begun with Hipparchus, who created the (counter-intuitive) magnitude system while cataloging the stars. However, it was Copernicus who initiated a great leap forward in our understanding with his claim that the Earth is not at the center of the Universe (Copernicus, 1543).

The process of putting physics to the skies continued with the work of Tycho Brahe, who took precise measurements of the positions of the planets, and Johannes Kepler, who used those measurements to compose his Laws of Planetary Motion. Though these laws were empirically derived, they formed much of the basis for Isaac Newton's Theory of Gravity (Newton, 1687), thus providing an early instance of astronomical measurements informing smaller-scale scientific questions. This process was, in many ways, repeated several hundred

years later with the work of Dyson et al. (1920), who confirmed that the bending of starlight by the sun agrees with the predictions of general relativity (Einstein, 1916).

Our understandings of the sky, and their workings, have only grown from that point. Progress exploded in the early 1900s with Edwin Hubble's discovery that many previously unidentified nebulous light sources were in fact galaxies beyond our own – a fact that conclusively demonstrated that our galaxy, the Milky Way (MW), is but one of many (Hubble, 1926). The "Hubble relation," which links the relative velocities of extra-galactic objects at "cosmological distances" ($\gtrsim 1$ Mpc) to their distance from the MW, lead to a variety of cosmological models, each of which sought to describe not only the history and future of the Universe as a whole, but also the nature by which structure grows within the Universe.

Two competing classes of cosmological models – "Big Bang" models, which include a beginning of the Universe, and "steady state" models, which hypothesized that the Universe is infinitely old – persisted for many years after the work of Edwin Hubble. However, with the discovery of the cosmic microwave background (CMB) by Penzias & Wilson (1965), a sea of background radiation with a perfect blackbody spectrum that is naturally predicted by Big Bang models but is unexplained by the steady state hypothesis, the latter class of models quickly fell out of favor.

The CMB proved to be even more useful, however. While early measurements found that the CMB is nearly exactly the same temperature in all directions (Mather et al., 1990), higher resolution observations found fluctuations of $\Delta T/T \sim 10^{-5}$ (Bennett et al., 2003). These fluctuations, which are linked to both the density of baryons as well as the overall matter density, helped to conclusively verify the hypotheses of Zwicky (1937) and Rubin & Ford (1970) that much of the gravitating mass in our Universe does not emit or absorb photons. This missing mass, which the CMB confirmed must dominate over baryons (ordinary matter), was dubbed "dark matter."

Dark matter (DM) may be the next great instance of large-scale astronomy ($\sim 10^{26}$ m) informing physics on very small scales ($\sim 10^{-35}$ m). While the existence of DM has been inferred from cluster dynamics, galaxy rotation curves, and the CMB, the its properties remain largely unknown. Microlensing surveys (e.g. Tisserand et al., 2007) imply that it cannot be large, dark objects (similar to Jupiter), resulting in the prevailing hypothesis that DM is an as-yet undiscovered fundamental particle that does not interact with photons, the electromagnetic force carrier, but which may annihilate with itself or even decay (with a very long half-life). However, questions such as how strongly DM "self interacts," how strongly it couples gravitationally to baryons, the smallest collapsed objects (known as DM halos) that exist in the Universe, how many of those objects exist, and how halos form and merge remain largely unanswered.

To address these questions, many astronomers have turned to dwarf galaxies. Dwarfs (stellar mass $M_\star \lesssim 10^9 M_\odot$) are the most numerous objects in the Universe (e.g. Baldry et al., 2012), but are also among the most difficult to detect, due to their low luminosities. Importantly, dwarfs are the most DM dominated objects known in the Universe (e.g. Behroozi et al., 2013c), making them ideal probes of DM physics. For example, several groups (e.g. The Fermi-LAT Collaboration et al., 2013, and references therein) have placed limits on the properties of DM through searches for gamma rays produced by either the annihilation or decay of DM; these limits are strongest due to the lack of contamination from non-DM gamma rays in dwarfs. Others (e.g. Elbert et al., 2014) have sought to constrain the cross section for self-interactions in DM.

Dwarfs are also highly useful for a variety of studies not focused on DM. They provide an ideal laboratory for studying star formation in shallow potential wells: how massive must a halo be before star formation can commence in it (Wheeler et al., 2015), and through what processes is that star formation ultimately quenched (e.g. Weisz et al., 2015; Fillingham et al., 2015; Wetzel et al., 2015)? Dwarfs may also contribute to the build-up of larger galaxies

through continual mergers (e.g. Johnston et al., 2008), and they are also useful as dynamical tracers of the larger-scale potential of their host galaxies (e.g. Boylan-Kolchin et al., 2013).

While dwarfs are demonstrably useful probes of DM and galaxy formation, their low luminosities render them invisible at large distances ($\gtrsim 1$ Mpc), resulting in a sample that is necessarily restricted to those in the immediate vicinity. It is therefore of utmost importance that we fully understand the predictions of the $\Lambda$CDM model for dwarfs near the MW. A large number of studies have focused on the virialized region ($r \lesssim 300$ kpc) of the MW, along with the dwarf satellites and subhalos that reside in that volume (e.g. Kuhlen et al., 2009; Springel et al., 2008, and references therein), which has been well studied with corresponding observational surveys (Ahn et al., 2014). However, next-generation telescopes, such as the Large Synoptic Sky Telescope (LSST), will probe the nearby sky to unprecedented depth and should reveal a wealth of new dwarf galaxies beyond the virial radius of the MW. In order to properly interpret these observations in the full context of the $\Lambda$CDM model, simulations must also begin to resolve not only the virialized volume of the MW, but the $\sim 1$ Mpc region surrounding it, including the nearby Andromeda (M31) galaxy.

Here I present a suite of simulations aimed at fully understanding the dark matter distribution in and around the MW and M31, which together comprise the Local Group (LG). Chapter 2 introduces the simulations, quantifies the bias introduced in the number and kinematics of field halos due to the presence of M31, count collapsed halos around the simulated LGs, and explores implications for galaxy formation the dwarf scale. In Chapter 3, I use these simulations to explore too-big-to-fail, an apparent discrepancy between simulations in the $\Lambda$CDM paradigm and observations, in a large number of MW-size hosts and in the field around the MW and M31. I then focus on two possible solutions to TBTF in depth: Chapter 4 details ultra-high resolution simulations exploring the response of an isolated dwarf halo to fluctuations in the baryonic potential, and Chapter 5 investigates the affect of a "rolling" initial power spectrum on dwarf halos. I summarize my conclusions in Chapter 6.

# Chapter 2

# ELVIS: Exploring the Local Volume in Simulations

## Chapter Abstract

We introduce a set of high-resolution dissipationless simulations that model the Local Group (LG) in a cosmological context: Exploring the Local Volume in Simulations (ELVIS). The suite contains 48 Galaxy-size halos, each within high-resolution volumes that span $2-5$ Mpc in size, and each resolving thousands of systems with masses below the atomic cooling limit. Half of the ELVIS galaxy halos are in paired configurations similar to the Milky Way (MW) and M31; the other half are isolated, mass-matched analogs. We find no difference in the abundance or kinematics of substructure within the virial radii of isolated versus paired hosts. On Mpc scales, however, LG-like pairs average almost twice as many companions and the velocity field is kinematically hotter and more complex. We present a refined abundance matching relation between stellar mass and halo mass that reproduces the observed satellite stellar mass functions of the MW and M31 down to the regime where incompleteness is an

issue, $M_\star \sim 5 \times 10^5\, M_\odot$. Within a larger region spanning approximately 3 Mpc, the same relation predicts that there should be $\sim 1000$ galaxies with $M_\star > 10^3\, M_\odot$ awaiting discovery. We show that up to 50% of halos within 1 Mpc of the MW or M31 could be systems that have previously been within the virial radius of either giant. By associating never-accreted halos with gas-rich dwarfs, we show that there are plausibly 50 undiscovered dwarf galaxies with HI masses $> 10^5 M_\odot$ within the Local Volume. The radial velocity distribution of these predicted gas-rich dwarfs can be used to inform follow-up searches based on ultra-compact high-velocity clouds found in the ALFALFA survey.

## 2.1 Introduction

The Local Group (LG) provides an important test bed for theories of galaxy formation, both in its connection to small-scale probes of the consensus dark energy plus cold dark matter ($\Lambda$CDM) cosmological model (Klypin et al., 1999; Moore et al., 1999; Strigari et al., 2008a; Walker & Peñarrubia, 2011; Boylan-Kolchin et al., 2011; Zolotov et al., 2012; Garrison-Kimmel et al., 2013; Arraki et al., 2013) and as a potential hunting ground for the descendants of reionization and first light (Bullock et al., 2000; Ricotti & Gnedin, 2005; Madau et al., 2008). The focus on these issues is well motivated: given inevitable completeness limitations, nearby galaxies offer our best avenue for characterizing the faint end of the global luminosity function and for studying resolved stellar populations as beacons from an earlier age (see, e.g. Makarov & Karachentsev, 2011; Weisz et al., 2011; McConnachie, 2012; Karachentsev & Kaisina, 2013; Tully et al., 2013).

Numerical simulations have emerged as the most useful tool for making predictions about non-linear structures in $\Lambda$CDM. While simulations of cosmologically large volumes enable statistical comparisons with a variety of observations (e.g. Davis et al., 1985; Gross et al., 1998; Springel et al., 2005; Boylan-Kolchin et al., 2009; Klypin et al., 2011), cosmological zoom-in

simulations are the de facto standard for the most detailed comparisons of individual objects. The zoom-in technique (Katz & White, 1993; Oñorbe et al., 2014) focuses computational power on a small, high resolution region nested within a lower resolution, cosmological-size volume, thereby retaining the large-scale, low frequency cosmological modes important for convergence but also allowing for the high resolutions required to obtain a wide dynamic range.

Very high resolution zoom-in simulations of Milky Way (MW) mass halos have been useful for making and testing predictions of the ΛCDM theory (e.g. Diemand et al., 2008; Kuhlen et al., 2008; Springel et al., 2008), often through comparisons to dwarf satellite galaxies of the LG (Koposov et al., 2009; Strigari et al., 2010; Boylan-Kolchin et al., 2012). However, in order to achieve the highest resolution possible, these simulations have concentrated on fairly isolated systems.[1] In reality, the Milky Way is not isolated, but has a nearby companion of comparable luminosity, the Andromeda galaxy (M31). The existence of M31 at a distance of approximately 800 kpc from the MW implies that isolated zoom simulations cannot be used to faithfully make predictions for the Local Volume[2] beyond $\sim$ 400 kpc of either system. Furthermore, several simulations that have explored the role of LG-like environments in shaping galaxy properties have found evidence that the local configuration may even bias galaxy properties within each giant's virial radius compared to isolated counterparts (Gottloeber et al., 2010; Libeskind et al., 2010; Forero-Romero et al., 2011; Few et al., 2012).

Motivated by these concerns, here we introduce a set of dissipationless simulations designed to confront the Local Volume in a cosmological context. We call this project Exploring the Local Volume in Simulations (ELVIS). The simulation suite consists of 12 zoom-in regions

[1] As noted in Teyssier et al. (2012), the Via Lactea II halo does indeed have a massive ($M_{\rm v} = 6.5\times10^{11}\,M_\odot$) companion at a distance comparable to M31. However, this companion halo and field galaxies nearby are not free of contamination from low-mass particles. The contamination reaches 50% by mass, which has potentially important effects on halo properties.

[2] A term we use roughly to correspond to a $\sim$ 2 Mpc sphere from the LG barycenter.

of LG analogue halo pairs and 24 isolated halos that are mass-matched to create a control sample for those pairs. Below, we describe the selection of ELVIS pairs, their simulation details, and properties of the host halos (§ 2.2). We investigate the environments that surround them in comparison to those of the control hosts as well as the dynamical histories of bound halos around the ELVIS giants by characterizing the fraction of 'backsplash' halos – systems that at one point had been within the virial radius of a giant – as a function of distance (§ 2.3). Finally, we compare number counts and kinematic properties of the subhalos found in paired and isolated samples, and we use abundance matching (AM) to make predictions for the stellar and HI mass functions within the Local Volume (§ 2.4).

With the publication of this paper, we publicly release all of the data in the ELVIS suite, including full merger trees, $z = 0$ halo catalogs, and particle information.[3]

## 2.2 The ELVIS Suite

The ELVIS simulations were run using `GADGET-3` and `GADGET-2` (Springel, 2005), both tree-based $N$-body codes. For the underlying cosmological model, we have adopted ΛCDM parameters set by the WMAP-7 results (Larson et al., 2011): $\sigma_8 = 0.801$, $\Omega_m = 0.266$, $\Omega_\Lambda = 0.734$, $n_s = 0.963$, and $h = 0.71$. Throughout this work, we use the term virial mass $M_{\rm v}$ to refer to the mass within a sphere of radius $R_{\rm v}$ that corresponds to an over density of 97 relative to the critical density of the Universe (Bryan & Norman, 1998). All simulations were initialized at redshift $z = 125$ unless otherwise specified.

[3]Present-day ($z = 0$) halo catalogs and the main branches of the merger trees are available for public download (`http://localgroup.ps.uci.edu/elvis`), while access to the full merger trees and particle information will be arranged via email contact with the authors.

### 2.2.1 Halo Selection

We select LG-like pairs from 50 medium-resolution cosmological simulations, each a cubic volume 70.4 Mpc on a side with particle mass $m_{\rm p} = 9.7 \times 10^7 M_\odot$ and Plummer-equivalent force softening length 1.4 kpc (comoving). From these cosmological volumes, we selected 12 halo pairs for resimulation using the criteria described below. For each of the 24 halos included in the ELVIS pairs, we also chose an isolated analogue of identical virial mass ($M_{\rm v}$) that is separated by at least 2.8 Mpc from all halos more massive than $M_{\rm v}/2$. The isolated set serves as a control sample for comparison.

Our approach to selecting LG regions differs from that of the well-known Constrained Local Universe Simulations (CLUES) project (Gottloeber et al., 2010), which relies on the 'constrained realization' technique to match the observed density and velocity fields on a $\sim 10\,$Mpc scales around the LG. The advantage to our approach is that it guarantees a good LG analogue in each re-simulation. The downside is that the larger scale density field will usually not be identical to that of the LG. The two initialization methods therefore have different, complementary strengths.

In selecting pairs, we targeted halos with phase-space characteristics similar to the MW/M31 system, with cuts similar to those of Forero-Romero et al. (2011), based on values of the virial mass of each host ($M_{\rm v,1}$ and $M_{\rm v,2}$, where $M_{\rm v,2} \geq M_{\rm v,1}$), the distance between host centers $\Delta R$, the pair approach velocity, and local environment:

- *Mass of each host:* $10^{12} \leq M_{\rm v} \leq 3 \times 10^{12} M_\odot$ (Tollerud et al., 2012; Boylan-Kolchin et al., 2013; Fardal et al., 2013; Piffl et al., 2013)
- *Total mass:* $2 \times 10^{12} \leq M_{\rm v,1} + M_{\rm v,2} \leq 5 \times 10^{12} M_\odot$ (Li & White, 2008; van der Marel et al., 2012)

- *Separation:* $0.6 \leq \Delta R \leq 1\,\mathrm{Mpc}$ (McConnachie et al., 2005, and references therein)
- *Radial velocity:* $V_{\mathrm{rad}} \leq 0$ km/s (van der Marel et al., 2012)
- *Isolation:* No halos with $M_{\mathrm{v}} \geq M_{\mathrm{v},1}$ within 2.8 Mpc of either center and no halos with $M_{\mathrm{v}} \geq 7 \times 10^{13} M_{\odot}$ within 7 Mpc of either center (Tikhonov & Klypin, 2009; Karachentsev et al., 2004).

We identified 146 halo pairs that met these criteria within the 50 simulations we ran (an equivalent volume of $1.76 \times 10^7$ Mpc$^3$) and selected 12 pairs for resimulation. We intentionally chose several pairs that consisted of hosts with massive ($V_{\mathrm{max}} > 75\,\mathrm{km\,s^{-1}}$) subhalos in order to ensure that we had a fair number of systems with realistic analogs to the Large Magellanic Cloud (LMC) and M33; had we selected pairs at random, it would have been unlikely to obtain such massive subhalos (Boylan-Kolchin et al., 2010). We further made an effort to include two pairs that had very low relative tangential velocities $< 15\,\mathrm{km\,s^{-1}}$ in order to mimic the low relative tangential speed of the MW/M31 pair (van der Marel et al., 2012). For the isolated control sample, we imposed no selection choices other than in matching virial masses and demanding that there are no halos with $M > M_{\mathrm{v}}/2$ within 2.8 Mpc. Most of the matches in mass are good to within 5%, though some differ by up to 10%. Though we attempted to match their masses at the percent level in the low-resolution simulations used to identify objects for resimulation, differences of this order are expected when using the zoom-in technique (Oñorbe et al., 2014).

For record-keeping purposes, each LG-analogue pair is named after a famous duo, as summarized in Table 2.1. The individual halos that make up the pairs are referenced by the same names in Tables 2.2 and 2.3. The isolated analogs are identified by the same name prefixed by $i$ in Tables 2.4 and 2.5. We discuss the information presented in these tables in Section 2.2.3. The first pair listed in Table 2.1, Zeus & Hera, is singled-out in several figures below as a good analogue to the M31/MW system in terms of observed galaxy counts in the

Local Volume region. The halo Hera is identified with the MW in this pairing.

### 2.2.2 Zoom Simulations

In creating the zoom-in initial conditions for the ELVIS halos, we broadly followed the methods outlined in Oñorbe et al. (2014), who give prescriptions for selecting regions that will be free from low-resolution particle contamination in the final run. For the pairs, we identified Lagrangian volumes for all particles within 4 $R_{\rm v}$ of either host in the final timestep; for the isolated analogs, we use particles within 5 $R_{\rm v}$ in all but one case (specified below). We relied on the public[4] code `MUSIC` (Hahn & Abel, 2011) to create initial conditions associated with these Lagrangian volumes at high resolution. The mass resolution in the zoom regions of our production runs is $m_p = 1.9 \times 10^5 M_\odot$, corresponding to an effective resolution of $4096^3$ in the box. The Plummer-equivalent force softening, $\epsilon$, in these runs was held constant in comoving units until $z = 9$, at which point it was held fixed at 141 pc (physical) for the remainder of each simulation.

The high resolution regions are surrounded by stepped levels of progressively lower force resolution and higher mass particles, with the majority of the parent boxes (70.4 Mpc cubes) filled with an effective resolution of $128^3$ ($m_p = 6.2 \times 10^9 M_\odot$) and each successive step increasing the effective resolution by a factor of 2 (decreasing the particle mass by a factor of 8). As in the high resolution regions, $\epsilon$ remains constant in comoving units until $z = 9$, then becomes fixed in physical units. These force softenings, however, are significantly larger than in the high resolution regions: at $z = 0$ in the main runs, the two highest particle masses utilize $\epsilon = 56$ kpc, the two intermediate regions use $\epsilon = 4.2$ kpc, and $\epsilon = 704$ pc for the particles immediately surrounding the high resolution volume.

Self-bound dark matter clumps are identified with the six-dimensional halo finder `Rockstar`

[4]The link is `http://www.phys.ethz.ch/~hahn/MUSIC/`

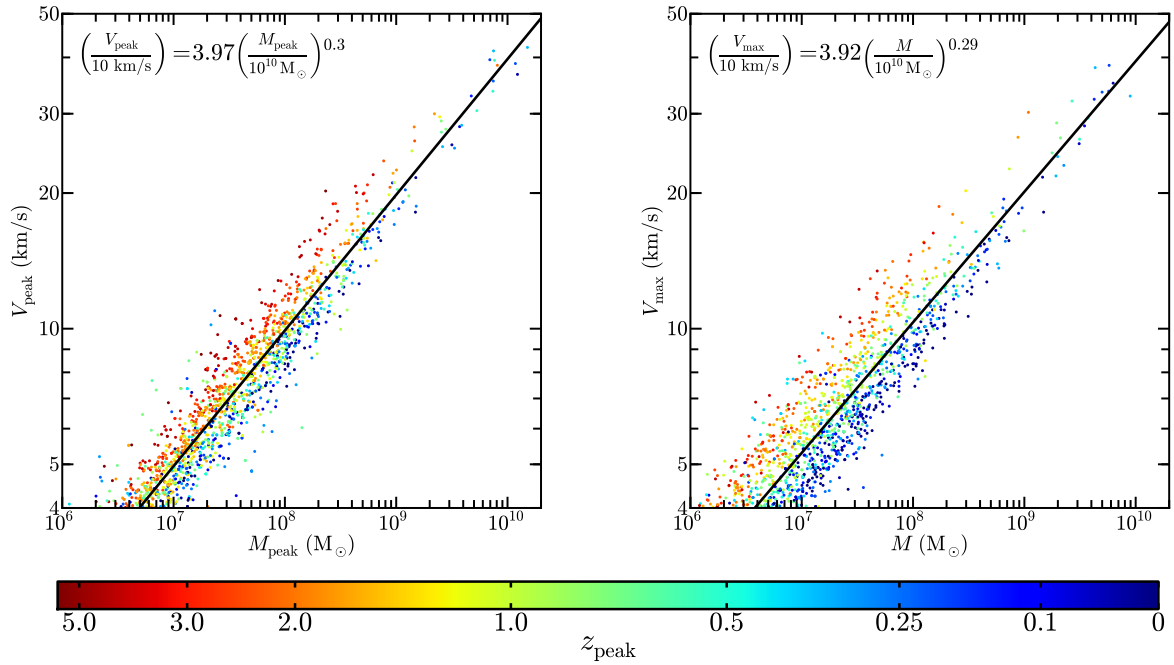


Figure 2.1: The relation between peak circular velocity and halo mass at $a_{\rm peak}$ (left) and at $z = 0$ (right) The indicated fit includes all resolved halos within 400 kpc of iKauket in the HiRes run (though the results do not differ at the fiducial resolution). Each subhalo is coloured by the redshift at which it reached its peak mass ($a_{\rm peak}$); this quantity is well-correlated with the scatter about the fits and, as is evident from the right panel, the amount of tidal stripping each subhalo has undergone.

(Behroozi et al., 2013a) and followed through cosmic time with `Consistent-Trees` (Behroozi et al., 2013b). Both of these codes are publicly available.[5] Subhalo masses ($M$) are calculated by `Rockstar` and correspond to the bound mass of the system. Maximum circular velocities ($V_{\rm max}$) correspond to the peak of the circular velocity curve, $V_c(r) = \sqrt{GM(r)/r}$, at a given redshift. We also checked results at the final timestep ($z = 0$) against the public[6], spherical overdensity-based `Amiga Halo Finder` (Knollmann & Knebe, 2009) and found that the results did not differ significantly and were identical within the statistical variation of our sample of halos.[7]

[5]The links are `http://code.google.com/p/rockstar/` and `http://code.google.com/p/consistent-trees/`.

[6]The link is `http://popia.ft.uam.es/AHF/`

[7]Though our results presented here and made publicly available upon publication rely on `Rockstar`, we are happy to supply associated `Amiga Halo Finder` catalogs upon request.

Three of the most useful quantities that can be determined for halos in our simulations are $M_{\rm peak}$ (the maximum mass of a dark matter structure over its history), $a_{\rm peak}$ (the latest scale factor at which $M_{\rm peak}$ occurs), and $V_{\rm peak}$ (the maximum circular velocity at $a_{\rm peak}$). To define these quantities, one must adopt an unambiguous definition of the main branch of each halo's merger tree. We assign the main progenitor at each timestep as the branch of the tree with the most total mass up to and including that timestep, i.e., the sum of $M_{\rm v}$ for all halos over all preceding timesteps in that branch. This definition weights both the formation time and the virial mass of halos in a given branch. The final step in our pipeline identifies the main branch of each merger tree and extracts $M_{\rm peak}$, $V_{\rm peak}$, and $a_{\rm peak}$ for each halo with $z = 0$ quantities $M$ (or $M_{\rm v}$ for hosts) and $V_{\rm max}$.

We simulated three of the isolated analogs (iScylla, iKauket, and iHall) at higher resolution, with $m_p = 2.35 \times 10^4 M_\odot$ ($8192^3$ effective particle number) and $\epsilon = 70.4\,{\rm pc}$; we refer to these runs as the HiRes simulations. The HiRes version of iKauket was originally simulated in the context of previous work (Oñorbe et al., 2014) and was initialized at a different redshift ($z = 250$) than the rest of our runs. It also used a Lagrangian volume chosen from all particles within $2\,R_{\rm v}$ (rather than our fiducial $5\,R_{\rm v}$ for the other isolated systems). The standard resolution version of iKauket also started at $z = 250$. As Oñorbe et al. (2014) showed, any variations in halo properties at low redshifts introduced by such a change in initial redshift are comparable to expected variations upon resimulation due to numerical "minichaos" (Miller, 1964), which should be unimportant for our purposes.

Our HiRes simulations are comparable in mass and force resolution to the Aquarius level 2 simulations (Springel et al., 2008) and to Via Lactea I (Diemand et al., 2007a), though two of them (iScylla and iHall) have uncontaminated high-resolution volumes – uncontaminated spheres of radius $\sim 1.5$ Mpc around each host – that extend much farther from the halo centers than any previous runs of this kind. The HiRes simulations will facilitate several inquiries that are not possible with our fiducial runs, but for the purposes of this paper,

they have allowed us to self-consistently identify the completeness limit for subhalos in our main ELVIS suite. We find that we are complete to $M > 2 \times 10^7\, M_\odot$, $V_{\rm max} > 8\,{\rm km\,s^{-1}}$, $M_{\rm peak} > 6 \times 10^7\, M_\odot$ and $V_{\rm peak} > 12\,{\rm km\,s^{-1}}$. The numerical convergence of our results in $V_{\rm max}$ and $M_{\rm peak}$ is demonstrated explicitly for iKauket in § 2.5.

In the bulk of this paper, we will enumerate halos and subhalos based on $M_{\rm peak}$. One could equivalently present results in terms of $M$, $V_{\rm max}$, or $V_{\rm peak}$ ($V_{\rm max}$ functions are presented in § 2.6). Figure 2.1 demonstrates the relationship between $M_{\rm peak}$ and $V_{\rm peak}$ (left panel) and $M$ and $V_{\rm max}$ (right panel) for halos within 400 kpc of the HiRes version of iKauket (the results are indistinguishable for the fiducial resolution runs for $V_{\rm max} > 8\,{\rm km\,s^{-1}}$ and $M_{\rm peak} > 6 \times 10^7\ M_\odot$.) The best-fitting $M_{\rm peak} - V_{\rm peak}$ and $M - V_{\rm max}$ relations are given by the formulas in the figures themselves.

What is the origin of the scatter in the $V - M$ relations? The points in Figure 2.1 are coloured by $z_{\rm peak} = a_{\rm peak}^{-1} - 1$. We see that this variable is strongly correlated with the scatter in $V$ at fixed $M$, such that earlier-forming halos have higher values of $V_{\rm peak}$ and $V_{\rm max}$. The correlation between $a_{\rm peak}$ and $V_{\rm peak}$ is related to the redshift dependence of the virial overdensity. At early times, halos at fixed mass have a higher $V_{\rm max}$. The red points effectively sample a population of halos at $z > 3$, whereas the blue points correspond to halos in the field at $z \lesssim 0.1$. The correlation between $a_{\rm peak}$ and $V_{\rm max}$ is a combination of the $a_{\rm peak} - V_{\rm peak}$ correlation and the effects of orbital evolution on subhalo density structure (for discussions on these expected trends see, e.g., Zentner & Bullock, 2003; Kazantzidis et al., 2004; Diemand et al., 2007b).

### 2.2.3 General Properties of the ELVIS halos

Table 2.1 summarizes the names and some properties of the ELVIS pairs at $z = 0$ (along with comparative information for the Milky Way and M31, where appropriate). We include

| **Pair Name** | $\Delta R$ | $\mathbf{V}_{\rm rad}$ | $\mathbf{V}_{\rm tan}$ | Total Mass[a] | Mass Ratio[b] | $\mathcal{V}_{\rm res}$[c] | $\mathbf{N}_{\rm halos}$[d] | $\mathbf{N}_{\rm p}$[e] | $[\mathbf{V}_3, \mathbf{D}_\ell, \mathbf{D}_{\rm s}]$[f] |
|---|---|---|---|---|---|---|---|---|---|
| Zeus & Hera | 595 | -158.4 | 173.6 | $3.98\times10^{12}$ | 2.05 | 39.7 | 3,956 | 44M | [73, 730, 1300] |
| Scylla & Charybdis | 705 | -21.1 | 132.4 | $3.97\times10^{12}$ | 1.45 | 38.1 | 4,381 | 47M | [105, 500, 1090] |
| Romulus & Remus | 935 | -20.4 | 13.2 | $3.15\times10^{12}$ | 1.53 | 34.6 | 2,522 | 30M | [62, 400, 1330] |
| Orion & Taurus | 829 | -69.8 | 62.9 | $4.04\times10^{12}$ | 2.38 | 24.7 | 2,856 | 36M | [56, 1060, 1900] |
| Kek & Kauket | 1040 | -32.3 | 38.6 | $3.25\times10^{12}$ | 2.06 | 43.2 | 3,461 | 40M | [114, 960, 1680] |
| Hamilton & Burr | 941 | -18.0 | 37.7 | $3.26\times10^{12}$ | 1.17 | 24.7 | 2,882 | 32M | [54, 1390, 570] |
| Lincoln & Douglas | 780 | -86.6 | 42.4 | $3.89\times10^{12}$ | 1.90 | 18.2 | 2,801 | 33M | [60, 1860, 1160] |
| Serena & Venus* | 687 | -109.0 | 71.0 | $4.26\times10^{12}$ | 1.94 | 24.9 | 4,797 | 55M | [159, 890, 1540] |
| Sonny & Cher | 966 | -104.9 | 42.0 | $3.69\times10^{12}$ | 1.05 | 9.7 | 2,290 | 29M | [84, 990, 840] |
| Hall & Oates | 980 | -8.9 | 43.7 | $2.71\times10^{12}$ | 1.26 | 14.5 | 1,713 | 24M | [64, 1070, 1590] |
| Thelma & Louise | 832 | -52.4 | 11.0 | $2.36\times10^{12}$ | 1.30 | 5.3 | 1,693 | 20M | [64, 1130, 460] |
| Siegfried & Roy* | 878 | -68.5 | 57.6 | $4.31\times10^{12}$ | 1.02 | 11.9 | 5,087 | 61M | [157, 610, 1090] |
| Milky Way & M31 | $770 \pm 80$[g] | $-109 \pm 9$[g] | $<52$[g] | $3.8 \pm 0.7\times10^{12}$[h] | $1.26\ ^{+0.69}_{-0.24}$[i] | – | – | – | [64, 890, 450][j] |

[a] Sum of virial masses: $M_{\rm v,1} + M_{\rm v,2}$

[b] Ratio of virial masses: $M_{\rm v,2}/M_{\rm v,1}$, where $M_{\rm v,2} \geq M_{\rm v,1}$.

[c] Bi-spherical volume of the high resolution region at $z = 0$ that is uncontaminated by low-resolution particles. Specifically, $\mathcal{V}_{\rm res}$ is defined as the union of the two maximal spheres, centered on each pair, that are uncontaminated.

[d] Number of resolved halos within the high-resolution volume $\mathcal{V}_{\rm res}$.

[e] Number of particles in millions (rounded to the nearest million) within the high-resolution volume $\mathcal{V}_{\rm res}$.

[f] The value of $V_{\rm max}$ (in km/s) for and distances to (in Mpc) the largest halo within 1.2 Mpc of either host that is not within 300 kpc of either host. The distances listed are relative to the larger and smaller of the two hosts, respectively.

[g] From van der Marel et al. (2012) with 2-$\sigma$ uncertainties quoted.

[h] In listing this value, we average the timing argument result $M_{\rm v,1} + M_{\rm v,2} = (4.3 \pm 1.1) \times 10^{12} M_\odot$ from van der Marel et al. (2012) and the sum of our fiducial $M_{\rm v}^{\rm MW}$ and $M_{\rm v}^{\rm M31}$ values listed in Tables 2.2 and 2.3. Quoted uncertainties are 2-$\sigma$.

[i] The quoted average and ratio takes into account that the quantity is defined to be larger than unity. It combines the constraints listed in Tables 2.2 and 2.3 and quotes 90% uncertainties.

[j] We list the most luminous galaxy within 1.2 Mpc of either the MW or M31 according to McConnachie (2012): NGC 6822 with $\rm L_V = 1.04 \times 10^8\ L_\odot$ and $M_\star = 8.3 \times 10^7\ M_\odot$. We let $\mathbf{D}_\ell = \mathbf{D}_{\rm M31}$ and $\mathbf{D}_{\rm s} = \mathbf{D}_{\rm MW}$. The $V_{\rm max}$ listed for NCG 6822 is very rough, and is based on assuming the abundance matching prescription described in Section 2.4.1 and the $V_{\rm max} - M$ relation in Figure 2.1. Note that the galaxy IC 1613 is only slightly less luminous than NGC 6822 but is approximately 370 kpc closer to M31 and 300 kpc farther from the MW.

* In order to avoid bias, these pairs are indicated with dashed lines in Figures 2.4, 2.5, 2.18, and 2.19 and have been excluded from Figures 2.6, 2.7, 2.8, 2.11, 2.12, and 2.13 because they have large companions at $\sim 1$ Mpc distances.

Table 2.1: Properties of the 12 ELVIS pairs together with associated properties of the MW/M31 pair, where appropriate. Detailed information about the individual halos that make up these pairs is given in Tables 2.2 and 2.3, where they are referred to by the same names used in Column 1. Distances (Column 1 and Column 10) are given in kpc, velocities are in km/s, masses are in $M_\odot$, and $\mathcal{V}_{\rm res}$ is given in Mpc$^3$.

the physical separation between halo centers, their relative radial and tangential velocities,[8] as well as their virial masses and virial mass ratios. Column 7 lists a conservative estimate of the high-resolution simulation volume $\mathcal{V}_{\rm res}$, defined as the union of the two maximal spheres, centred on each pair, that is uncontaminated by any lower resolution particles. Columns 8 and 9 list the overall number of halos (above our completeness limit of $V_{\rm max} > 8\ {\rm km\,s^{-1}}$) and number of simulation particles contained within the volume $\mathcal{V}_{\rm res}$. The final column lists the $V_{\rm max}$ value of and distances to the largest halo within 1.2 Mpc of either host (but outside of the 300 kpc virial region), which serve as an indication of the larger-scale environment. Note that the virial volumes of Hera and Zeus slightly overlap; however, only a single subhalo is identified in that overlapping volume, so the effect on subsequent results is negligible.

Two of the pairs – Siegfried & Roy and Serena & Venus – have a particularly large halo ($V_{\rm max} = 157,\ 159\,{\rm km\,s^{-1}}$) within 1.2 Mpc of one of the hosts. This may seem contrary to our isolation criteria, but in both cases this third halo is less massive than either of the paired hosts. Nevertheless, the presence of the massive companions may render these pairs less than ideal comparison sets for the real Local Group. In all figures below that make predictions for the overall count of galaxies expected within $\sim$ Mpc scales, we either remove these two pairs entirely, or show the affected systems with dashed lines.

Figure 2.2 shows visualizations of our LG analogs coloured by the locally smoothed density; each box renders a cube 1.5 Mpc on a side centred on the midpoint of the two hosts. Pair names are indicated and the visualizations are rotated such that the pair is aligned with the horizontal axis, though not necessarily with an orientation that maximizes the apparent separation. Each of these images is fully resolved without contamination from low-resolution particles, so the shape of the density fields represented are accurate. There are a number of features of interest in these images. For example, it is readily apparent that Sonny (of Sonny & Cher in the bottom row) is undergoing a major merger. It has a subhalo of

[8]The kinematics of our pairs as listed in Table 2.1 are consistent with those found for a larger number of pairs in simulations by Forero-Romero et al. (2013).

$V_{\rm max} = 115$ km s$^{-1}$, which is comparable to the host halo's $V_{\rm max} = 180$ km s$^{-1}$ — not unlike M33 paired with M31. Also, the third massive object near Siegfried & Roy (as discussed above) is evident in the bottom-right panel. As we will discuss below, Zeus & Hera (upper left) furnishes a particularly good match to the LG in many observational comparisons — the 89 km s$^{-1}$ subhalo of Hera is shown on the right.

We list the properties of the individual halos that comprise each pair in Tables 2.2 and 2.3 along with comparative information for the MW and M31, when appropriate; the lower mass halo in each pair is listed in the former, while the more massive halos are listed in the latter. Similar lists for the isolated mass-matched analogs are given in Tables 2.4 and 2.5. In each table, Columns 2 through 5 list $M_{\rm v}$, $V_{\rm v}$, $V_{\rm max}$, and $R_{\rm v}$, respectively. Column 6 gives a measure of the halo concentration, $c_{-2} \equiv R_{\rm v}/r_{-2}$, where $r_{-2}$ is the radius where $\rho r^2$ peaks [equivalent to the concentration parameter for halos that follow Navarro et al. (1996b, NFW) profiles]. Column 7 provides a measure of the halo formation redshift, $z_{0.5}$, defined when the main progenitor first obtains half its current mass. Columns 8 and 9 list the number of $V_{\rm max} > 8$ km s$^{-1}$ subhalos within $R_{\rm v}$ and 300 kpc, respectively, and column 10 lists the $V_{\rm max}$ of the largest subhalo within 300 kpc. Column 11 gives $R_{\rm res}$, the radius of the largest sphere within which there are no low-resolution particles (an indication of the high-resolution volume size). Columns 12 and 13 list the number of particles (in millions, rounded to the nearest million) and number of identified halos (with $V_{\rm max} > 8$ km s$^{-1}$) within $R_{\rm res}$ for each halo.

Note that in what follows we will occasionally present results for a region we define as the Local Volume – the union of two spheres of radius 1.2 Mpc centred on each host. As can be seen from Column 11 of Tables 2.2 and 2.3, four of our pairs are technically contaminated in this region (Sonny & Cher, Hall & Oats, Thelma & Louise, and Siegfried & Roy). However the mass fraction of low-resolution particles in the effected volumes is minimal (0.01, 0.007, 0.06, and 0.0008 per cent respectively) so the practical effects on our results should be

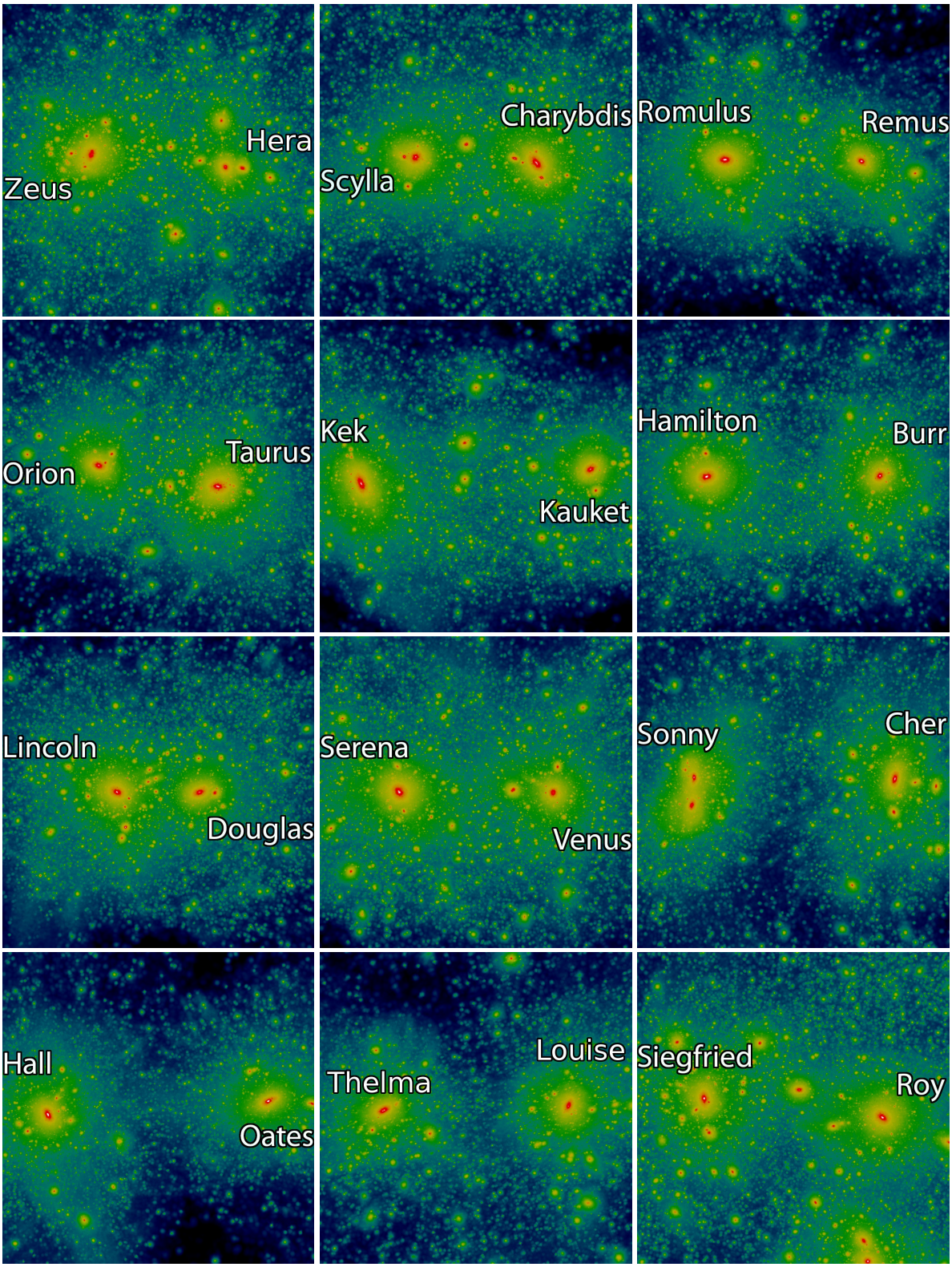


Figure 2.2: Visualizations of the ELVIS pairs, shown in cubes 1.5 Mpc on a side, each centred on the mean centre of the pair with names given.

| **Halo** | $\mathbf{M_v}$ | $\mathbf{V_v}$ | $\mathbf{V_{max}}$ | $\mathbf{R_v}$ | $\mathbf{c_{-2}}$ [a] | $\mathbf{z_{0.5}}$ [b] | $\mathbf{N_{halos}}$ [c] | $\mathbf{N_{halos}}$ [d] | $_{\mathrm{Max}}\mathbf{V_{max}}$ [e] | $\mathbf{R_{res}}$ [f] | $\mathbf{N_p}$ [g] | $\mathbf{N_{halos}}$ [h] |
|---|---|---|---|---|---|---|---|---|---|---|---|---|
| Hera | 1.30 | 140 | 159 | 285 | 7.9 | 0.79 | 397 | 435 | 89 | 1330 | 39M | 3,348 |
| Scylla | 1.62 | 151 | 179 | 306 | 6.4 | 1.24 | 577 | 567 | 84 | 1280 | 36M | 3,171 |
| Remus | 1.24 | 138 | 177 | 280 | 12.3 | 1.53 | 440 | 463 | 40 | 1420 | 26M | 2,027 |
| Taurus | 1.19 | 136 | 169 | 276 | 10.9 | 1.08 | 383 | 419 | 61 | 1210 | 31M | 2,321 |
| Kauket | 1.06 | 131 | 157 | 266 | 9.6 | 1.10 | 388 | 426 | 64 | 1560 | 32M | 2,687 |
| Burr | 1.50 | 147 | 173 | 299 | 10.6 | 1.18 | 613 | 615 | 39 | 1480 | 29M | 2,529 |
| Douglas | 1.34 | 142 | 169 | 287 | 9.6 | 0.99 | 412 | 430 | 89 | 1320 | 31M | 2,558 |
| Venus | 1.45 | 145 | 156 | 295 | 1.8 | 0.98 | 612 | 623 | 83 | 1390 | 45M | 3,879 |
| Cher | 1.80 | 156 | 171 | 317 | 11.0 | 0.66 | 580 | 552 | 81 | 1120 | 27M | 2,082 |
| Oates | 1.20 | 136 | 167 | 277 | 8.4 | 0.62 | 317 | 346 | 76 | 1010 | 17M | 1,085 |
| Louise | 1.03 | 130 | 157 | 263 | 17.0 | 1.61 | 357 | 407 | 54 | 800 | 11M | 928 |
| Roy | 2.14 | 166 | 194 | 336 | 11.1 | 1.14 | 702 | 628 | 64 | 1150 | 53M | 4,325 |
| Milky Way | $1.6\ ^{+0.8}_{-0.6}$ [i] | $150\ ^{+22}_{-22}$ | – | $304^{+45}_{-45}$ | – | – | – | $\geq 27$ [j] | 88 [k] | – | – | – |

[a] Halo concentration defined as $c_{-2} \equiv R_v/r_{-2}$, where $r_{-2}$ is the radius where $\rho r^2$ peaks. This parameter is equivalent to the NFW concentration for halos that follow perfect NFW profiles (Navarro et al., 1996b).

[b] Formation time proxy defined as the redshift $z$ when the main progenitor mass first equaled $0.5\,M_v(z=0)$.

[c] Number of subhalos within $R_v$ with $V_{max} > 8$ km/s.

[d] Number of subhalos within 300 kpc with $V_{max} > 8$ km/s.

[e] $V_{max}$ value of the largest identified subhalo within 300 kpc.

[f] The high-resolution radius, defining a sphere centered on the halo within which there is zero contamination from low-resolution particles.

[g] Number of particles in millions (rounded to the nearest million) within the high-resolution radius $R_{res}$.

[h] Number of subhalos within $R_{res}$ with $V_{max} > 8$ km/s.

[i] Taken from Boylan-Kolchin et al. (2013) with 90% c.l. quoted.

[j] As enumerated in McConnachie (2012).

[k] The LMC, from Olsen et al. (2011)

Table 2.2: Properties of the 12 paired halos in our Local Group sample that are the less massive of their pair, along with the properties of the MW, where appropriate. The halos are listed in the same order as in Tables 2.1 and 2.3; they are identified by the names used in Column 1 of the former Table and are in paired configurations with the halos listed in the latter Table at $z = 0$. All values in this table are relative to the center of the each host; equivalent properties for the isolated sample are listed in Table 2.4, where identical names with preceding $i$'s may be used to identified mass-matched analogues. The table is discussed in § 2.2. Masses are listed in $10^{12} M_\odot$, velocities are given in km/s, and radii (Columns 5 and 11) are in kpc.

| **Halo** | $\mathbf{M_v}$ | $\mathbf{V_v}$ | $\mathbf{V_{max}}$ | $\mathbf{R_v}$ | $\mathbf{c_{-2}}$ | $\mathbf{z_{0.5}}$ | $\mathbf{N_{halos}}$ | $\mathbf{N_{halos}}$ | $^{\mathrm{Max}}\,\mathbf{V_{max}}$ | $\mathbf{R_{res}}$ | $\mathbf{N_p}$ | $\mathbf{N_{halos}}$ |
|---|---|---|---|---|---|---|---|---|---|---|---|---|
| Zeus | 2.67 | 178 | 203 | 362 | 5.6 | 1.08 | 1,029 | 880 | 70 | 1920 | 44M | 3,955 |
| Charybdis | 2.35 | 171 | 208 | 346 | 7.6 | 0.89 | 896 | 785 | 77 | 1910 | 47M | 4,368 |
| Romulus | 1.90 | 159 | 197 | 323 | 9.6 | 1.57 | 623 | 579 | 54 | 1760 | 30M | 2,427 |
| Orion | 2.84 | 182 | 225 | 369 | 5.3 | 1.61 | 955 | 775 | 47 | 1600 | 35M | 2,784 |
| Kek | 2.19 | 167 | 205 | 338 | 13.7 | 0.64 | 685 | 609 | 43 | 1870 | 39M | 3,333 |
| Hamilton | 1.76 | 155 | 197 | 315 | 9.9 | 1.47 | 582 | 560 | 62 | 1390 | 28M | 2,494 |
| Lincoln | 2.55 | 176 | 199 | 356 | 8.4 | 1.36 | 941 | 780 | 75 | 1270 | 31M | 2,559 |
| Serena | 2.81 | 181 | 222 | 368 | 14.4 | 1.77 | 911 | 743 | 61 | 1480 | 51M | 4,418 |
| Sonny | 1.89 | 159 | 180 | 322 | 2.4 | 0.30 | 664 | 637 | 115 | 970 | 20M | 1,480 |
| Hall | 1.52 | 148 | 180 | 299 | 10.3 | 1.04 | 437 | 438 | 50 | 1350 | 23M | 1,560 |
| Thelma | 1.34 | 141 | 169 | 287 | 7.1 | 1.44 | 421 | 438 | 48 | 910 | 18M | 1,379 |
| Siegfried | 2.17 | 166 | 195 | 337 | 6.5 | 0.67 | 827 | 734 | 62 | 1090 | 46M | 3,674 |
| M31 | $1.8 \pm 0.65$ [a] | $156\ ^{+17}_{-22}$ | – | $317^{+35}_{-44}$ | – | – | – | $\geq 32$ [b] | 130 [c] | – | – | – |

[a] Combining results from Fardal et al. (2013) and van der Marel et al. (2012) who obtain $M_{\mathrm{v}}^{M31} = (2.1 \pm 1.0) \times 10^{12}$ and $(1.5 \pm 0.8) \times 10^{12}$, respectively, with 2-$\sigma$ errors quoted.

[b] As enumerated in McConnachie (2012).

[c] The Triangulum galaxy (M33), from Corbelli (2003).

Table 2.3: Properties of the 12 paired halos in our Local Group sample that are the more massive of their pair, along with the properties of M31, where appropriate. The halos are listed in the same order as in Tables 2.1 and 2.2; they are identified by the names used in Column 1 of the former Table and are in paired configurations with the halos listed in the latter Table at $z = 0$. All values in this table are again relative to the center of the each host; equivalent properties for the isolated sample are listed in Table 2.5, where identical names with preceding $i$'s may be used to identified mass-matched analogues. The table is discussed in § 2.2. Columns are identical to those in Table 2.2; masses are again listed in $10^{12} M_{\odot}$, velocities are given in km/s, and radii (Columns 5 and 11) are in kpc.

| **Halo** | $\mathbf{M_v}$ | $\mathbf{V_v}$ | $\mathbf{V_{max}}$ | $\mathbf{R_v}$ | $\mathbf{c_{-2}}$ | $\mathbf{z_{0.5}}$ | $\mathbf{N_{halos}}$ | $\mathbf{N_{halos}}$ | $_{\text{Max}}\,\mathbf{V_{max}}$ | $\mathbf{R_{res}}$ | $\mathbf{N_p}$ | $\mathbf{N_{halos}}$ |
|---|---|---|---|---|---|---|---|---|---|---|---|---|
| iHera | 1.22 | 137 | 163 | 278 | 7.9 | 0.8 | 420 | 450 | 41 | 1540 | 17M | 1,348 |
| iScylla | 1.59 | 150 | 176 | 304 | 9.9 | 0.97 | 437 | 436 | 84 | 1560 | 20M | 1,500 |
| iRemus | 1.31 | 141 | 166 | 285 | 8.0 | 0.91 | 494 | 515 | 54 | 1400 | 14M | 1,261 |
| iTaurus | 1.23 | 138 | 165 | 279 | 10.4 | 1.36 | 453 | 481 | 46 | 1750 | 14M | 1,315 |
| iKauket[†] | 1.02 | 129 | 157 | 262 | 11.1 | 0.97 | 278 | 327 | 39 | 2120 | 21M | 1,730 |
| iBurr | 1.56 | 149 | 179 | 302 | 13.6 | 0.75 | 548 | 540 | 66 | 1610 | 15M | 1,279 |
| iDouglas | 1.30 | 140 | 180 | 285 | 16.1 | 1.76 | 375 | 383 | 49 | 1930 | 15M | 1,107 |
| iVenus | 1.39 | 143 | 179 | 291 | 14.3 | 1.41 | 461 | 483 | 46 | 2150 | 32M | 2,684 |
| iSonny | 1.68 | 153 | 187 | 310 | 4.5 | 0.69 | 647 | 632 | 117 | 2010 | 20M | 1,877 |
| iOates | 1.20 | 136 | 157 | 277 | 8.4 | 0.72 | 444 | 478 | 78 | 1580 | 13M | 1,068 |
| iLouise | 1.01 | 129 | 155 | 261 | 8.4 | 1.22 | 378 | 414 | 49 | 2410 | 14M | 1,253 |
| iRoy | 2.26 | 169 | 205 | 342 | 3.9 | 1.11 | 844 | 769 | 103 | 1750 | 22M | 1,850 |
| iScilla HiRes | 1.61 | 150 | 175 | 305 | 9.5 | 0.95 | 419 (3,824)[⋆] | 413 (3,770)[⋆] | 87 | 1540 | 155M | 1,491 (12,509)[⋆] |
| iKauket HiRes [‡] | 1.03 | 130 | 158 | 263 | 11.8 | 1.0 | 277 (2,279)[⋆] | 324 (2,620)[⋆] | 38 | 400 | 56M | 446 (3,493)[⋆] |

[†] iKauket was initialized at $z = 250$ for both the fiducial and HiRes runs.

[⋆] Values in parentheses correspond to subhalo counts down to $V_{\rm max} > 4$ km/s, the estimated completeness limit of the HiRes simulations.

[‡] This halo was initialized with a smaller Lagrange volume of high-resolution particles than the rest, which is why it has an anomalously small high-resolution radius.

Table 2.4: Properties of the 12 isolated halos in our Local Group sample that are the less massive of their "pair." The halos are mass matched to those in our Local Group samples. The name identifies the paired halo with a nearly identical mass, the properties of which are listed in Table 2.2, and the preceding $i$ indicates an isolated analogue. The last two rows correspond to HiRes simulations of two of the isolated halos; the third is detailed in Table 2.5. Columns are identical to those of Tables 2.2 and 2.3; masses are again listed in $10^{12} M_\odot$, velocities are given in km/s, and radii (Columns 5 and 11) are in kpc.

| **Halo** | $\mathbf{M_v}$ | $\mathbf{V_v}$ | $\mathbf{V_{max}}$ | $\mathbf{R_v}$ | $\mathbf{c_{-2}}$ | $\mathbf{z_{0.5}}$ | $\mathbf{N_{halos}}$ | $\mathbf{N_{halos}}$ | $_{\text{Max}}\,\mathbf{V_{max}}$ | $\mathbf{R_{res}}$ | $\mathbf{N_p}$ | $\mathbf{N_{halos}}$ |
|---|---|---|---|---|---|---|---|---|---|---|---|---|
| iZeus | 2.59 | 176 | 205 | 358 | 5.5 | 1.3 | 925 | 773 | 60 | 1760 | 27M | 2,312 |
| iScylla | 1.59 | 150 | 176 | 304 | 9.9 | 0.97 | 437 | 436 | 84 | 1560 | 20M | 1,500 |
| iRomulus | 1.97 | 161 | 186 | 327 | 11.3 | 0.88 | 792 | 734 | 75 | 1890 | 21M | 1,899 |
| iOrion | 2.84 | 182 | 218 | 369 | 4.9 | 1.64 | 1,179 | 1,015 | 54 | 2060 | 37M | 3,315 |
| iKek | 2.41 | 172 | 204 | 349 | 5.5 | 0.74 | 705 | 618 | 71 | 1630 | 27M | 2,267 |
| iHamilton | 1.86 | 158 | 203 | 321 | 14.2 | 2.11 | 566 | 523 | 57 | 1550 | 17M | 1,309 |
| iLincoln | 2.62 | 177 | 213 | 359 | 13.8 | 0.89 | 813 | 702 | 83 | 1350 | 27M | 2,017 |
| iSerena | 2.67 | 178 | 212 | 361 | 11.4 | 1.15 | 952 | 817 | 81 | 1660 | 26M | 2,218 |
| iCher | 1.92 | 160 | 170 | 324 | 6.4 | 0.6 | 701 | 660 | 63 | 2230 | 22M | 1,888 |
| iHall$^{\diamond}$ | 1.71 | 148 | 172 | 300 | 6.0 | 1.13 | 528 | 528 | 92 | 1590 | 16M | 1,264 |
| iThelma | 1.39 | 143 | 188 | 291 | 9.6 | 1.56 | 407 | 421 | 37 | 1950 | 14M | 1,043 |
| iSiegfried | 2.40 | 172 | 211 | 349 | 11.1 | 1.42 | 733 | 643 | 55 | 1360 | 21M | 1,589 |
| iHall HiRes | 1.67 | 152 | 167 | 309 | 5.8 | 1.07 | 608$^{\star}$ (5,266)$^{\star}$ | 592$^{\star}$ (5,114)$^{\star}$ | 93 | 1.59 | 125M | 1,286$^{\star}$ (11,176)$^{\star}$ |

$^{\diamond}$ Differences in the phase of subhalo orbits between this run and the HiRes equivalent result in the largest subhalo ($V_{\rm max} = 93 {\rm km\,s^{-1}}$) being located just beyond $R_{\rm v}$ at the fiducial resolution. To show convergence with the HiRes run, we include the mass of that halo in the virial mass of iHall and list it in Column 10, though it is just beyond 300 kpc. The uncorrected substructure counts are also divergent, but the number of objects within 400 kpc agrees within 5%. The uncorrected mass ($1.53 \times 10^{12} M_{\odot}$) also agrees with the paired halo, Hall, to within 1%.

$^{\star}$ Values in parentheses correspond to subhalo counts down to $V_{\rm max} > 4$ km/s, the estimated completeness limit of the HiRes simulations.

Table 2.5: Properties of the 12 isolated halos in our Local Group sample that are the more massive of their pair. The halos are mass matched to those in our Local Group sample. The name identifies the paired halo with a nearly identical mass, the properties of which are listed in Table 2.3, and the preceding $i$ indicates an isolated analogue. The last row again corresponds to a HiRes simulation of one of the isolated halos; the remaining two are detailed in Table 2.4. Columns are identical to those of Tables 2.2, 2.3, and 2.4; masses are again listed in $10^{12} M_{\odot}$, velocities are given in km/s, and radii (Columns 5 and 11) are in kpc.

negligible (see, e.g. Oñorbe et al., 2014).

Before devoting the next section to a detailed comparison of paired versus unpaired hosts, we mention that we find no statistical difference in the $c_{-2}$ and $z_{0.5}$ distributions between the two sets. Though two of our halos (Serena and Sonny) that happen to be members of pairs have anomalously low $c_{-2}$ values, we suspect that in Sonny's case this is a result of an ongoing major merger. The median formation redshifts for our paired and unpaired samples are both $z_{0.5} \simeq 1.1$, with no indication that paired halo formation times correlate.

The lack of difference in the $z_{0.5}$ distribution between the two samples is consistent with the comparison made by Forero-Romero et al. (2011) using similarly paired halos found in the Bolshoi simulations. These authors point out that the three LG-like pairs identified in the constrained CLUES simulations have anomalously early formation times, all three with half-mass formation times $z_{0.5} \gtrsim 1.5$. Three of our 12 paired systems are similarly early-forming (Romulus & Remus, each with $z_{0.5} \simeq 1.6$), Orion & Taurus (with $z_{0.5} = 1.6$ and 1.3, respectively), and Thelma & Louise (with $z_{0.5} = 1.4$ and 1.6).

## 2.3 Paired versus Isolated Galaxies

### 2.3.1 Halo abundances

We begin by examining the abundance of dark matter structures, characterized by their $M_{\rm peak}$ values, within various radial boundaries; counts as a function of $V_{\rm max}$ are presented in § 2.6.

Figure 2.3 shows the cumulative $M_{\rm peak}$ functions for subhalos within $R_{\rm v}$, normalized to the host halo virial mass $M_{\rm v}$, for each of the 48 hosts in ELVIS. Isolated hosts are shown as thin magenta lines and the paired hosts are plotted in black. The two distributions clearly

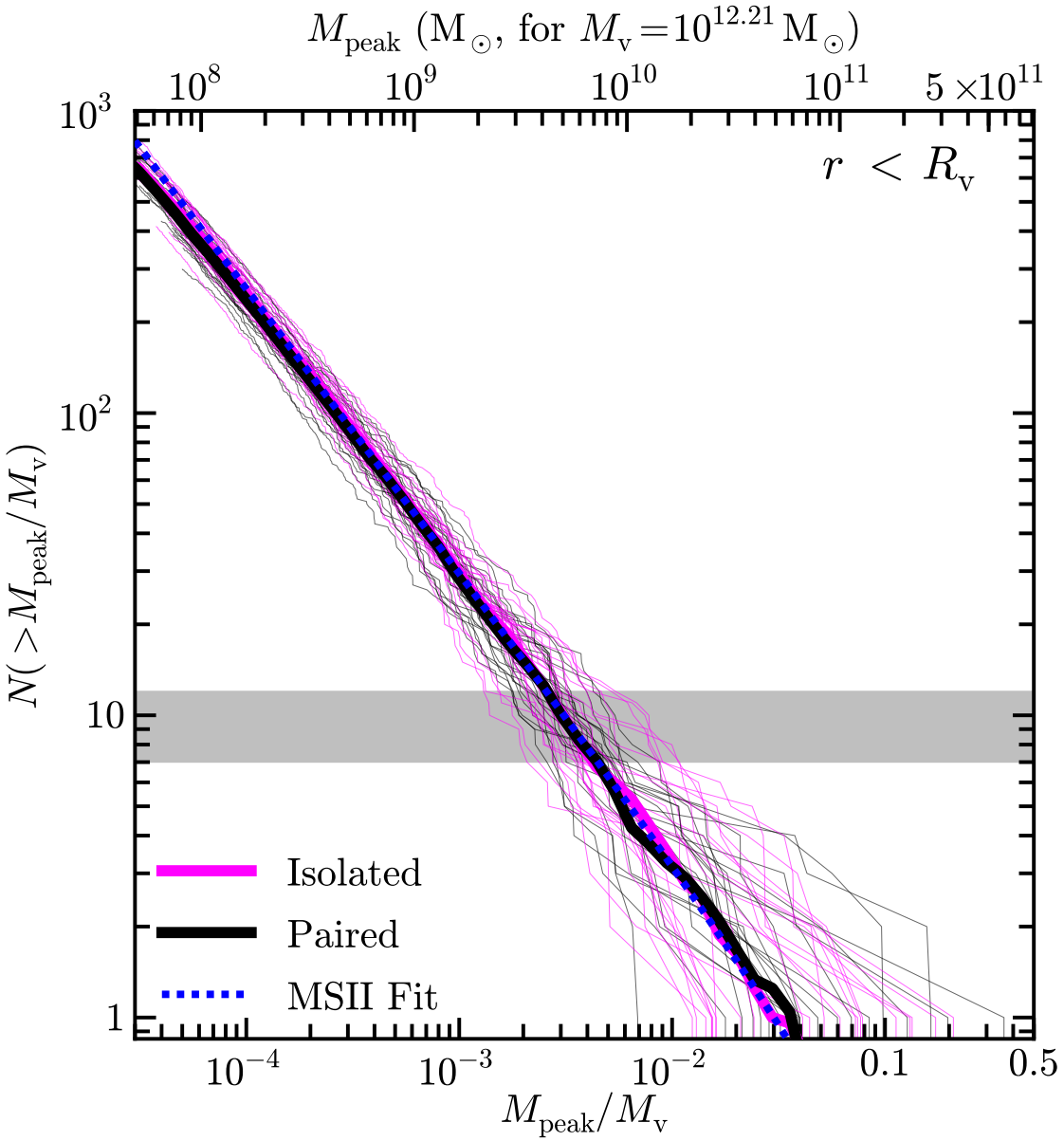


Figure 2.3: Cumulative subhalo peak mass function ($M_{\rm peak}$) normalized by host $M_{\rm v}$ for each isolated (thin magenta lines) and paired (thin black lines) host. All objects within $R_{\rm v}$ are plotted. The average for each population is shown by the thick lines of corresponding colour. Statistically, the mass functions for paired and isolated hosts are indistinguishable, though the halo-to-halo scatter is large. The upper axis is scaled to the subhalo $M_{\rm peak}$ values assuming a host virial mass of $M_{\rm v} = 1.6 \times 10^{12} M_\odot$, which is our fiducial MW mass. Thin lines are truncated at $M_{\rm peak} = 6 \times 10^7 M_\odot$, the completeness limit of our simulation catalogs. The grey band shows the range in number of satellites around the MW and M31 with stellar masses above $10^6 M_\odot$; from this band, one can see that such galaxies would be expected to form in halos more massive than $M_{\rm peak} \simeq 3 \times 10^{-3} M_{\rm v} \simeq 5 \times 10^9 M_\odot$.

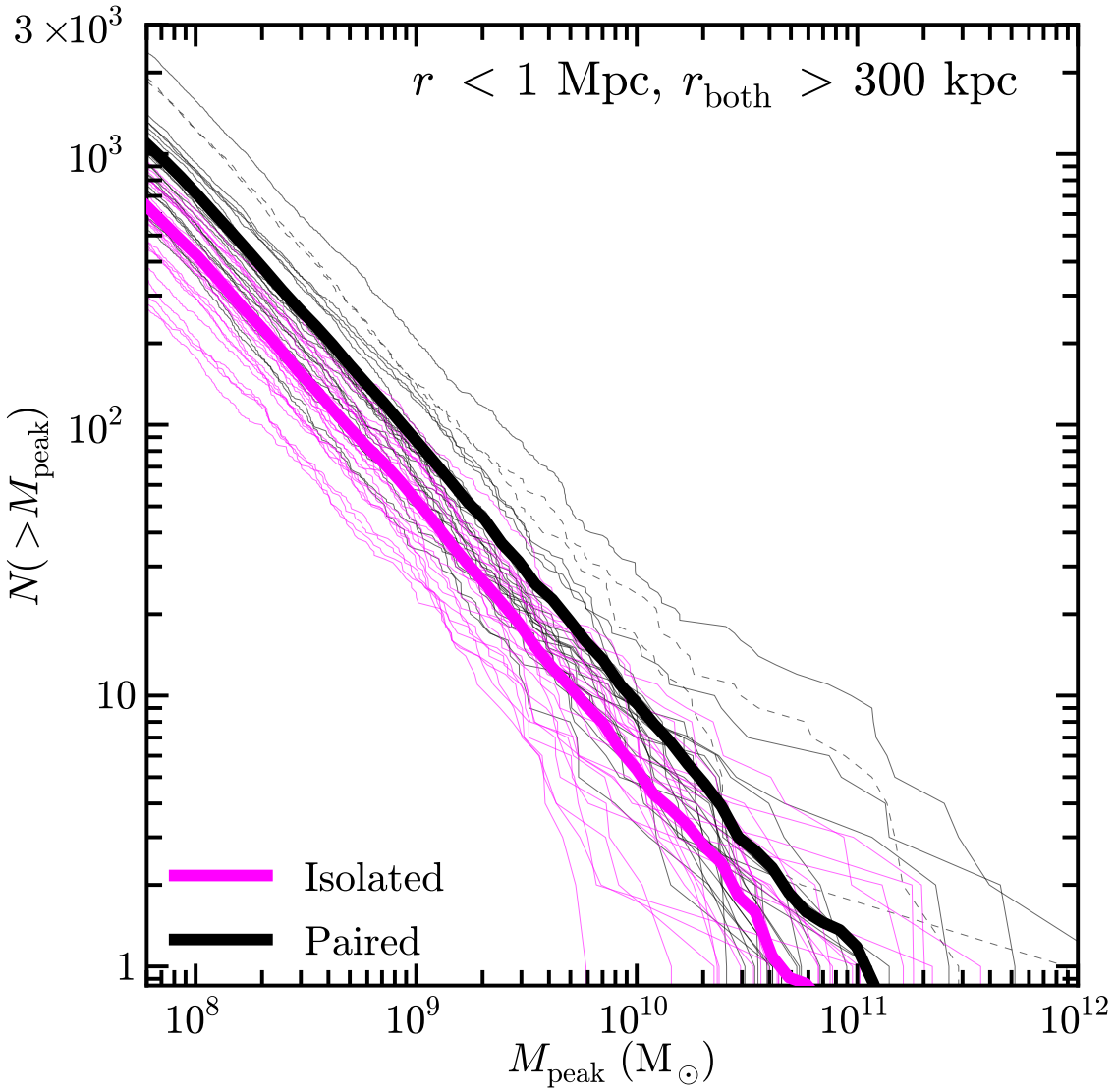


Figure 2.4: Cumulative counts, as a function of $M_{\rm peak}$, for halos that are between 300 kpc and 1 Mpc of any host. The paired population (black) has an amplitude that is approximately 80% larger at fixed $M_{\rm peak}$ than that of the isolated analogs (magenta). The environment around a LG pair thus differs noticeably from that of an isolated MW-size halo, even though such differences are not manifest within the virial radius (Figure 2.3).

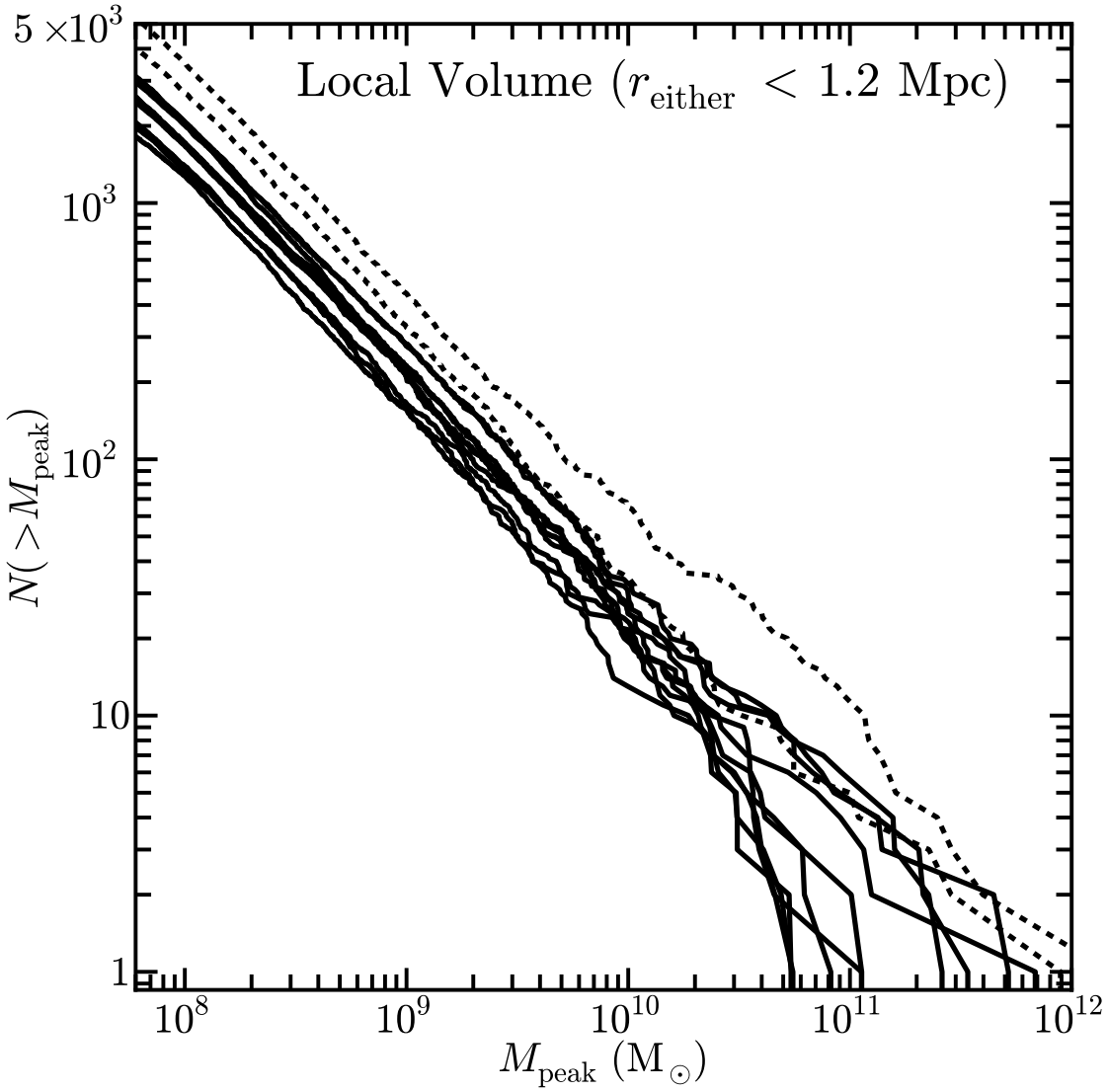


Figure 2.5: The $M_{\rm peak}$ functions around the LG pairs; each line represents a pair of giants and includes all halos (excluding the MW and M31 analogs) within 1.2 Mpc of either host, which we define as the Local Volume. Two pairs contain a third large system within the volume and are thus shown as dashed lines. We predict $\sim 2000-3000$ objects with $M_{\rm peak} > 6\times10^7 M_\odot$ within the region.

overlap. The thick lines denote the mean cumulative count at fixed $M_{\rm peak}/M_{\rm v}$ for the isolated (magenta) and paired (black) populations. Both distributions are well fitted at the low mass end by a power-law:

$$N_{\rm v}(> M_{\rm peak}) = 3.85 \left( \frac{M_{\rm peak}}{0.01\, M_{\rm v}} \right)^{-0.9} . \tag{2.1}$$

Within $R_{\rm v}$, subhalo counts within isolated and paired halos in ELVIS are indistinguishable. Even for high-mass subhalos, where the intrinsic scatter in the counts is large, the means agree well. The blue dashed line, which sits practically on top of the ELVIS means, shows the mean power-law fit obtained by Boylan-Kolchin et al. (2010) for subhalos in a large sample of MW-mass halos from the Millennium-II Simulation (MS-II; Boylan-Kolchin et al., 2009). The same fit also matches the substructure counts from the Aquarius simulations (Springel et al., 2008) well. The agreement between our simulations and MS-II/Aquarius is remarkable, especially given that the cosmology of these older simulations is slightly different from our adopted values, which are based on more recent constraints.

Broadly speaking, the scatter in subhalo counts among halos also agrees between the two samples. At small masses ($M_{\rm peak}/M_{\rm v} \lesssim 10^{-3}$) we find that the standard deviation divided by the mean approaches $\sigma/\langle N \rangle \simeq 0.15$, and that the scatter increases towards higher masses, with $\sigma/\langle N \rangle \simeq 0.4$ at $M_{\rm peak} \simeq 0.01 M_{\rm v}$. This result is consistent with an intrinsic halo-to-halo scatter of $\sim 15\%$ in the abundance of substructure reported elsewhere (Boylan-Kolchin et al., 2010; Busha et al., 2011; Wu et al., 2013).

Though we do not plot it, the $z = 0$ (bound) mass functions also agree well within $R_{\rm v}$ and are both well fitted by

$$N_{\rm v}(> M) = 1.11 \left( \frac{M}{0.01\, M_{\rm v}} \right)^{-0.95} , \tag{2.2}$$

though the scatter is slightly larger than in the $M_{\rm peak}$ function ($\sigma/\langle N \rangle \sim 0.2$ at small masses).

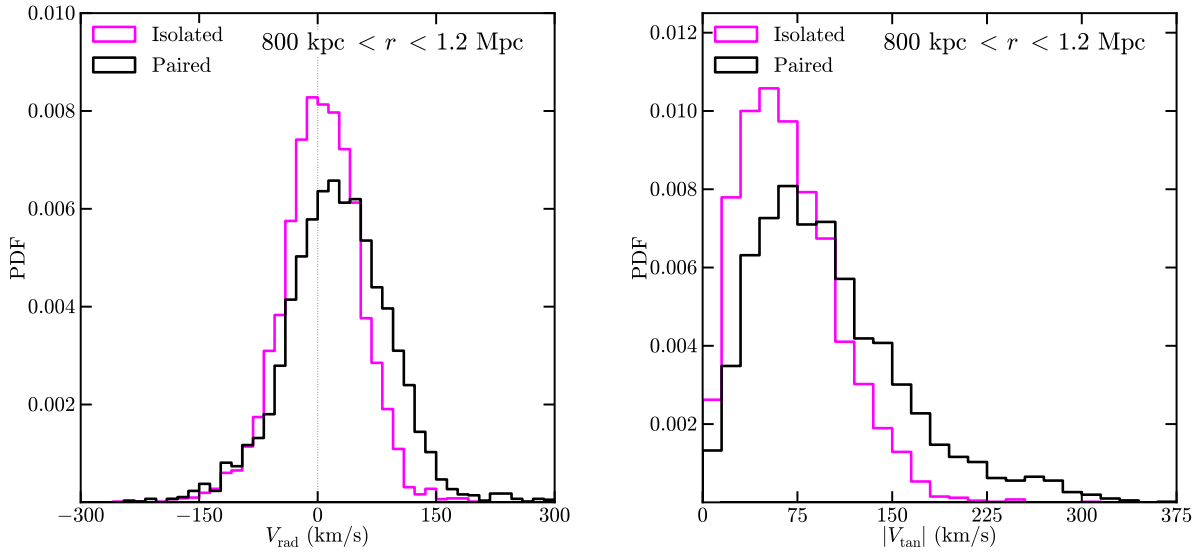


Figure 2.6: Stacked distributions of radial (left panel) and tangential (right panel) velocities for halos around the isolated (magenta) and paired (black) halos at distance of $0.8-1.2\,$Mpc from the *nearest* host. While the distributions for paired and isolated halos are the same within $R_{\rm v}$ (not plotted), the differences become pronounced at large radii, with paired environments being substantially hotter. While essentially all halos $\sim 1$ Mpc from isolated MW analogs have $V_{\rm tan} < 200\,{\rm km\,s^{-1}}$, a large fraction around LG analogs have $V_{\rm tan} > 200\,{\rm km\,s^{-1}}$. It is also apparent that while the radial velocities of halos at $\sim 1$ Mpc distance from isolated MW-like hosts are centred on zero, the paired analogs have an excess population of outflowing systems. These outflowing systems include a "backslash" population that is larger among pairs (see § 2.3.3) and also objects that have yet to turn around from the Hubble flow (the zero velocity surface is centred on the pair at $\sim 1$ Mpc distance, not the individual host). One broad implication of this Figure is that in order to correctly predict the large-scale velocity field around the MW, one must account for the presence of M31.

One take away from this initial result is that predictions for subhalo counts within the virial radius from previous high resolution simulations that studied isolated MW-size hosts (e.g. Diemand et al., 2008; Kuhlen et al., 2008; Springel et al., 2008) are not expected to be significantly different than those for paired halos like the MW and M31.

At distances beyond the virial radii of either host, the presence of a massive companion should affect halo abundances. To compare the counts at large distances between isolated and paired MW-size halos, we must avoid the bias that would be introduced by simply counting all halos at a given distance, as many will be subhalos of the M31 analogue in the

paired systems. We attempt to remove this bias by defining a region around each host that we call the "Local Field": a spherical shell between 300 kpc and 1 Mpc of the centre of that host, but excluding the region within 300 kpc of the centre of the other giant. That is, no subhalos of either LG giant analogue are included in this region.

We plot the $M_{\rm peak}$ function for these Local Field regions around all the ELVIS halos in Figure 2.4. The environment surrounding a typical LG-like halo is richer than that around an isolated system, even when the partner's subhalos are removed. Specifically, the average relations are again well fitted at the low mass end by power laws, but the normalization for the paired sample is about 80% higher than that of the isolated sample:

$$N_{0.3-1}(> M_{\rm peak}) = N_0 \left( \frac{M_{\rm peak}}{10^{10} M_\odot} \right)^{-0.9} , \tag{2.3}$$

with $N_0 = 6.4$ for the isolated sample and $N_0 = 11$ for the paired sample. The dashed lines in Figure 2.4 indicate the two halos that have a large companion within the $0.3 - 1$ Mpc region (see § 2.2.3 and Table 2.1). It is possible that these systems are poor comparison sets to the Local Group, which appears to lack such a galaxy (Table 2.1). If we remove the dashed lines from the fit, the normalization for the paired systems becomes $N_0 = 9.2$, which is $\sim 56\%$ higher than that for the isolated sample (removing the isolated counterparts to those halos also gives a slightly lower normalization $N_0 = 5.9$). While the distributions show some overlap, the presence of a paired companion appears to bias the overall large-scale environment to be substantially richer in small halos, even when the subhalos of the paired host are excluded from the counts.

Figure 2.5 presents total halo number counts as a function of $M_{\rm peak}$ within a bi-spherical volume defined by overlapping spheres of radius 1.2 Mpc of each paired host. There is one line for every ELVIS pair, thus each can be regarded as a realization of the LG itself. The dashed lines indicate the two pairs that have large companions in the region, possibly

making them less than ideal comparison sets for the LG. Neglecting those two systems, the group-to-group scatter in this Local Volume mass function is remarkably tight, spanning less than a factor of $\sim 2$ over all 10 realizations for masses $M_{\rm peak} \lesssim 10^{10}, M_{\odot}$. In total, the best LG analogs in the ELVIS suite have $2000 - 3000$ halos with $M_{\rm peak} > 6 \times 10^7\, M_{\odot}$ in this Local Volume region. Of course, many of these small halos likely contain galaxies that are either devoid of stars entirely, or too faint to detect with current methods. We investigate implications for the number of observable galaxies throughout this region in §4.

### 2.3.2 Halo Dynamics

We expect that the presence of M31 alters the dynamical structure of the Milky Way's local environment relative to the environment of an isolated analogue. While we find that, within $\sim$ 300 kpc of the hosts, the paired and isolated samples have indistinguishable subhalo kinematics, regions beyond this distance show distinct kinematical differences.

Figure 2.6 shows stacked distributions of radial and tangential velocities for $M_{\rm peak} > 6 \times 10^7 M_{\odot}$ halos having distances between 800 kpc and 1.2 Mpc of a giant. Note that in these histograms, we compute the distance to both of the hosts and only use the smaller of the two distances (i.e., all halos at distance $r$ from one host are at least that same distance $r$ from the other host). Regions surrounding isolated hosts are shown in magenta while regions around paired systems are in black. The kinematic distinction is clear: paired halos are both kinematically hotter and show an excess of systems that are outflowing at this radius. As we discuss in the next subsection, this enhanced population of outflowing halos includes a large number of objects that were once within the virial radius of one of the giants. This fraction appears to be higher in paired hosts. A complication when interpreting the radial velocity figure is that the zero-velocity/turn-around surface (at $\sim$ 1 Mpc distance) for the pairs is centred between the hosts rather than on the main halo as it is for the isolated analogs. This

means that some fraction of the halos in this diagram may not have turned around from the Hubble flow.

In the histograms shown in Figure 2.6, we have removed halos belonging to the pairs Siegfried & Roy and Serena & Venus. As discussed above, these pairs have a particularly large halo within 1.2 Mpc of one of the hosts, and therefore may be poor analogs to the real LG. Including them only serves to make the overall paired histograms even hotter compared to the isolated analogs.

### 2.3.3 Backsplash Halos

Here we investigate the dynamical histories of each small halo in the vicinity of our MW analogs at $z = 0$, and specifically ask whether a halo has been within the virial radius of either giant since $z = 5$. If so, then in principle, environmental effects such as ram pressure, harassment, or strangulation could have quenched the galaxy it hosts (Kawata & Mulchaey, 2008; Boselli et al., 2008; Grcevich & Putman, 2009; Woo et al., 2013; Phillips et al., 2014). We refer to previously-interacted objects of this kind as "backsplash" halos (e.g., Gill et al. 2005 and references therein). Knebe et al. (2011) identified an additional population of halos, which they termed "renegade", that have been a member of both the M31 and MW halo analogs. We reserve a more detailed study of these interesting objects for a future work – for this paper, we combine renegade halos beyond $R_{\rm v}$ with all other backsplash halos and those within $R_{\rm v}$ with all other subhalos.

Figure 2.7 presents the differential fraction of halos that are backsplash objects as a function of distance from each host in radial bins of width $R_{\rm v}/2$. Systems around our LG-analogs are shown in black, where the distance assigned is the minimum of the distances to the two giants in the group. As in Figure 2.6, we have removed halos belonging to the two pairs in our sample with large companions at $\sim 1$ Mpc distance. The subsample of halos that meet

the radial cut from the centre of both giants simultaneously are shown in cyan. The isolated sample is shown in magenta. We indicate with open symbols bins where the full halo sample was not used, either due to contamination at large radii or because there are no halos that meet the radial cut in the bin. The points correspond to the average over all hosts and the error bars denote the full width of the distribution, measured system-by-system.

Unsurprisingly, the backsplash fraction is largest at small radii. In the regions spanning $1 - 1.5\,R_{\rm v}$, typically 70% of halos have been within $R_{\rm v}$ since $z = 5$, though that number can be as high as 80% in some cases (also see Mamon et al., 2004; Gill et al., 2005). The interaction fraction in the environment of LG-like pairs is systematically higher than in isolated analogs at large radii, and the overlapping volume (cyan) is particularly rich in objects that have interacted. Indeed, the shared region in the real LG may be the best hunting ground for potential backsplash candidate dwarfs. Remarkably, in our LG-analogue systems, the probability that a halo has interacted only drops to zero at approximately $5\,R_{\rm v}$ ($\sim$ 1.5 Mpc). Expressed cumulatively (rather than differentially), we find that the overall fraction of backsplash halos within the 1.2 Mpc Local Volume regions of our paired hosts ranges from 30% to 52%.

How might backsplash halos be distinguished observationally throughout the LG? In Figure 2.8, we compare the relative tangential and radial velocities of backsplash halos (grey line) in the $r = 400 - 800$ kpc radial bins to those that have never accreted (black line). Here we limit ourselves to paired hosts. As in Teyssier et al. (2012), we find that backsplash halos tend to be outflowing from the host that they have interacted with, whereas those that have not yet accreted are preferentially inflowing. As the right plot shows, we also expect backsplash halos to have low tangential velocities compared to those that have never been within $R_{\rm v}$. The implication is that backslash systems are more likely to be on radial orbits and to be on their way out. At the same time, there is significant overlap in the distributions and it is difficult to disentangle the populations on these specific kinematic properties alone.

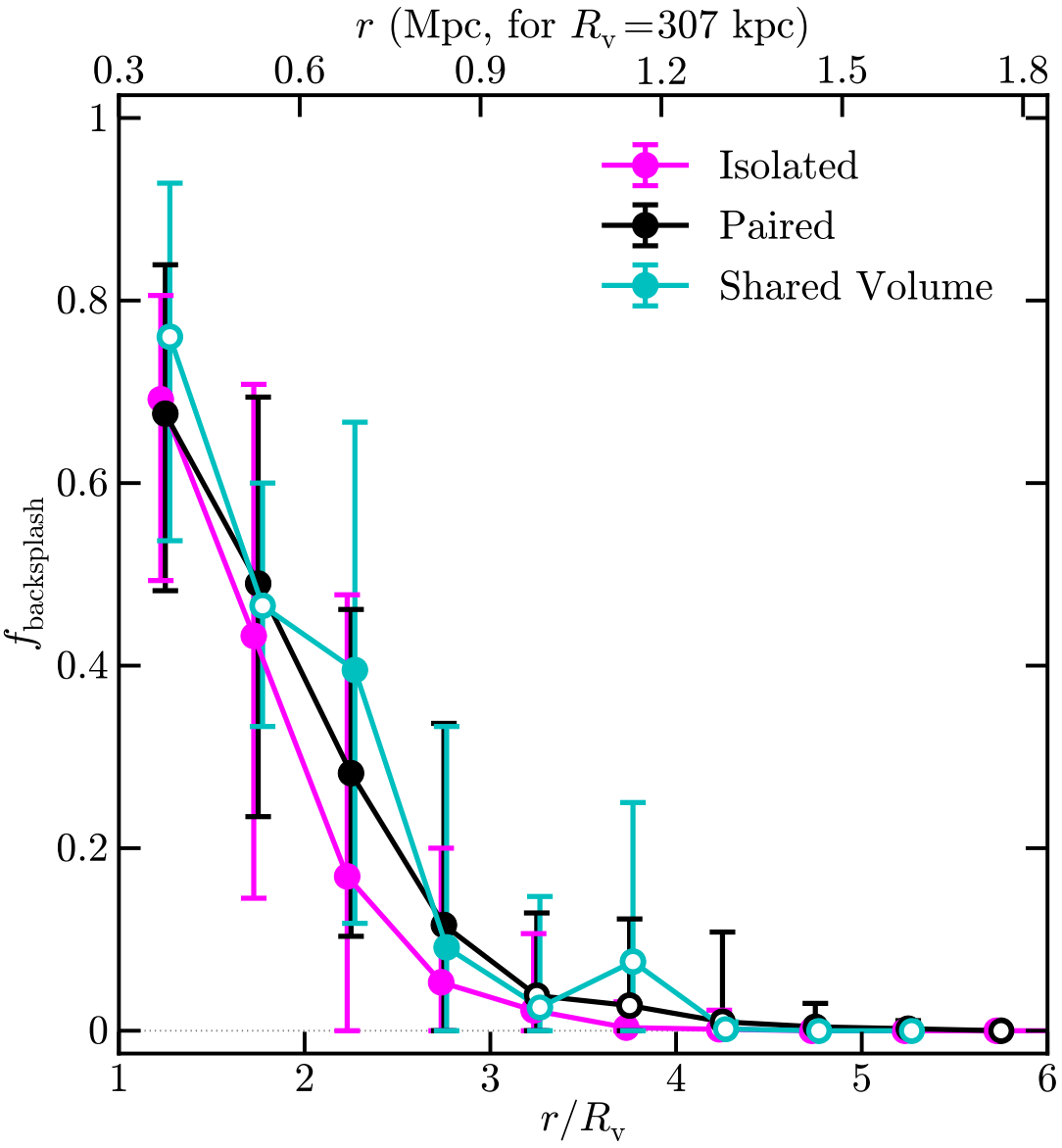


Figure 2.7: The fraction of $M_{\rm peak} > 6 \times 10^7 M_\odot$ halos at $z = 0$ that have been within $R_{\rm v}$ of a MW size host as a function of $r/R_{\rm v}$ from the centre of each host. The points show the average in each radial bin and the error bars denote the full width of the distribution over all hosts. The magenta line corresponds to the isolated sample, and the black line corresponds to paired hosts, where the distance is to the nearest of the two giants. The cyan line also counts systems in the paired simulations, but counts only those systems that simultaneously meet the radial cut for both hosts. The most likely location for backsplash halos is in this shared volume and between 1 and 2 $R_{\rm v}$ of both hosts (i.e., in between the two halos rather than on one side or the other of the LG pair).

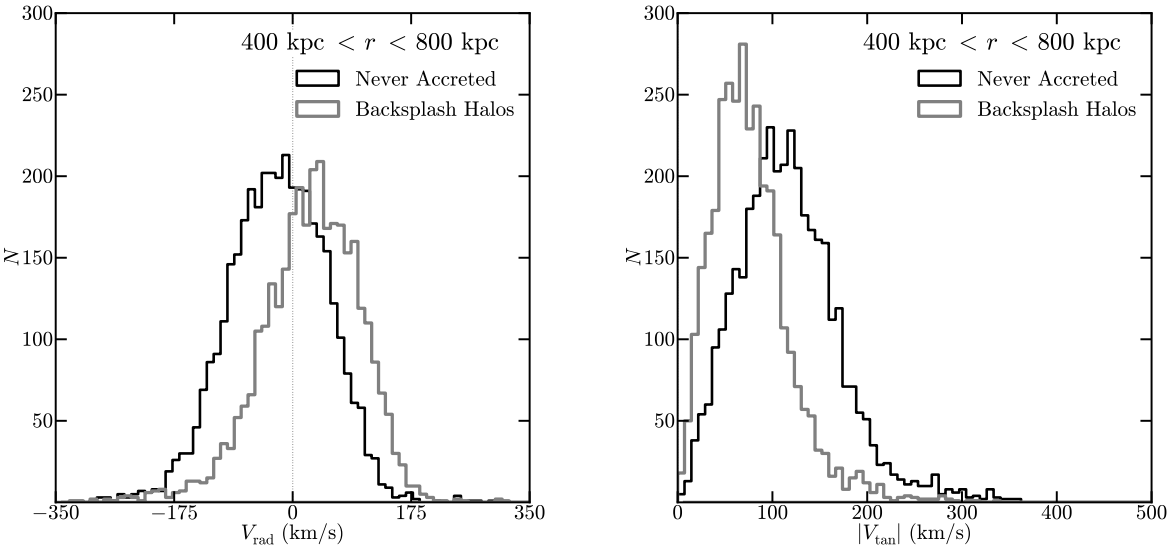


Figure 2.8: The radial (left) and tangential (right) velocity distributions of field halos in the spherical shell 400–800 kpc from the centre of each paired host, truncated in the same manner as Figures 2.6 and 2.7. The black lines plot only those halos that have never been within $R_{\rm v}$ and the grey lines includes only backsplash halos. The latter are comparatively outflowing with relatively low tangential velocities. Note that in this figure we have excluded the two pairs in our sample with large companions at $\sim 1$ Mpc distance.

We reserve a more thorough analysis of this question for a future paper.

## 2.4 Expectations for the Local Group

As the previous section showed, number counts and velocity distributions within $R_{\rm v}$ are consistent between isolated and paired MW-size halos, but differences are evident at greater radii. In this section, we will focus on predictions in the $\sim 1$ Mpc scale environment around the Milky Way and will present results for the paired sample only.

### 2.4.1 Stellar Mass Functions

Although the ELVIS simulations are dissipationless, the abundance matching (AM) technique (Kravtsov et al., 2004; Vale & Ostriker, 2004; Conroy et al., 2006; Behroozi et al., 2013c; Moster et al., 2013) makes it possible to assign stellar masses to dark matter halos and convert the halo mass functions in Figures 2.3 and 2.5 into reasonably proxies for stellar mass functions. The connection between galaxy mass and halo mass remains highly uncertain at low masses $M_\star \lesssim 10^8\,M_\odot$, however, as it is difficult to measure luminosity functions over large volumes for dim galaxies. In this sense, comparisons to galaxy counts within the LG, where luminosity functions are more complete, can help test and refine AM relationships that have been built upon cosmological samples.

Figure 2.9 shows the $z = 0$ AM relation published by Behroozi et al. (2013c) as the orange line. The plotted relation becomes dashed at $M_\star < 10^{8.5}\,M_\odot$, reflecting the approximate completeness limit of the SDSS-derived stellar mass function of Baldry et al. (2008), on which the Behroozi et al. (2013c) relation was based. The black line shows a modified version of the Behroozi et al. (2013c) relation, motivated by the updated stellar mass function of Baldry et al. (2012), who found flatter faint-end slope ($a_* = -1.47$ versus $-1.6$ in Baldry et al. 2008) using the Galaxy And Mass Assembly (GAMA) survey (Driver et al., 2011), which probes $\sim 2$ mag deeper than SDSS, albeit over a smaller area of sky. In this modified relation we have simply altered the asymptotic slope $\alpha$ to be 1.92 in equation 3 of Behroozi et al. (2013c), such that at small masses $M_\star \propto M_{\rm peak}^{1.92}$. This is based on the expectation that $\alpha = (1 + a_{\rm dm})/(1 + a_*)$ and assuming an asymptotic halo mass function slope of $a_{\rm dm} = -1.9$ (e.g. Jenkins et al., 2001). As we show below, this modified relation does a better job in reproducing dwarf galaxy counts in the LG than the original Behroozi et al. (2013c) formulation. Our preferred relation is well described by a power law for $M_\star < 10^8 M_\odot$:

$$M_\star(M_{\rm peak}) = 3 \times 10^6\,M_\odot \left(\frac{M_{\rm peak}}{10^{10} M_\odot}\right)^{1.92} . \tag{2.4}$$

In the mass range of interest, this modified $M_\star - M_{\rm peak}$ relation is more similar to the AM prescription presented in Moster et al. (2013). This relation is valid only at $z = 0$; our technique does not allow for a constraint at higher redshifts.

Figure 2.10 shows the stellar mass functions of galaxies within 300 kpc of either the Milky Way (cyan) or M31 (dashed cyan) compared to the predicted stellar mass functions for our ELVIS pairs based on the two AM relations shown in Figure 2.9. For the galaxy stellar mass functions, we use the masses from Woo et al. (2008), where available, and the luminosity data cataloged in McConnachie (2012), assuming $M_\star/L = 2$, otherwise. The lines become dashed where incompleteness may become an issue (see, e.g. Koposov et al., 2008; Tollerud et al., 2008; Richardson et al., 2011; Yniguez et al., 2014).

The orange lines in Figure 2.10 show the stellar mass functions for each of the 24 paired ELVIS hosts derived from the $M_\star(M_{\rm peak})$ relation of Behroozi et al. (2013c). The average relation is shown by the thick line. For this exercise we have applied the $z = 0$ relation to all subhalos using their $M_{\rm peak}$ masses, which follows the prescription of Behroozi et al. (2013c). As can be seen, the standard Behroozi et al. (2013c) relation gives a stellar mass function that is too steep, over-predicting the count of galaxies smaller than $M_\star \simeq 10^7 M_\odot$ significantly. Our modified relation (applied to ELVIS halos in black) does a better job by assigning less stellar mass to smaller halos. For this reason we will adopt this preferred AM relation in all relevant figures to follow. In magenta, we highlight the satellites of the host Hera, which happens to be a particularly good match to the data (at least in the regime where it is likely complete) in this and several figures that follow. Based on our preferred AM relation, we predict $\sim 200 - 300$ galaxies with $M_\star \geq 10^3 M_\odot$ within 300 kpc of the MW / M31.

We note that both AM prescriptions under-predict the satellite stellar mass function for the MW / M31 at $M_\star \geq 10^8 M_\odot$ when considering the average satellite mass function. At these relatively high masses, however, the halo-to-halo scatter is large and the well-established

rarity of LMC-like objects (Boylan-Kolchin et al., 2010; Busha et al., 2011; Tollerud et al., 2011) biases the mean result relative to observations of the LG. The stellar mass functions around individual hosts with large subhalos, e.g. Hera in magenta, match observations well over four decades in stellar mass after applying the preferred AM relation.

Figure 2.11 presents stellar mass functions for simulated Local Volumes (unions of 1.2 Mpc spheres around either host) using our preferred AM relation. There is one line for each pair of halos in the ELVIS sample, excluding the two cases that contain a third large halo nearby (detailed in § 2.2.3). Our AM-based prediction agrees reasonably well with the data for $M_\star \gtrsim 5 \times 10^6 M_\odot$, but rises much more steeply towards lower masses, in the regime where the current census is almost certainly incomplete. We highlight the pair Zeus & Hera in magenta. This pair has an $M_\star$ function that happens to be very similar to that of the LG. We see that if the AM relation is extrapolated down to $M_\star \sim 10^3 M_\odot$ we expect $\sim 1000$ galaxies within the Local Volume (compared to the $\sim$ 70 systems currently known). Future surveys like those performed with LSST (Ivezic et al., 2008) will help test such extrapolations, exploring the relationship between halo mass and galaxy mass at the very threshold luminosities of galaxy formation.

### 2.4.2 HI Mass Functions

While future resolved-star surveys promise to discover faint optical galaxies throughout the Local Volume, HI surveys offer a complementary approach for the discovery of dwarfs in the near-field (Blitz et al., 1999; Blitz & Robishaw, 2000; Sternberg et al., 2002; Adams et al., 2013; Faerman et al., 2013). While the faintest dwarfs within $\sim$ 300 kpc of either the MW or M31 are gas-poor dSphs, gas-rich dwarfs are the norm beyond the virial regions of either giant (Grcevich & Putman, 2009; McConnachie, 2012). Leo T, at distance of $\sim$ 400 kpc from the MW, is an example of a very faint system that is gas-rich ($M_\star \simeq M_{HI} \simeq 10^5 M_\odot$;

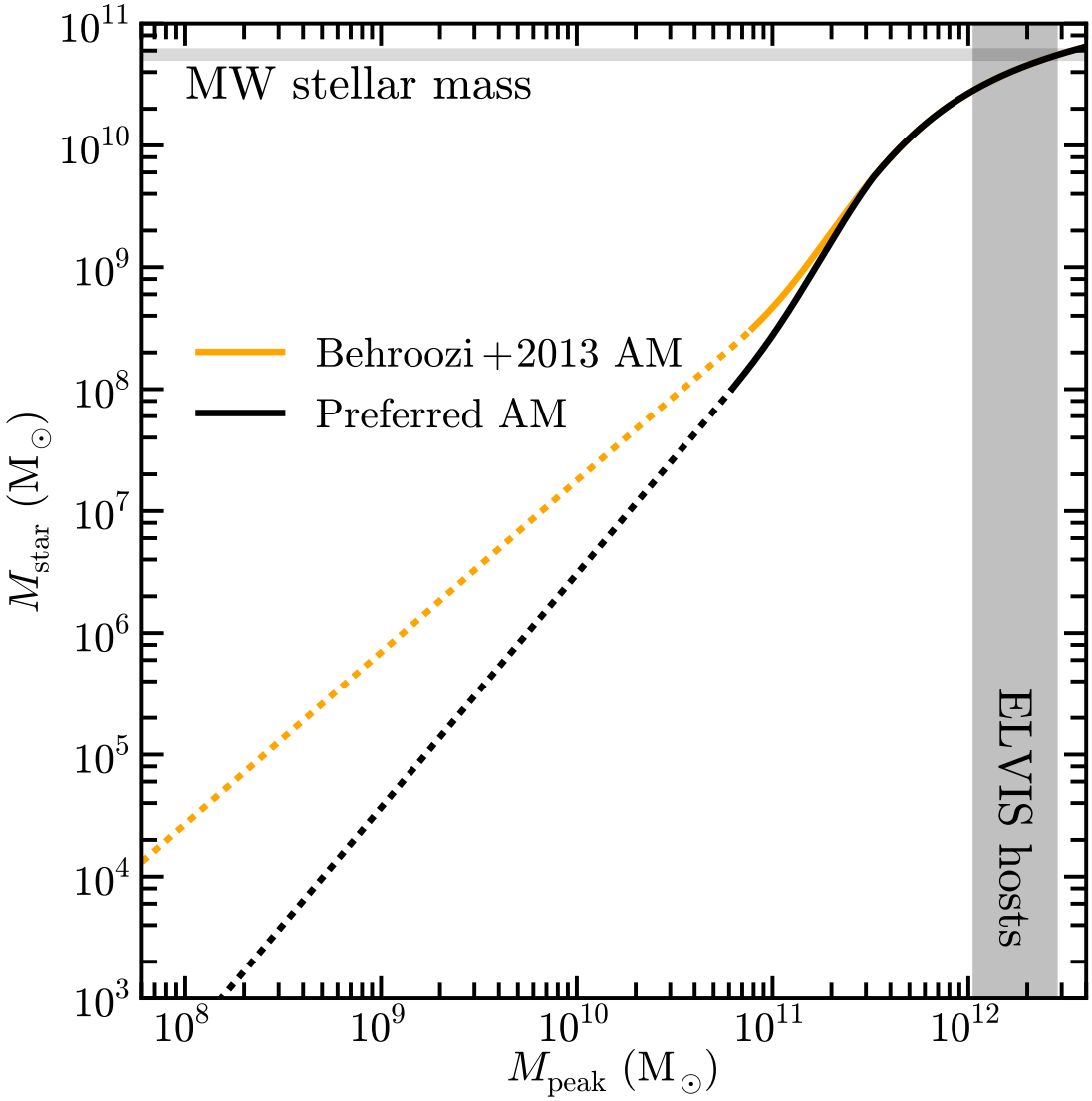


Figure 2.9: The abundance matching relation between stellar mass and halo mass from Behroozi et al. (2013c, orange line), extrapolated to low halo masses, compared to a modified relation (black) motivated by the updated stellar mass function of Baldry et al. (2012). As shown in Figure 2.10, this modified relation does a better job of reproducing faint ($M_\star \sim 10^6 - 10^8 M_\odot$) galaxies in the Local Group. The two lines are solid over the range where the input stellar mass functions are complete and become dashed in the regime associated with pure extrapolation. For reference, the horizontal grey band shows the stellar mass of the MW from Bovy & Rix (2013). The virial masses of our ELVIS hosts span the vertical grey band. Note that while our halo virial masses are consistent with dynamic estimates of MW and M31 virial masses, they are at the low-mass end of AM expectations for a system with the stellar mass of the MW.

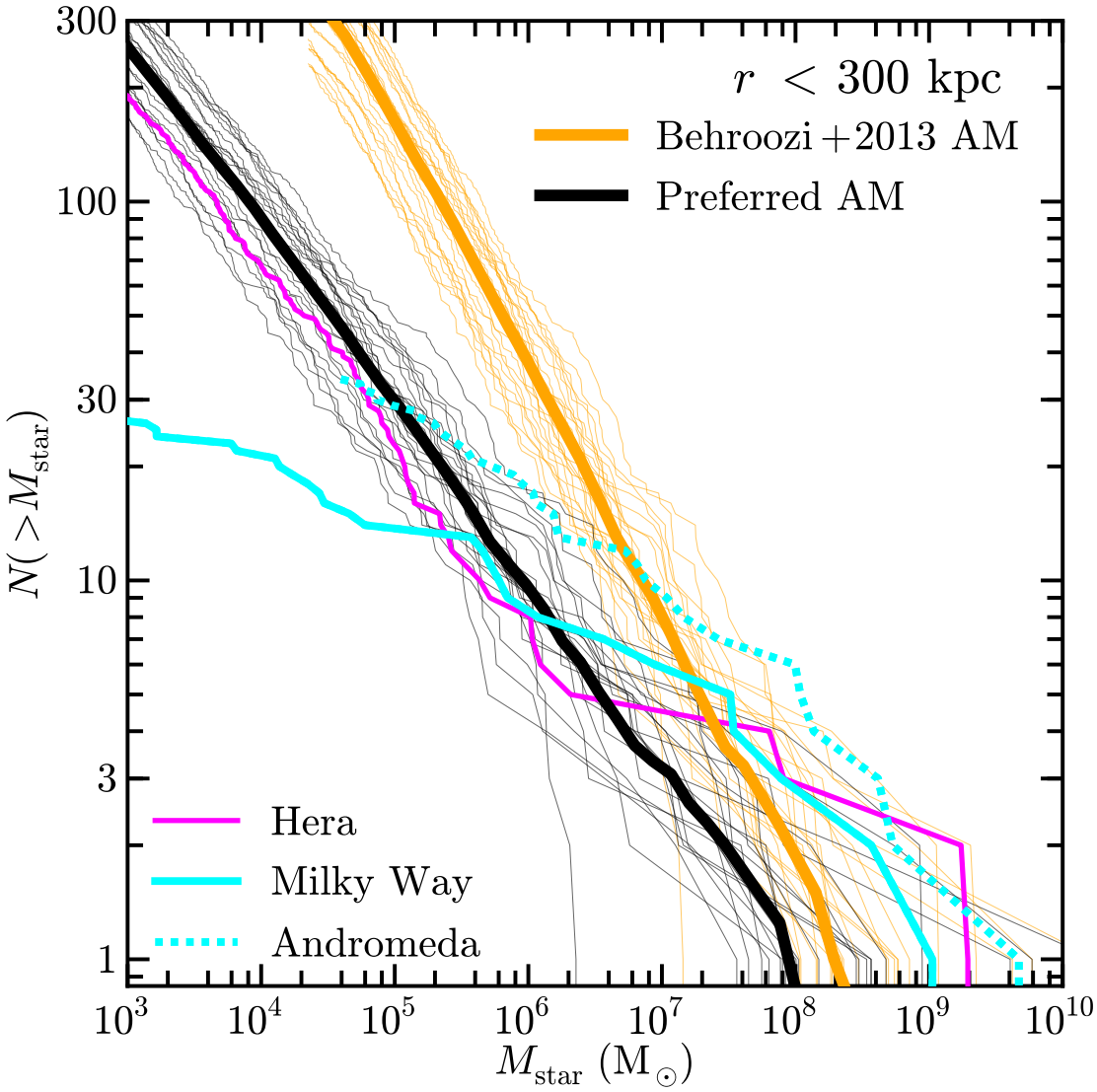


Figure 2.10: A comparison of observed stellar mass functions within 300 kpc of the MW (cyan) and M31 (dashed cyan) with predictions from the ELVIS subhalo catalogs and extrapolated AM relations. The orange lines use the AM prescription of Behroozi et al. (2013c), which adopts a faint-end slope of the luminosity function of $-1.6$ (Baldry et al., 2008), while the black curves modify the Behroozi relation by assuming a slightly shallower faint-end slope of the luminosity function of $-1.47$ (Baldry et al., 2012). The standard Behroozi et al. (2013c) relation over-predicts the LG data significantly at $M_\star = 5 \times 10^5 M_\odot$, a regime where the census of satellites is believed to be complete. The modified Behroozi relation (given in the text) is a better match to the observed counts.

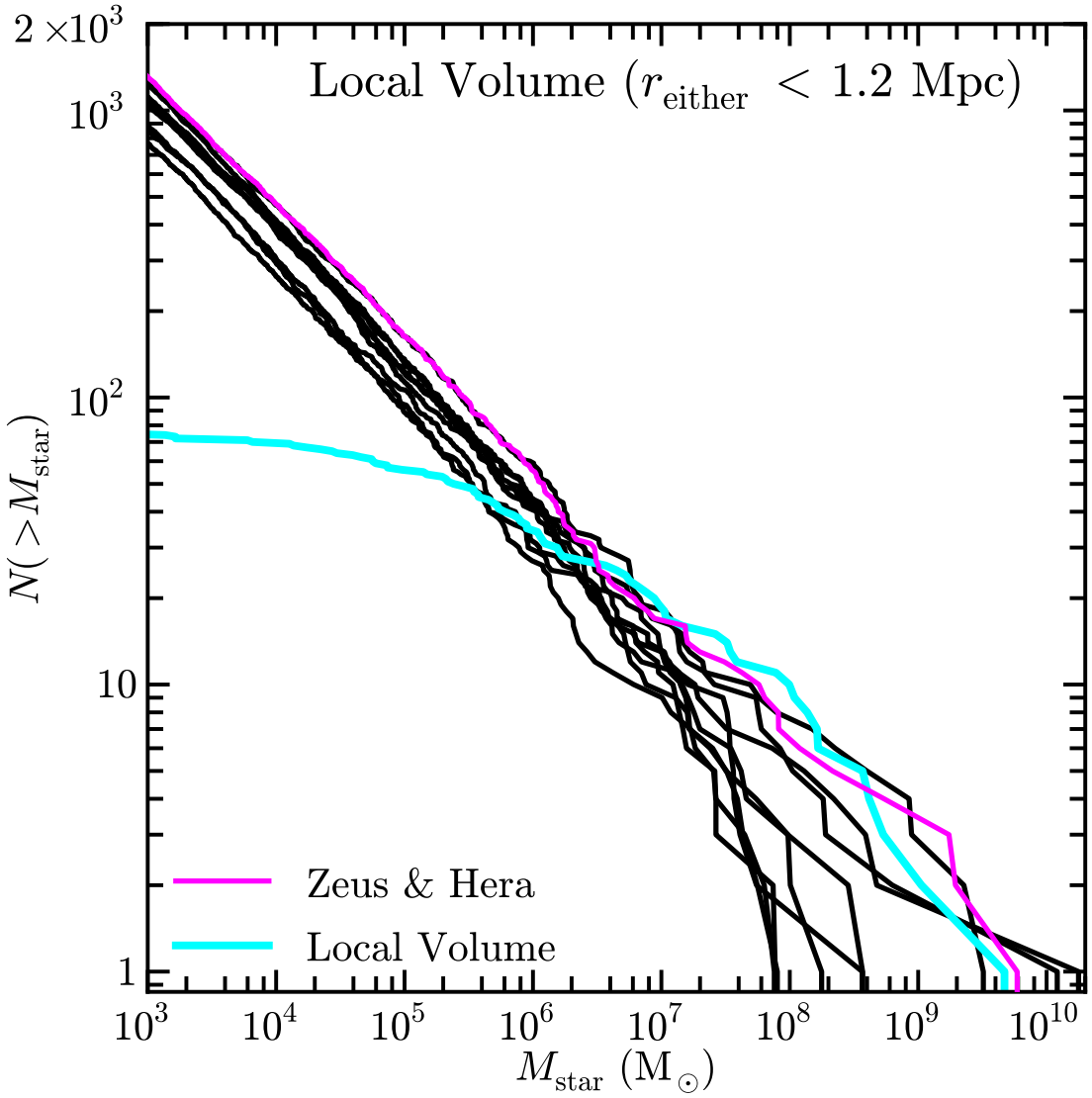


Figure 2.11: Cumulative stellar mass functions around paired hosts within the Local Volume using the preferred AM relation discussed in the text; not shown are those systems that include a third massive halo nearby (Siegfried & Roy and Serena & Venus). The pair Zeus & Hera are highlighted in magenta. The current count of galaxies within the same volume around the MW and M31 is shown in cyan (McConnachie, 2012), which flattens at small mass, likely because of incompleteness. We predict $\sim$ 1000 galaxies having $M_\star \geq 10^3 M_\odot$ within this volume, compared to the $\sim$ 70 currently known.

Ryan-Weber et al., 2008) and apparently falling in to the MW virial radius for the first time (Rocha et al., 2012). Similar, though possibly even less luminous, objects may fill the Local

Volume, and if so, could be detected in blind searches for neutral hydrogen. Recently, for example, the gas-rich galaxy Leo P ($M_{HI} \simeq 3\,M_\star \simeq 10^6 M_\odot$) was discovered at a distance of $\sim 1.5 - 2$ Mpc using HI observations (Giovanelli et al., 2013; Rhode et al., 2013).

Here we use the ELVIS suite to provide some general expectations for the HI mass function in the Local Volume. Building off of the results presented in § 2.4.1, we use our preferred AM relation coupled with an empirically-derived $M_\star$-$M_{\rm HI}$ relation to assign HI masses to halos in our simulated Local Volumes. Specifically, we fit a power-law relation to the gas-rich dwarfs in the LG from McConnachie (2012), ensuring that the gas-fraction relation matches that found by Huang et al. (2012b) at higher masses:

$$M_{\rm HI} = 7.7 \times 10^4 M_\odot \left(\frac{M_\star}{10^5 M_\odot}\right)^{1.2} . \tag{2.5}$$

Of course, this simple assumption of a one-to-one relation between stellar mass and HI mass is highly idealized. In reality, the gas-to-stellar-mass relation shows a considerable amount of scatter (Kannappan, 2004; McGaugh, 2005; Stewart et al., 2009; Huang et al., 2012b,a; Kannappan et al., 2013), and this is especially true for the faintest systems in the LG (as summarized in McConnachie, 2012). A more realistic investigation of the HI content of LG galaxies is reserved for future work.

We further assume that any halo that has been within the virial radius of a giant has had all of its HI gas removed. This presupposes that a process such as ram pressure stripping removes the gas from satellites upon infall and is motivated by observations demonstrating that the vast majority of Local Group satellites have negligible neutral gas content (Grcevich & Putman, 2009). The small number of gas-poor dwarfs that lie beyond the virial radii of either M31 or the MW (i.e. Cetus and Tucana) may very well be explained as backslash halos (see Sales et al., 2007; Teyssier et al., 2012). Of course, some of the largest satellite galaxies in the LG (e.g. the LMC and NGC 205) are clearly able to retain HI for a non-negligible

period of time after infall. This would suggest that our assumptions will lead to some under-counting of HI-rich galaxies, primarily at the highest masses. Some never-accreted halos, however, may have lost their gas via interactions with other field objects or with the cosmic web (Benítez-Llambay et al., 2013), which may lead to some over-counting at small masses.

The predicted HI mass functions within our simulated Local Volumes are plotted in Figure 2.12. The two systems with large interlopers have again been removed, and the line indicating Zeus & Hera is again plotted in magenta. The local HI mass function agrees well with predictions from ELVIS for $M_{\rm HI} \gtrsim 5 \times 10^6 M_\odot$, at which point the local data break sharply, likely indicating incompleteness. We estimate that there are as many as $\sim 50$ ($\sim 300$) unidentified galaxies with $M_{\rm HI} \gtrsim 10^5 M_\odot$ ($10^3 M_\odot$) within 1.2 Mpc of the MW or M31.

### 2.4.3 Compact High Velocity Clouds as Minihalos

It is possible that some of these gas-rich objects have already been detected. Recently, Adams, Giovanelli, & Haynes (2013) presented a catalog of ultra-compact high velocity clouds (UCVHCs) extracted from the Arecibo Legacy Fast ALFA (ALFALFA; Giovanelli et al., 2005; Haynes et al., 2011) survey and discussed the possibility that some of these objects may be dwarf galaxies (see also Blitz et al., 1999; Faerman et al., 2013). Adams et al. (2013) present 53 candidates, with HI properties that correspond to sizes of $\sim 3$ kpc and masses of $M_{\rm HI} \simeq 10^5 - 10^6 M_\odot$ if they reside at $\sim 1$ Mpc distances. These characteristics are suggestively similar to those of known LG galaxies like Leo T. The ELVIS suite can be used to test whether these UCHVCs have properties (radial velocities and overall counts) that are consistent with those expected in ΛCDM for small halos in the Local Volume.

From Figure 2.12, we can immediately see that it is unlikely that *all* of the Adams et al. (2013) candidates are associated with small dark matter halos in the Local Volume. We

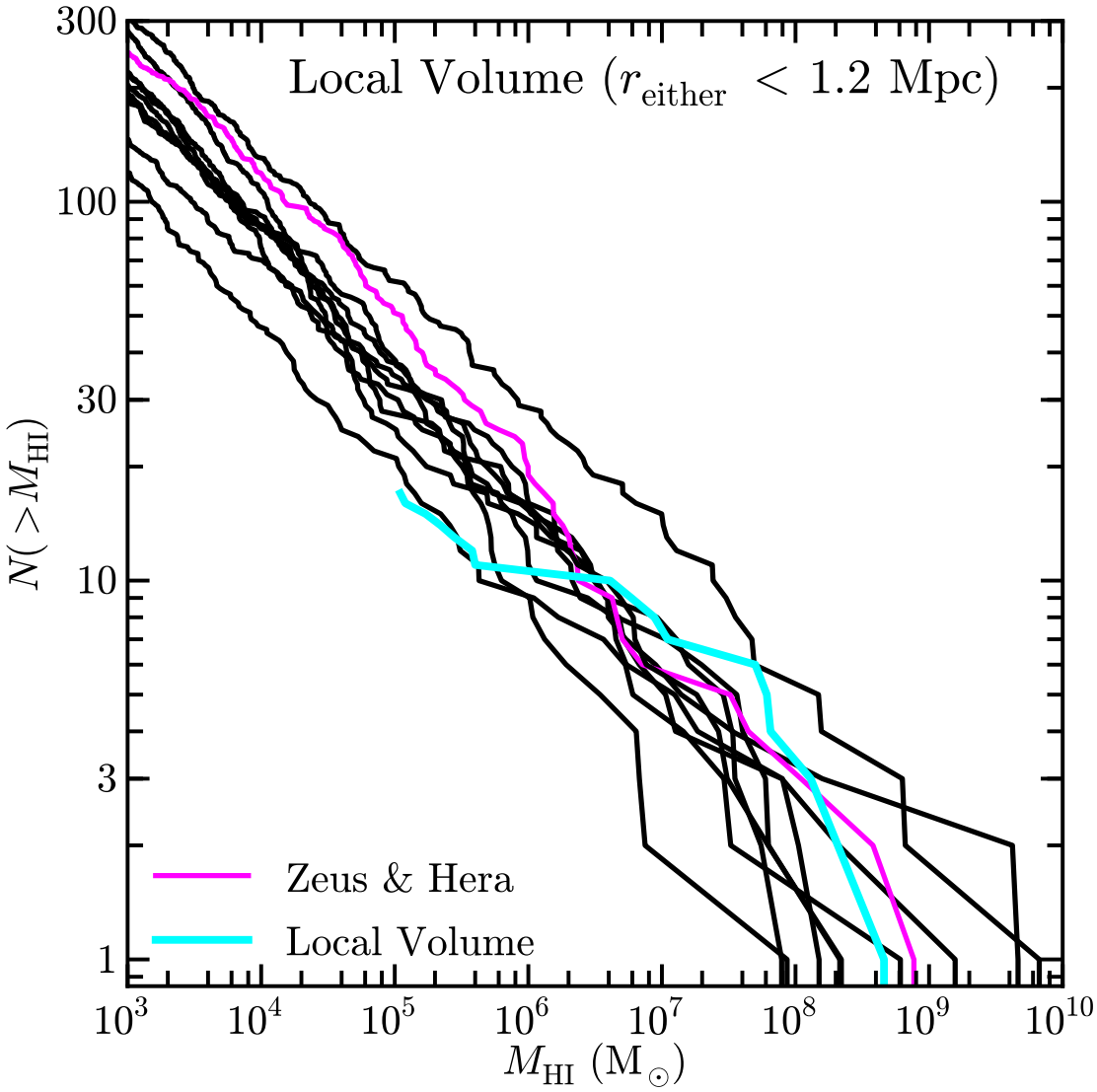


Figure 2.12: The HI mass functions within our simulated Local Volumes, excluding the systems with a third large host nearby. We assign gas masses via Equation 2.5, assuming that any halos that have passed within the virial radius of either giant since $z = 5$ have been stripped of all gas. The local HI mass function is consistent for $M_{\rm HI} \gtrsim 5 \times 10^6 M_\odot$; below this value, incompleteness likely sets in. We expect perhaps $\sim 50$ undiscovered galaxies with $M_{\rm HI} \geq 10^5 M_\odot$ within 1.2 Mpc of either host.

expect fewer than 100 undiscovered objects *over the whole sky* with $M_{\rm HI} \gtrsim 10^5 M_\odot$ within 1.2 Mpc of either host, while the ALFALFA sample has 53 candidates over only $\sim 10\%$ of the sky. Nevertheless, it would not be surprising if some of the identified candidates are

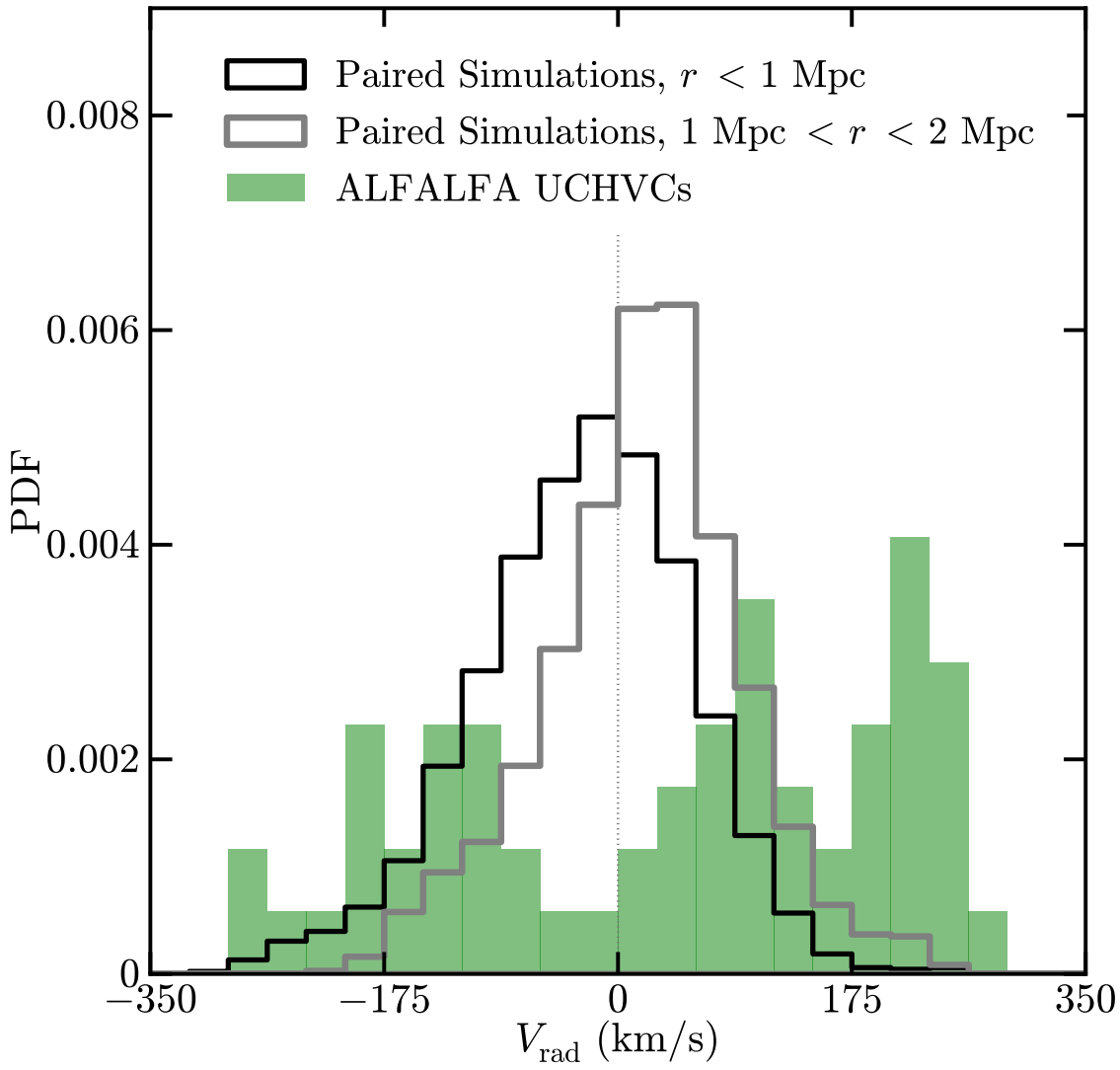


Figure 2.13: The black (grey) lines show the normalized radial velocity distribution of all predicted galaxies with $M_{\rm HI} > 10^5 M_\odot$ within 1 Mpc (2 Mpc) of each host. The shaded green histogram shows the radial velocities of the UCHVC halo candidates from Adams et al. (2013). While a selection bias limits the abundance of UCHVCs with $V_{\rm rad} \sim 0$ km s$^{-1}$, the differences at the high radial velocity tail is illuminating. Specifically, UCHVCs with $V_{\rm rad} > 175\,{\rm km\,s^{-1}}$ are highly unlikely to be associated with small halos in the Local Volume according to our predictions. Systems with lower radial velocities are likely better candidates for follow up.

indeed associated with dark-matter-dominated dwarfs.

The observed radial velocities of these clouds may provide clues for selecting the best candidates for follow-up. Figure 2.13 shows the normalized stacked radial velocity distribution of $M_{\rm HI} > 10^5 M_\odot$ halos that sit between $R_{\rm v}$ and 1 Mpc (black curve), and between 1 and 2 Mpc (grey curve) of our ELVIS pairs, measured from the centre of each host. We again exclude those objects with a third nearby giant from the black curve, and include only those objects with $R_{\rm res} > 1.75$ Mpc (Zeus, Charybdis, Romulus, and Kek) in the grey curve, so as to minimize the effects of contamination from low resolution particles. The shaded green histogram shows the radial velocity distribution of candidate mini-halos from the Adams et al. (2013) UCHVC sample. It is important to recognize that the UCHVC sample is biased to avoid the region near $V_{\rm rad} \approx 0\,{\rm km\,s^{-1}}$ by construction. Nevertheless, the high-velocity tail of distribution shows some interesting differences compared to the predicted distribution.

The most important distinction between the simulated halos and the candidate objects is that there is a substantial population of UCHVCs with $175\,{\rm km\,s^{-1}} \lesssim V_{\rm rad} \lesssim 350\,{\rm km\,s^{-1}}$. There are very few halos predicted with such high recessional velocities within 1 Mpc, and only slightly more out to 2 Mpc. We conclude that the sub-population of UCHVCs with these high velocities is unlikely to be associated with dark matter halos unless they are substantially more distant than 2 Mpc (in which case their total gas mass would become very large and thus the expected count would drop considerably). Based on these results, we suggest that targeted follow-up searches for nearby mini-halos may want to focus on UCHVC candidates with $V_{\rm rad} \lesssim 150\,{\rm km\,s^{-1}}$.

We also compare the on-the-sky positions of the possible minihalos around the Milky Way to those of the gas rich objects near Hera, the host that we have highlighted throughout this work, in a Hammer projection in Figure 2.14. The diamonds indicate the predicted galaxies around Hera and the circles denote the minihalo candidates from ALFALFA; both are coloured by their relative radial velocities according to the colour bar. We have oriented the coordinate system such that Hera's partner halo Zeus sits at the $(l, b)$ of M31 (indicated

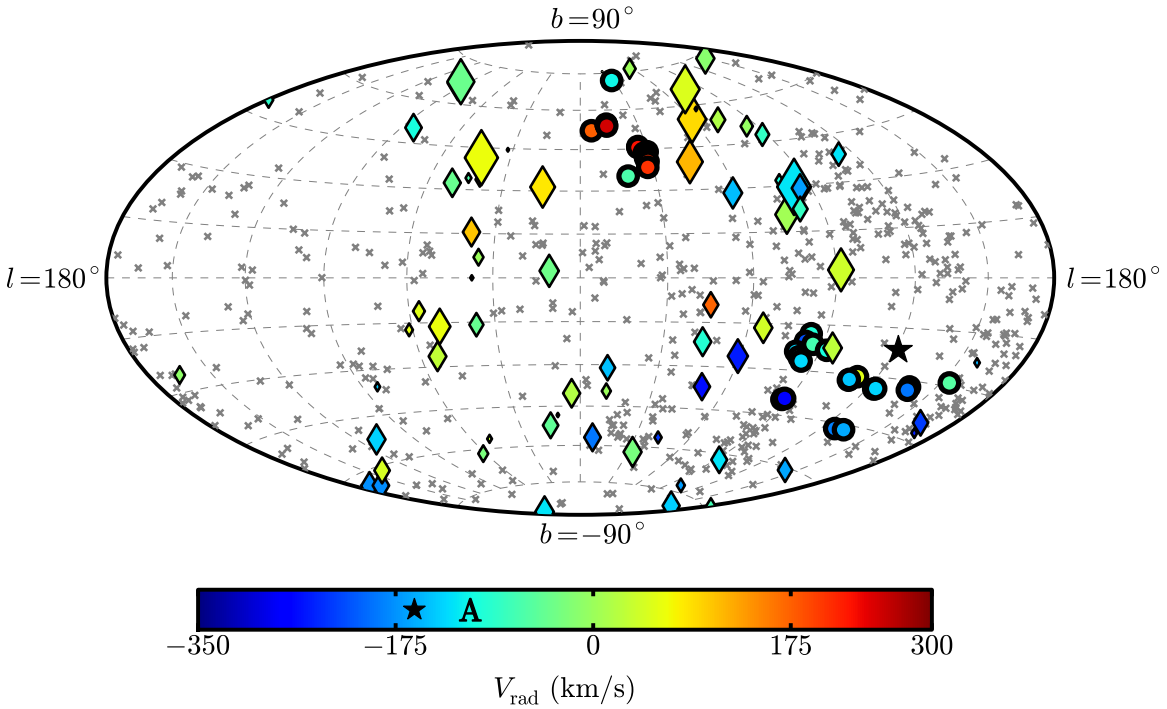


Figure 2.14: A Hammer projection of the halos within 1 Mpc of Hera in mock Galactic coordinates, highlighting the halos we expect to be gas rich with diamonds and marking backsplash halos with crosses; no subhalos of either giant are plotted. The simulation is rotated such that Zeus and M31 lie in the same position on the sky; this point is marked with a star. The size of the diamonds is proportional to our modeled gas mass values and distances as $\log(M_{\rm HI}/r^2)$. The UCHVC minihalo candidates from Adams et al. (2013) are plotted as circles with thick outlines. These and the gas rich objects are coloured by their radial velocities according to the colour bar; the approach velocities of Zeus and Andromeda are indicated on the colour bar by the star and the A, respectively. The velocities of the fastest (outflowing) UCHVCs in the north are clearly outliers compared to the expected velocities of halos in this region and therefore may be poor candidates for follow-up to discover dwarf galaxies. The infalling systems in the south are more in line with our kinematic expectations for mini-halos.

by the star). The grey crosses are backsplash halos. There is a clear clustering of backsplash objects near Zeus and a corresponding dearth of gas-rich halos. Suggestively, the receding ALFALFA objects, which seem most inconsistent with the velocity distributions in ELVIS, are located near one another. We do note, however, that the gas clouds identified by ALFALFA may instead be more distant objects that are perhaps still a part of the Hubble Flow.

We find that most objects more than 1.5 Mpc from the centre of each host are receding.

### 2.4.4 The Local $r - V_r$ Relation

The velocity field within the Local Volume contains a wealth of information on the assembly history and mass of the Local Group (Kahn & Woltjer, 1959; Karachentsev et al., 2002; Karachentsev, 2005; Peirani & de Freitas Pacheco, 2006; Teyssier et al., 2012; van der Marel et al., 2012). The ELVIS simulations supply a potentially valuable basis for interpreting these data, and we intend to utilize them for this purpose in future work. Here we briefly examine the local velocity-distance relation in one of our simulations in order to demonstrate broad agreement with data and illustrate the potential for a more in-depth interpretive analysis.

Figure 2.15 shows the local relation between distance and radial velocity, centred on the Local-Group barycenter, along with data from the Zeus & Hera simulation. MW and M31 are indicated as magenta and cyan squares, respectively, calculated from the separation and radial velocity given in Table 2.1 and the masses in Tables 2.2 and 2.3. Known Local Group galaxies that reside beyond 300 kpc of either giant are shown as large diamonds; the two highlighted in yellow are the gas-free dwarfs Cetus and Tucana, which are backsplash candidates. The Leo P data point is calculated from Tables 2.1, 2.2, and 2.3, assuming that its distance from the MW is 1.75 Mpc (McQuinn et al., 2013); the remainder of the observational data is taken from McConnachie (2012). For comparison, circles show all halos within the Zeus & Hera simulation that are large enough, according to our preferred AM relation, to have stellar masses exceeding 3000 $M_\odot$. Halos within 300 kpc of either simulated giant are excluded, but galaxies that have been within the virial radii of Zeus or Hera are coloured cyan and magenta, respectively.

As expected from the previous discussion (e.g. Figure 8), backsplash halos tend to populate the outflowing, positive-velocity envelope of the relation. The gas-free dwarfs Cetus and

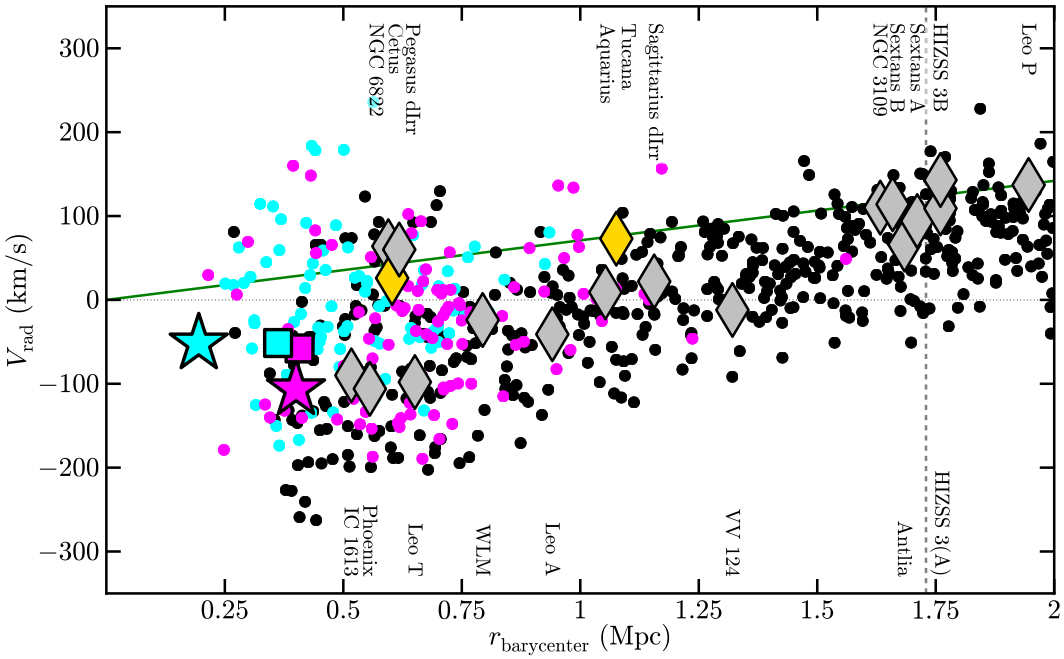


Figure 2.15: Barycentric radial velocity versus barycentric distance for Local Group galaxies compared to expectations from the Zeus & Hera simulation. The centers of Zeus (cyan) and Hera (magenta) are indicated by large stars, while M31 (cyan) and the MW (magenta) are shown by squares. All halos with $M_\star > 3 \times 10^3 M_\odot$ and beyond 300 kpc of either Zeus or Hera are plotted as circles. Large diamonds indicate known galaxies in the Local Group beyond 300 kpc of either giant. Backsplash halos of Zeus are shown as cyan while those that have interacted with Hera are plotted in magenta. The black points are halos that have yet to be accreted by either host. The grey diamonds mark LG galaxies that have gas while the yellow diamonds correspond to Cetus and Tucana, two gas-free dwarf that are good backslash candidates. For reference, the green line shows the asymptotic linear Hubble relation for our simulated cosmology.

Tucana are similarly consistent with inhabiting this upper envelope. More generally, the simulated relation is a reasonably good match to the data shown. The relative lack of known galaxies with $V_{\rm r} \lesssim -100\,{\rm km\,s^{-1}}$ is likely related to the barycentric velocities of the MW and M31, which are moving $\sim 50\,{\rm km\,s^{-1}}$ slower than Zeus and Hera.

Finally, we note that the vertical dashed line near 1.75 Mpc in Figure 2.15 indicates the position of the first low-resolution (contamination) particle in the simulation. In principle, our predictions could be compromised beyond this point, but based on larger (lower reso-

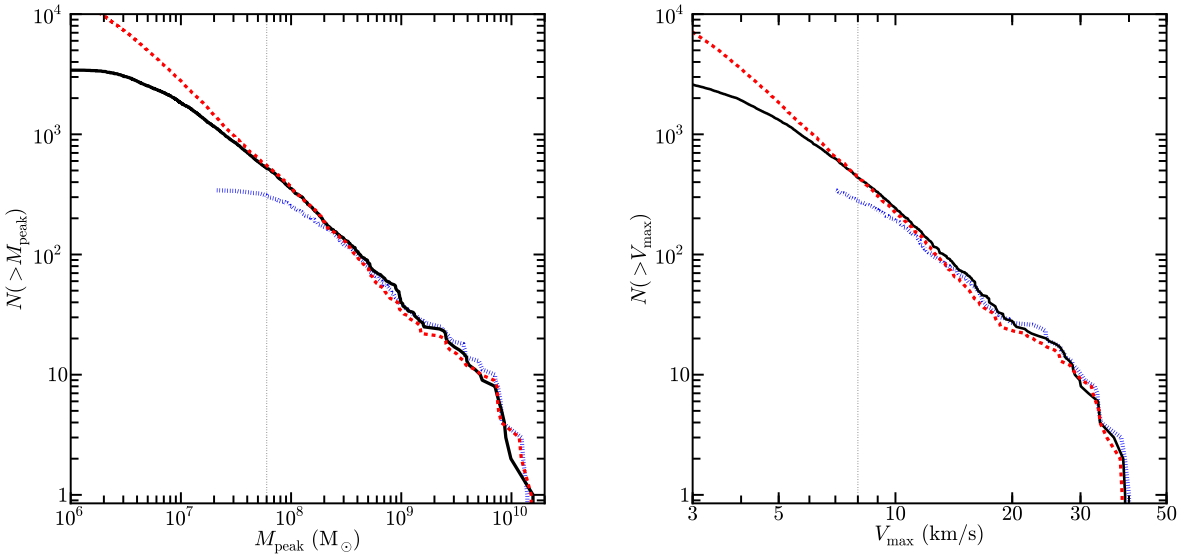


Figure 2.16: Resolution test indicating the smallest halos `Rockstar` reliably identifies in the ELVIS simulations. Here we plot the $M_{\rm peak}$ (left) and $V_{\rm max}$ (right) functions for halos within 400 kpc of the smallest of our isolated halos, iKauket. The black line indicates the fiducial resolution; the red line is from the HiRes simulation, and the blue line is from a lower resolution run, for illustrative purposes. The mass and circular velocity at which the lines begin to systematically disagree, $M_{\rm peak} = 6 \times 10^7 M_\odot$ and $V_{\rm max} = 8\,{\rm km\,s^{-1}}$, constitute our resolution limits for the fiducial resolution.

lution) simulation comparisons we find no evidence that contamination biases bulk velocity predictions.

## 2.5 Numerical Convergence

In this Section, we compare the $M_{\rm peak}$ and $V_{\rm max}$ functions within 400 kpc of iKauket at three different levels of numerical resolution. Figure 2.16 contains this comparison: results from the HiRes simulation ($m_p = 2.35 \times 10^4\,M_\odot$, $\epsilon = 70.4\,{\rm pc}$) are shown as a red dashed line, while results from the run at our fiducial resolution ($m_p = 1.89 \times 10^5\,M_\odot$, $\epsilon = 141\,{\rm pc}$) are shown as a solid black line. For comparison, the blue line shows a lower resolution run as well ($m_p = 1.55 \times 10^6 M_\odot$, $\epsilon = 469\,{\rm pc}$).

The left panel plots the number of halos identified by our pipeline with $M_{\rm peak}$ greater than a given mass; on the right, we plot the current $V_{\rm max}$ function. By locating where our fiducial resolution begins to systematically differ from the HiRes run, it is clear that halos with $V_{\rm max} > 8$ km/s and $M_{\rm peak} > 6 \times 10^7 M_\odot$ are reliably identified at the fiducial resolution. These resolution limits are marked by dashed vertical lines in the plots.

## 2.6 $\mathbf{V_{max}}$ Functions

For most galaxies, it is more convenient to measure circular velocities or velocity dispersions than virial mass. Although we do show stellar mass functions in the main body, our relation is not a mapping between $M_\star$ and $V_{\rm max}$; thus, we show $V_{\rm max}$ functions for direct comparison with such observations here. As with the $M_{\rm peak}$ functions, counts as a function of $V_{\rm max}$ agree well within $R_{\rm v}$ (Figure 2.17), and are both well fit by a power law at the low mass end:

$$N_{\rm v}(> V_{\rm max}/V_{\rm v}) = 0.038(V_{\rm max}/V_{\rm v})^{-3.3}.$$

The $V_{\rm max}$ function in the Local Fields are also similarly offset (Figure 2.18), with the paired simulations lying 75% higher than the isolated analogs:

$$N_{0.3-1}(> V_{\rm max}) = N_0 \left(\frac{V_{\rm max}}{10\,{\rm km/s}}\right)^{-3.1},$$

with $N_0 = 540$ for the paired sample and 300 for the isolated analogs. Likewise, we predict similar numbers of objects with $V_{\rm max} > 8\,{\rm km\,s^{-1}}$ within the 1 Mpc of each host and within the Local Volume around each pair as predicted in Figure 2.5 for $M_{\rm peak} > 6 \times 10^7 M_\odot$; these $V_{\rm max}$ functions are plotted in Figure 2.19.

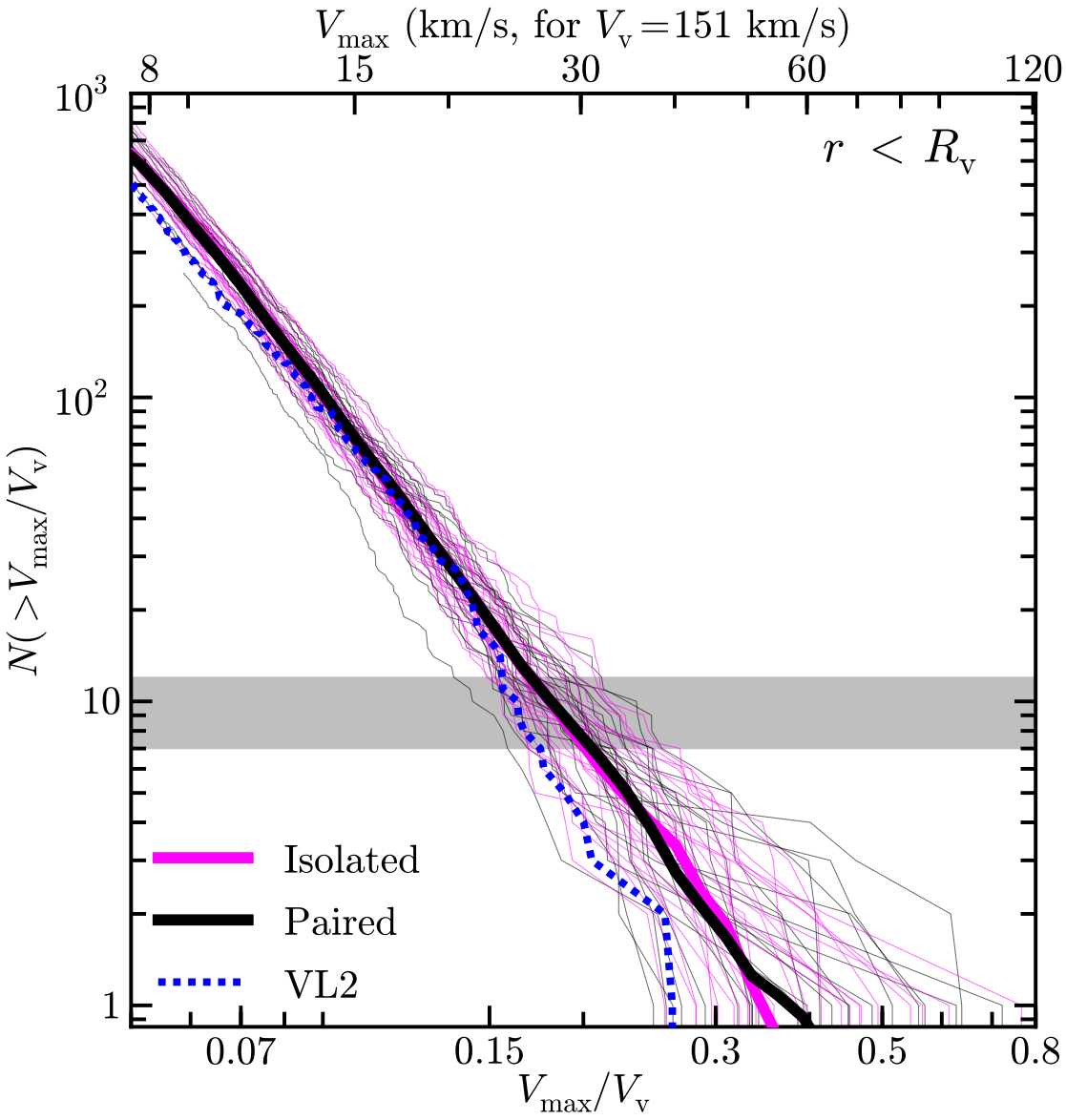


Figure 2.17: The $V_{\rm max}$ function within $R_{\rm v}$ of each host, scaled by the virial velocity of that host, analogous to Figure 2.3. As in that Figure, the two populations agree well within the virial radius and are both well fit at the low-mass end by a power law of slope -3.1, as given in the text. The blue dashed line plots the $V_{\rm max}$ function within the virial radius of the high-resolution Via Lactea II halo (Kuhlen et al., 2009), which agrees within the halo-to-halo scatter.

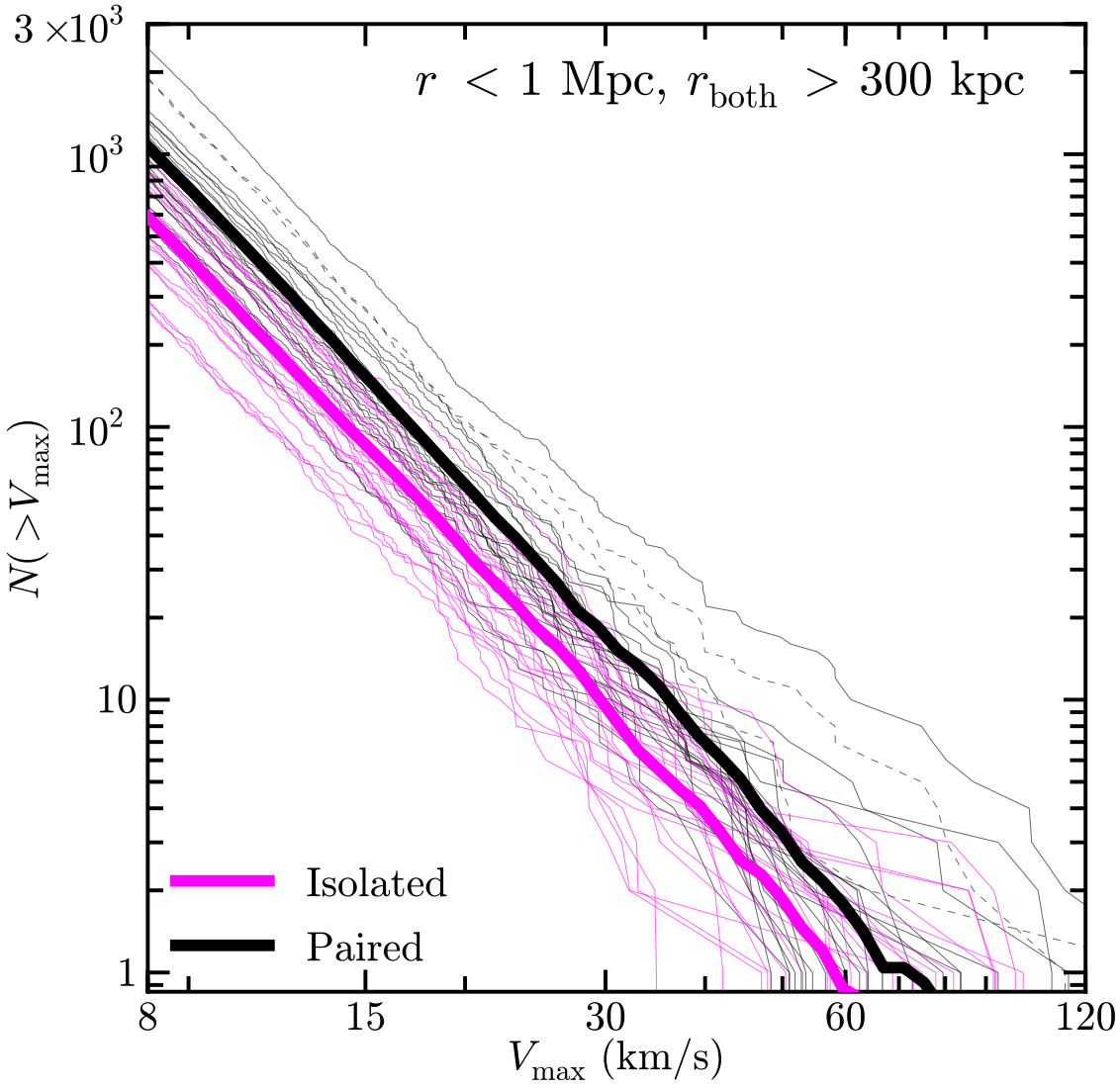


Figure 2.18: The $V_{\rm max}$ functions for objects in the Local Field (within 1 Mpc of the host, but more than 300 pc from both giants). The average relations are offset from one another, with the paired simulations having an amplitude that is 75% higher. The power law fits to the average relations are given in the text.

## 2.7 Conclusions

This work presents the ELVIS suite, a set of collisionless cosmological simulations consisting of 12 Local Group-like pairs of MW/M31-size dark matter halos and 24 isolated analogs

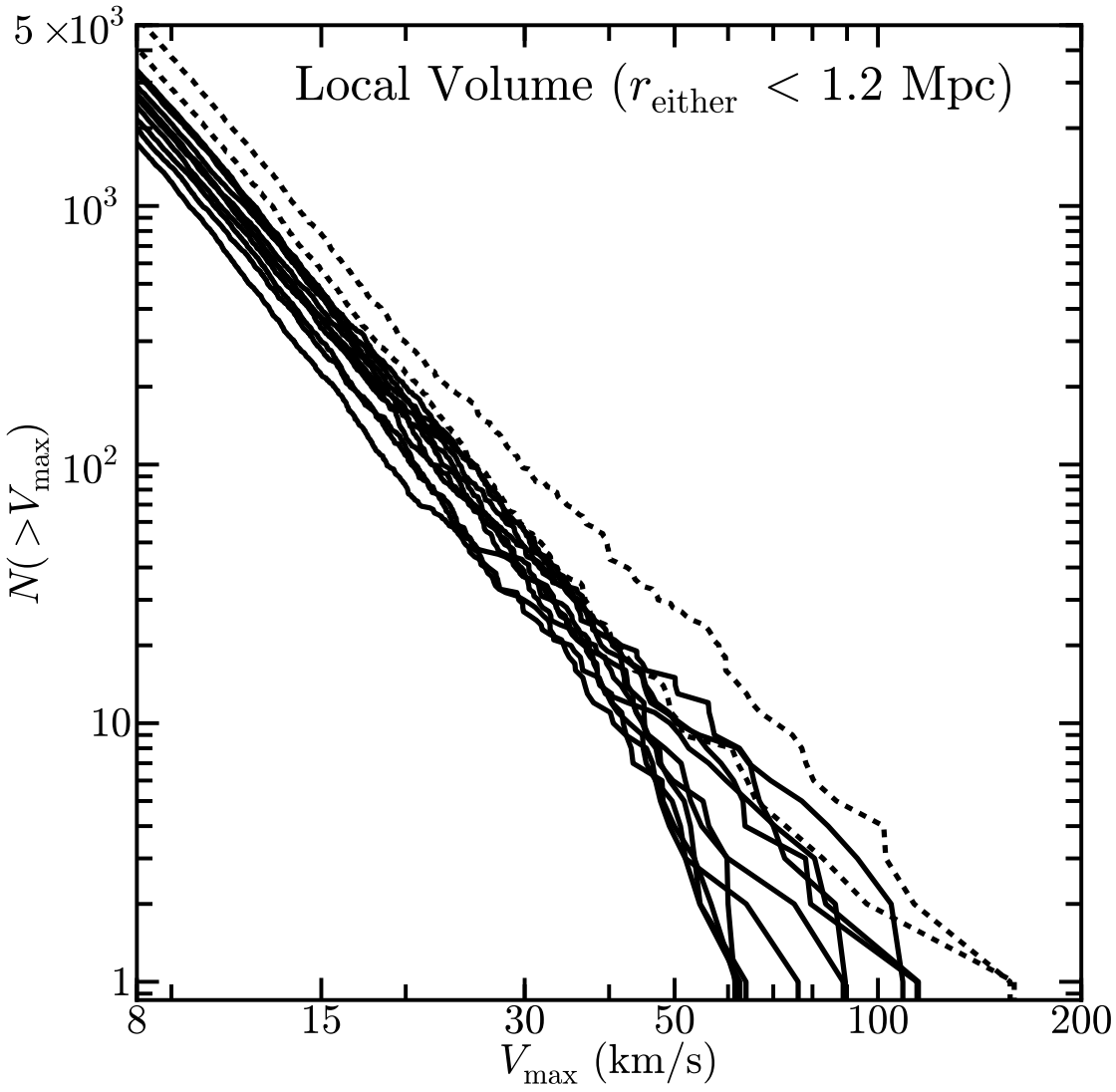


Figure 2.19: The $V_{\rm max}$ functions in the Local Volume (1.2 Mpc of either host), analogous to Figure 2.5.

mass-matched to those in the pairs. Each simulation resolves mini-halos down to $M_{\rm peak} = 6 \times 10^7 M_\odot$ within high-resolution, contamination-free volumes that span 2 to 5 Mpc in size.

One of the goals of this work is to determine if the Milky Way and M31 are expected to be biased in any way with respect to typical field halos as a result of their paired configuration. We find no evidence that this is the case (c.f. Figure 2.3). Statistically, subhalo properties

(counts and kinematics) and host halo properties (formation times and concentrations) are indistinguishable between our paired and unpaired samples. We provided analytic fits to subhalo mass functions in § 2.3.1 (and for $V_{\rm max}$ functions in Section 2.6). Apparently, as long as measures are restricted to the virial volumes, simulated field halos provide an adequate comparison set for the MW and M31.

As might be expected, differences become more apparent between paired and isolated samples when we explore measures beyond the virial volumes of either hosts (Figures 2.4–2.6). The Local Volume at 1.2 Mpc distance around each paired host contains, on average, 80% more halos at fixed $M_{\rm peak}$ than the corresponding region surrounding each isolated host. Similarly, the kinematic properties of the mini-halo population around LG -like pairs show distinct differences from isolated MWs: the tangential velocity distributions for halos around pairs are significantly hotter, and the radial velocity distributions are skewed towards more outflowing systems. The tendency to see more outwardly moving halos around paired hosts is likely related to another difference we see: an increase in the backsplash fraction. We find evidence that paired halos have an increased fraction of satellite systems that are now beyond the virial radius of either host, but that had previously been inside (Figure 2.7). These backsplash objects are preferentially moving outward along more radial orbits at $z = 0$ (Figure 2.8).

With these basic comparisons in place, we investigate our sample of LG-like pairs more closely, focusing on comparisons with data throughout the Local Volume. A summary of the resultant work is as follows:

- We find that the abundance matching relation presented by Behroozi et al. (2013c) over-predicts the number of $M_\star \sim 5 \times 10^6 M_\odot$ satellites within 300 kpc of the MW and M31 (Figure 2.10), a regime where the satellite census is believed to be complete.
- We present a modified Behroozi relation, motivated by the stellar mass function reported by Baldry et al. (2012) from GAMA data (Figure 2.9 and Equation 2.4), that

reproduces the observed satellite count down to $M_\star \sim 5 \times 10^5 M_\odot$, a point where incompleteness likely becomes an issue. It also reproduces galaxy counts throughout the Local Volume down to $M_\star \sim 5 \times 10^6 M_\odot$, below which incompleteness is almost certainly an issue (Figure 2.11).

- By extrapolating our preferred AM relation to low halo masses, we find there should be $\sim 300$ galaxies with $M_\star \geq 10^3 M_\odot$ within 300 kpc of the Milky Way and $\sim 1000$ such galaxies within 1.2 Mpc of either host. LSST (along with ongoing surveys) will test this expectation. If faint galaxies are not discovered in large numbers, it could point to a break in the stellar-mass to halo-mass relation at the low-mass end.

- Using empirical relations between HI mass and stellar mass, we predict the number of gas-rich galaxies within the Local Volume (Figure 2.12). The observed LG HI mass function agrees well with our expectations down to $M_{\rm HI} \sim 10^7 M_\odot$, below which the data may suffer from incompleteness. We conclude that there may be approximately 50 undiscovered gas-rich halos with $M_{\rm HI} > 10^5 M_\odot$ within 1.2 Mpc of the Milky Way and M31.

- We compare the properties of our modeled gas-rich halos to the UCHVC mini-halo candidates presented by ALFALFA (Adams et al., 2013, Figures 2.13 and 2.14). While the characteristics of many of these clouds make them good candidates for gas-rich halos, it is highly unlikely that more than $\sim 10\%$ are true mini-halos. In particular, positive radial velocities in excess of 175 $\mathrm{km\,s^{-1}}$ are drastically inconsistent with our expectations for halo kinematics within $\sim 2$ Mpc of the MW.

Our results generally indicate that studies focusing on basic properties within the virial volumes of the MW or M31 can be fairly compared to predictions from more isolated field-halo simulations (e.g. Diemand et al., 2008; Kuhlen et al., 2008; Springel et al., 2008). However, simulations investigating the volume surrounding the Milky Way *must* account for

the overall environment that it lives in – specifically, the presence of the approaching M31 galaxy.

## Chapter Acknowledgements

Support for this work was provided by NASA through a *Hubble Space Telescope* theory grant (program AR-12836) from the Space Telescope Science Institute (STScI), which is operated by the Association of Universities for Research in Astronomy (AURA), Inc., under NASA contract NAS5-26555. This work was also funded in part by NSF grants AST-1009999, AST-1009973, and NASA grant NNX09AD09G. M.B.-K. acknowledges support from the Southern California Center for Galaxy Evolution, a multi-campus research program funded by the University of California Office of Research. J.S.B. was partially supported by the Miller Institute for Basic Research in Science during a Visiting Miller Professorship in the Department of Astronomy at the University of California Berkeley.

The authors thank Frank van den Bosch, Michael Cooper, Manoj Kaplinghat, Evan Kirby, Jose Oñorbe, Julio Navarro, Annika Peter, and Risa Wechsler for helpful comments, and Erik Tollerud for aid in creating the visualizations. We also thank Volker Springel for making `Gadget-2` publicly available and for providing a version of `Gadget-3` for our use, Peter Behroozi for making `Rockstar` and `consistent-trees` publicly available, and Oliver Hahn for making `MUSIC` publicly available. Finally, we gratefully acknowledge the computational support of the NASA Advanced Supercomputing Division and the NASA Center for Climate Simulation, upon whose *Pleiades* and *Discover* systems these simulations were run, and the *Greenplanet* cluster at UCI, upon which much of the secondary analysis was performed.

# Chapter 3

# Too Big to Fail in the Local Group

## Chapter Abstract

We compare the dynamical masses of dwarf galaxies in the Local Group (LG) to those of halos in the ELVIS suite of ΛCDM simulations. We enumerate unaccounted-for, dense halos ($V_{\rm max} \gtrsim 25$ km s$^{-1}$) that became massive enough to have formed stars in the presence of an ionizing background ($V_{\rm peak} > 30$ km s$^{-1}$). Within 300 kpc of the Milky Way, the number of these objects ranges from 2 – 25 over our full sample. Moreover, this "too big to fail" count grows when extended to the outer regions of the LG: there are 12 – 40 unaccounted-for massive halos in the outskirts of the LG, a region that should be largely unaffected by any environmental processes. According to models that reproduce the LG stellar mass function, all of these missing massive systems should have $M_\star > 10^6 M_\odot$. We find, unexpectedly, that there is no obvious trend in the $M_\star - V_{\rm max}$ relation for LG field galaxies with stellar masses in the range of $\sim 10^5 - 10^8$ $M_\odot$. Solutions to the too big to fail problem that rely on ram pressure stripping, tidal effects, or statistical flukes appear less likely in the face of these results.

## 3.1 Introduction

Numerical simulations of structure formation have emerged as a standard technique for making and testing predictions of the ΛCDM model of hierarchical galaxy formation (Davis et al., 1985; Frenk et al., 1988; Warren et al., 1992; Gelb & Bertschinger, 1994; Cen et al., 1994; Hernquist et al., 1996; Gross et al., 1998; Jenkins et al., 2001; Wambsganss et al., 2004; Springel et al., 2005; Boylan-Kolchin et al., 2009; Klypin et al., 2011). These studies have been remarkably successful at reproducing the large-scale properties of the Universe, but disagreements have periodically emerged on smaller scales.

The smallest dwarf galaxies (stellar mass $M_\star \lesssim 10^8 M_\odot$) can be detected and studied best locally, and thus many of these small-scale problems have been identified by comparing observations of Milky Way (MW) satellites with subhalos of simulated MW-size hosts. For example, the "missing satellites problem" (Kauffmann et al., 1993; Klypin et al., 1999; Moore et al., 1999; Bullock, 2010), points out that although dark matter (DM)-only simulations predicted a wealth of collapsed substructure around the MW, only $\sim 10$ bright satellite galaxies are known. Though the known count of MW satellites has more than doubled in the past ten years, all of these new satellites have been of fairly low luminosity (e.g. Willman et al., 2005; Belokurov et al., 2006, 2007). Moreover, even allowing for these new detections in the overall count, one must still assume that only a small percentage of subhalos are populated by luminous galaxies in order to explain the discrepancy. Because larger halos have deeper potential wells and should, in the absence of strong feedback, be able to retain gas and form stars, perhaps the simplest assumption is that the brightest "classical" dwarf spheroidal (dSph) galaxies are hosted by the largest subhalos typical of MW-size hosts ($V_{\rm max} \sim 30$ km s$^{-1}$).

The idea that the most luminous galaxies reside in the most massive halos is reinforced by the success of the abundance matching (AM) technique, which accurately reproduces

clustering statistics and luminosity functions for $M_\star > 10^8 M_\odot$ galaxies (Kravtsov et al., 2004; Vale & Ostriker, 2004; Conroy et al., 2006; Behroozi et al., 2013c; Moster et al., 2013). Specifically, AM provides an $M_\star - M_{\rm halo}$ relation by matching DM halo mass functions from cosmological simulations with stellar mass functions from large-volume surveys, implicitly assuming that the most luminous galaxies reside in the largest dark matter halos. There is no direct observational evidence that there exists a tight relationship between stellar mass and halo mass in the dwarf regime, but by extrapolating AM relationships at higher masses, one obtains stellar mass functions that agree well with those of the MW and M31 satellites for $M_\star \gtrsim 10^5 M_\odot$ (Koposov et al., 2009; Busha et al., 2010; Kravtsov, 2010; Lunnan et al., 2012; Boylan-Kolchin et al., 2012; Brook et al., 2013; Garrison-Kimmel et al., 2014a). Below $M_\star \sim 10^5 M_\odot$, the abundance of galaxies may become more strongly suppressed than expected in power-law AM extrapolations because the smallest subhalos ($V_{\rm peak} < 30$ km s$^{-1}$) may not have formed stars because of reionization (Bullock et al., 2000; Somerville, 2002; Sawala et al., 2014). As discussed in Garrison-Kimmel et al. (2014a), surveys like LSST will test this possibility.

With the advent of the zoom-in technique (Katz & White, 1993; Oñorbe et al., 2014), which focuses the majority of the computational power of a cosmological simulation on a small high-resolution region, simulations can now test whether these largest subhalos are indeed compatible with the luminous MW dSphs, as AM predicts.

Boylan-Kolchin et al. (2011, 2012) used the zoom-in simulations of the Aquarius Suite (Springel et al., 2008), which includes six ultra-high resolution MW-size hosts, to compare the internal kinematics of the massive subhalos of MW hosts to the brightest MW satellites (those with $M_\star > 10^5 M_\odot$). They discovered that measurements of the stellar velocity dispersions, $\sigma_\star$, indicate systematically lower central mass estimates than simulations predict for large subhalos – that is, the MW dSphs are systematically less dense than the subhalos expected to host them, a problem that has been dubbed "Too Big to Fail" (TBTF). While

possibly related to the missing satellites problem, in that the largest subhalos may not have been found, TBTF is a distinct problem related to the internal structure of subhalos, rather than strictly their abundances. Therefore, the TBTF problem is largely independent of the exact relationship between halo mass and stellar mass (e.g. from AM). It may, however, be viewed as a prediction for the number of missing *dense* satellites and could be alleviated by the discovery of several new high-density dwarf satellites, regardless of their present day stellar masses.

Like the cusp-core problem in slightly more mass low surface brightness galaxies (Flores & Primack, 1994; Moore, 1994; Kuzio de Naray et al., 2008; Trachternach et al., 2008; de Blok, 2010; Kuzio de Naray & Kaufmann, 2011), TBTF may also be tied to the shapes of the inner density profiles of dwarf halos. Collisionless simulations predict cuspy central regions, whereas many observational results have found evidence of cored profiles. For example, measurements of stellar kinematics in dSphs using both kinematically distinct populations (Walker & Peñarrubia, 2011; Agnello & Evans, 2012; Amorisco et al., 2013) indicate cored matter distributions in the larger dSphs (Fornax and Sculptor) and treating the system as a single population (Jardel & Gebhardt, 2012) indicate cored matter distributions in the larger dSphs (Fornax and Sculptor). The slope of the central density profiles are still under debate, however: both methods (Breddels & Helmi 2014 using multiple populations and Jardel & Gebhardt 2013 with single population studies[1]) have also found that it is unlikely that Fornax, Sculptor, Carina, and Sextans are hosted by cored dark matter halos, with Breddels & Helmi (2013) explicitly showing that a subset of cored profiles are disfavored. The TBTF problem is independent of the inner slope, however, as it is phrased in terms of the integrated mass within the half-light radii of dwarfs, quantities that are much more robustly determined observationally than density profile slopes.

There have been a number of suggestions proposed for resolving TBTF. Some authors have

[1]However, we note that much of their evidence for cusps is derived from points interior to the measured stellar kinematics of the studied galaxies.

pointed out that self-interactions in the dark matter, possibly with a velocity dependent cross section (e.g. Feng et al., 2010; Loeb & Weiner, 2011; Zavala et al., 2013), naturally lead to $0.5 - 1$ kpc cores in dwarf subhalos (Vogelsberger et al., 2012; Rocha et al., 2013; Elbert et al., 2014). Others have investigated whether TBTF may be a result of the underlying cosmology of the Aquarius simulations, where TBTF was first identified, such as the adopted values of $\sigma_8$ and $n_s$ (Polisensky & Ricotti, 2014) or the assumed coldness of the dark matter (Anderhalden et al., 2013; Lovell et al., 2014, and references therein). Others have argued that TBTF is a result of the mass of the targeted halos, pointing to simulations that indicate that smaller hosts, $M_{\rm v} \sim 8 \times 10^{11}\ M_\odot$, do not typically contain these large, dense subhalos (di Cintio et al., 2011; Wang et al., 2012; Vera-Ciro et al., 2013). It may also be that a fraction of the MW-size halos in the Universe do not host these dense subhalos (Purcell & Zentner, 2012), though the statistical study of Rodríguez-Puebla et al. (2013) found that the TBTF problem is typical of MW-size hosts.

Many authors have also noted that TBTF was first identified in collisionless simulations, which do not account for baryonic forces, and that it is therefore possible that these missing physics, such as supernova feedback, ram pressure stripping, and tidal interactions, may account for the discrepancy (e.g. Pontzen & Governato, 2012; Zolotov et al., 2012; Arraki et al., 2013; Brooks & Zolotov, 2014; Del Popolo, 2012a; Brooks et al., 2013; Gritschneder & Lin, 2013; Amorisco et al., 2014; Del Popolo et al., 2014). Although energetic arguments indicate that the former is unlikely in most cases (Peñarrubia et al., 2012; Garrison-Kimmel et al., 2013), there is ample evidence that dwarfs are strongly affected by their environment – for example, there are only two galaxies within 300 kpc of the MW with detected gas (the Magellanic Clouds); conversely, there are only two known gas-free field dwarfs within $\sim$ 1 Mpc of the MW (Cetus and Tucana; Grcevich & Putman, 2009; McConnachie, 2012).

Thus far, work on TBTF has focused largely on the subhalos and dSph satellites of the MW, while Tollerud et al. (2014) have shown the same issue is seen around M31. To eliminate

the uncertain effects introduced by environment, however, one should study galaxies beyond the virial radii of the MW and M31, where ram pressure and tidal stripping are minimal. Isolated dwarf galaxies in the Local Field (a term we will use to refer to the region within 1.2 Mpc of either the MW or M31, but more than 300 kpc from both) do not appear to be denser than the MW dSphs (Kirby et al., 2014), but predictions for halo properties in the Local Field have thus far been sparse.

In this paper, we examine both satellite and field dwarf halos around the hosts of the Exploring the Local Volume in Simulations (ELVIS) Suite (Garrison-Kimmel et al., 2014a, hereafter GK14), a set of zoom-in simulations focused on LG-like environments that resolve $\sim 3$ Mpc regions without contamination from low resolution particles, for the TBTF problem. Specifically, we count the number of "massive failures" – large halos ($V_{\rm peak} > 30\,{\rm km\,s^{-1}}$) that do not have luminous counterparts – both within 300 kpc of the 48 MW-size hosts and in the fields surrounding the LG analogs. Because the ELVIS Suite adopts cosmological parameters from the WMAP-7 results ($\sigma_8 = 0.801$, $\Omega_m = 0.266$, $\Omega_\Lambda = 0.734$, $n_s = 0.963$, and $h = 0.71$; Larson et al., 2011), which includes a significantly lower value of $\sigma_8$ than the WMAP-1 parameter set adopted for the Aquarius simulations, we will also test whether an updated cosmology alleviates the problem. As we show below, however, we predict that there are many such unaccounted-for dense halos throughout the Local Volume. If these halos preferentially host low-luminosity or low-surface brightness galaxies, then future surveys may detect them.

This paper is organized as follows. In §3.2, we briefly describe the simulations and analysis pipeline used in this work. In §3.3, we present empirical scaling relations between the structural parameters of subhalos and field halos and explicitly compare the properties of small halos near isolated hosts with those in paired environments. §3.4 presents the counts of massive failures around each host both within 300 kpc of each host (§3.4.1) and in the field surrounding the Local Group analogs (§3.4.2), as well as a discussion of incompleteness (§3.4.2). We conclude with an analysis of the relationship between $M_\star$ and $V_{\rm max}$ for the

known dwarfs in the Local Field in §3.4.3. Our results are summarized in §3.7.

## 3.2 Simulations: The ELVIS Suite

The simulations used in this work, the ELVIS Suite, are described in detail in GK14. The large scale properties of the LG analogs and the individual properties of the paired and isolated halos (along with their identifying names) are given in that work. Here we briefly summarize the simulations and the analysis pipeline used in this paper.

The suite is comprised of 36 collisionless simulations, half of which are focused on a pair of dark matter halos whose masses, relative kinematics, and environments are similar to the dark matter halos that host the MW and Andromeda (M31) galaxies. The remaining twenty-four simulations are focused on isolated halos that are mass-matched to those in the pairs. Because the mass estimates for the MW and M31 agree within errors (van der Marel et al., 2012; Boylan-Kolchin et al., 2013), both hosts in each paired simulation may separately be considered as an MW analog; the ELVIS Suite therefore contains a total of 48 MW-size systems. The distribution of virial masses[2] $M_{\rm v}$ of the ELVIS hosts nearly evenly samples the mass range between $10^{12} M_{\odot}$ and $2.85 \times 10^{12} M_{\odot}$. All halos in the suite were simulated with a $z = 0$ Plummer equivalent force softening of 141 pc in the high resolution region, which contains particles with a mass $m_{\rm p} = 1.89 \times 10^5 M_{\odot}$. Additionally, three of the isolated hosts were re-simulated with a factor of $2^3$ more particles ($m_{\rm p} = 2.4 \times 10^4 M_{\odot}$) in the high-resolution region and a corresponding $z = 0$ softening length of 70 pc. We use these runs to demonstrate the convergence of subhalo structural parameters in § 3.5.

Bound substructures are identified with `Rockstar`, a six dimensional friend-of-friends halo finder (Behroozi et al., 2013a). For this analysis, the relevant properties are $V_{\rm max}$, the

[2]Throughout, we define $M_{\rm v}$ as the mass within a sphere of radius $R_{\rm v}$ that corresponds to an over density of 97 relative to the critical density.

maximum of the circular velocity profile, and $R_{\rm max}$, the radius at which the circular velocity peaks. We additionally select halos that are expected to have formed stars based upon $V_{\rm peak}$, which is defined as $V_{\rm max}$ of the main branch of the halo's merger tree, built with `Consistent Trees` (Behroozi et al., 2013b), at the timestep when the halo reaches its maximal mass (see GK14 for more details).

Each run in the ELVIS Suite was initialized with a large high-resolution region to specifically enable study beyond the virial radius of the giant halos without contamination due to low resolution (high mass) particles. Specifically, only four (Thelma & Louise, Sonny & Cher, Hall & Oates, and Siegfried & Roy) of the twelve LG realizations contain such contaminating particles within 1.2 Mpc of either halo center. In those cases, moreover, the contamination is minimal: within 1.2 Mpc of either halo center, the contamination by mass is only 0.06%, 0.01%, 0.007%, and 0.0008%, respectively. In addition, the nearest low resolution particles in these four systems are quite distant: 0.8 Mpc, 0.97 Mpc, 1.01 Mpc, and 1.09 Mpc. Catalogs of halos in the fields around the ELVIS hosts are therefore complete and nearly entirely free of contamination at much larger distances than previous high-resolution simulations (the well known CLUES project, Gottloeber et al. 2010, and recent work by Sawala et al. 2014, are notable exceptions).

The goal of this work is to compare predicted halo densities to those of LG dwarfs at scales comparable to their observed half-light radii ($\sim 200 - 1000$ pc). Because our fiducial set of simulations lacks the resolution required make direct predictions at scales below $\sim 1000$ pc, we instead use the well-converged structural parameters ($V_{\rm max}$ and $R_{\rm max}$) together with several reasonable choices for analytic profiles in order to extrapolate to the scales of observed dwarfs.

$R_{\rm max}$ and $V_{\rm max}$ together uniquely define a Navarro-Frenk-White (NFW; Navarro et al., 1996b)

profile:

$$\rho(r) = \rho_0 \left(\frac{2.1626\, r}{R_{\rm max}}\right)^{-1} \left(1 + \frac{2.1626\, r}{R_{\rm max}}\right)^{-2}, \tag{3.1}$$

where $\rho_0$ is defined such that the mass within $R_{\rm v}$ is equal to $M_{\rm v}$. For a given shape parameter $\alpha$, one may also calculate a unique Einasto profile (Einasto, 1965) based upon $R_{\rm max}$ and $V_{\rm max}$, though the scalings between the characteristic radius $r_{-2}$ and $R_{\rm max}$ and between $\rho_{-2}$, the density at $r_{-2}$, and $V_{\rm max}$ depend upon the shape parameter:

$$\rho(r) = \rho_{-2} \exp\left(-\frac{2}{\alpha}\left[\left(\frac{A(\alpha)\, r}{R_{\rm max}}\right)^{\alpha} - 1\right]\right), \tag{3.2}$$

where $r_{-2} = R_{\rm max}/A(\alpha)$. § 3.6 defines $A(\alpha)$ and explicitly compares the NFW and Einasto profiles.

As mentioned above, in addition to the forty-eight halos simulated at the fiducial resolution, the ELVIS Suite also contains high-resolution re-simulations of three of the isolated hosts. We use these halos to ensure the convergence of $V_{\rm max}$ and $R_{\rm max}$ (see § 3.5) and find that a power law fit to the $R_{\rm max} - V_{\rm max}$ relationship,

$$\left(\frac{R_{\rm max}}{1\ {\rm kpc}}\right) = A \left(\frac{V_{\rm max}}{10\ {\rm km\,s^{-1}}}\right)^{1.47}, \tag{3.3}$$

describes both populations well. For $V_{\rm max} > 15$ km s$^{-1}$ and $R_{\rm max} > 0.5$ kpc, the normalizations, $A$, differ by less than 3%.

Therefore, although the standard ELVIS runs lack the resolving power to determine inner differential density profiles, the integral properties of the halos of interest are well constrained. As pointed out by Di Cintio et al. (2013), however, the number of massive failures is dependent on the individual subhalo density profiles. We therefore investigate both the NFW profile and a range of Einasto profiles. We primarily present results with $\alpha = 0.18$,

| Sample | $A_{\rm fit}$ | $A_{+68\%}$ | $A_{-68\%}$ |
|---|---|---|---|
| Isolated | 0.747 | 1.09 | 0.521 |
| Paired | 0.704 | 1.00 | 0.499 |
| Combined | 0.725 | 1.06 | 0.511 |

Table 3.1: Fit results for the $R_{\rm max} - V_{\rm max}$ relationship defined in Equation 3.3. Listed are the normalizations resulting from fitting the data (Column 1) and from fitting the 68% scatter about that relation in bins of 100 points (Columns 2 and 3), separately for subhalos ($r < 300$ kpc) of the isolated and paired hosts, and when combining the datasets (the green lines in Figure 3.1).

which Springel et al. (2008) showed is generally a slightly better fit to subhalos in ultra-high resolution DM-only simulations than an NFW profile, but also use $\alpha = 0.15$ as an example of a peaky Einasto profile and $\alpha = 0.28$ to sample flatter density profiles (this range also encompasses the results of Gao et al. (2008) and Navarro et al. (2010), though both works investigated more massive halos). We will see below that, while exact numbers may depend strongly on the assumed density profile, our overall conclusions hold for all profiles in this regime.

## 3.3 $\mathbf{R_{max} - V_{max}}$ Relationships

As stated above, the parameters $R_{\rm max}$ and $V_{\rm max}$, plus an assumed functional form for the density profile, fully define the circular velocity curve of a halo. The relationship between these parameters is therefore fundamental to the TBTF problem. In this section, we present fits to $R_{\rm max}$ as a function of $V_{\rm max}$ and compare the paired and isolated samples to search for biases in the structure of dwarf halos related to the environments of their hosts.

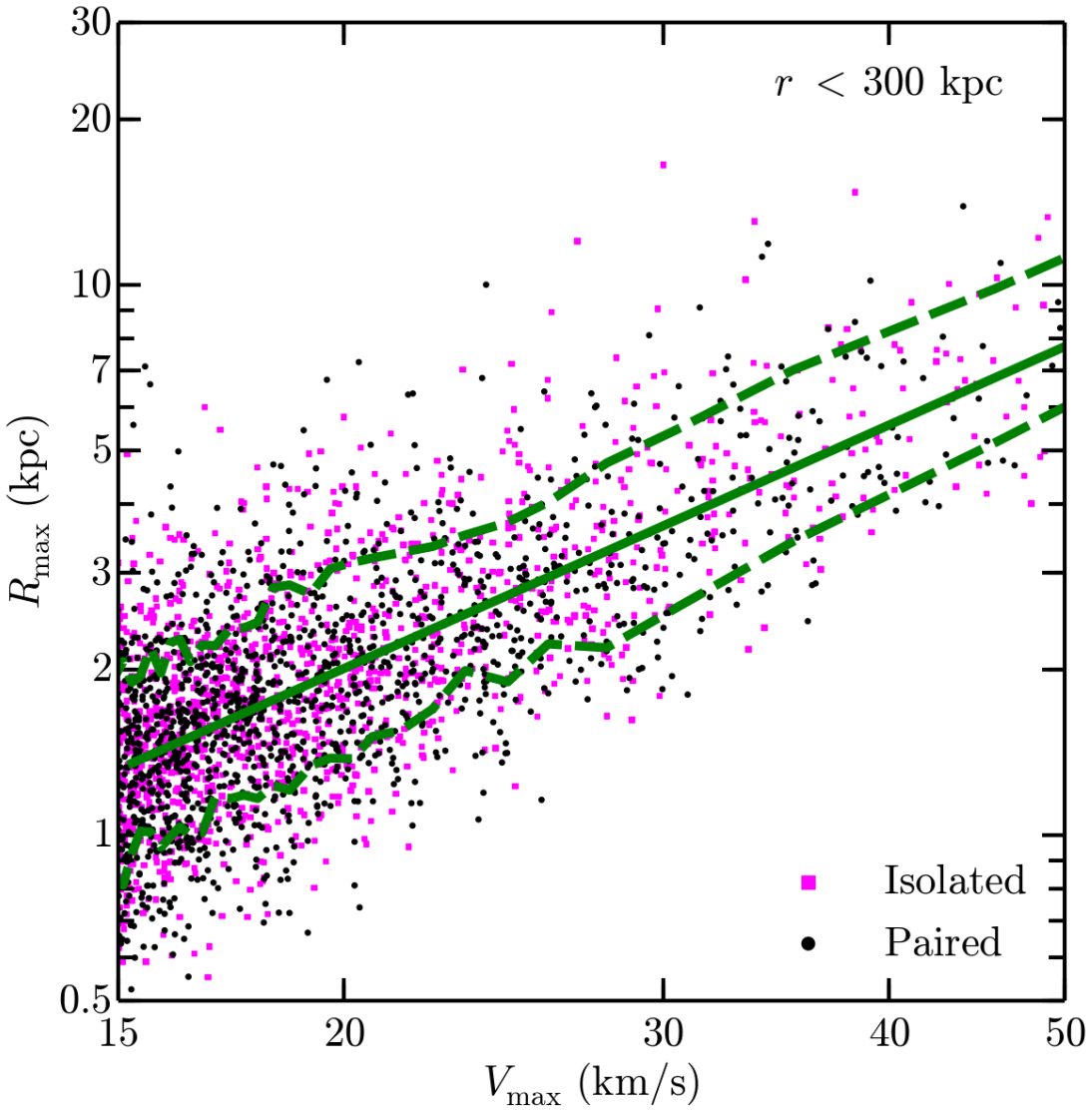


Figure 3.1: The relationship between $R_{\rm max}$ and $V_{\rm max}$ for subhalos in the ELVIS Suite within 300 kpc of each host. Subhalos near the paired hosts are plotted as black circles; those near isolated hosts are indicated by magenta squares. The thick green line plots the fit to all the halos and the dotted green lines encompass 68% of the points; the fits to these relations and the isolated and paired populations separately are given in Table 3.1. As the two datasets follow nearly identical relations and have consistent mass functions within the virial radii (GK14), we will combine the samples for better statistics when counting discrepant halos within 300 kpc of the hosts.

### 3.3.1 Subhalo scaling relations within 300 kpc

Though the ELVIS Suite contains 48 MW-size halos, only those in the paired sample are truly fair comparisons to the MW. However, GK14 showed that subhalo counts at fixed mass are identical between the two samples (when controlling for the host mass); we therefore begin by comparing the structural properties of subhalos of isolated and paired hosts to determine if the samples may be combined when counting massive failures within 300 kpc of the hosts.

Figure 3.1 plots the relationship between $R_{\rm max}$ and $V_{\rm max}$ for all subhalos within 300 kpc of the ELVIS hosts. Subhalos of the isolated hosts are plotted as magenta squares and those of hosts in LGs are indicated by black circles. The green line plots a fit to all the subhalos, holding the slope fixed to that in Equation 3.3; the dashed lines indicate the 68% scatter about that relation, calculated in running bins of 100 subhalos. The normalization of the fit, along with that of fits to the scatter above and below the relation, are given in Table 3.1 separately for the two populations, which differ only at the 5% level, and when combining the datasets. Any variance between subhalos of isolated and paired halos is well within the intrinsic scatter, and we therefore perform the remainder of our analysis within 300 kpc using subhalos of both isolated and paired hosts to maximize our statistics.

Because the subhalo properties in the paired and isolated system agree, we find no evidence that the results of Boylan-Kolchin et al. (2011, 2012) are affected by their study of isolated hosts. However, at the typical size of a TBTF halo ($V_{\rm max} \sim 30 - 50$ km s$^{-1}$), the median $R_{\rm max}$ of a subhalo in the ELVIS systems is $25\% - 30\%$ larger than those in the Aquarius simulations, consistent with the offset in $\sigma_8$ (Zentner & Bullock, 2003; Polisensky & Ricotti, 2014). This allows each dwarf to live in more massive hosts, and will lead to fewer discrepant halos. We will discuss this further in Section 3.4.1.

### 3.3.2 Halo scaling relations in the Local Field

GK14 showed that there are systematic differences between the environments surrounding isolated and paired halos, but did not compare the internal structure of halos in each environment. We therefore search for biases in the Local Field (LF) related to the larger-scale environments by comparing the relationship between $R_{\rm max}$ and $V_{\rm max}$ for field halos around isolated MWs and those in LGs.

Figure 3.2 plots this relationship in the LF (the region within 1.2 Mpc of either giant, but more than 300 kpc from both). The relation is again well fit by a power law with a log slope of 1.47 (Equation 3.3); such a fit is plotted as a light blue line and the 68% scatter about that fit, again calculated in running bins of 100 halos, is indicated by the dashed lines. As expected from tidal stripping arguments (see Zentner & Bullock, 2003; Kazantzidis et al., 2004; Diemand et al., 2007b), the average densities of field halos are significantly lower than subhalos at fixed $V_{\rm max}$, as can be seen from the green line, which indicates the fit within 300 kpc plotted in Figure 3.1. We again fix the slope of the fits and find the normalizations given in Table 3.2.

Although the normalizations presented in Table 3.2 for the isolated and paired samples agree at the percent level, GK14 showed that the number counts do not agree beyond the virial radius of each host. As we are explicitly concerned with both the number and structure of field halos, we will use only those surrounding the paired hosts to count massive failures in the LF. Moreover, as in GK14, we will exclude the two systems with a third large halo in the Local Volume (Siegfried & Roy and Serena & Venus) when studying the LF. However, the apparent lack of structural differences indicates that detailed ultra-high resolution simulations of isolated dwarf galaxies in the field should be accurate analogs to Local Field dwarfs that have not yet interacted with either giant.

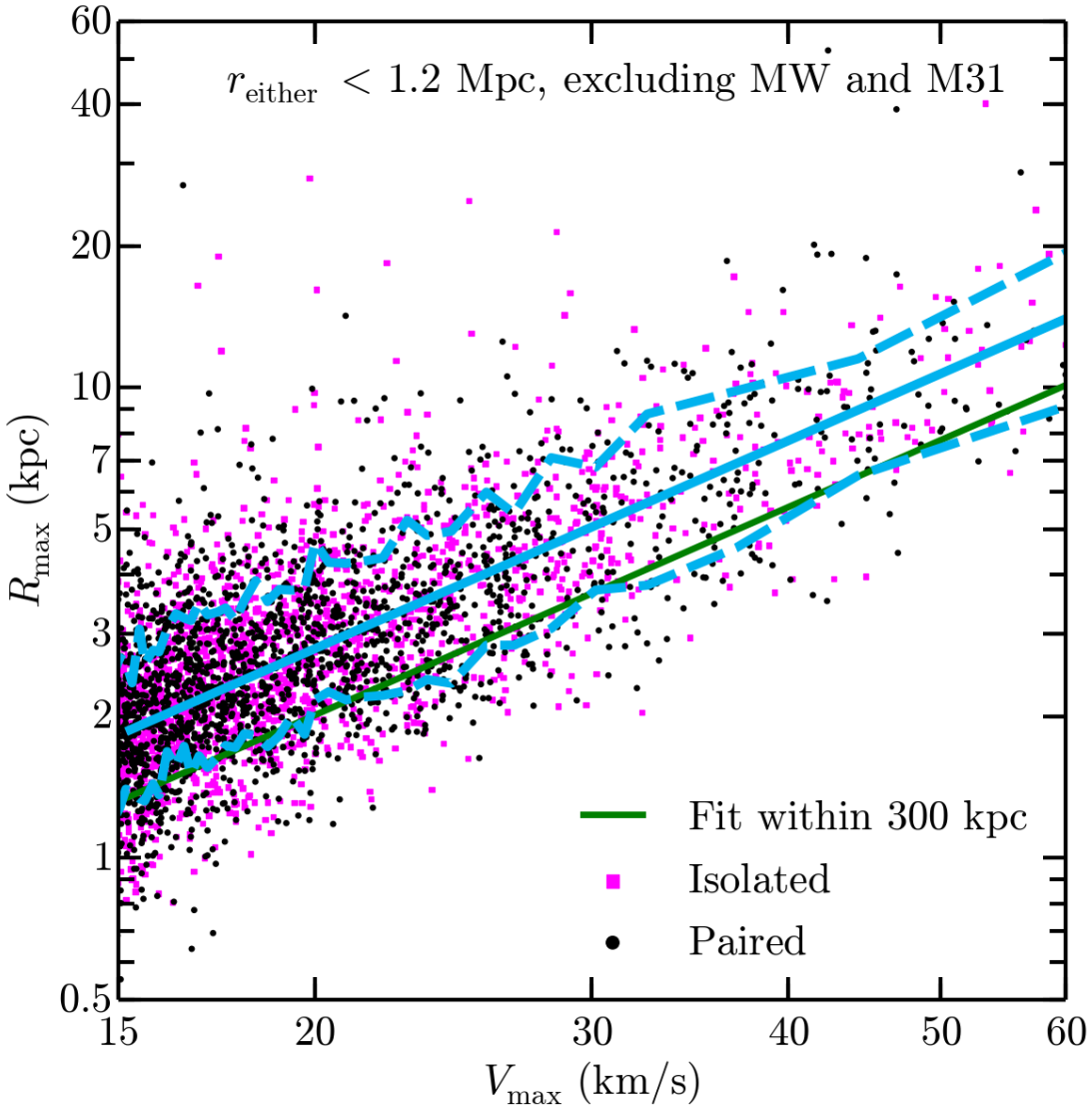


Figure 3.2: Identical to Figure 3.1, but plotting the relationship between $R_{\rm max}$ and $V_{\rm max}$ of halos that reside in the Local Field – the region within 1.2 Mpc of either host, but more than 300 kpc from both giants. The cyan line plots a power-law fit to all the halos with a log slope held equal to that in Equation 3.3; the normalization for all the data and for the individual datasets, along with fits to the scatter (dashed lines) are given in Table 3.2. The green line plots the fit within 300 kpc, where halos are systematically denser at fixed $V_{\rm max}$ due to tidal stripping.

| Sample | $A_{\rm fit}$ | $A_{+68\%}$ | $A_{-68\%}$ |
|---|---|---|---|
| Isolated | 1.016 | 1.443 | 0.723 |
| Paired | 0.994 | 1.437 | 0.709 |
| Combined | 1.005 | 1.448 | 0.719 |

Table 3.2: The normalizations for the $R_{\rm max}$-$V_{\rm max}$ relationship (Equation 3.3) in the Local Field as well as fits to the envelope that contains 68% of the halos, as in Table 3.1. For the paired systems, the Local Field is defined as the region within 1.2 Mpc of either host, but excluding all subhalos within 300 kpc of both hosts; the isolated "Local Fields" include all halos within 1.2 Mpc of the main host only, again excluding all subhalos within 300 kpc.

## 3.4 Massive Failures in the ELVIS Suite

### 3.4.1 Counting massive failures within 300 kpc

Qualitatively, we are concerned with counting halos that are massive enough that they should have formed stars, but that have no obvious luminous counterparts in the local Universe. We select halos with $V_{\rm peak} > 30$ km s$^{-1}$ as "massive enough" because halos larger than 30 km/s should be able to retain substantial gas in the presence of an ionizing background and therefore, *in principle*, should form stars (Babul & Rees, 1992; Efstathiou, 1992; Thoul & Weinberg, 1996; Gnedin, 2000; Okamoto et al., 2008); however, we must also carefully define the criteria to be a "luminous counterpart" of a galaxy in our sample. In what follows, we describe two ways of counting subhalos that have no obvious luminous counterparts.

As in Boylan-Kolchin et al. (2011), our observational sample is comprised of the satellites within 300 kpc of the MW with $M_\star > 2 \times 10^5 M_\odot$, excluding the Sagittarius dwarf and the Magellanic Clouds. Sagittarius is currently undergoing an interaction with the MW disk and is therefore likely not in equilibrium; the dwarf irregular Magellanic Clouds are removed from the sample because satellites as large as the Magellanic Clouds are rare around MW-size hosts (Boylan-Kolchin et al., 2010; Busha et al., 2011; Tollerud et al., 2011; Robotham et al., 2012), and therefore do not have corresponding subhalos in many of the ELVIS systems. Our observational sample is thus likewise comprised of nine galaxies with $L > 10^5 L_\odot$: the

classical dSphs and Canes Venatici (CVnI).

We now turn to the problem of assigning galaxies to subhalos, and identifying subhalos without luminous counterparts. The original formulation of TBTF counted unidentified subhalos as objects with circular velocity profiles that were at least $2\sigma$ above the observed circular velocity of each dwarf at its half-light radius ($V_{1/2} = V_{\rm circ}(r = r_{1/2})$). These subhalos clearly lack observational counterparts. We will adopt a similar counting procedure, but instead use $1\sigma$ errors to define over-dense outliers. Specifically, we will refer to subhalos with $V_{\rm peak} > 30$ km s$^{-1}$ that are more than $1\sigma$ denser (at $r_{1/2}$) than any of the MW dwarfs as "strong massive failures."

This "strong massive failure" formulation, which mirrors that originally used in Boylan-Kolchin et al. (2011, 2012), is particularly conservative. By counting only subhalos that are denser than all of the MW dwarfs, it ignores the potentially large number of subhalos that are consistent with hosting only the densest observed dwarfs. Most MW-size hosts contain several subhalos that can *only* host either Draco or Ursa Minor, but nothing else. Since clearly only one halo can actually host Draco, this way of counting under-estimates the magnitude of the problem. Moreover, the "strong massive failure" definition is highly dependent on a single object, the densest MW dSph (Draco). If Draco did not exist, the strong massive failure count would be much larger. Similarly, if Draco were twice as dense, the strong massive failure count would approach zero. Ideally, we would like to find a measure that is less sensitive to the properties of a single object.

With these issues in mind, we introduce a second way of counting unidentified massive subhalos, which we refer to as the "massive failure" count. These are halos that were massive at infall (with $V_{\rm peak} > 30$ km s$^{-1}$) and that have no observational counterpart after each dense satellite is assigned to a single subhalo. Specifically, we find all halos that are *at least* as dense as Draco and Ursa Minor (in practice this demands that today halos have $V_{\rm max} \gtrsim 25$ km s$^{-1}$). We then examine the subset that are consistent with either Ursa Minor

or Draco and remove the most massive possible counterpart to those galaxies. The remaining set allows us to enumerate unaccounted-for, yet massive, halos. We will discuss the impact of selecting Draco and Ursa Minor for this process below.

To summarize, we will count two classes of discrepant halos in the ELVIS Suite. **Strong massive failures** are too dense to host any of the *known* bright MW dSphs, with circular velocities at $r_{1/2}$ that are above the $1\sigma$ constraints for all the dwarfs in the sample. **Massive failures** include all strong massive failures plus all massive halos that have densities consistent with the high density dwarfs (Draco and Ursa Minor) but that can't be associated with them without allowing a single galaxy to be hosted by multiple halos. For typical profiles, subhalos with $V_{\rm max} \lesssim 25 - 30$ km s$^{-1}$ can host a low density dwarf, and thus are never selected as a massive failure; the **massive failures** are therefore generally subhalos that started out dense ($V_{\rm peak} > 30$ km s$^{-1}$) and remain dense ($V_{\rm max} \gtrsim 25$ km s$^{-1}$) at $z = 0$.

Figure 3.3 provides an illustration of these definitions. Shown are rotation curves of all $V_{\rm peak} > 30$ km s$^{-1}$ halos identified within 300 kpc of an $M_{\rm v} = 1.3 \times 10^{12}\ M_{\odot}$ halo (Douglas, a paired host in the ELVIS sample). The solid black lines and solid cyan lines plot massive failures; the latter are *strong* massive failures because they are denser than every dwarf. The dotted curves indicate subhalos that had $V_{\rm peak} > 30$ km s$^{-1}$ but that are *not* massive failures – the magenta dotted lines are those selected to host Draco and Ursa Minor, and the grey dotted lines plot systems that have been stripped enough to host the lower density galaxies at $z = 0$. The curves correspond to Einasto profiles with $\alpha = 0.18$, normalized using the measured $R_{\rm max}$ and $V_{\rm max}$ values for each identified system. The dashed grey line indicates the lone Magellanic Cloud analog in Douglas, defined as subhalos with present day $V_{\rm max} > 60$ km s$^{-1}$ (Stanimirović et al., 2004), which is eliminated from our analysis. Our cut is again less conservative than that in Boylan-Kolchin et al. (2011): the criterion used by those authors would eliminate approximately one additional subhalo per host, on average (i.e. they would measure one fewer strong massive failure per host).

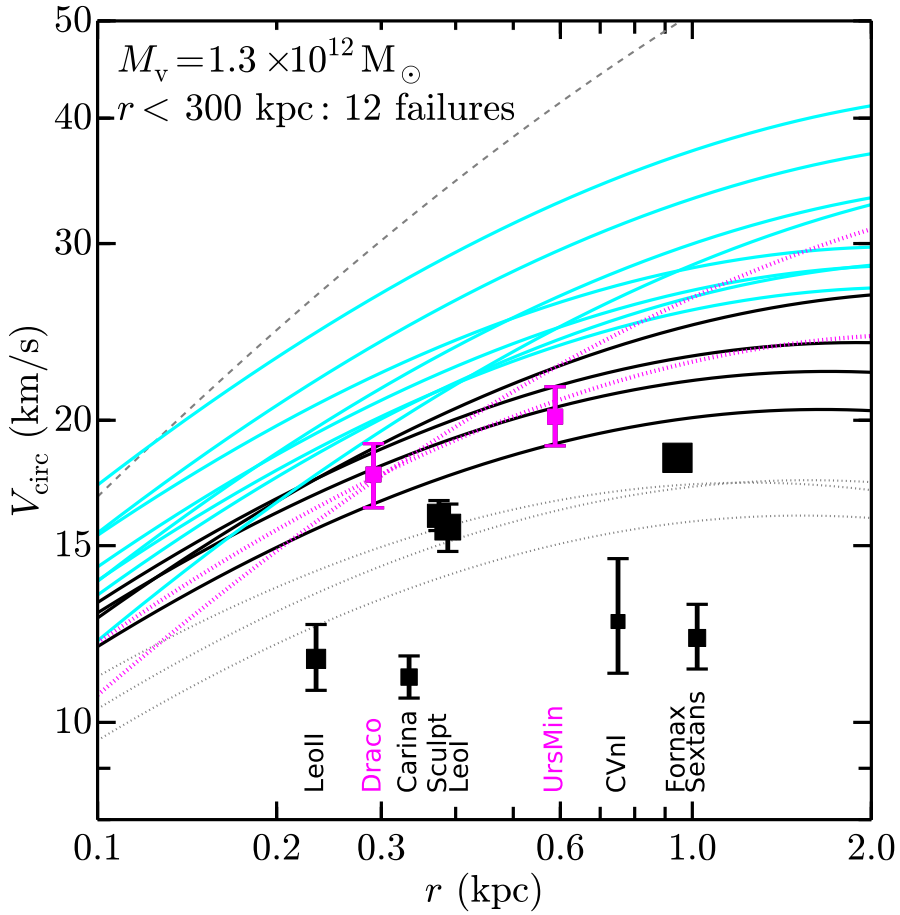


Figure 3.3: Rotation curves, assuming Einasto profiles with $\alpha = 0.18$, of all resolved halos with $V_{\rm peak} > 30$ km s$^{-1}$ within 300 kpc of the center of Douglas (based on measured $V_{\rm max}$ and $R_{\rm max}$ values in the simulation). Plotted as black points are the data for the MW satellites brighter than $2 \times 10^5$ L$_\odot$ compiled in Wolf et al. (2010), with sizes proportional to the log of their stellar masses. The cyan lines indicate strong massive failures – subhalos that are too dense to host *any* of the MW dSphs. The black lines plot the additional subhalos that are identified as massive failures according to the stricter definition given in the text: halos with $V_{\rm peak} > 30$ km s$^{-1}$ that are not accounted for by the dense galaxies in the observational sample. The subhalos with $V_{\rm peak} > 30$ km s$^{-1}$ that are selected to host the high density galaxies, Draco and Ursa Minor, are indicated by dotted magenta lines, with their associated galaxies plotted as magenta squares. The dotted lines plot the subhalos that are consistent with at least one of the remaining seven dwarfs in our sample, which are allowed to reside in multiple such subhalos. The grey dashed line indicates the sole subhalo of Douglas expected to host a Magellanic Cloud ($V_{\rm max} > 60$ km s$^{-1}$), which we exclude from our analysis. Not plotted are 40 resolved ($V_{\rm max} > 15$ km s$^{-1}$) subhalos with $V_{\rm peak} < 30$ km s$^{-1}$. In all, Douglas hosts twelve unaccounted-for massive failures, including eight strong massive failures that are too dense to host any bright MW dSph.

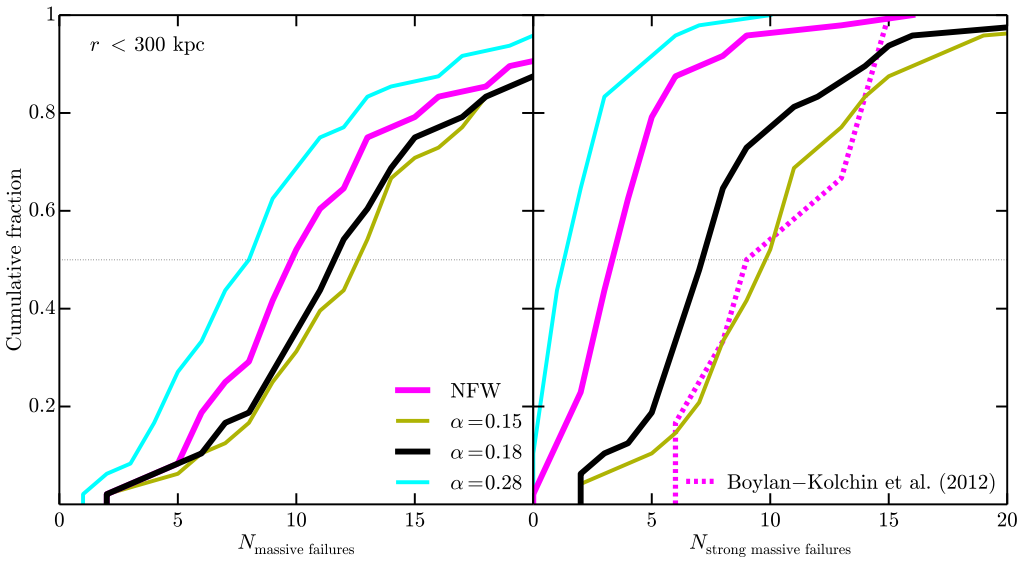


Figure 3.4: The fraction of hosts (out of 48) with fewer than $N$ massive failures on the left and $N$ strong massive failures on the right within 300 kpc of each host, as a function of $N$. Plotted are results assuming an NFW density profile (magenta) and Einasto profiles with $\alpha = 0.15$ (dark yellow), 0.18 (black), and 0.28 (cyan). In the left panel, we plot the number of strong massive failures in the Aquarius hosts as a dashed magenta line. Less than 10% of the ELVIS hosts contain no strong massive failures and we predict $\sim 12$ massive failures within 300 kpc of the MW.

The data points in Figure 3.3 indicate measurements of $V_{1/2}$ at $r_{1/2}$ for the MW dSphs in our sample (taken from Wolf et al. 2010, who used data from Walker et al. 2009 along with data from Muñoz et al. 2005; Koch et al. 2007; Simon & Geha 2007 and Mateo et al. 2008).[3] The Wolf et al. formula is analytically exact for spherically symmetric systems with flat velocity dispersion profiles. However, for strongly non-spherical systems the mass (circular velocity) at $r_{1/2}$ can be under-estimated by as much as 40% (18%) if the satellite is viewed along the long-axis, and similarly over-estimated by as much as 50% (22%) if viewed from along the short axis (Kowalczyk et al., 2013). Shifts of order 20% in $V_{1/2}$ in Figure 3.3 (roughly the size of the error bars on Draco and Ursa Minor) would not strongly affect our overall

[3]For simplicity, we exclude galaxies within 300 kpc of M31 – many of the M31 satellites have substantial contributions from baryons within $r_{1/2}$, making a measurement of the central dark matter density very difficult. However, the central masses of the M31 dSphs appear to be consistent with the MW dSphs (Tollerud et al., 2012), and are therefore inconsistent with the subhalos expected to host them (Tollerud et al., 2014).

conclusions. Other mass estimators in the literature (e.g. Breddels & Helmi, 2013; Jardel & Gebhardt, 2013) yield results that are consistent with those plotted in Figure 3.3.

The points in Figure 3.3 are sized by the log of the stellar mass of each galaxy. Plotted in black are the low density MW dSph galaxies. The magenta points indicate the high density dSphs, Draco and Ursa Minor, which may only be associated with a single subhalo in each host (indicated by the dotted magenta lines) when counting massive failures. If the data points for Draco or Ursa Minor were 10 $\mathrm{km\,s^{-1}}$ higher (e.g. if $V_{1/2}$ were underestimated), the strong massive failures (cyan lines) would vanish but the number of massive failures (cyan and black lines) would remain unchanged.

Figure 3.4 summarizes the results of counting massive failures in the complete set of forty-eight hosts, where each line corresponds to a different assumed density profile shape. Black lines show results for our fiducial choice, an $\alpha = 0.18$ Einasto profile; also shown are the implied distributions for NFW profiles (magenta), an underdense Einasto (cyan; $\alpha = 0.28$), and an overdense Einasto (dark yellow, $\alpha = 0.15$). The left panel indicates the cumulative distribution of massive failures and the right plots the same for strong massive failures; also plotted as a dashed magenta line is the distribution of $1\sigma$ discrepant subhalos from the Aquarius simulations, which we discuss below. As explained above, the strong definition is highly sensitive to the densest dwarf; it is likewise strongly dependent on the density profile, with medians varying between 2 and 10 for those chosen here. The number of massive failures, however, is more consistent and varies by a maximum of $\sim 5$ – the median varies from 8.5 for $\alpha = 0.28$ to 13 for $\alpha = 0.15$.

All of the forty-eight hosts contain at least two strong massive failures for $\alpha = 0.18$; using the slightly less dense NFW profile results in only one (iHera, with $M_{\mathrm{v}} = 1.22 \times 10^{12} M_{\odot}$) of the forty-eight hosts (2%) containing no strong massive failures.[4] Even the least dense

[4]However, iHera does not host any LMC or SMC candidate subhalos and therefore remains an imperfect match to the MW satellite system.

profile considered here ($\alpha = 0.28$) leads to only five hosts (10%) with no strong failures.[5] These results are similar to the expectations of Purcell & Zentner (2012), who estimated the prevalence of strong massive failures in Milky-Way size hosts using a semi-analytic formalism, though in detail we have found slightly higher fractions of systems with strong massive failures.

The problem is revealed as more serious when we enumerate all unaccounted-for massive halos, however. None of the ELVIS hosts are without massive failures: the least problematic MW analogs host $\sim 3$ dense subhalos without bright counterparts – more than twice the number of known dense satellites. Unless the spatial distribution of dense satellites is highly anisotropic such that their on-the-sky density drastically increases behind the plane of the disk, it is unlikely that this disagreement can be reconciled via incompleteness arguments. However, one explanation of the observed lack of bright satellites between $100 - 400$ kpc of the MW (Yniguez et al., 2014) is that there are as many as $\sim 10$ missing MW satellites with $L > 10^5 L_\odot$ – TBTF may be explained if the majority of these missing galaxies are as dense or denser than Draco, though there is no a priori reason to believe this to be the case.

The choice of Draco and Ursa Minor as our high-density dwarfs is based on the observation that they are the only two systems that demand to be hosted by $V_{\rm max} > 20$ km s$^{-1}$ halos to high significance. Nevertheless, it is useful to investigate how our massive failure count would change if we altered this choice. The number of massive failures shrinks if only Draco or only Ursa Minor is selected to be uniquely hosted (the medians vary between $5 - 11$ for Draco only and $6 - 11$ for Ursa Minor only), but adding more dSphs to this list identifies only a few more subhalos as massive failures: including the three additional galaxies with $V_{1/2} > 15$ km s$^{-1}$ (Fornax, Leo I, and Sculptor) raises the median per host to only $11 - 13$. That is, there are $\sim 10$ subhalos per host as dense or denser than Draco and Ursa Minor, but there are only $\lesssim 4$ additional subhalos with central densities similar to Fornax, Leo I,

[5]For completeness sake, we note that the massive failures are drastically reduced in number or disappear completely if we assume a strongly cored or flat inner profile ($\alpha = 0.5 - 1$).

and Sculptor that have reached $V_{\rm peak} \geq 30$ km s$^{-1}$.

Our results are consistent with the expectation that lowering $\sigma_8$ helps to alleviate TBTF. The distribution of the number of strong massive failures in the Aquarius hosts is plotted as the dotted magenta line in Figure 3.4. As in Boylan-Kolchin et al. (2012), NFW profiles have been assumed in the inner region of the halos. Though the sample size is much smaller (6 instead of 48), there are significantly more massive failures in the WMAP-1 cosmology than result from the updated WMAP-7 values, in agreement with Lovell et al. (2014) and Polisensky & Ricotti (2014). Note, however, that the $\sigma_8$ we have adopted (based on WMAP-7) is somewhat lower than the favored value from the first-year Planck results (Planck Collaboration et al., 2013), and even so the number of massive failures remains high.

We have also checked for correlations with host mass, and find a weak positive correlation, as expected from the scaling of the subhalo mass function. The scatter about the trend is very large, but an extrapolation of the fit suggests that the MW mass must be below $\sim 7 \times 10^{11} M_\odot$ to eliminate the massive failures (see also Boylan-Kolchin et al., 2012; Wang et al., 2012; Purcell & Zentner, 2012), which is in conflict with large-scale dynamical mass estimates of the MW (van der Marel et al., 2012; Boylan-Kolchin et al., 2013, and references therein).

### 3.4.2 Massive failures in the Local Field

#### Counting discrepant field halos

Now we extend our count of expected massive halos to the Local Field (LF) – a volume defined to be within 1.2 Mpc of either giant host, but excluding 300 kpc spherical regions around each in order to avoid satellites (and thus the potential for large tidal influences). Figure 3.5 is analogous to Figure 3.3, in that it compares halos within the LF of the ELVIS

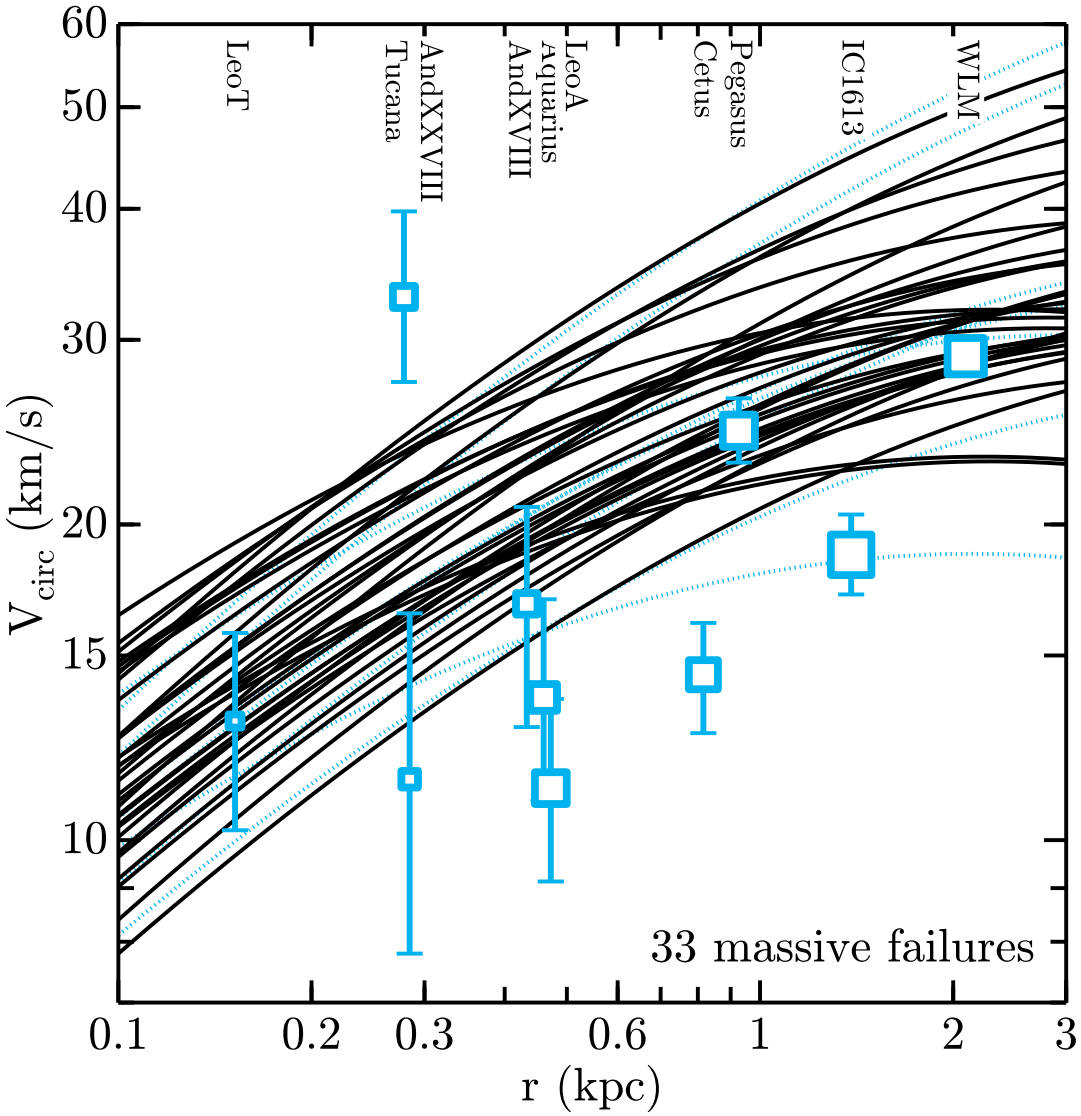


Figure 3.5: Rotation curves ($\alpha = 0.18$) for all resolved field halos in the LF around Zeus & Hera with $V_{\rm peak} > 30$ km s$^{-1}$ (extrapolated from measured $V_{\rm max}$ and $R_{\rm max}$ values in the simulation). Massive failures (unaccounted-for satellite halos that became large enough to from stars) are plotted as black lines; halos that are hosting one of the field dwarfs are indicated by light blue dotted lines. As in Figure 3.3, halos with $V_{\rm peak} < 30$ km s$^{-1}$ are not plotted – there are 254 such resolved halos in the Local Field around Zeus & Hera. The light blue points indicate the kinematic constraints on the galaxies in the LF; their sizes are again proportional to the log of the stellar mass of each galaxy. Many of the massive failures are denser than all the known field dwarfs except for Tucana.

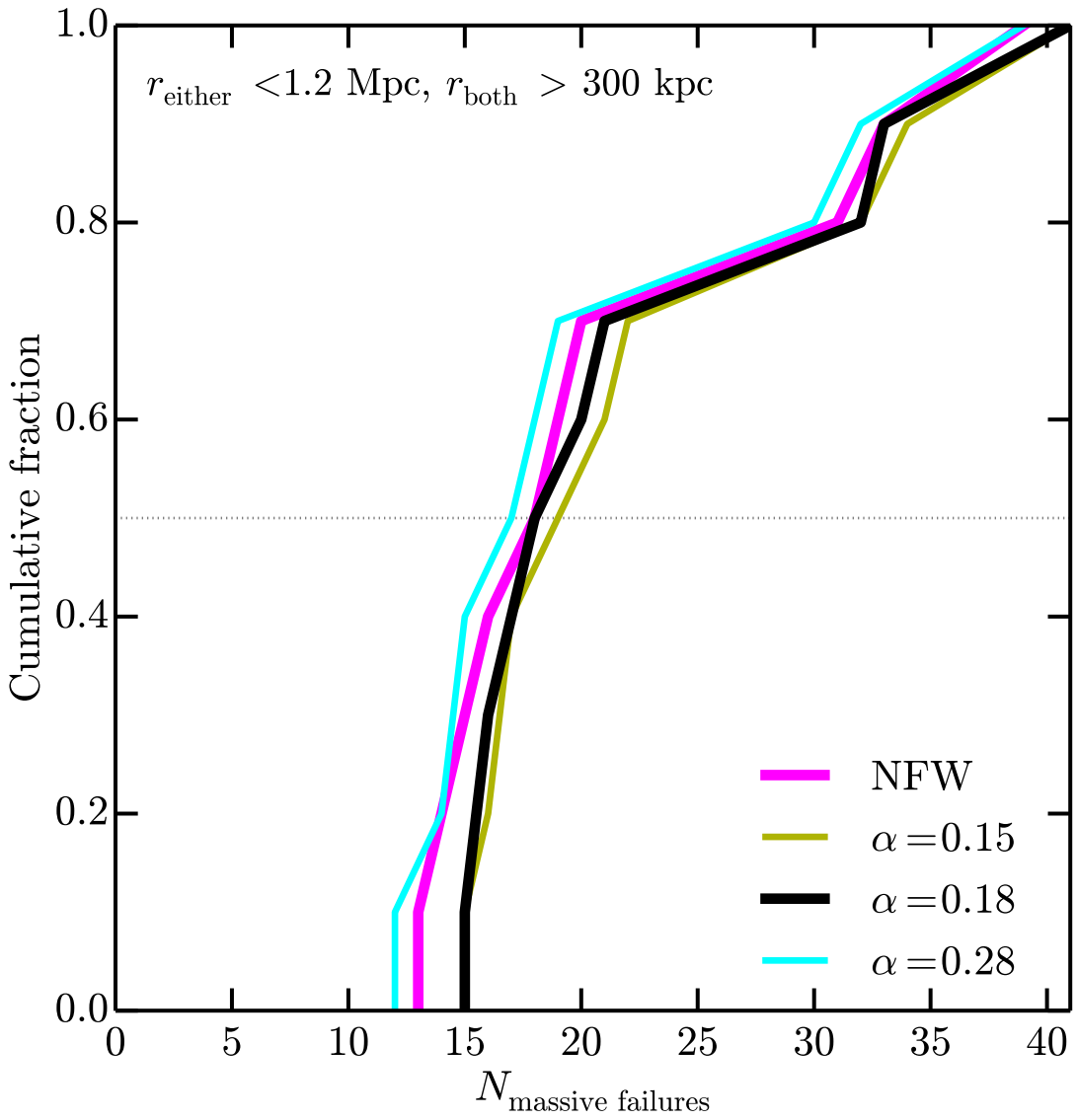


Figure 3.6: The distribution of the number of massive failures in the fields surrounding the ten LG analogs in the ELVIS pairs without a third giant nearby. Plotted are the number of field halos with $V_{\rm peak} > 30$ km s$^{-1}$ that do not have a corresponding bright galaxy in the field for the four profiles that we consider in this work; the colors are as in Figure 3.4. The ELVIS simulations predict that there are $\sim 18-20$ missing galaxies in the Local Field, many of which should be denser than the majority of the known field dwarfs (i.e. comparable to Tucana and Leo T).

pair Zeus & Hera to observed galaxies within the same volume around the MW and M31.

In GK14, we showed that the Zeus & Hera pair provides a good match to the observed

stellar mass function in the Local Group when abundance matching is applied (see Figure 9 of GK14). The open light blue data points plot constraints on $V_{1/2}$ at $r_{1/2}$ for the ten dark matter-dominated galaxies in the LF with measured line-of-sight stellar velocity dispersions, $\sigma_\star$, again with sizes proportional to the log of their stellar masses.[6]

There are four known galaxies that meet the distance cuts but that we exclude from our analysis: NGC 6822, Sagittarius dIrr, Andromeda XVI, and Phoenix. Of these four, all but NGC 6822 lack definitive mass measurements. The galaxy NGC 6822 is baryon dominated (Kirby et al., 2014) and we exclude it because determining its dark matter mass is difficult and because its host halo is likely to have undergone adiabatic contraction. There have been no attempts to measure the stellar velocity dispersion of the Sagittarius dIrr galaxy. Letarte et al. (2009) established an upper limit of $V_{1/2} < 17.3$ km s$^{-1}$ at $r_{1/2} = 0.18$ kpc for Andromeda XVI, similar to the measurement for Leo T in ($V_{\rm circ}$, $r$) space. In a conference proceeding, Zaggia et al. (2011) published $(V_{1/2}, r_{1/2}) \approx (14$ km s$^{-1}$, 0.6 kpc) for Phoenix, placing it between Aquarius and Cetus in Figure 3.5, and therefore among the lower density dwarfs. Therefore, our massive failure counts may be high by 3 (before accounting for incompleteness, which we discuss further in §3.4.2).

For the seven galaxies that are purely dispersion supported, we calculate $V_{1/2}$ from $\sigma_\star$ via the Wolf et al. (2010) formula. Velocity dispersions for the two Andromeda dwarfs with constraints on $\sigma_\star$ that meet the distance cuts are from Collins et al. (2013). Measurements for the field dwarfs are from Kirby et al. (2014) where available; the constraints on Leo T and Tucana are from Simon & Geha (2007) and Fraternali et al. (2009), respectively. Three of the field dwarfs – WLM, Pegasus, and Tucana – also display evidence of rotation support, and are therefore not well described by the Wolf et al. (2010) methodology. We use the result from Leaman et al. (2012) for WLM, who calculated the mass within $r_{1/2}$ with a detailed dynamical model. For the latter two, we follow Weiner et al. (2006) in replacing $\sigma_\star^2$ with

[6]See §3.4.2 for a summary of the origin of the $M_\star$ estimates.

$\sigma_\star^2 + \frac{1}{2}(v \sin i)^2$ when calculating $V_{1/2}$, where $v \sin i$ is the projected rotation velocity (see also §5.2 of Kirby et al., 2014).

The lines in Figure 3.5 plot the extrapolated rotation curves of the resolved dwarf halos with $V_{\rm peak} > 30$ km s$^{-1}$ around Zeus & Hera, again assuming an Einasto profile with $\alpha = 0.18$. That the lower-right section of the plot is empty is typical of the ELVIS fields – only ∼10-25% of the field halos that meet the "massive" cut ($V_{\rm peak} > 30$ km s$^{-1}$) have been sufficiently stripped to have $V_{\rm max} < 25$ km s$^{-1}$. Blue dotted lines indicate individual halos that are consistent with observed dwarfs; we do not count these systems as massive failures.

The black lines in Figure 3.5 indicates the massive failures in the Local Field. Due strictly to the published mass for Tucana, which is above *every* halo in the sample for $\alpha = 0.18$; there are no strong massive failures in the LFs around the ELVIS hosts.[7] However, the systematic over-abundance of large halos remains: though Tucana eliminates any strong massive failures in the LF, the median number of halos per field that are consistent *only* with Tucana, i.e. the number of halos that would be identified as strong massive failures if Tucana did not exist, is 7.5, again assuming $\alpha = 0.18$. We will further show below that, if abundance matching holds at these masses, most of these galaxies should be bright ($M_\star > 10^6 M_\odot$). Moreover, the lack of environmental stripping at larger radii leaves the vast majority of these objects with $V_{\rm max} > 30$ km s$^{-1}$ today.

The distribution of the number of massive failures in the Local Field is plotted in Figure 3.6. The number of halos that are naively expected to host luminous galaxies ($V_{\rm peak} > 30$ km s$^{-1}$) exceeds the number of known dwarfs by a factor $\gtrsim 2$ in every case – no system has fewer than thirteen massive failures, even for $\alpha = 0.28$. Importantly, the exact number is insensitive to the assumed profile, with the minimum count of massive failures varying only by ±3 among the pairs studied here. In a relative sense, the LF massive failure counts are even more

[7]The field around Scylla & Charybdis contains two halos with circular velocities that marginally exceed that of Tucana at $r_{1/2}$ if $\alpha = 0.15$, but they agree within $1\sigma$.

robust than the counts within 300 kpc. The minimum number of massive failures in the LF varies from $12 - 15$ (depending on assumed profile shape) and the median number varies from $16 - 18$.[8]

Of course, the count given in Figure 3.6 ignores massive failures within the virial radii of either M31 or the MW. In order to give a more complete picture of TBTF problem throughout the Local Group, Figure 3.7 plots the rotation curves of all the massive failures near Douglas (excluding only those within 300 kpc of its M31 analog, Lincoln); i.e. it combines Figure 3.3 with a plot equivalent to Figure 3.5. Plotted as black lines are massive failures within 300 kpc; the light blue lines plot massive failures in the LF. The black and light blue points again plot constraints on the MW satellites and galaxies in the LF, respectively. Halos selected to host those galaxies are not plotted. We have not included a comparison of the full Local Group including M31 satellites because, as explained above, M31 contains several baryon-dominated satellites, making the accounting more complicated. A more in-depth analysis of the M31 system is given in Tollerud et al. (2014).

Figure 3.8 provides an overview of the TBTF problem in the LG. As before, we combined the results of Figures 3.4 and 3.6, adding together the counts within 300 kpc and the Local Field for each MW analog, excluding the 300 kpc volume around the M31 analog. The distribution is therefore based on twenty virial volumes combined with ten LF analogs; none of these combinations contain fewer than thirteen massive failures. We find typically $\sim 26 - 34$ massive failures in the Local Volume, even excluding halos and galaxies within 300 kpc of M31. We find no trend between the number of massive failures within 300 kpc of a host and the number within the LF surrounding it.

Tides from disk interactions and ram pressure stripping are baryonic process that have been invoked to lower the density of massive failure halos beyond what is predicted in

[8]Unlike the situation within 300 kpc, the missing halos are not explained by cored profiles: due to the relatively large half-light radii of WLM and IC 1613, there are at least eleven massive failures in each LF, even assuming $\alpha = 1$.

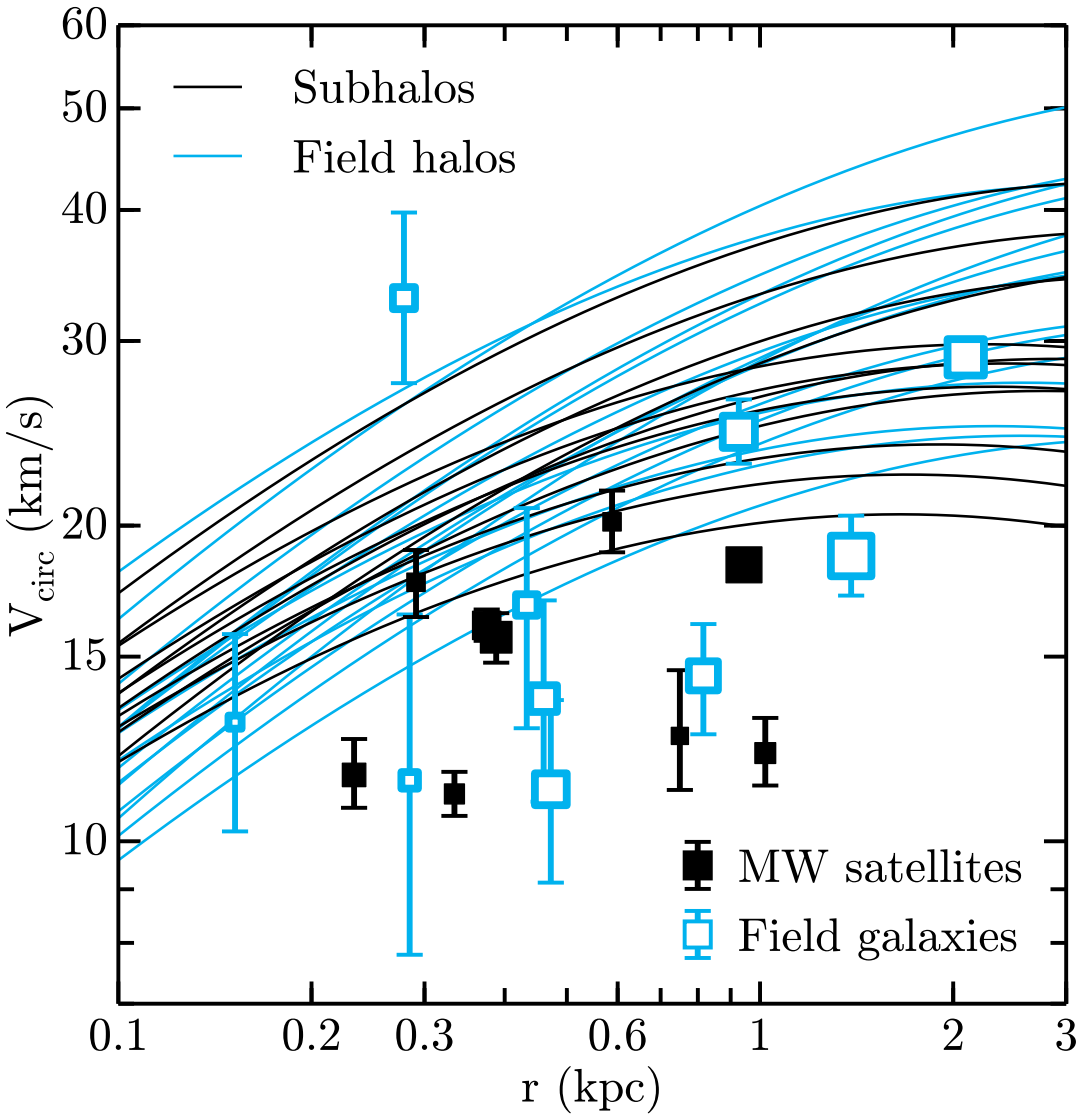


Figure 3.7: Plotted are the rotation curves for all halos identified as massive failures around Douglas, both within 300 kpc (black lines) and in the Local Field surrounding it (light blue lines), along with constraints on the dwarf galaxies in each region (black squares denote MW satellites and open light blue squares indicate field galaxies – sizes are again proportional to $M_\star$); i.e. combining Figure 3.3 with a plot equivalent to Figure 3.5. Explicitly excluded are halos with $V_{\rm peak} < 30$ km s$^{-1}$; also not plotted are the halos selected to host a galaxy.

dissipationless simulations (Zolotov et al., 2012; Arraki et al., 2013; Brooks & Zolotov, 2014; Brooks et al., 2013). However, in the Local Field, particularly more than $\sim 500$ kpc from the nearest giant where the backsplash fraction is below 50% (GK14), central halo densities

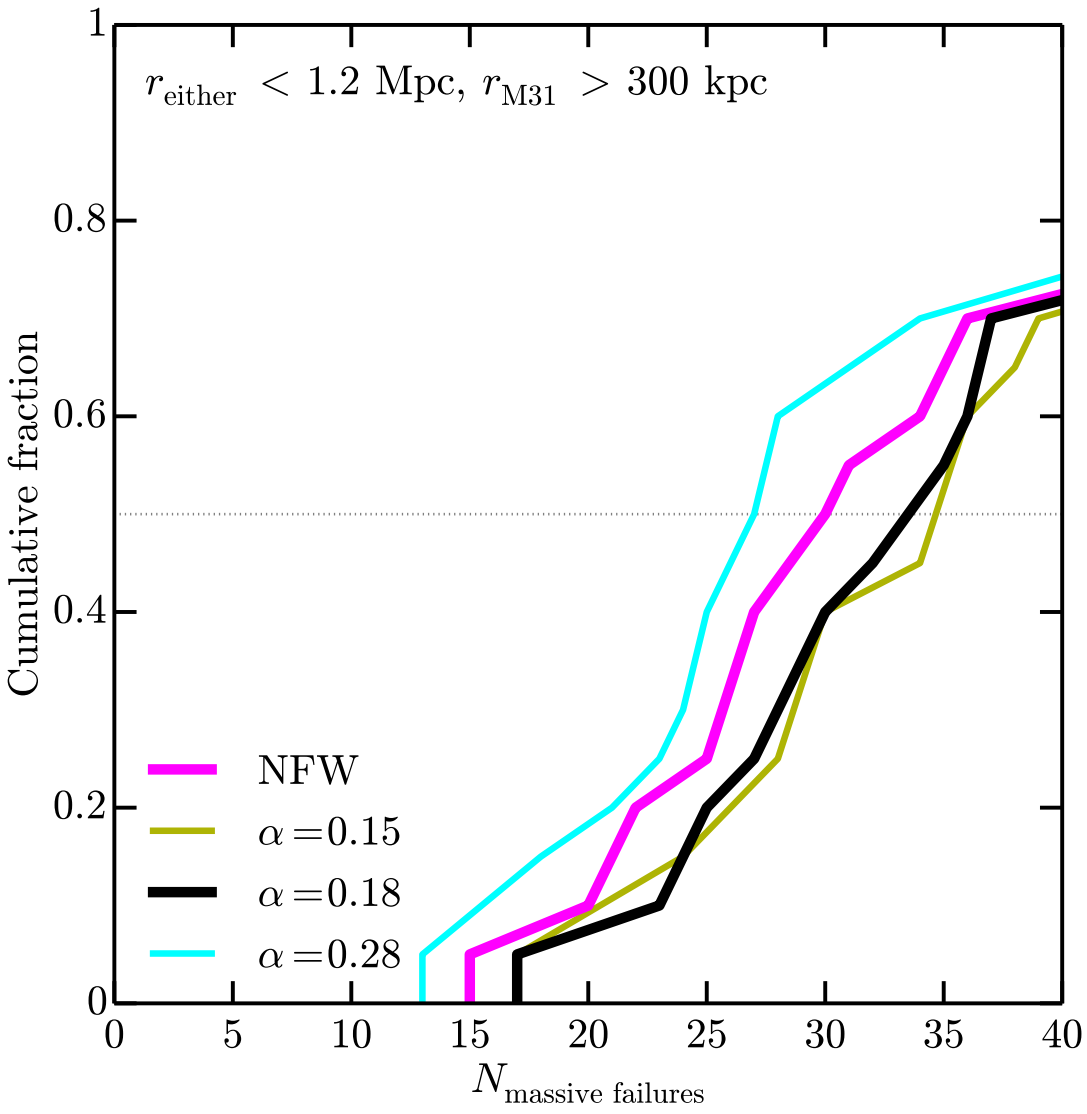


Figure 3.8: The distribution of the number of massive failures in each of twenty paired halos plus the field around them, i.e. combining results from Figures 3.4 and 3.6 but excluding failures that are within 300 kpc of the M31 analog. Colors are as in Figures 3.4 and 3.6. The exact number of massive failures depends on the specific density profile, but the conclusion that there are many missing large, dense halos in the Local Field is robust: each system has at least 14 massive failures, with a median between $\sim 26 - 34$.

should remain largely unaffected by tidal and ram pressure stripping. Moreover, Tucana, which shows evidence of having interacted with the MW (Teyssier et al., 2012), is the most dense galaxy in the field, calling into question proposed environmental mechanisms. Galaxies large enough to have affected their density profiles via supernovae feedback may be lurking unseen on the outer edge of the LF, but no galaxies brighter than $10^7 L_\odot$ have been discovered in the LF within the past fifty-five years (Pegasus dIrr; Holmberg, 1958).

**Missing galaxies in the Local Field?**

In this Section, we present the stellar masses of those halos identified as massive failures, from abundance matching, and investigate whether the they can be explained as unidentified dwarf galaxies in the LF. Though no galaxies have been discovered within the distance cut since the discovery of Andromeda XXVIII (Slater et al., 2011), the recent discovery of Leo P (Giovanelli et al., 2013; Rhode et al., 2013) at a distance of $\sim$ 1.5 Mpc from the MW suggests that there may be new galaxies in the Local Volume that will be identified via HI observations or upcoming deep stellar surveys.

We begin by plotting the predicted stellar mass functions implied by our favored AM extrapolation from GK14, along with the observed stellar mass function of galaxies that meet the same radial cuts in the LG (in blue) in Figure 3.9. [9] Stellar masses are from Woo et al. (2008) where available and are otherwise taken from the data cataloged in McConnachie (2012), assuming $M_\star/L = 2$. We emphasize that the adopted AM relation does well in reproducing the observed stellar mass function above stellar masses $M_\star = 4 \times 10^6 M_\odot$. The shaded region below this point draws attention to the region where the known census of galaxies lies below that predicted. Above this mass, however, the galaxy count around Zeus & Hera, the pair

[9] We emphasize that the stellar mass range shown is large enough that an AM-inspired power-law relationship between $M_\star$ and $M_{\rm v}$ is well-motivated. Specifically, this is above the mass regime ($M_\star < 10^6\ M_\odot$, $V_{\rm peak} < 30\ {\rm km\,s^{-1}}$) where processes like reionization might act to "bend" the relation (Sawala et al., 2014), possibly suppressing the count of faint galaxies in the Local Group.

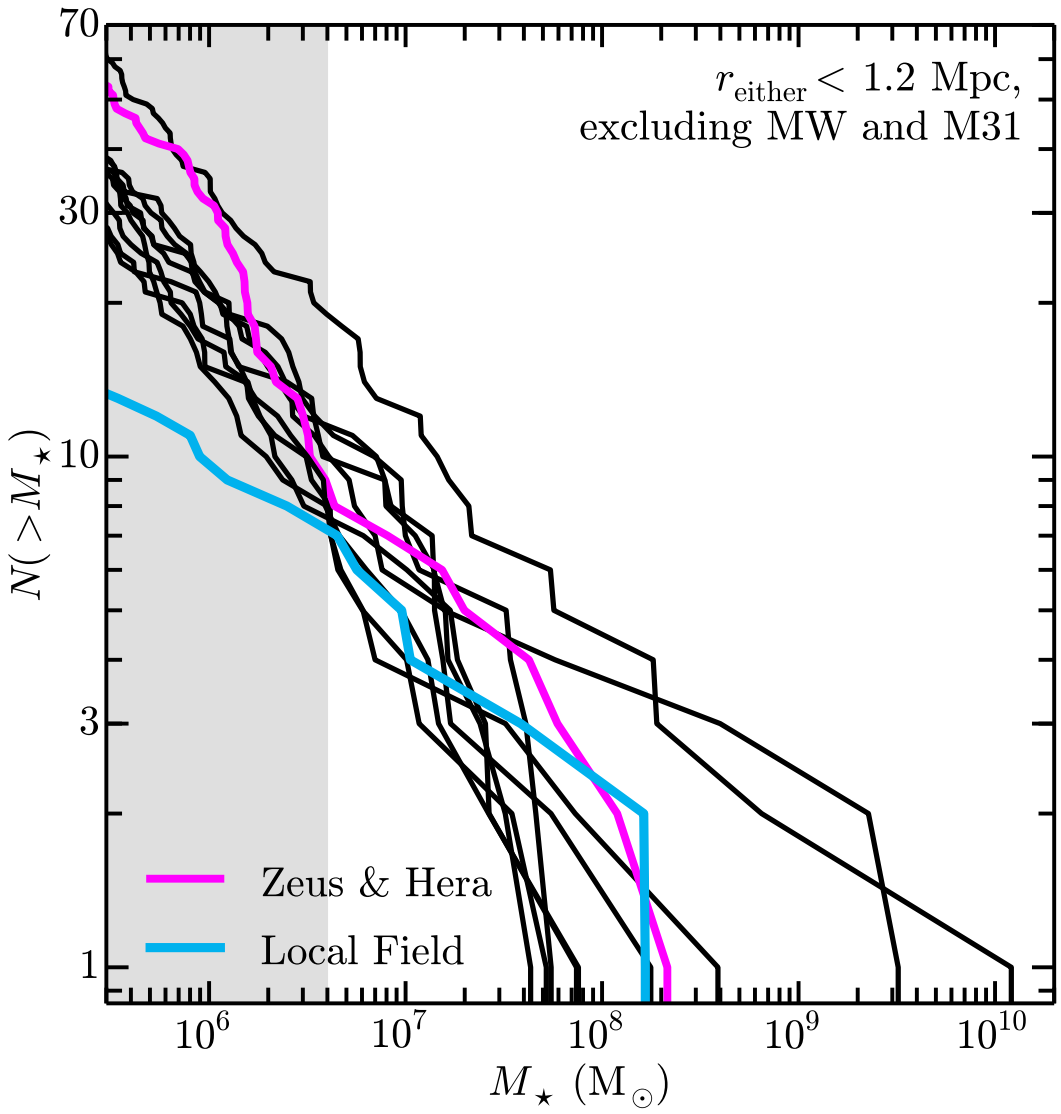


Figure 3.9: The stellar mass function observed in the Local Field (light blue) along with the stellar mass functions in the fields surrounding the ELVIS pairs, assuming the AM relation presented in GK14. The shaded region indicates stellar masses where the current census of galaxies lies below that of all the ELVIS pairs, $M_\star < 4 \times 10^6\ M_\odot$; at this mass, however, the count of known field galaxies nearly matches that around Zeus & Hera (highlighted in magenta), the LF shown in Figure 3.5.

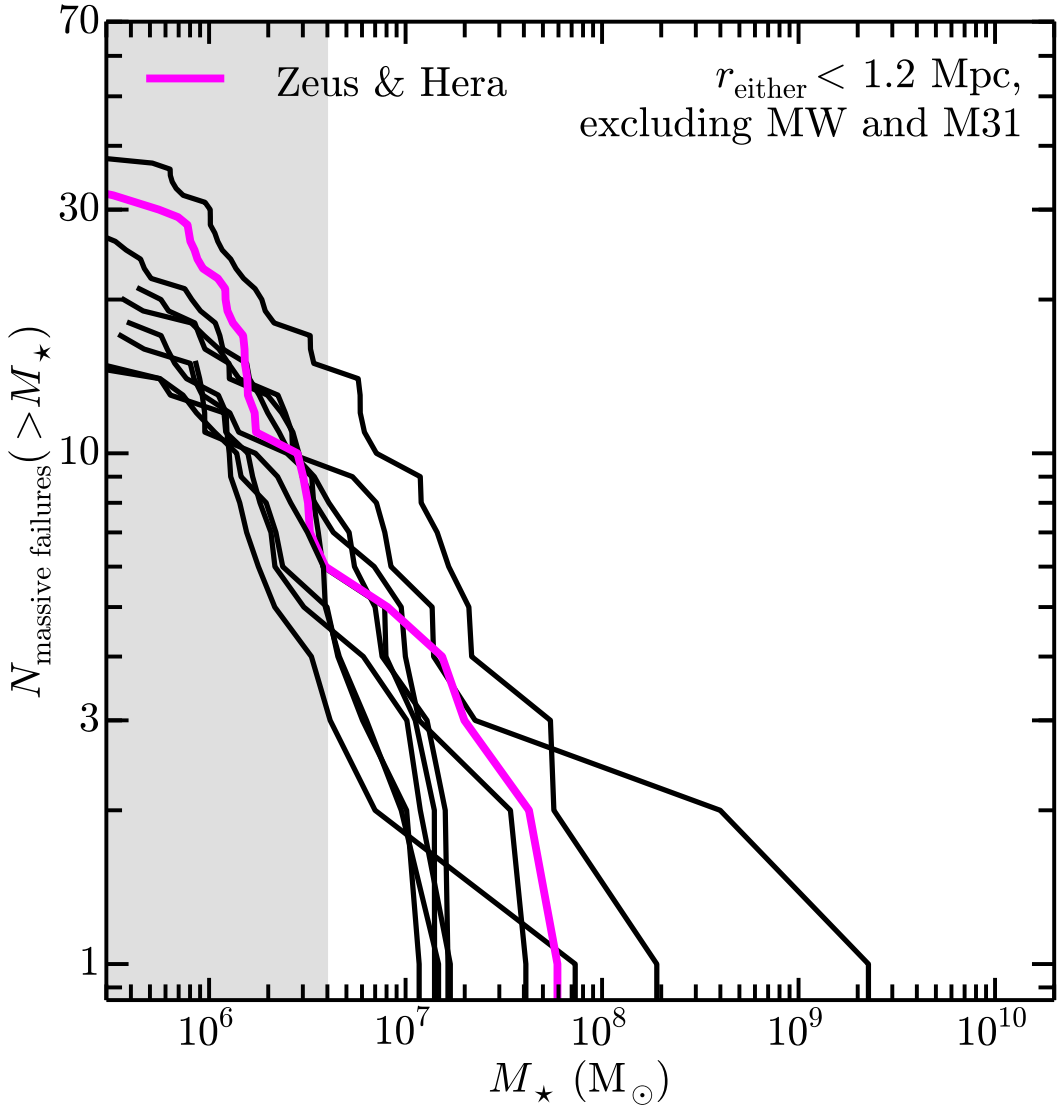


Figure 3.10: The stellar mass function, again from abundance matching, of the halos identified as massive failures in the LF; i.e. the black lines in Figure 3.5 counted in Figure 3.6. The magenta line again highlights the LF around Zeus & Hera. Even selecting those halos with the highest possible $M_\star$ to host the known dwarfs, the massive failures stellar mass functions are largely unchanged at the high mass end from Figure 3.9. Therefore, although the number count agree from $M_\star \gtrsim 10^{6.5} M_\odot$, only lower mass field halos are kinematically compatible with the known LF galaxies.

plotted in Figure 3.5 and highlighted in magenta in Figure 3.9, nearly matches that observed in the LF.

While a simple extrapolation of abundance matching creates a stellar mass function that agrees well with galaxy counts, *it does so by matching galaxies with halos that are too dense to reproduce the observed kinematics of those same galaxies* (see also Boylan-Kolchin et al., 2012; Ferrero et al., 2012). Specifically, it is difficult to match both the observed luminosity function and the observed densities of galaxies at the same time. The magnitude of the problem is demonstrated explicitly in Figure 3.10, which plots the stellar mass function of only the halos identified as massive failures (i.e. the stellar masses associated with the black lines in Figure 3.5, specifically with $\alpha = 0.18$.) This is the subset of the stellar mass function[10] shown in Figure 3.9 that includes only $V_{\rm peak} > 30$ km s$^{-1}$ halos that remain dense today ($V_{\rm max} \gtrsim 25\,{\rm km\,s^{-1}}$) and that are unaccounted for by any known galaxy. The takeaway point from Figure 3.10 is this: the TBTF halos should naively be hosting fairly bright galaxies, many of which should be more massive than $M_\star \simeq 5 \times 10^6 M_\odot$.

As we show in the next section, based on the densities measured, the stellar mass of a galaxy does not seem to scale at all with the maximum circular velocity of the dark matter halo that it resides in. In the absence of baryonic processes that strongly affect halo densities, it is hard to understand how the relation could be as stochastic as it appears to be.

### 3.4.3 The $V_{\rm max}$-$M_\star$ relation in the Local Field

As the previous sections showed, it is likely that either there are roughly 15 dense galaxies living in high $V_{\rm max}$ halos in the Local Field that have yet to be discovered, or that the densities of $M_\star \sim 10^{6.5} M_\odot$ *field* galaxies are much less dense than expected from straightforward

[10]When selecting hosts for each galaxy, the candidate halos were sorted by $M_\star$ – that is, the halos plotted in Figure 3.10 are selected to have the *smallest* possible stellar masses. Nonetheless, the high mass end is largely unchanged from Figure 3.9, clearly showing that many of the massive failures are among the highest mass halos in the field and would naively be expected to host *bright* galaxies.

ΛCDM predictions.

In this subsection, we make this point explicitly by working out the inferred relationship between galaxy stellar mass and dark matter halo mass under the assumption that LF halos are unaffected by baryonic processes, and then compare that relationship to that expected from AM in the same volume.

Our approach is demonstrated in Figure 3.11, where the shaded bands show typical rotation curves for halos of various $V_{\rm max}$ values. The width of the bands correspond to the $1\sigma$ scatter $R_{\rm max}$ at fixed $V_{\rm max}$ given in Equation 3.3 and Table 3.2, assuming Einasto profiles with $\alpha = 0.18$. The points correspond to dwarfs and are identical to those in Figure 3.5 with sizes that are again proportional to their stellar masses. Note that the least luminous dwarf (Leo T) appears to reside in a fairly massive ($V_{\rm max} \simeq 30{\rm km\,s^{-1}}$) halo, while the galaxy IC1613, which is $\sim 1000$ times more luminous, appears to reside in a halo that is less massive ($V_{\rm max} \simeq 20{\rm km\,s^{-1}}$). Given the large errors in Leo T's mass, the inferred halo sizes could be equal, but if there is any positive correlation between halo $V_{\rm max}$ and stellar mass, it must be extremely weak.

How does the implied relation compare to that expected from abundance matching? In Figure 3.12 we quantify the inferred relation, using the observational errors on dwarf masses together with the scatter in $R_{\rm max}$ at fixed $V_{\rm max}$ measured for LF halos in the ELVIS suite. Specifically, we plot the inferred $V_{\rm max}$ for each LF galaxy as a function of $M_\star$ as open light blue points. Error bars are $1\sigma$. Due to its small half-light radius, Leo T may be hosted by any halo with $V_{\rm max} \gtrsim 14$ km s$^{-1}$ at the $1\sigma$ level, though the median relation predicts that it is hosted by a halo with $V_{\rm max} = 29$ km s$^{-1}$. The upward arrows indicate the lower limits for Tucana and NGC 6822. Assuming the median relation between $R_{\rm max}$ and $V_{\rm max}$, Tucana is incompatible with an Einasto profile with $\alpha = 0.18$ for all values of $V_{\rm max}$, though it may be hosted by a halo that is only a $1\sigma$ outlier. NGC 6822, as mentioned above, is dominated by baryonic mass within $r_{1/2}$ and is therefore unlikely to follow either an Einasto or NFW

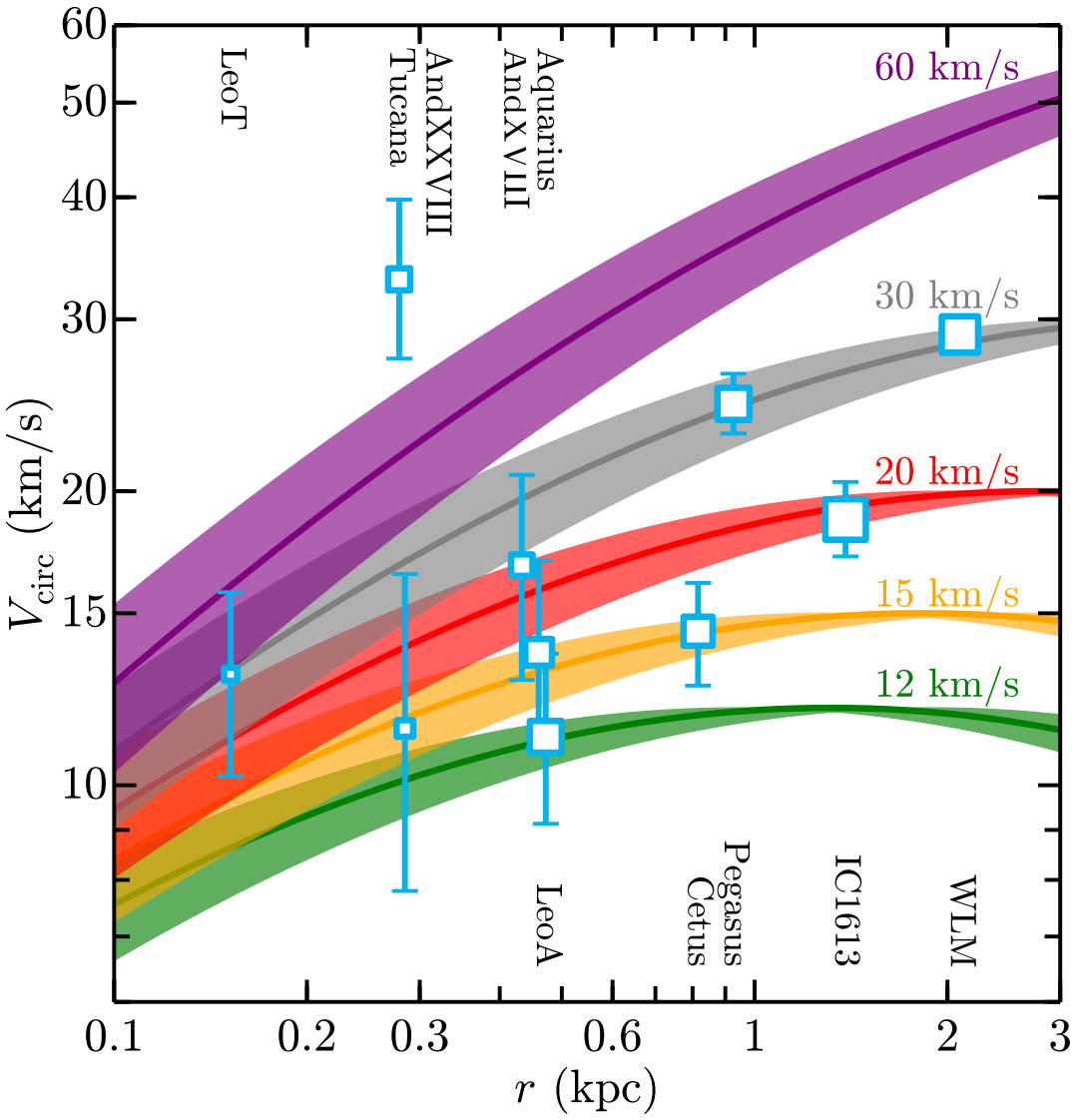


Figure 3.11: Typical rotation curves of halos in the Local Field for $\alpha = 0.18$, from the relations in Figure 3.2. Also plotted as open light blue points are the ten galaxies in the LF used in § 3.4.2 as in Figures 3.5 and 3.7; the points are again sized according to their stellar masses. The stellar masses of the halos do not appear to scale with $V_{\rm max}$, assuming a universal density profile.

profile.

The circles in Figure 3.12 indicate theoretical expectations from the AM relation in GK14, the same relation that produces the *observationally-consistent* stellar mass function shown

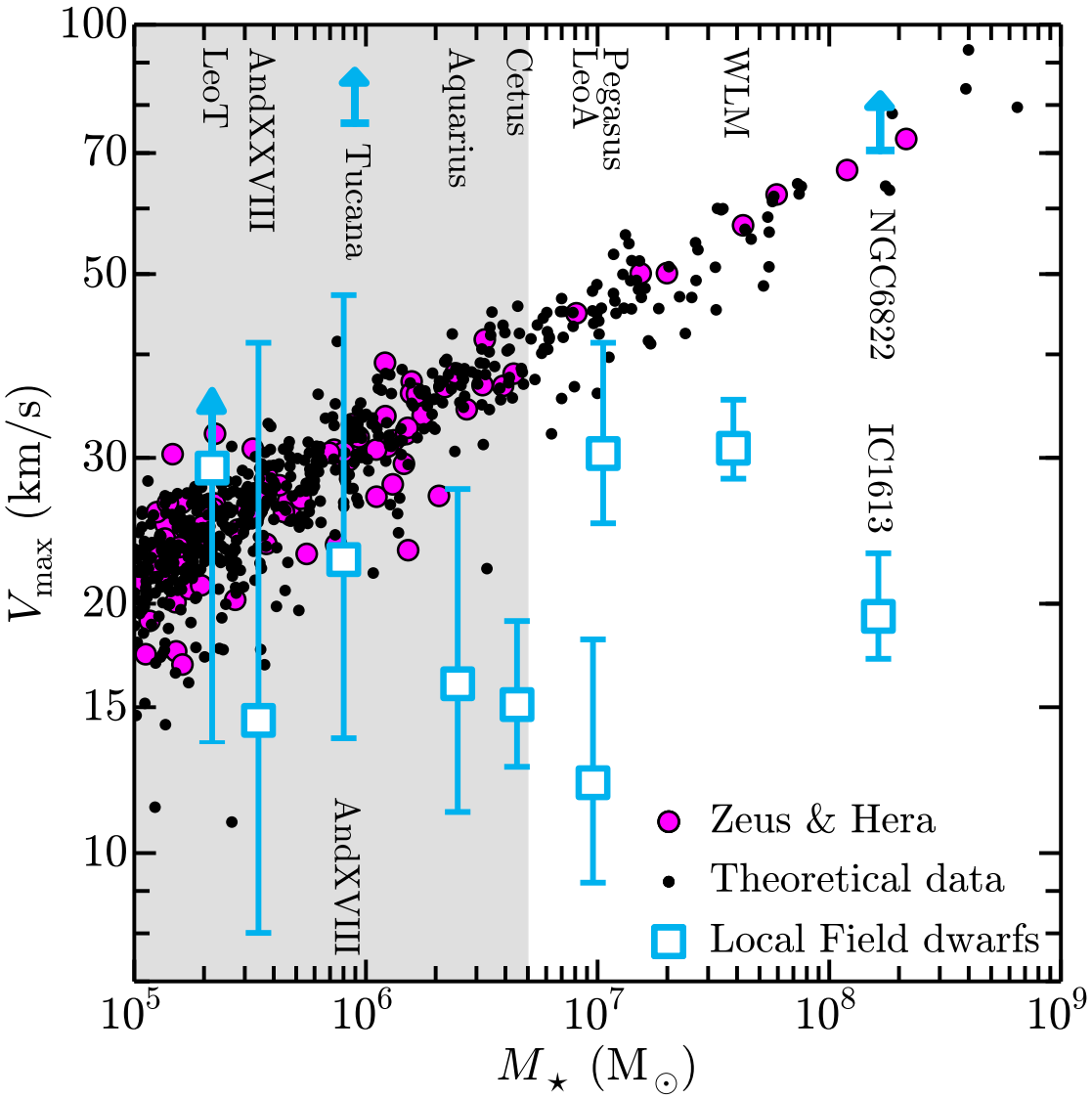


Figure 3.12: A comparison between the best-fit values of $V_{\rm max}$ (assuming $\alpha = 0.18$) of the Local Field dwarfs to the stellar masses implied by the preferred AM relation in GK14. As expected, the latter follow a power law; the scatter is due to the scatter between $V_{\rm max}$ and $M_{\rm peak}$, upon which stellar masses are based. The former, however, appear to follow an extremely weak trend, indicating that stellar mass may not scale with $V_{\rm max}$ at these low luminosities. Halos near Zeus & Hera are highlighted in magenta; the shaded region is the same as that in Figure 3.9. Due to the scaling of $R_{\rm max}$ with $V_{\rm max}$, the measurement for Tucana is incompatible with the median relation; the $1\sigma$ bound is indicated by the arrow. Similarly, Leo T is unconstrained at the upper-end. The $1\sigma$ lower limit for NGC 6822 is also indicated, though it is baryon dominated and unlikely to be well described by an Einasto profile.

in Figure 3.9. The magenta circles highlight those halos around Zeus & Hera – the same hosts that have a stellar mass function that masses the Local Group well in Figure 3.9.

Assuming that galaxies in the Local Field have density profiles of the kind predicted in our dissipationless simulations, any relation between $V_{\rm max}$ and $M_\star$ for galaxies in the LF must be very weak – a "common mass" relation very similar to that found by Strigari et al. (2008a) for the observed MW satellites (also see Boylan-Kolchin et al., 2012). As for satellite galaxies, this may suggest that the scaling between halo mass and stellar mass breaks down for small $M_\star \lesssim 10^8 M_\odot$. If the underlying relation followed something close to $M_\star \sim V_{\rm max}^0$ over the mass range shown (and with a scatter similar to that shown in the data plotted), however, then such a relation would drastically over-predicted the number of $M_\star \sim 10^{6.5} M_\odot$ galaxies in the Local Group.

Another option is that the shape of the density profiles of the halos hosting LF galaxies vary strongly from system to system. Because these galaxies exist in the field, tidal interactions and ram pressure stripping will not strongly affect their dark matter halos. Moreover, unless these galaxies formed with top-heavy initial mass functions or live in much smaller halos than abundance matching suggests, the energy available from supernovae is likely below that required to alter their density profiles significantly (Peñarrubia et al., 2012; Garrison-Kimmel et al., 2013).

We caution that the error bars in Figure 3.12 account only for the observational errors on $V_{1/2}$ and for the scatter in the $R_{\rm max} - V_{\rm max}$ relationship; that is, we are requiring that all galaxies reside in halos with identical density profile shapes. Additionally, we impose no sampling prior based on the predicted number of halos of a given $V_{\rm max}$, which would serve to shrink the error bars in Figure 3.12 and systematically push some of the inferred $V_{\rm max}$ values lower (Martinez, 2013). A more detailed analysis should be performed, but we leave that effort for future work.

## 3.5 Numerical Convergence

Three of the isolated hosts in the ELVIS Suite were re-simulated with eight times better mass resolution than the fiducial runs ($m_{\rm p} = 2.35 \times 10^4\ M_\odot$) and with a $z = 0$ softening length of 70 pc for the high resolution particles. Although the individual halo properties vary slightly between these HiRes simulations and the fiducial analogs, as expected from Oñorbe et al. (2014), we use those simulations here to determine the limits of our full sample. In Figure 3.13, we plot the relationship between $R_{\rm max}$ and $V_{\rm max}$ for subhalos within 310 kpc of these three hosts. We use 310 kpc to include a large subhalo that, owing to phase differences between the resolutions, is beyond 300 kpc at the standard resolution. Subhalos from the HiRes simulations are shown as cyan points and those from the standard resolution runs are plotted in black; the symbol types indicate the three host halos.

Fits to both of these populations, including only halos with $V_{\rm max} > 15$ km s$^{-1}$ and $R_{\rm max} > 0.5$ kpc, are also plotted in Figure 3.13. The power law given by Equation 3.3 fits both populations well, with a difference in the normalizations of less than 3%, indicating that our results are robust to resolution errors. We have also checked that our results do not depend on the specific halo finder by repeating this analysis with halo catalogs produced by `Amiga Halo Finder` (Knollmann & Knebe, 2009), which locates spherical overdensities in the three-dimensional matter distribution – the normalizations differ by 5% at most. `Rockstar` also appears to misidentify $R_{\rm max}$ for a single small halo in the high resolution run; this halo, however, is not used in the full analysis and does not strongly bias the fit.

## 3.6 Density Profiles

Rather than individually fit profiles to each subhalo (an inaccurate approach, due to the insufficient resolution at low radii and relatively small differences in the profiles near $R_{\rm max}$),

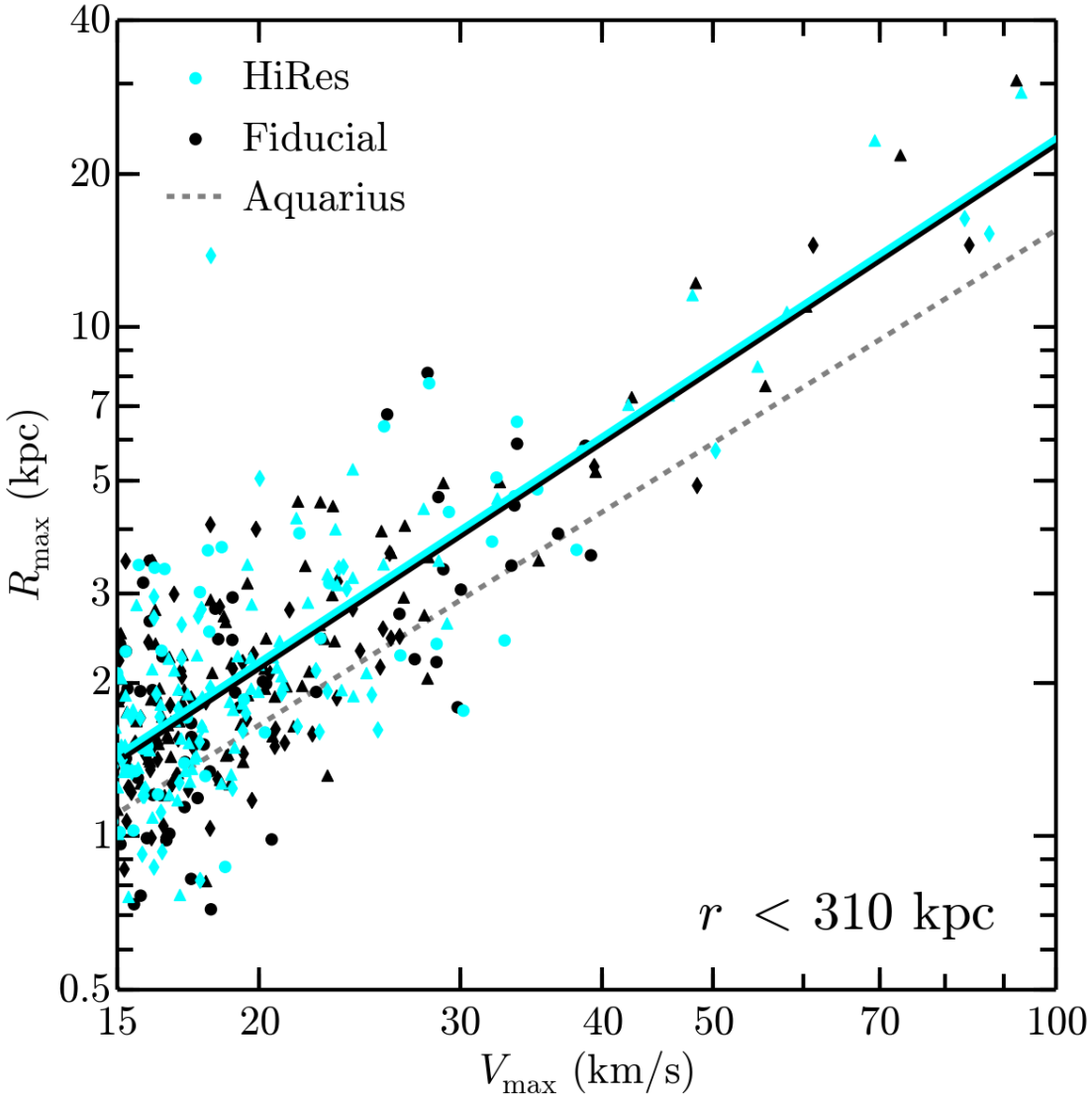


Figure 3.13: Resolution test comparing subhalos within 310 kpc of three of the isolated analogs in the ELVIS Suite, iKauket (circles), iHall (triangles), and iScylla (diamonds), at the standard resolution of the ELVIS suite (black points) and with eight times better mass resolution (cyan points); the fits to the data, weighted by $V_{\rm max}$, are also plotted. The normalizations of the fits to halos with $V_{\rm max} > 15$ km s$^{-1}$ and $R_{\rm max} > 0.5$ kpc agree to within 3%, indicating that our results are not affected by numerical errors. The dashed grey line plots the relation found in Springel et al. (2008); the offset ($\sim 20\%$) is consistent with the updated $\sigma_8$ used in the ELVIS cosmology. We also find nearly identical relations using halo catalogs produced by `AHF`.

we perform our analysis using three Einasto profiles ($\alpha = 0.15,\ 0.18$, and 0.28). As shown in Springel et al. (2008), an Einasto profile with $\alpha$ fixed at 0.18 is a better fit to most subhalos than a standard NFW profile – we therefore focus our efforts on this profile. Though a comprehensive analysis of the distribution of best-fit shape parameters of ultra-high resolution subhalos and field dwarfs does not exist in the literature, $\alpha = 0.15$ and 0.28 are the extreme values plotted in Springel et al. (2008) and we therefore consider those shape parameters as an estimate of appropriate scatter.

For a given $\alpha$, the circular velocity may be expressed as a function of $R_{\rm max}$ and $V_{\rm max}$, parameters which are robustly determined for the halos considered in this work (see Figure 3.13). For the Einasto profile,

$$\frac{V_{\rm circ}^2(r)}{V_{\rm max}^2} = \frac{4\pi/\alpha}{A(\alpha)B(\alpha)} \exp\left(\frac{2 - \log(8) + 3\log(\alpha)}{\alpha}\right) \gamma\left(\frac{3}{\alpha}, \frac{2}{\alpha}\left(\frac{A(\alpha)r}{R_{\rm max}}\right)^{\alpha}\right) \frac{R_{\rm max}}{r}, \quad (3.4)$$

where $\gamma(x, y)$ is the lower incomplete gamma function. $A(\alpha)$ and $B(\alpha)$ relate $V_{\rm max}$ and $R_{\rm max}$ to $r_{-2}$ and $\rho_{-2}$, the radius at which the log slope of the density profile is $-2$ and the density at that radius, via

$$\begin{aligned} R_{\rm max} &= A(\alpha) r_{-2} \\ V_{\rm max}^2 &= B(\alpha) G \rho_{-2} r_{-2}^2, \end{aligned} \quad (3.5)$$

By finding the maximum of Equation 3.4, one can show that $A(\alpha)$ is given by the root of

$$e^{-2x^{\alpha}/\alpha} \alpha^{\frac{\alpha-3}{\alpha}} x^3 - 8^{-1/\alpha} \gamma\left(\frac{3}{\alpha}, \frac{2x^{\alpha}}{\alpha}\right) = 0, \quad (3.6)$$

where $x = r/r_{-2}$. $B(\alpha)$ may then be obtained by directly calculating $V_{\rm circ}(r)$ at $R_{\rm max}$. For

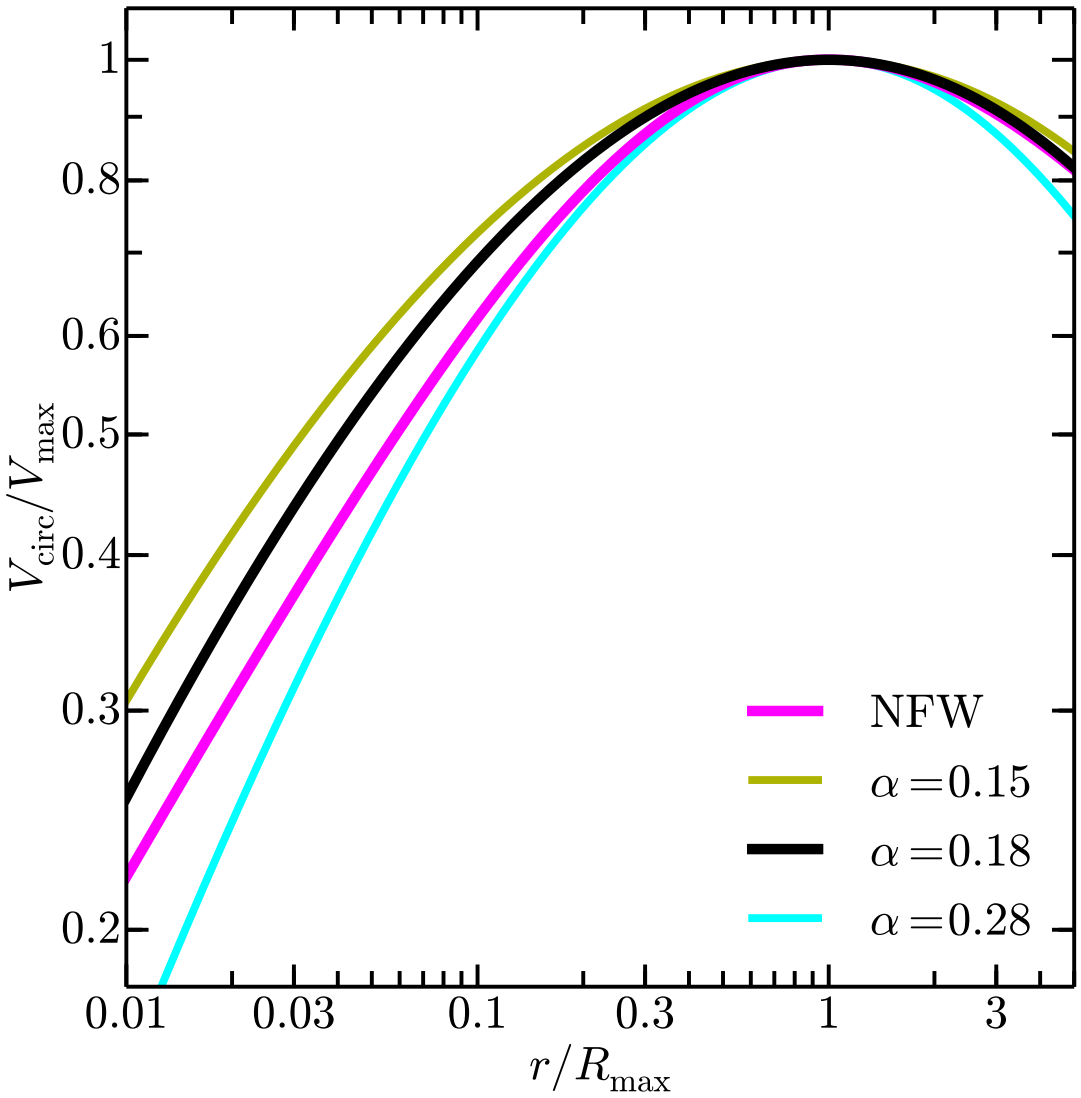


Figure 3.14: Circular velocities profiles, normalized by $R_{\rm max}$ and $V_{\rm max}$ for the three shape parameters considered above: $\alpha = 0.15$ (dark yellow), $\alpha = 0.18$ (black), and $\alpha = 0.28$ (cyan), along with that of an NFW profile (magenta). Smaller shape parameters result in denser halos, and therefore more massive failures.

$0 < \alpha < 1$, $A(\alpha)$ and $B(\alpha)$ are well fit by two-power functions:

$$\begin{aligned} A(\alpha) &= 1.715\alpha^{-0.00183}(\alpha + 0.0817)^{-0.179488} \\ B(\alpha) &= 9.529\alpha^{-0.00635}(\alpha + 0.3036)^{-0.206886} \end{aligned} \tag{3.7}$$

In Figure 3.14, we compare the resultant circular velocity curves for these three shape parameters, along with that of an NFW profile. Smaller values of $\alpha$ result in more mass near the center of halos and therefore lead to more unaccounted-for objects and massive failures in the simulations.

## 3.7 Conclusions

In this paper, we have analyzed the structural properties of the small halos in the ELVIS Suite – both those within the virialized volumes of the two giant halos and those in the fields surrounding them. Our results indicate that the Too Big to Fail problem, the discrepancy in central masses between the large subhalos of simulated MWs and the dSphs surrounding the MW, is an issue not only within 300 kpc, where environmental physics may be able to resolve the disagreement, but also in the Local Field, where such effects should be small. Specifically, we find that

- For NFW-like density profiles, nearly all of the ELVIS hosts contain at least one "strong massive failure" – satellite halos that are too dense to host any of the classical dSphs. The median number of strong massive failures per host is highly dependent on the assumed density profile, varying between 2 and 10, and would change dramatically if a dwarf much denser than Draco is discovered.

- The number of "massive failures," $V_{\rm peak} > 30$ km s$^{-1}$ halos that remain dense at z = 0 and cannot be accounted for with the *known* census of dSphs, is much less dependent on the assumed profile. All of the ELVIS hosts contain at least one massive failure for the profiles considered in the work, with a median varying between 8.5 and 13. Unlike the count of strong massive failures, a newly discovered high-density dwarf would only alter these numbers by one. Moreover, this overabundance is independent of the exact

$M_\star$-$M_{\rm halo}$ relation and assumes only that halos with $V_{\rm peak} > 30$ km s$^{-1}$ form stars.

- Though there are typically no strong massive failures in the Local Field (i.e. more than 300 kpc from both giants in the LG), the overall discrepancy between *known* galaxies that appear to live in dense (typically high mass) halos and the number of these halos predicted is even stronger. Most simulated LFs contain $\gtrsim 15$ more of these dense halos than can be accounted for observationally, a count that again assumes only that large halos form stars.

- If the discrepancy is to be resolved by discovering new galaxies, and *if* the stellar mass of a galaxy scales in a reasonable way with $V_{\rm max}$, then the abundance matching technique predicts that there should be $\sim 2-10$ undiscovered galaxies with $M_\star > 10^7 M_\odot$ within the LF, though there have been none found since 1958. However, perhaps more puzzlingly, the stellar masses of the known field galaxies do not appear to correlate with the apparent $V_{\rm max}$ of their host halos, as estimated from $V_{1/2}$, suggesting either that the density profiles of the dwarfs vary strongly or that the scaling of $M_\star$ with $V_{\rm max}$ breaks down at low luminosities.

The results presented in this work do not necessarily indicate the need to move beyond the standard ΛCDM model with collisionless dark matter. They can largely be viewed as predictions for results from future surveys, such as LSST and DES. However, if these missing dense galaxies are not discovered as we probe the nearby Universe to an increasing depth, these large dark matter halos must somehow be explained.

## Chapter Acknowledgements

The authors thank Manoj Kaplinghat, Anna Nierenberg, Mike Cooper, Erik Tollerud, Arianna Di Cintio, Shunsaku Horiuchi, and Jose Oñorbe for helpful discussions, and the anony-

mous referee for many helpful comments.

Support for this work was provided by NASA through a *Hubble Space Telescope* theory grant (program AR-12836) from the Space Telescope Science Institute (STScI), which is operated by the Association of Universities for Research in Astronomy (AURA), Inc., under NASA contract NAS5-26555. This work was also supported by a matching equipment grant from UC-HiPACC, a multicampus research program funded by the University of California Office of Research.

We also acknowledge the computational support of the NASA Advanced Supercomputing Division and the NASA Center for Climate Simulation, upon whose *Pleiades* and *Discover* systems the ELVIS simulations were run, and the *Greenplanet* cluster at UCI, upon which much of the secondary analysis was performed.

# Chapter 4

# Can Feedback Solve the Too Big to Fail Problem?

## Chapter Abstract

The observed central densities of Milky Way dwarf spheroidal galaxies (dSphs) are significantly lower than the densities of the largest ($V_{\rm max} \sim 35$ km/s) subhalos found in dissipationless simulations of Galaxy-size dark matter hosts. One possible explanation is that gas removal from feedback can lower core densities enough to match observations. We model the dynamical effects of supernova feedback through the use of a time-varying central potential in high resolution, idealized numerical simulations and explore the resulting impact on the mass distributions of dwarf dark matter halos. We find that in order to match the observed central masses of $M_\star \sim 10^6 M_\odot$ dSphs, the energy equivalent of more than 40,000 supernovae must be delivered with 100% efficiency directly to the dark matter. This energy requirement exceeds the number of supernovae that have ever exploded in most dSphs for typical initial mass functions. We also find that, per unit energy delivered and per cumulative mass re-

moved from the galaxy, single blow-out events are more effective than repeated small bursts in reducing central dark matter densities. We conclude that it is unlikely that supernova feedback alone can solve the "Too Big to Fail" problem for Milky Way subhalos.

## 4.1 Introduction

The current paradigm for structure formation, cold dark matter with a cosmological constant ($\Lambda$CDM), has proven successful at reproducing the large scale universe (Hinshaw et al., 2013; Ho et al., 2012, and references therein); however, disparities exist between the theory and observations on small scales. For example, the rotation curves of dwarf and low surface brightness (LSB) galaxies appear to favor core-like density distributions rather than the cuspy distributions seen in dissipationless simulations (Flores & Primack, 1994; Moore, 1994; Kuzio de Naray et al., 2008; Trachternach et al., 2008; de Blok, 2010; Kuzio de Naray & Kaufmann, 2011). There has been much discussion in the literature regarding the ability of baryonic processes, i.e. feedback, to displace dark matter and resolve the problem (Navarro et al., 1996a; Mashchenko et al., 2006; Pontzen & Governato, 2012; Ogiya & Mori, 2012; Teyssier et al., 2013) – such arguments seem reasonable given the fairly large stellar mass ($M_\star \sim 10^8 M_\odot$) of a typical LSB galaxy.

Perhaps more troubling is that a similar problem appears to exist for even lower luminosity dwarf spheroidal (dSph) galaxies ($M_\star \sim 10^6 M_\odot$) in the Local Group. Walker & Peñarrubia (2011), Jardel & Gebhardt (2012), Agnello & Evans (2012), and Amorisco et al. (2013), among others, find evidence for cores in the Fornax and Sculptor dSphs. This is particularly important if true, as the same mechanisms shown to to flatten dark matter profiles in larger galaxies appear to have little effect in galaxies with so few stars (Governato et al., 2012). The density profiles of these dSphs is a matter of active debate, however: Breddels & Helmi (2013) argue that it is unlikely that Fornax, Sculptor, Carina, and Sextans are embedded in cored

dark matter profiles, and Strigari et al. (2014) find that, while cored profiles provide a better fit, it is indeed possible to match the kinematics and photometry of Fornax and Sculptor in cuspy dark matter potentials for generalized forms of the stellar density distribution and stellar velocity anisotropy profile, such that cuspy profiles cannot be eliminated with current data.

Independent of the functional shape of the dark matter density profile of the Milky Way dSphs, it has become clear that the dark matter masses of the dSphs are significantly lower than expected for the most massive subhalos in dissipationless ΛCDM simulations (the so-called "too big to fail" (TBTF) problem; Boylan-Kolchin et al. 2011, 2012). The core/cusp and Too Big To Fail problems may be closely related: if the majority of the bright dSphs in the Milky Way have dark matter cores of $500 - 1000$ pc, then their central masses would be reduced by a factor of 2-3, precisely the amount that is required to explain TBTF. If most or all of the dSphs have non-cored profiles, however, the two issues are distinct.

The TBTF problem is illustrated in Figure 4.1, in which a circular velocity profile typical of one of these "massive failures" is plotted along with observed values of the mass enclosed within the deprojected half-light radius of each of the bright dSphs around the Milky Way (computed by Wolf et al. 2010, who used data from Walker et al. 2009 in addition to data from Muñoz et al. 2005; Koch et al. 2007; Simon & Geha 2007 and Mateo et al. 2008). If the largest subhalos do host the bright dwarfs, then the dark matter must be less dense in their centers than predicted in dissipationless CDM simulations, possibly because of a combination of star formation feedback, tidal interactions, and ram-pressure stripping (e.g. Brooks & Zolotov, 2014; Arraki et al., 2013), or non-standard dark matter physics (e.g. Lovell et al., 2012; Anderhalden et al., 2012; Vogelsberger et al., 2012; Rocha et al., 2013). Other authors have pointed out that a statistically rare or low-mass Milky Way (e.g. Purcell & Zentner, 2012; Wang et al., 2012) can also explain the discrepancy; however, the former option is called into question by Strigari & Wechsler (2012) and the latter is in conflict with

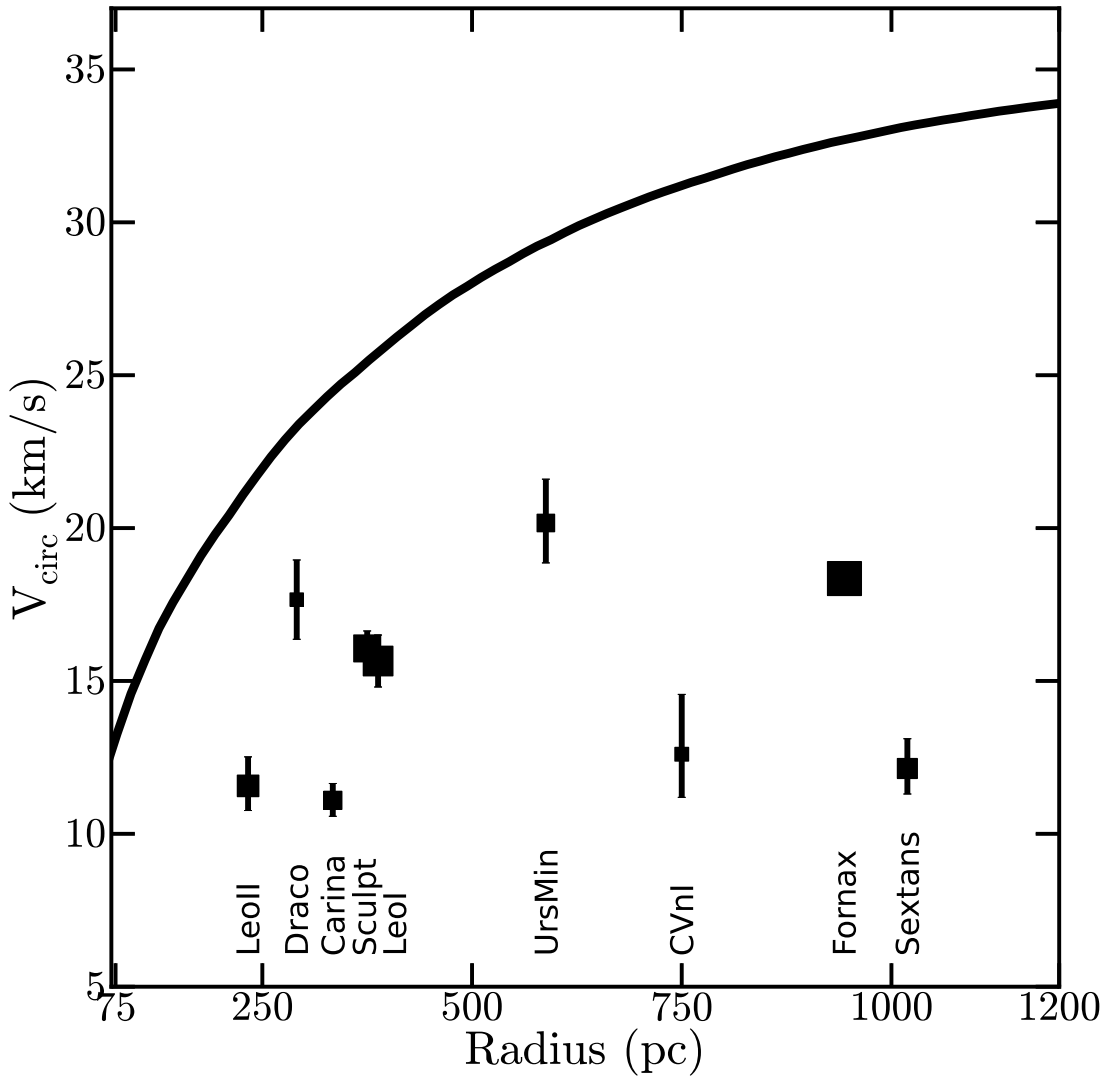


Figure 4.1: The simulated circular velocity profile as a function of subhalo radius along with observed circular velocities. The solid line shows the circular velocity profile of our idealized halo in the initial conditions, which is representative of the largest subhalos found in dark-matter-only simulations of Milky Way-size halos, a Too Big to Fail subhalo. The observational values are data for the bright dSphs ($L_V > 10^5\,L_\odot$; see text for details) and the size of each point is proportional to the luminosity of that satellite. The Milky Way satellites have significantly less mass near their center than the halos in which abundance matching predicts they form.

constraints derived by Boylan-Kolchin et al. (2013) from the orbit of Leo I.

While feedback appears a plausible solution to the cusp/core problem in brighter dwarf galaxies and LSBs — and more generally, to reducing their central dark matter content relative to predictions from dissipationless ΛCDM simulations — dSph galaxies are much more dark-matter dominated, with observed mass-to-light ratios within the stellar radius in excess of 100 in some cases (e.g. Walker, 2012). Moreover, according to the theoretical extrapolation of abundance matching, we expect the stellar mass to drop by $\sim 2.5$ dex for a difference of only one decade in halo mass at these mass scales (Behroozi et al., 2013c). The expectation is that the dark matter's gravitational potential should overwhelm that of the baryons, even at the centers of halos. Finally, the fact that these systems are so deficient in stars means that the total energy available to alter the gravitational potential is minimal.

Some groups (e.g. Governato et al., 2012; Del Popolo, 2012a) have successfully reproduced the low central densities of LSBs by invoking supernovae feedback in cosmological zoom-in simulations. Others (e.g. Read & Gilmore, 2005; Zolotov et al., 2012; Teyssier et al., 2013) have managed to flatten the central density profiles of larger dwarf galaxies ($M_\star \sim 10^7 - 10^8 M_\odot$) via similar techniques. Reduced central densities are not generic outcomes of simulations including gas physics, however: other groups find profiles that are either unchanged (Parry et al., 2012) or steeper than those in the dark-matter-only case owing to adiabatic contraction (di Cintio et al., 2011). Such studies typically rely upon hydrodynamical sub-grid models, which may be responsible for these divergent outcomes. Our approach is complementary to these fully self-consistent approaches in that we focus on the effect that blowouts have on centrally located dark matter without regard to the chain of mechanisms responsible for blowing out the gas.

Compared to studies of LSB galaxies, moreover, dwarf spheroidals present a much more difficult problem numerically owing to their small physical size $\sim 300$ pc. Indeed, the central regions of dSph-size subhalos remain extremely difficult to resolve even in collisionless zoom simulations (Boylan-Kolchin et al., 2012), let alone hydrodynamical simulations: the mass

within $\sim 4-5$ force resolution elements is systematically understimated by 20% because of the gravitational softening adopted in simulations (Font et al., 2011). Poor resolution can give rise to two-body relaxation errors that tend to flatten the inner density profile, and this undesired effect propagates radially outwards in the cumulative velocity profile. Moreover, if the dark matter potential is shallower due to the lack of adequate resolution, gas outflows and tidal effects may over-predict the removal of mass. These issues motivate our use of controlled, idealized simulations to achieve the required force ($\sim 10$ pc) and mass resolution ($\sim 1000\,M_{\odot}$).

Recently, Peñarrubia et al. (2012) highlighted the tension associated with suppressing star formation in dwarfs while simultaneously producing observable cores in their dark matter distributions. These authors primarily investigated the energy requirements for creating constant-density cores in the density profiles of dwarf halos. By contrast, we focus on the central masses of the dwarf spheroidals in this work: we use idealized simulations to explore whether blow-out feedback of any kind can realistically solve the TBTF problem in all the Milky Way dSphs, including those with stellar masses as small as $\sim 10^5 M_{\odot}$. We predominantly examine the normalization problem pointed out by TBTF, rather than the issue of the slope of the density profile that the cusp/core problem implies.

Our approach is to examine the effects of feedback on isolated dark matter halos with peak circular velocities of $\sim 35$ km/s, the mass range associated with TBTF halos (Boylan-Kolchin et al., 2012). We mimic baryonic feedback using an externally tunable gravitational potential. This allows us to test the amount of gas that must be removed from the center of the halo in order to bring the circular velocity into agreement with observations, as well as the energy required to do so. Our implementation also allows us to test whether cyclic blowouts are effective at removing dark matter, as discussed by Pontzen & Governato (2012), and their relative efficiency compared to a single blowout of the same total mass.

The layout of this work is as follows: in §4.2, we describe our methods for producing the

initial conditions and for emulating star formation cycles, as well as present a resolution test; in §4.3, we study the dark matter distribution as a function of gas blown out and investigate the energetic requirements; finally, in §4.4, we discuss the results, focusing specifically on the implications for the Too Big to Fail problem.

## 4.2 Simulations

### 4.2.1 Initial Conditions

Cosmological abundance matching models predict that galaxies with $L_V \sim 10^5 L_\odot$ form in dark matter halos with $V_{\rm max} \sim 35$ km/s (Guo et al., 2010). Moreover, the five largest subhalos found in simulations of Milky Way-size halos typically have $V_{\rm max} > 35$ km/s (Boylan-Kolchin et al., 2012). This pinpoints halos with $V_{\rm max} \sim 35$ km/s as a characteristic size of concern. Such a halo (with the circular velocity curve peaking at a radius of 2.2 kpc, as expected for subhalos) is shown in Figure 4.1; the points are circular velocity curve determinations at the half light radii $r_{1/2}$ of each of the nine brightest Milky Way dSphs (taken from Wolf et al., 2010, who relied on data from the literature). Six of these nine have luminosities $L_V < 10^6$ L$_\odot$. The data points are sized in proportion to their luminosities, which range from $L_V = 2.2 \times 10^5$ L$_\odot$ (Draco) to $1.7 \times 10^7$ L$_\odot$ (Fornax). Their associated densities are clearly low compared to both the naive expectations of abundance matching and the expected densities of the most massive Milky Way subhalos.

With this as motivation, we initialize a dark matter halo with $V_{\rm max} = 35$ km/s at 2.2 kpc using a Hernquist 1990 sphere, which follows the roughly-expected $\rho \propto r^{-1}$ dependence at small radius. We do this by self-consistently sampling the phase space distribution function of the model (see also Kazantzidis et al., 2004; Bullock & Johnston, 2005; Zemp et al., 2008). As long as the resolution is appropriate, generating initial conditions in this manner can

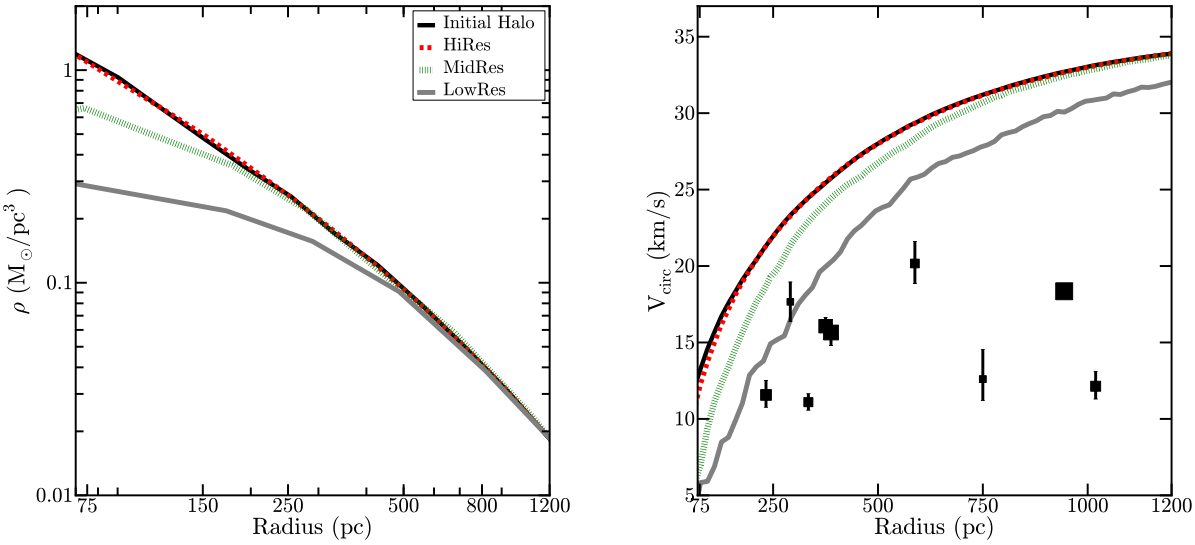


Figure 4.2: Resolution test. Plotted are the density (left) and circular velocity (right) profiles for the isolated halo initially (solid black) and after running with no external potential for 5 Gyr with three different mass and force resolutions as labeled in the caption and in Table 1. The highest resolution Milky Way cosmological simulations that have been run and can test feedback effects on dSph satellites have mass and force resolutions comparable to our LowRes runs though non-cosmological simulations are able to exceed the resolution of the MidRes run (Teyssier et al., 2013). Although the density converges in the LowRes run at $\sim 500$ pc, the circular velocity does not converge until beyond 1 kpc; to compare with the half-light radii of the dSph satellites, one requires convergence within $\sim 250$ pc, the smallest half-light radius of the Milky Way dwarfs. Since only the HiRes run does not suffer from numerical effects in this region, we use this resolution exclusively for the experiments presented in the rest of this paper.

produce systems that stay in equilibrium for over a Hubble time (Kazantzidis et al., 2004). We have developed a code that applies this technique to generate initial conditions for a variety of density profiles assuming isotropic velocity dispersions. Our code, named *spherIC*, is publicly available[1]and can also generate systems with an embedded stellar component that follows its own density distribution, chosen from a set of profiles typical for stellar systems.

In order to ensure that our results are stable to numerical effects, we simulate our initial halo in isolation at increasing force ($\epsilon = 10$, 70, 120 pc) and mass ($m_p = 760$, 24000, 150000 $M_\odot$) resolution as detailed in Table 4.1. Figure 4.2 shows the resultant density and circular

[1]https://bitbucket.org/migroch/spheric

| **Simulation** | $m_p$ ($M_\odot$) | $\epsilon$ **(pc)** | $N_p$ |
|---|---|---|---|
| HiRes | $7.6 \times 10^2$ | 10 | 3,000,000 |
| MidRes | $2.4 \times 10^4$ | 70 | 96,891 |
| LowRes | $1.5 \times 10^5$ | 120 | 30,000 |

Table 4.1: Parameters of the runs used in the resolution test (Figure 4.2) where $\epsilon$ is the Plummer-equivalent softening length. The remainder of the simulations we discuss in this paper use the HiRes parameters.

velocity profiles after 5 Gyr for each of these runs. The highest resolution hydrodynamic simulations to date that study the formation and evolution of a Milky Way-like halo and its dwarf satellites have been run with force softenings comparable to our lowest resolution test (e.g. Brooks & Zolotov, 2014; Zolotov et al., 2012). We see that the circular velocity curves for runs at this resolution are under-resolved at all relevant radii. Though numerical effects set in at $\sim 4\epsilon$ in density, the cumulative circular velocity remains divergent to larger radii. Zolotov et al. (2012), who examined the TBTF problem in hydrodynamic simulations, limit their analysis to scales of 1 kpc or larger, where their mass profiles (circular velocity profiles) are converged to 80% (90%). Smaller scales, $r < 1\,\mathrm{kpc}$, are most relevant for the TBTF problem, however: all of the Milky Way dSphs have $r_{1/2} \lesssim 1$ kpc, with five <500 pc and the smallest, Leo II, has $r_{1/2} \sim 250$ pc. To ensure that the circular velocity has converged at these radii, the remainder of our work relies on simulations with 760 $M_\odot$ particles and 10 pc force resolution, equivalent to the HiRes runs shown in Figure 4.2.

### 4.2.2 Modeling Gas Blowouts

We model a star formation cycle (i.e. gas accretion onto a central galaxy and the subsequent ejection of that gas) by varying the properties of a spherically-symmetric gravitational potential placed at the center of the halo. Specifically, we added an externally tunable Hernquist potential to the N-body code Gadget2 (Springel, 2005) such that each particle has an

additional acceleration given by

$$\vec{a} = \frac{-GM_{\rm gal}(t)}{[r + b(t)]^2} \frac{\vec{r}}{r}, \tag{4.1}$$

where $M_{\rm gal}(t)$ is the total mass in the potential at time $t$ and $b(t)$ is related to the half-mass radius of the potential, $r_{1/2}$, by $r_{1/2} = b/(\sqrt{2} - 1)$. To prevent the acceleration of a particle from becoming unphysically large when $r \to 0$, we "soften" the potential by setting $\vec{r}/r \to \vec{r}/\epsilon$ when $r < \epsilon$, the Plummer-equivalent softening length.

Our implementation allows us to specify the properties of the potential ($M_{\rm gal}$ and $r_{1/2}$) at any time. Our fiducial runs fix $r_{1/2}$ and vary $M_{\rm gal}$. Most of our runs force $r_{1/2} = 500$ pc, which is a typical half-light radius among the bright Milky Way dSphs. We vary $M_{\rm gal}$ over a series of cycles, with a fiducial period of 500 Myr (see Figure 4.3). Specifically, $M_{\rm gal}$ grows linearly from zero over 200 Myr to its maximum mass, $M_{\rm max}$, then remains constant for 100 Myr to allow the halo to come to equilibrium. We then mimic a blowout by forcing $M_{\rm gal}$ to instantaneously return to zero, where it remains for 200 Myr before beginning the next cycle. We have tested a number of other models for blowouts, including those with different periods, models without a relaxation time, sinusoidal modulations, and models with $M_{\rm gal}$ constant and $r_{1/2}$ varying. The model we show here produces the maximal effect on the rotation curve, though the qualitative results are very similar in most cases. The only exception is the sinusoidal model, which is symmetric and effectively produces no change in the density distribution. We have also tested a cylindrically symmetric potential, and found qualitatively similar results to the spherical cases.

In what follows we present results for models with $M_{\rm max} = 10^6 M_\odot$, $10^7 M_\odot$, $10^8 M_\odot$, and $10^9 M_\odot$. For each of these we vary $M_{\rm gal}$ from zero to $M_{\rm max}$ and back to zero ten times over a total of 5 Gyr. We output snapshots after every blowout, so that we can investigate the effect of any number of star formation cycles on the associated dark matter profile. For example,

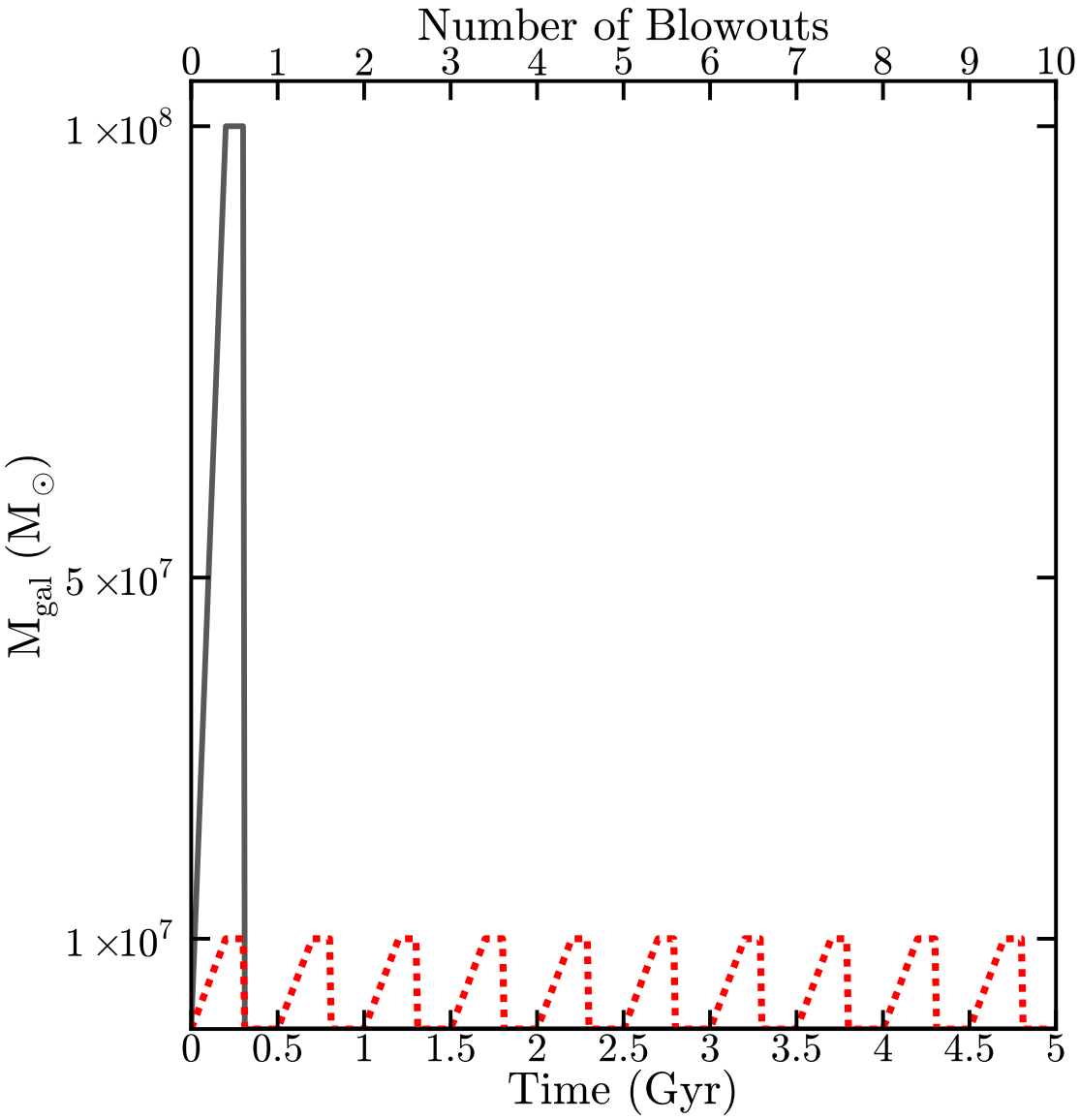


Figure 4.3: A representative example of our blowout scheme. Plotted is the mass in the central potential as a function of time for two of our runs that blow out the same total amount of gas. In grey is the mass as a function of time for a single blowout with $M_{\rm max} = 10^8 M_\odot$; the red dotted line shows the same for repeated blowouts with $M_{\rm max} = 10^7 M_\odot$. A single cycle takes 500 Myr. These two cases result in the same cumulative total of mass displaced, but as shown in Figure 4.4, the single large burst affects the dark matter density to a larger extent.

the grey line in Figure 4.3 illustrates the galaxy mass as a function of time over one cycle of $10^8 M_\odot$ while the red line shows ten cycles of $10^7 M_\odot$ each – in both of these runs, a total of $10^8 M_\odot$ is blown out from the halo. We also test how strongly the results depend on the scale radius by presenting new runs with $r_{1/2} = 100$ pc and $M_{\rm max} = 10^7 M_\odot$ and $10^8 M_\odot$.

## 4.3 Results

Figure 4.4 shows changes in the density and circular velocity profiles of our initial halo after undergoing blowout(s) of various masses. We directly compare ten blowouts of $10^7 M_\odot$ ($10^8 M_\odot$) to one blowout of $10^8 M_\odot$ ($10^9 M_\odot$), and find that for both values of $M_{\rm max}$, a single blowout (grey line in Figure 4.3) removes more dark matter from the center of the halo than repeated blowouts that amount to the same total baryonic mass cycled through the halo (red line in Figure 4.3). While we do see some evidence that cyclic, lower mass blowouts remove mass preferentially from the inner regions compared to a more massive blowout, being more effective at forming a "core," the density distribution never becomes perfectly flat in the center – some degree of cuspiness always remains.

Figure 4.4 illustrates that in order to bring our fiducial TBTF halo (solid black) into agreement with the density of a typical dSph, a total of $\sim 10^9 M_\odot$ of material must be cumulatively ejected from the halo in either one massive blowout (dashed green, the biggest effect) or in a few repeated smaller blowouts (solid blue) totaling this amount. This mass exceeds the entire baryonic allotment for a field halo of $M_{\rm vir} \simeq 5 \times 10^9 M_\odot$, which is the mass associated with an $M_\star \simeq 10^6 M_\odot$ galaxy according to the extrapolated abundance matching of Behroozi et al. (2013c) and also the virial mass associated with a typical TBTF halo at the time of infall (Boylan-Kolchin et al., 2012). This suggests that if feedback is responsible for the change in the density profile, it must be cyclic, such that a baryonic mass element may be reused in repeated blowouts.

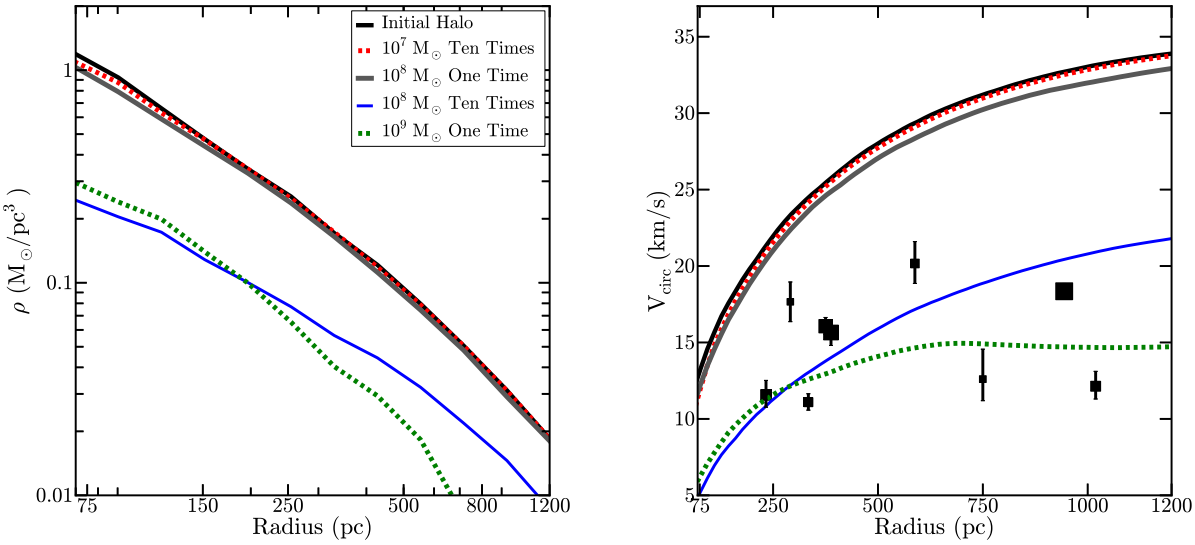


Figure 4.4: The density (left) and circular velocity (right) profiles of the halo after ten blowouts of $10^7 M_\odot$ and one blowout of $10^8 M_\odot$ (upper lines; as illustrated in Figure 4.3), and after ten blowouts of $10^8 M_\odot$ and one blowout of $10^9 M_\odot$ (lower lines), all with $r_{1/2} = 500$ pc (the qualitative results are similar for $r_{1/2} = 100$ pc). Removing $10^7 M_\odot$ ($10^8 M_\odot$) ten times is less effective at removing dark matter from the inner region of the halo than removing $10^8 M_\odot$ ($10^9 M_\odot$) once. Furthermore, note that $\sim 10^9 M_\odot$ of baryons must be removed from the galaxy – though it does not have to leave the halo – to bring the circular velocity into agreement with the data.

A more general presentation of our results is given in Figure 4.5. Each panel shows the dark matter remaining within 500 pc after multiple blowout runs. On the left, we present the mass of dark matter remaining as a function of total mass ejected and on the right we show the same quantity as a function of the total energy added to the dark matter (see below). For reference, the horizontal dotted line shows the initial dark matter mass within 500 pc and the shaded horizontal bands show estimates of the dark matter mass within 500 pc for three representative dwarfs, as determined in Boylan-Kolchin et al. (2012).

In the left panel of Figure 4.5, the different symbol types correspond to different values of the mass blown out per cycle, spanning $10^6 M_\odot$ to $10^9 M_\odot$ as indicated in the figure. Multiple points with the same symbol type correspond to repeated blowouts of the same mass. The points here are from runs with $r_{1/2} = 500$ pc. As discussed above, a single massive blowout

removes more mass from the center of the halo than the cumulative effect of 10 smaller blowouts that result in the same total mass expelled. For reference, the upper axis shows the implied mass loading factor, normalized for a dSph with $M_* = 10^6\,M_\odot$. We see that a minimum of $7 \times 10^8 M_\odot$ of material must be removed in order to reach the observed density of the densest dwarfs shown, Ursa Minor (cyan band), though each individual blowout cycle may be far less massive. This would imply a mass loading factor of $\sim 1000$ if we assume a stellar mass-to-light ratio of $M_\star/L_V = 2$ for this system. We note that we are defining the mass loading factor as the mass removed from the *galaxy* divided by the mass formed in stars. This number is the same whether or not a gas parcel is lost from the halo entirely or if it eventually falls back into the galaxy and is blown out multiple times.

The mass of Fornax is represented by the grey band. Though the density of Fornax is significantly lower than that of Ursa Minor, it may be the easiest dwarf to explain because its reservoir of stars is much greater ($M_\star \simeq 4 \times 10^7$). We see that a cumulative expulsion of $\sim 10^9 M_\odot$ can in principle match the central density of Fornax, which would require a more modest – though still large – cumulative mass-loading of $\sim 25$. However, this is only one system and it does not explain the unexpectedly low densities of the other, less luminous dwarfs.

Another way to characterize the problem inherent in lowering the densities in the faintest dwarfs is to consider the energy required to bring densities into accordance with observations (Peñarrubia et al., 2012). The right hand panel of Figure 4.5 presents the mass remaining within 500 pc as a function of the cumulative energy injected into the dark matter after a series of $10^7 M_\odot$ (squares) and $10^8 M_\odot$ (triangles) blowouts for two values of $r_{1/2}$. Green symbols correspond to $r_{1/2} = 100$ pc blowouts and the black symbols correspond to $r_{1/2} = 500$ pc blowouts. The smaller $r_{1/2}$ runs produce marginally bigger effects for the same energy. However, the three dwarfs shown by bands in Figure 4.5 have $r_{1/2} \simeq 600$ pc, 900 pc, and 1000 pc, respectively. Thus we regard our 100 pc blowout models as quite conservative limits.

We calculate the energy injected into the dark matter by measuring the energy difference in the dark matter before and after each blowout. We ignore the energy "lost" when the dark matter re-contracts in response to central potential regrowth. This is because we are interested in the energy imparted to the dark matter by explosive feedback, which has nothing to do with how the gas falls back in to regrow the central galaxy (ignoring this component amounts to changes in the presented values at the factor of $\sim 2$ level). For our fiducial runs with $r_{1/2} = 500$ pc, we see that more than $4 \times 10^{55}$ ergs of energy must be delivered to the dark matter before the inner mass becomes consistent with Ursa Minor. Assuming an energy per explosion of $E_{SN} = 10^{51}$ erg, this corresponds to more than 40,000 supernovae worth of energy injected directly into the dark matter with 100% coupling. Given that we expect approximately one SNII explosion per 100 $M_\star$ formed for a typical IMF (Kroupa, 2002), this exceeds the total available energy budget for all of the type II supernova that have occurred in Ursa Minor. Indeed, it exceeds the associated supernovae budget for six of the nine galaxies of concern in Figure 1, all of which, according to extrapolated abundance matching, should be sitting in massive halos. The three most luminous dSphs may be in the range of viability, but we must assume that the energy couples directly to the dark matter, ignoring the energy required to expel the gas from the halo and radiative losses. The real energetic requirements may be more than a factor of 10 larger (Creasey et al., 2012). We also note that a single, large blowout injects more energy into the dark matter than is imparted by ten successive, smaller blowouts of the same total mass.

As discussed above, Fornax (with $r_{1/2} \simeq 1$ kpc and $L_V \simeq 1.7 \times 10^7 L_\odot$) appears to be the best candidate for having its density lowered significantly by feedback effects. We expect Fornax to have had $\sim 3 \times 10^5$ supernovae explosions over its history. According to Figure 4.5, a $\sim 20\%$ coupling of $E_{SN}$ to the dark matter could in principle have lowered the central density of a 35 km/s halo enough to match the observed density of Fornax. Interestingly, however, if we run multiple blowouts at $\sim 10^9 M_\odot$, we find that our host halo becomes unbound all together. This suggests that even in cases where the required blowout is plausible

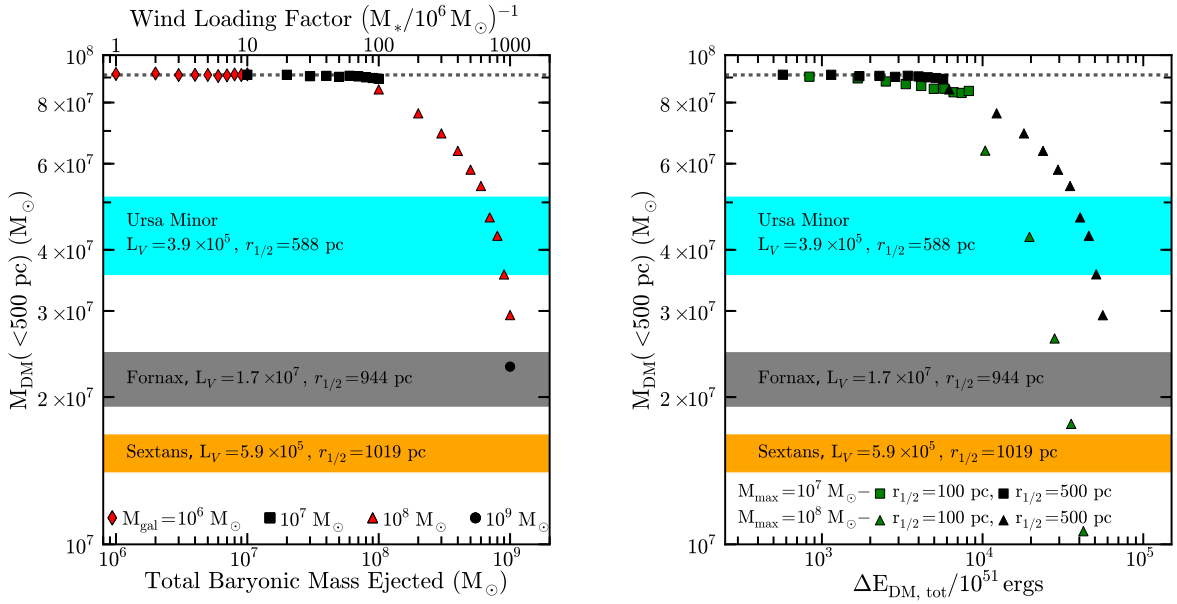


Figure 4.5: *Left*: The mass remaining within 500 pc after repeated blowouts of a galaxy with $M_{\rm max} = 10^6$, $10^7$, $10^8$, and $10^9 M_\odot$, all with $r_{1/2} = 500$ pc, as a function of mass blown out. *Right*: The mass remaining after blowouts of $10^7 M_\odot$ and $10^8 M_\odot$ with either $r_{1/2} = 100$ pc (in green) or 500 pc (in black) as a function of the cumulative change in the dark matter energy. The dotted line indicates the original mass within 500 pc, and the colored bands indicate the dark matter within 500 pc for Ursa Minor, Fornax, and Sextans. As the stellar component of Fornax contributes non-negligibly to the mass near its center, we have subtracted $7 \times 10^6 M_\odot$ from the dynamical mass in order to account for the stellar mass within 500 pc for this galaxy (Jardel & Gebhardt, 2012). More than several times $10^8 M_\odot$ must be ejected to bring the mass into agreement with Ursa Minor (though each blowout may be $\sim 10^8 M_\odot$), and the requisite energy also exceeds the total supernovae budget for six of the nine classical dSphs. Furthermore, we note that $\Delta E_{\rm DM}$ is a lower limit on the energy that must be injected, as it does not account for energy escaping via radiation or the energy required to eject the baryons.

energetically, there is something of a fine-tuning problem: if feedback is really as effective as required, then many of these halos may be destroyed all together. If this level of coupling is generic, one might expect slightly more star-rich galaxies to not exist at all. Alternatively, the presence of these galaxies may indicate that star formation is strongly suppressed by flatter central densities, such that the changing potential regulates further outflows; however, more detailed tests are necessary to determine the strength of such a feedback loop, if it exists.

One of the main results presented above is that repeated, cyclic blowouts do not help in

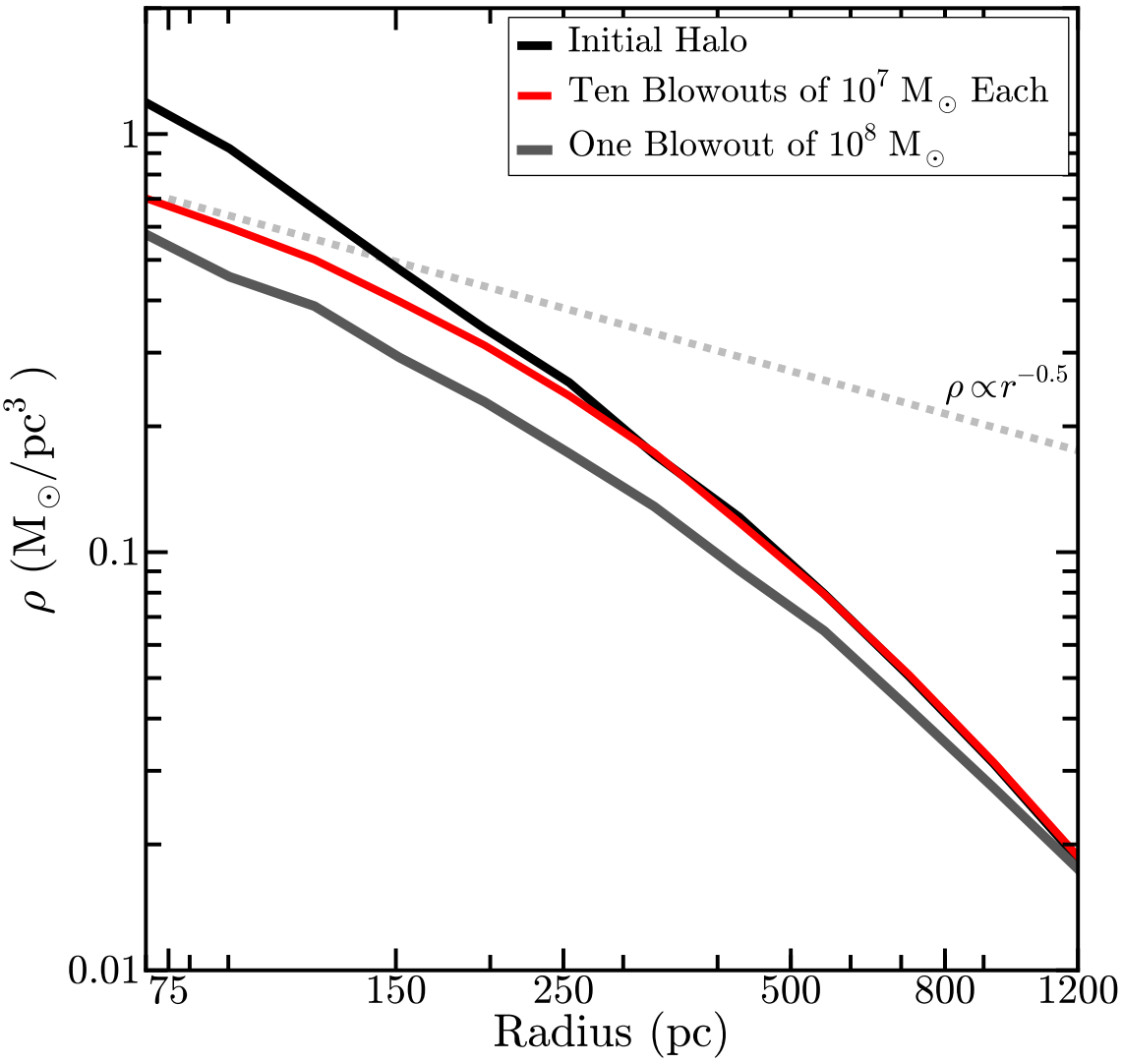


Figure 4.6: The density profile of the halo after ten blowouts of $10^7 M_\odot$ and one blowout of $10^8 M_\odot$ with $r_{1/2} = 100$ pc. As with blowouts with $r_{1/2} = 500$ pc, repeated blowouts are less effective than a single, more massive, blowout at displacing dark matter. However, repeated small blowouts from the very center of the halo do begin to flatten the inner density profile, whereas a more massive potential removes mass even at $10r_{1/2}$.

lowering the central densities of galaxies compared to single bursts. However, we find that for a fixed amount of mass expelled from the galaxy (and possibly cycled through the halo) cyclic blowouts preferentially remove dark matter mass from the centers of halos, making them more effective at shallowing cusps. We find that the effect is most dramatic for the smallest

$r_{1/2}$ runs. Figure 4.6 compares the density profile after ten blowouts of $M_{\rm max} = 10^7 M_\odot$ to one blowout with $M_{\rm max} = 10^8 M_\odot$, both with $r_{1/2} = 100$ pc. We see that several small blowouts begins to flatten the density profile at the center of the halo, whereas one large blowout displaces mass more evenly at all radii. Though a thorough investigation of this is outside the scope of this work, there does appear to be evidence that the scheme proposed by Pontzen & Governato (2012) can lead to more core-like dark matter profiles, perhaps consistent with those derived by Walker & Peñarrubia (2011); however, it appears unlikely that it can affect the total mass within the stellar extent at the level required to resolve the TBTF problem. In practice, we are never able to produce true constant-density cores. Rather we find mild cusps, $\rho \propto r^{-\alpha}$, with $\alpha \gtrsim 0.5$ – significantly steeper than those observed in dSphs by Walker & Peñarrubia (2011) and Amorisco & Evans (2012).

## 4.4 Conclusions

In this paper we have used a series of idealized numerical experiments to investigate whether blowout feedback can plausibly resolve the Too Big to Fail (TBTF) problem for subhalos seen in ΛCDM simulations (Boylan-Kolchin et al., 2011, 2012). We relied on a tunable central potential to mimic the effects of cyclic baryonic feedback events within a $V_{\rm max} = 35$ km/s halo – the mass scale of concern for the TBTF problem.

Our overall conclusion is that supernovae feedback appears to be incapable of solving the TBTF problem. More specifically, our findings are as follows:

- In order to bring massive subhalo densities in line with those observed for Milky Way dSphs, a total of $\sim 10^9\, M_\odot$ of material must be ejected from the galaxy (though not necessarily from the halo). This requires wind loading factors in excess of $\sim 500$ for the majority of Milky Way satellites.

- Our fiducial feedback models that match the observed densities of Milky Way dwarfs require the deposition of >40,000 supernovae worth of energy directly into the dark matter with 100% efficiency. For typical initial mass functions, this exceeds the expected number of Type II supernova explosions for six of the nine brightest dSph satellites. The most plausible exception is Fornax, with a density that may be explained with a $\sim 20\%$ coupling of its full allotment of SN energy directly to the dark matter. If this were the case, it might pose a fine-tuning problem for somewhat more luminous galaxies, as they might be expected to completely unbind their host halos.

- Repeated blowouts are less effective at lowering the central densities of dark matter halos than a single blowout of the same cumulative mass and similar total energy imparted (see Figure 5). Repeated small bursts do produce shallower central cusps than a few large bursts. However, we are unable to produce a true constant-density core from cyclic blowouts, even in the most extreme cases. Importantly, the overall density remains higher at all radii when the same total mass is blown out in a few smaller events (see Figure 6). We conclude that, per unit energy delivered or per cumulative mass removed, cyclic blowouts are less effective than a single large blowout at reducing central densities of dark matter halos.

This work has focused on the effects of internal feedback on the density structure of dark matter halos that are similar to those that will become massive subhalos in Milky Way-mass halos at redshift zero. We have not considered the effects of subsequent evolution, including stripping from ram pressure and tides, that may be important for some Milky Way subhalos (Read et al., 2006; Brooks & Zolotov, 2014; Zolotov et al., 2012; Arraki et al., 2013). Indeed, Arraki et al. (2013) have shown that, while tidal evolution alone is insufficient to bring the simulated subhalo population into agreement with observations of the MW dSphs, it may be sufficient to produce the requisite changes in a subhalo that has undergone adiabatic expansion due to baryon removal as a result of ram-pressure stripping. We note, however,

that several Milky Way dSphs do not seem to have had close pericentric passages with the Galaxy (Lux et al., 2010; Sohn et al., 2012), which calls into question the influence of tides on their mass distributions.

In light of the uncertainties associated with environmental influences on dark matter halo structure, the results presented here point to isolated, low-mass galaxies as particularly important objects for testing the predictions of CDM-based models. Future optical and radio surveys will be capable of detecting objects with stellar masses similar to the MW dSphs outside of the Local Group; comparing their density structure to predictions from simulations will be particularly enlightening.

## Chapter Acknowledgements

This work was funded in part by NSF grants AST-1009999, AST-1009973, and NASA grant NNX09AD09G. M.B.-K. acknowledges support from the Southern California Center for Galaxy Evolution, a multi-campus research program funded by the University of California Office of Research. J.S.B. was partially supported by the Miller Institute for Basic Research in Science during a Visiting Miller Professorship in the Department of Astronomy at the University of California Berkeley. The authors thank Manoj Kaplinghat for insightful discussions, and also thank Alyson Brooks, Arianna di Cintio, Avishai Dekel, Anatoly Klypin, Andrea Maccio, Jorge Peñarrubia, Andrew Pontzen, Antonio Del Popolo, Chris Purcell, Justin Read, Romain Teyssier, Erik Tollerud, Matthew Walker, and particularly the anonymous referee for many helpful comments.

# Chapter 5

# Running with *BICEP2*: Implications for Small-Scale Problems in CDM

## Chapter Abstract

The *BICEP*2 results, when interpreted as a gravitational wave signal and combined with other CMB data, suggest a roll-off in power towards small scales in the primordial matter power spectrum. Among the simplest possibilities is a running of the spectral index. Here we show that the preferred level of running alleviates small-scale issues within the ΛCDM model, more so even than viable WDM models. We use cosmological zoom-in simulations of a Milky Way-size halo along with full-box simulations to compare predictions among four separate cosmologies: a *BICEP*2-inspired running index model ($\alpha_s = -0.024$), two fixed-tilt ΛCDM models motivated by *Planck*, and a 2.6 keV thermal WDM model. We find that the running *BICEP*2 model reduces the central densities of large dwarf-size halos ($V_{\rm max} \sim 30 - 80\,{\rm km\,s^{-1}}$) and alleviates the too-big-to-fail problem significantly compared to our adopted *Planck* and WDM cases. Further, the *BICEP*2 model suppresses the count of

small subhalos by $\sim 50\%$ relative to *Planck* models, and yields a significantly lower "boost" factor for dark matter annihilation signals. Our findings highlight the need to understand the shape of the primordial power spectrum in order to correctly interpret small-scale data.

## 5.1 Introduction

The discovery of the cosmic microwave background (CMB) and measurements of its temperature anisotropy have lead to a standard cosmological model consisting of a flat universe dominated by cold dark matter and a cosmological constant that drives accelerated expansion at late times (e.g., Planck Collaboration et al., 2013). Inflation extends this standard cosmology by positing an earlier period of rapid exponential expansion that sets the initial conditions for the hot big bang; this period alleviates a number of "fine-tuning" problems, but lacked supporting observational evidence. Recently, however, the *BICEP*2 experiment reported the detection of primordial B-modes in the CMB (BICEP2 Collaboration et al., 2014; Ade et al., 2014). One explanation for this signal is the stochastic background of gravitational waves generated by inflation, providing potentially the first direct evidence for an inflationary phase in the early Universe. This explanation will have to be verified by other experiments and in other frequencies. For the rest of this paper, we will assume this explanation is correct as we await confirmation by other experiments and in other frequency bands. [1]

The tensor-to-scalar ratio measured by *BICEP*2, $r = 0.20^{+0.07}_{-0.05}$ (68% confidence-interval), is at face value inconsistent with the limit quoted from a combination of *Planck* (Planck Collaboration et al., 2013; Ade et al., 2013), *SPT* (Hou et al., 2014), *ACT* (Das et al., 2014), and *WMAP* polarization (Hinshaw et al., 2013) data: $r < 0.11$ at 95% confidence.[2]

[1] In this regard, note that there has been concern that foreground contamination could have affected this measurement (e.g. Liu et al., 2014).

[2] As noted by Audren et al. (2014), however, the measured tension may be significantly reduced ($\sim 1.3\sigma$)

However, these pre-*BICEP*2 limits assumed a constant spectral index $n_s$ for scalar fluctuations in the primordial power spectrum. The discrepancy could be explained by a non-trivial primordial power spectrum, one that deviates from a pure power law (e.g., Hazra et al., 2014); suppressing the large-scale scalar power spectrum relative to that expected in a constant spectral index model allows for a larger contribution from tensor modes to the temperature-temperature anisotropy $C_l^{TT}$ at large scales . Abazajian et al. (2014) explored several scenarios including a running spectral index, a cutoff in the spectrum, and a break in the power spectrum, finding evidence for a negative running index (see also McDonald, 2014; Ashoorioon et al., 2014) or for a broken spectrum. Of these possibilities, the running spectral index is arguably the simplest, and we focus on the small-scale implications of this solution for the remainder of this work. More generally, however, our results explore the possible implications of non-trivial primordial power spectra on galaxy formation. Here we specifically show that viable deviations from power-law primordial power spectrum can have a significant impact on important questions facing ΛCDM today.

Any modifications to the primordial power spectrum and cosmological parameters will manifest itself in the formation and evolution of large-scale structure. On large scales, the standard ΛCDM cosmology provides an excellent model for the observed Universe (Ho et al., 2012; Hinshaw et al., 2013); any changes that compromise this success would thus be a sign of an inconsistent scenario.

On the other hand, discrepancies currently exist between the ΛCDM paradigm and the observed Universe on smaller scales. Examples include the "core/cusp problem," where dissipationless $N$-body simulations in ΛCDM predict a rising dark matter density with smaller radius $\rho \propto r^{-1}$, in contrast to observations that show a core-like profile at small radii (Flores & Primack, 1994; Moore et al., 1999). The discrepancy is seen in low-surface brightness (LSB) galaxies (Simon et al., 2005; Donato et al., 2009; Kuzio de Naray & Kaufmann, 2011;

by assuming identical values for the pivot scale and the tensor spectral index in both analyses, effectively raising the upper limits on the running measured by *Planck*.

Oh et al., 2011), but also seems to appear in lower luminosity dwarf spheroidal (dSph) galaxies [3] (Walker & Peñarrubia, 2011; Agnello & Evans, 2012; Amorisco & Evans, 2012). A second discrepancy is that the count of known satellite galaxies around the Milky Way is much smaller than the count of subhalos expected to be massive enough to form stars (Klypin et al., 1999; Moore et al., 1999, the "missing satellites problem"). Independently, it has also been shown that the central densities of dSphs are significantly lower than predicted by dissipationless ΛCDM simulations, dubbed the "too-big-to-fail problem" (TBTF; Boylan-Kolchin et al., 2011, 2012). The severity of TBTF remains an active debate in the literature, with some authors pointing out that a reduced MW mass would effectively eliminate the problematic halos (e.g. Wang et al., 2012; Cautun et al., 2014) and others arguing that baryonic processes, such as reionization, supernovae feedback, tidal interactions, and ram pressure stripping, may reduce the central densities of simulated dwarf halos (e.g. Bullock et al., 2000; Somerville, 2002; Pontzen & Governato, 2012; Zolotov et al., 2012; Brooks & Zolotov, 2014; Arraki et al., 2013; Gritschneder & Lin, 2013; Garrison-Kimmel et al., 2013; Amorisco et al., 2014; Del Popolo et al., 2014; Sawala et al., 2014; Pontzen & Governato, 2014).

Quantitatively, the magnitude of these small-scale problems and the degree to which feedback and other baryonic processes can operate to solve them depend on the underlying power spectrum and cosmological parameters, which fundamentally affect the collapse times and central densities of dark matter halos. For example, Zentner & Bullock (2002, 2003) showed that non-trivial primordial power spectra of the type expected in basic inflation models can alleviate many of the small-scale problems faced by ΛCDM, and used semi-analytic models to show that running at the level of $\alpha_s \simeq -0.03$ can reduce discrepancies significantly. Later, using numerical simulations, Polisensky & Ricotti (2014) showed that differences in best-fit $\sigma_8$ and $n_s$ values between WMAP data releases impact small-scale predictions in

[3] We note that the density profiles of dSphs are currently a matter of some debate (e.g. Breddels & Helmi, 2013).

important ways. The implication is that changes that follow from the *BICEP*2 results can affect the magnitude of small-scale discrepancies significantly. Similarly, imposing a free-streaming cutoff in the initial power spectrum (e.g. from warm dark matter, WDM, or from a non-trivial inflation model) may also aid in resolving problems (Kamionkowski & Liddle, 2000; Zentner & Bullock, 2003; Kaplinghat, 2005; Lovell et al., 2014; Schneider et al., 2014). Specifically, WDM with a thermal mass of 2 keV has been shown to be sufficient to solve some of the problems (Anderhalden et al., 2013). Although this mass is in conflict with existing limits on free-streaming cutoffs (e.g., Polisensky & Ricotti, 2011; Viel et al., 2013; Schneider et al., 2014), the limits are subject to systematic uncertainties, and more robust limits based on phase-space arguments and subhalo counting are just below 2 keV (Boyarsky et al., 2009; Gorbunov et al., 2008; Horiuchi et al., 2014).

The *BICEP*2 measurement may also have interesting consequences on searches for potential annihilation signals from dark matter itself (indirect detection studies). The annihilation signal from a single halo scales as the square of the dark matter density, $\rho^2_{\rm DM}$ (Strigari et al., 2008a), and the total "boost" factor, the contribution to the expected annihilation signal due to substructure, is dependent on the slope and normalization of the substructure mass function. Reducing any of these quantities could significantly loosen the upper limits placed by the searches that employ substructure boost (Kamionkowski et al., 2010; Anderson et al., 2010; Sánchez-Conde & Prada, 2014; Ng et al., 2014).

In this paper, we investigate the impact of the running power spectrum on structure formation in the Universe by simulating the evolution of a MW-size host in four separate cosmologies: the model motivated by *BICEP*2, the *Planck* cosmological model, a WDM model with the *Planck* parameter set, and a flat universe with a lowered $\Omega_{\rm m}$ but otherwise identical to the *Planck* universe in order to control for the difference in $\Omega_{\rm m}$ between the *Planck* and *BICEP*2 models.

This paper is organized as follows: § 5.2 describes the simulations, including the cosmological

models that we compare; § 5.3 presents our results for the cosmological mass function at $z = 3$, the subhalo $V_{\rm max}$ function of a MW-size host at $z = 0$, and discuss the changes in the internal kinematics of the highest mass subhalos (the TBTF problem) as well as implications for the substructure boost; we summarize our findings in § 5.4.

## 5.2 Simulations and Analysis

We have run collisionless, dark matter-only simulations of a $50h^{-1}\,$Mpc periodic region with the Tree-PM code `Gadget-3` (Springel, 2005), beginning at $z = 125$. We present seven simulations, three of which model the full volume at medium resolution ($n_{\rm p} = 1024^3$) and four of which are "zoom-in" simulations aimed at a Milky Way (MW)-size host. Initial conditions were created with `MUSIC` (Hahn & Abel, 2011). We include the running in the *BICEP*2 universe by defining

$$T'^2(k) = \left(\frac{k}{k_\star}\right)^{\frac{1}{2}\alpha_{\rm s}\ln\left(\frac{k}{k_\star}\right)} T^2(k), \tag{5.1}$$

where $\alpha_{\rm s} = dn_{\rm s}/d\ln k$ is the running of the spectral index, $k_\star = 0.05\,{\rm Mpc}^{-1}$ (Abazajian et al., 2014), and $T(k)$ is the standard definition of the transfer function. We pass $T'^(k)$ to `MUSIC` as the transfer function.

We list the four underlying cosmological models that we adopt in Table 5.1. For the *BICEP*2 universe, we select the "running" model from Abazajian et al. (2014), who performed a joint Bayesian analysis on the *BICEP*2 *B*-mode polarization data and the temperature and lensing data from Planck Collaboration et al. (2013); those parameters are listed in the first column. We elect to compare this model to that suggested by the *Planck* temperature power spectrum data alone (Table 2, Column 2 of Planck Collaboration et al., 2013), reproduced in the second column. We additionally simulate structure formation in two *Planck*-like control

| Parameter | *BICEP*2 | *Planck* | *Low*-$\Omega_{\rm M}$ | $WDM_{\rm 2.6keV}$ |
|---|---|---|---|---|
| $\alpha_{\rm s}$ | -0.024 | 0 | 0 | 0 |
| $h$ | 0.698 | 0.6711 | 0.6711 | 0.6711 |
| $\Omega_{\rm m}$ | 0.285 | 0.3175 | 0.26 | 0.3175 |
| $\Omega_\Lambda$ | 0.715 | 0.6825 | 0.74 | 0.6825 |
| $\sigma_8$ | 0.835 | 0.8344 | 0.8344 | 0.8344 |
| $n_{\rm s}$ | 0.967 | 0.9624 | 0.9624 | 0.9624 |
| $m_{\rm WDM}$ | — | — | — | 2.6 keV |
| $m_{\rm p,\,HR}$ | 1.44 | 1.6 | 1.31 | 1.6 |
| $m_{\rm p,\,FB}$ | 92.1 | 102.6 | 84 | — |

Table 5.1: The four sets of cosmological parameters used in this work. The first column indicates the parameter, the second lists the adopted *BICEP*2 cosmology from Abazajian et al. (2014), the third gives the parameters from *Planck* adopted here (taken from the temperature power spectrum; Planck Collaboration et al., 2013), the fourth column lists the "*Low*-$\Omega_{\rm M}$" cosmology, which is identical to the *Planck* parameter set but with an overall matter density below that suggested by *BICEP*2. The final column, which we refer to as "$WDM_{\rm 2.6keV}$," is identical to the *Planck* cosmology, but includes a WDM free-streaming cut-off in the power spectrum for a thermal WDM particle mass of $m_{\rm WDM} = 2.6$keV (see Figure 5.1). Particle masses are given in units of $10^5 h^{-1}\,M_\odot$. $\alpha_{\rm s}$ is the running, defined in the text.

models, *Low*-$\Omega_{\rm M}$ and $WDM_{\rm 2.6keV}$. Both adopt the majority of the *Planck* parameters, but *Low*-$\Omega_{\rm M}$ artificially lowers the overall matter density, $\Omega_{\rm m}$, to $\sim 3\sigma$ below that suggested by Abazajian et al. (2014) (while maintaining flatness) in order to control for the lowered $\Omega_{\rm m}$ in the *BICEP*2 cosmology. The $WDM_{\rm 2.6keV}$ cosmology is identical to the *Planck* model, but imposes a relativistic free-streaming cut-off in the power spectrum for a thermal WDM particle equivalent mass of $m_{\rm WDM} = 2.6$ keV. The mass is chosen to obey the robust limits from phase-space arguments of MW dSphs galaxies and strict counting of M31 satellites (Horiuchi et al., 2014), and is also marginally consistent with measurements of the Ly-$\alpha$ at $3\sigma$ (Viel et al., 2013). A WDM particle mass of 2 keV has been shown to solve small-scale issues in CDM (Anderhalden et al., 2013), but we opt for a slightly more massive particle in order to explore a value distinct from other works.

The initial ($z = 125$) matter power spectra for these cosmologies are shown in Figure 5.1. The upper panel plots $k^3P(k)$ for the *BICEP*2 parameters in black, the *Planck* model in

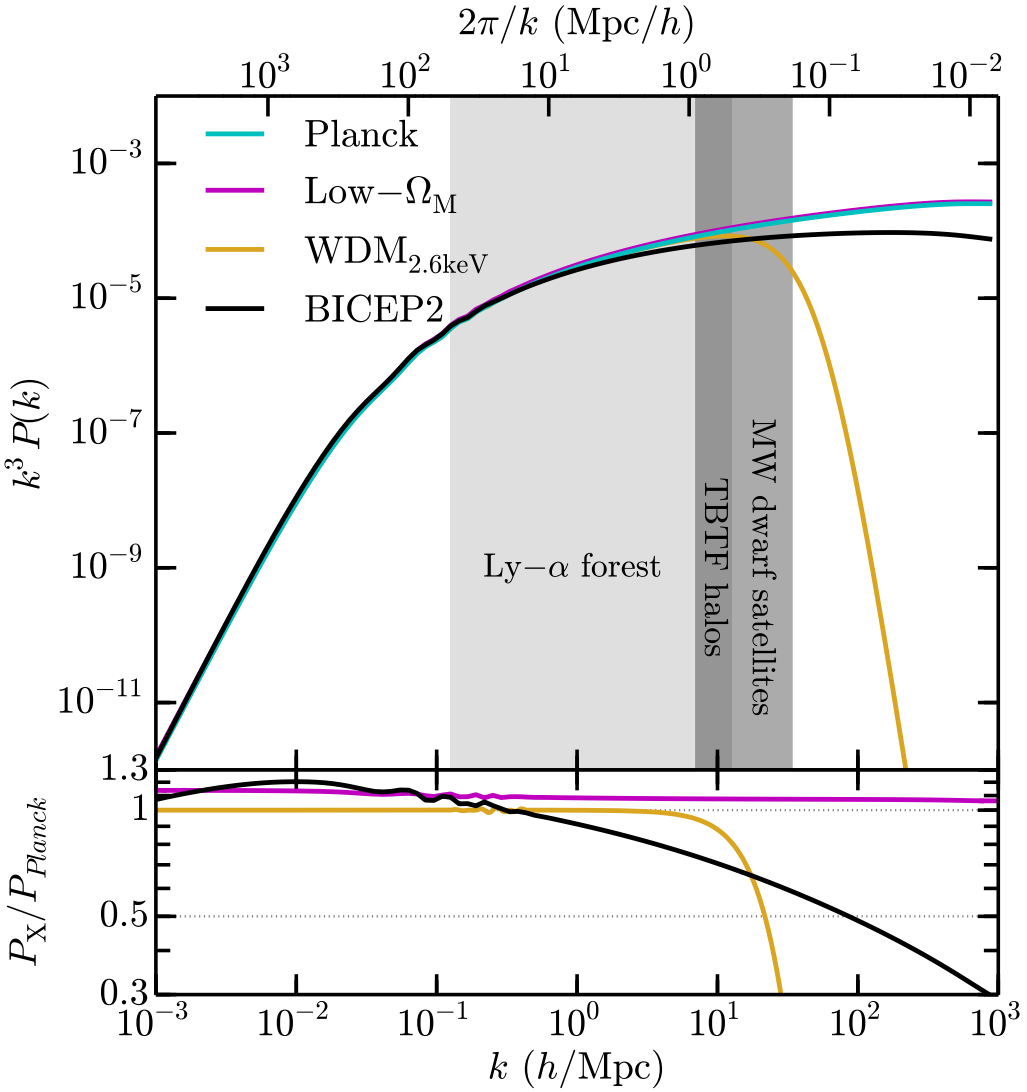


Figure 5.1: Top: The primordial power spectrum in the *BICEP2* (black), *Planck* (cyan), *WDM*$_{2.6\rm keV}$ (yellow), and *Low*-$\Omega_{\rm M}$ (magenta) cosmologies adopted in this paper, used for creating the initial conditions for the simulations. Bottom: The ratio of the power spectra relative to that of *Planck*. The light shaded region in both panels indicates the regime that Viel et al. (2013) probe with the Lyman-$\alpha$ forest, where the *BICEP2* power spectrum differs by $\lesssim 30\%$ and where that of *WDM*$_{2.6\rm keV}$ agrees nearly perfectly, until the sharp cutoff just below the smallest scales probed by Ly-$\alpha$. On the mass scales relevant to small-scale galaxy formation ($M_{\rm halo} \sim 10^9 - 10^{11} h^{-1}\,M_\odot$, indicated in dark grey) however, *BICEP2* differs by nearly a factor of 2 and *WDM*$_{2.6\rm keV}$ quickly falls off due to relativistic free-streaming in the early Universe. The overlap region roughly corresponds to the mass scales of halos characteristic of the too-big-to-fail problem. The *Low*-$\Omega_{\rm M}$ model is everywhere $\sim 10\%$ higher than the standard *Planck* model at $z = 125$ due to the constraint that the linear power spectra agree at $z = 0$.

cyan, and the *Low*-$\Omega_{\rm M}$ and $WDM_{2.6{\rm keV}}$ control models in magenta and yellow, respectively. The ratio of each model, relative to the *Planck* power spectrum is plotted in the lower panel. The light-grey region indicates the scales that are currently probed by the Lyman-$\alpha$ forest ($50h^{-1}\,{\rm Mpc} - 0.5h^{-1}\,{\rm Mpc}$; Viel et al., 2013) and the dark grey region indicates the mass ranges of interest to dwarf galaxy formation ($M_{\rm halo} \sim 10^9 - 10^{11} M_\odot$); the darkest overlap region roughly corresponds to the mass scales of $V_{\rm max} \sim 35\,{\rm km\,s^{-1}}$ halos, which are characteristic of the problematic halos identified in TBTF. The *BICEP*2 power spectrum differs from that of *Planck* by as much as $\sim 30\%$ at the scales probed by the Ly-$\alpha$ forest; studies of the Ly-$\alpha$ forest power spectrum are sensitive to running, and the most recent results have found values consistent with the running we adopt here $\alpha_s = -0.028 \pm 0.018$ (Lesgourgues et al., 2007). The $\gtrsim 30\%$ reduction in the primordial power at the smaller scales associated with the formation of dwarf halos, however, has interesting consequences for the small-scale problems discussed above. The unlabeled region to the right of the dwarf scales are associated with so-called "mini-halos," which may be probed by gravitational lensing studies (e.g., Keeton & Moustakas, 2009) or tidal stream analyses (Ngan & Carlberg, 2014). This range is also important for the overall "boost" factor due to dark matter annihilation in substructure (Sánchez-Conde & Prada, 2014), indicating that the *BICEP*2 power spectrum will likely produce a much smaller DM annihilation signal from these mini-halos.

We first compare the cosmologies by simulating the entire 50 $h^{-1}\,{\rm Mpc}$ volume at moderate resolution ($n_{\rm p} = 1024^3$) until $z = 3$ with the *Planck*, *Low*-$\Omega_{\rm M}$, and *BICEP*2 cosmologies.[4] The particle masses for these "full-box" simulations are given in Table 5.1 as $m_{\rm p,\,FB}$ in units of $10^5 M_\odot$. We fix the Plummer-equivalent softening lengths of the full-box simulations at 5 comoving $h^{-1}\,{\rm kpc}$ until $z = 9$, at which time they become 500 physical $h^{-1}$ pc. Dark matter structure is identified with the `AMIGA Halo Finder` (`AHF`; Knollmann & Knebe, 2009), a publicly-available three-dimensional spherical overdensity halo finder.[5] A slice of the simula-

[4] We do not simulate the volume with the $WDM_{2.6{\rm keV}}$ cosmology as the model is designed to agree with our *Planck* run at the scales probed by such a simulation.

[5] `AHF` is available at `http://popia.ft.uam.es/AHF/Download.html`.

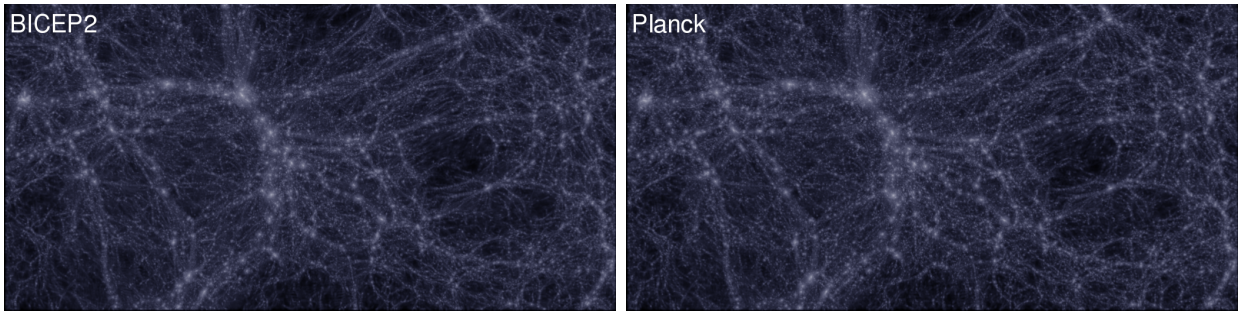


Figure 5.2: Visualizations of the large-scale dark matter density field at $z = 3$ in the *BICEP*2 (top) and *Planck* (bottom) cosmologies. Shown is a slab 25 $h^{-1}$ Mpc wide, 12.5 $h^{-1}$ Mpc tall, and 5 $h^{-1}$ Mpc deep. The two matter fields initially appear indistinguishable on these scales, though we will show below that there are small differences in the halo mass function, which become even stronger on the scales of dwarf galaxies.

tion volume at $z = 3$ is shown in Figure 5.2 for the *BICEP*2 cosmology (top) and the fiducial *Planck* model (bottom) – the two appear indistinguishable at these scales, though we will show below that there is a small systematic offset in the halo mass function, consistent with expectations from linear theory.

In order to study the highly non-linear regime, however, we primarily focus our efforts on "zoom-in" simulations (Katz & White, 1993; Oñorbe et al., 2014) aimed at a MW-size host, similar to the Via Lactea II (Diemand et al., 2008; Kuhlen et al., 2008) and Aquarius (Springel et al., 2008) projects. Specifically, we selected a highly isolated host from the ELVIS simulations (Garrison-Kimmel et al., 2014a) and re-create the parent box, oversampling the region from which the halo forms with higher resolution, with the four underlying cosmological models given in Table 5.1. The zoom-in simulations are initialized with an effective resolution of $4096^3$ particles in the high resolution region. Similar to the full-box simulations, the softening lengths of these lowest mass particles is kept fixed at 1 comoving $h^{-1}$ kpc until $z = 9$, after which it is held fixed at 100 physical $h^{-1}$ pc until $z = 0$. The particle masses for each cosmological model are listed as $m_{\mathrm{p,HR}}$ in Table 5.1, again in units of $10^5 h^{-1}\, M_\odot$. Each cosmological model was initialized with identical phases for the perturbations at all scales in order to reduce numerical differences (e.g., in the subhalo orbits) between the models. As in the full-box simulations, we search for collapsed structures

in the $z = 0$ particle data with `AHF`.[6] A visualization of a cube 500 $h^{-1}$ kpc on a side, centered on the zoom-in target, is shown in Figure 5.3. The images are colored by the local matter density and show, from top left to bottom right, the *BICEP*2 simulation, the *Planck* model, the *Low*-$\Omega_{\rm M}$ cosmology, and the $WDM_{\rm 2.6keV}$ model. The agreement between the *Planck* models, in spite of the free-streaming cutoff or shift in $\Omega_{\rm m}$, is uncanny; the *BICEP*2 cosmology, however, has less overall substructure and clearly distinct orbits for the largest subhalos, indicative of the significant differences in power at $M \sim 10^9 - 10^{11} M_\odot$ scales seen in Figure 5.1.

Our zoom-in simulations are run with identical particle numbers, box sizes, and softening lengths (in $h^{-1}$ units) as the fiducial simulations in the ELVIS Suite (Garrison-Kimmel et al., 2014a); we therefore adopt the ELVIS resolution cut here and study only halos with maximum circular velocities $V_{\rm max} > 8$ km s$^{-1}$. Similarly, Garrison-Kimmel et al. (2014b) showed that the relationship between $V_{\rm max}$ and the radius at which $V_{\rm max}$ occurs, $R_{\rm max}$, is converged for halos larger than 15 km s$^{-1}$ and with $R_{\rm max} > 0.36$ $h^{-1}$ kpc for simulations at this resolution; we again use the same criteria when examining the internal structure of small halos.

## 5.3 Results

We begin by examining the halo mass function in the 50 $h^{-1}$ Mpc full-box runs at $z = 3$. Plotted as solid lines in the top panel of Figure 5.4 is the anti-cumulative number density of host halos, defined as those with their centers outside the virial volumes [7] of all halos larger than itself, as a function of virial mass $M_{\rm v}$; the lower panel plots the ratio of each line

[6] We also find identical results using the 6D friend-of-friends halo finder `ROCKSTAR` (Behroozi et al., 2013a).

[7] We use the term "virial radius" to refer to the radius at which the overdensity relative to the critical density drops to 173.8 (*BICEP*2), 174.3 (*Planck*), and 173.3 (*Low*-$\Omega_{\rm M}$) at $z = 3$ and 99.8 (*BICEP*2), 104.1 (*Planck*), 96.5 (*Low*-$\Omega_{\rm M}$), and 104.1 ($WDM_{\rm 2.6keV}$) at $z = 0$, and "virial mass" to refer to the total mass contained within that radius.

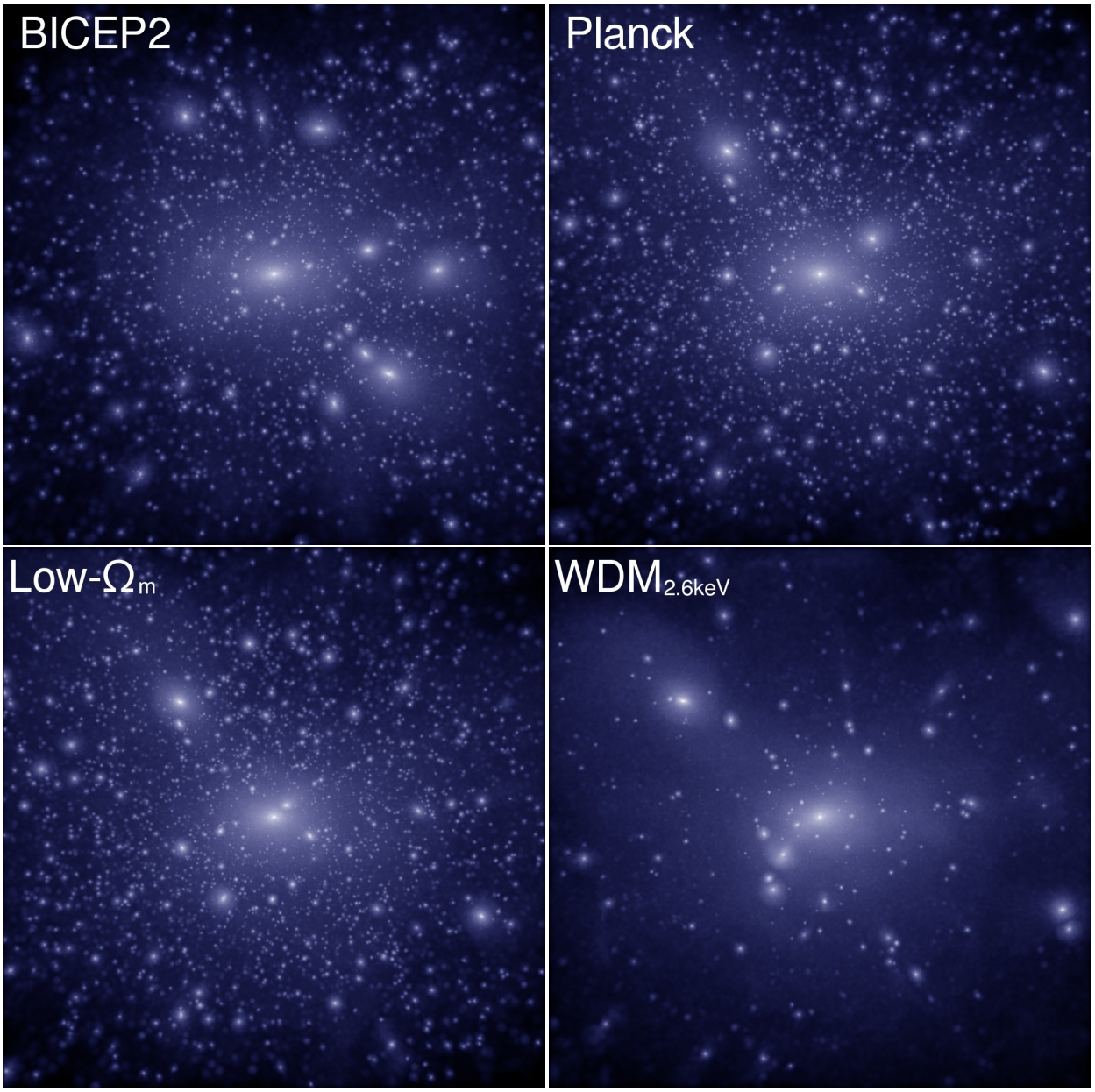


Figure 5.3: Visualizations of the zoom-in halo, colored by the local matter density, in the *BICEP*2 (top left), *Planck* (top right), *Low*-$\Omega_{\rm M}$ (bottom left), and $WDM_{2.6{\rm keV}}$ (bottom right) cosmologies. Shown are cubes 500 $h^{-1}$ kpc on a side, centered on the targeted host. The relative lack of substructure in the $WDM_{2.6{\rm keV}}$ run and the agreement between the orbits of the largest halos between the *Planck* models are visible even by eye. The *BICEP*2 simulation, however, displays clearly different subhalo orbits and hints at reduced substructure at the smallest masses.

relative to the fiducial *Planck* model. The *BICEP*2 cosmology exhibits a suppression on all mass scales such that the Planck mass function is offset by $\sim 30\%$ at fixed number, though the offset rises slighter at lower masses, consistent with the running in the power spectrum. We note that presenting results in $M_\odot$ rather than $h^{-1}\,M_\odot$ would only increase the difference between the two simulations as the *Planck* cosmology adopts a smaller Hubble parameter.

This offset, however, is consistent with expectations from linear theory of structure collapse. Plotted as dashed lines in Figure 5.4 are the results of applying the analytical fitting function of Tinker et al. (2008); [8] the ratios of these fitting functions are plotted as dashed lines in the lower panel. The Tinker et al. fit agrees nearly perfectly with our simulated mass functions, and the relative offsets from the *Planck* model are also in excellent agreement with the simulations. We conclude that analytic mass functions based on linear theory may be used to make accurate predictions (at least until $z = 3$) in the *BICEP*2 cosmology.

Given that the differences in the primordial power spectrum increase with decreasing scales, we can expect to see even more extreme differences on the scales of dwarf galaxy halos. We therefore turn our analysis to the zoom-in simulations described in Section 5.2, which we exclusively use for the remainder of the work. The properties of the main host halo, given in Table 5.2, vary slightly between the four models; we therefore present subhalo counts as a function of $V_{\rm max}/V_{\rm v}$, where $V_{\rm v}$ is the circular velocity of the host halo at the virial radius. This minimizes the halo-to-halo scatter and normalizes for the effects of varying host mass.

This normalized $V_{\rm max}$ function is plotted in the top panel of Figure 5.5 for all four cosmological models; the lower panel again plots the ratio of each model to the *Planck* cosmology. The upper axis is scaled to $V_{\rm v} = 160$ km s$^{-1}$, roughly the virial velocity of a MW-size host and the mean $V_{\rm v}$ of the host in the four simulations. When normalizing by $V_{\rm v}$, the agreement between the *Planck* and *Low*-$\Omega_{\rm M}$ models is nearly perfect at all $V_{\rm max}/V_{\rm v}$, even at the

[8] Theoretical mass functions are calculated via the publicly available code provided by Murray et al. (2013).

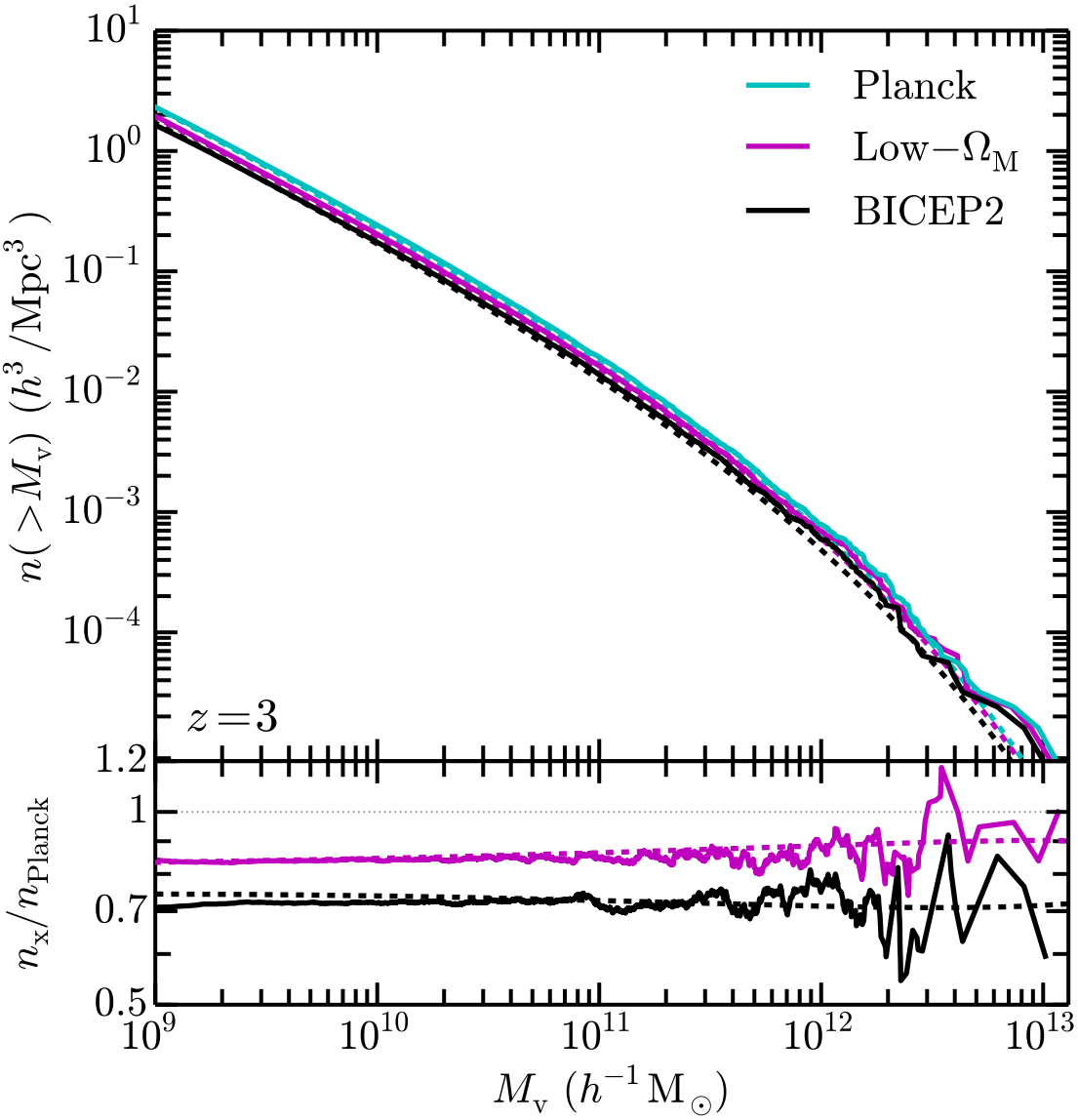


Figure 5.4: The anti-cumulative mass function, per unit volume, of all host halos in the 50 $h^{-1}$ Mpc volume at $z = 3$ from the simulations (solid lines) and from applying the Tinker et al. (2008) analytical fitting function (dashed lines) for the *BICEP*2 (black), *Planck* (cyan) and *Low*-$\Omega_{\rm M}$ (magenta) models (upper panel) and the ratios of the *BICEP*2 and *Low*-$\Omega_{\rm M}$ models to the *Planck* model (lower panel). At fixed mass, the *BICEP*2 cosmology predicts $\sim 30\%$ fewer halos than the *Planck* model, consistent with expectations from linear theory. Alternatively, halo masses at fixed number counts are $\sim 20 - 30\%$ lower in the *BICEP*2 model, again compared to *Planck*.

| | $M_{\rm v}$ $(10^{12}\ h^{-1}\,M_\odot)$ | $R_{\rm v}$ $(h^{-1}\,{\rm kpc})$ | $V_{\rm max}$ $({\rm km\,s^{-1}})$ | $V_{\rm v}$ $({\rm km\,s^{-1}})$ | $N_{\rm h}(<R_{\rm v})$ $[>8\ {\rm km\,s^{-1}}]$ | $N_{\rm p}(<R_{\rm v})$ | $r_{\rm uncontam}$ $(h^{-1}\,{\rm Mpc})$ | $N_{\rm h}(<1\,h^{-1}\,{\rm Mpc})$ $[>15\ {\rm km\,s^{-1}}]$ |
|---|---|---|---|---|---|---|---|---|
| *BICEP2* | 1.26 | 221 | 164 | 156 | 460 | $8.8\times10^6$ | 1.27 | 125 |
| *Planck* | 1.49 | 231 | 187 | 166 | 944 | $9.4\times10^6$ | 1.04 | 216 |
| *Low-*$\Omega_{\rm M}$ | 1.21 | 222 | 176 | 153 | 709 | $9.3\times10^6$ | 1.05 | 166 |
| $WDM_{\rm 2.6keV}$ | 1.49 | 231 | 194 | 167 | 119 | $9.4\times10^6$ | 0.97 | 76 |

Table 5.2: The properties of the main host halo in the zoom-in simulations. In order, the columns are the virial mass $M_{\rm v}$, virial radius $R_{\rm v}$, maximum circular velocity $V_{\rm max}$, virial velocity $V_{\rm v}=\sqrt{GM_{\rm v}/R_{\rm v}}$, the number of resolved ($V_{\rm max}>8\ {\rm km\,s^{-1}}$) subhalos within the virial radius $N_{\rm h}(<R_{\rm v})$, the number of simulation particles within the virial radius $N_{\rm p}$, the distance to the nearest low resolution particle $r_{\rm uncontam}$, and the number of halos with resolved internal structure ($V_{\rm max}>15\ {\rm km\,s^{-1}}$) within 1 $h^{-1}\,{\rm Mpc}$, $N_{\rm h}(<1\ h^{-1}\,{\rm Mpc})$.

high $V_{\rm max}$ end where small-number statistics typically dominate; if the counts are not normalized by the virial velocity, however, the *Low*-$\Omega_{\rm M}$ model lies $\sim 25\%$ below the Planck cosmology at fixed subhalo $V_{\rm max}$. The *BICEP*2 counts, however, are suppressed even after normalizing by $V_{\rm v}$, particularly for subhalos less massive than $V_{\rm max} \sim 30$ km s$^{-1}$. The total count is $\sim 50\%$ below the *Planck* line at the resolution limit, alleviating the severity of the missing satellites problem. As expected, subhalos are even more strongly suppressed in the $WDM_{\rm 2.6keV}$ universe, with counts a factor of $\sim 6$ lower than the fiducial *Planck* model at the resolution limit. While this suppression drastically reduces the severity of the missing satellites problem, it may actually under-produce the required subhalo count compared to the known count of M31 satellite galaxies (e.g. Horiuchi et al., 2014).[9] The *BICEP*2 model has no such difficulties.

Due to the overall suppression of substructure in *BICEP*2 it is possible that counts of high mass ($V_{\rm max} \sim 80$ km s$^{-1}$) satellites will provide an additional constraint on the running. While we do not see any significant differences in the few subhalos that exist in the simulated host at that mass range, it is possible that some reduction exists on a statistical level, particularly for close pairs. As Tollerud et al. (2011) showed that ΛCDMlike cosmologies reproduce observations reasonably well at Large Magellanic Cloud (LMC)-like masses, such counts may be used as a probe of the initial power spectrum in the future. Such a study, however, would require large simulations with higher resolution than those presented here, simulated until $z = 0$.

We now turn our attention to the internal structure of the subhalos. The simulations used in this work do not fully resolve density profiles in the innermost $\sim 500$ pc of dwarf halos, but integral properties such as $V_{\rm max}$ and $R_{\rm max}$ are converged for $V_{\rm max} > 15$ km s$^{-1}$ objects. These two quantities fully define the two-parameter Navarro-Frenk-White (NFW; Navarro

[9] WDM N-body simulations are known to suffer from artificial fragmentation on small scales, leading to a non-negligible contribution to the halo catalog from spurious objects (e.g. Wang & White, 2007; Lovell et al., 2014). We do not explicitly account for this effect, which would act to suppress counts of small halos even further.

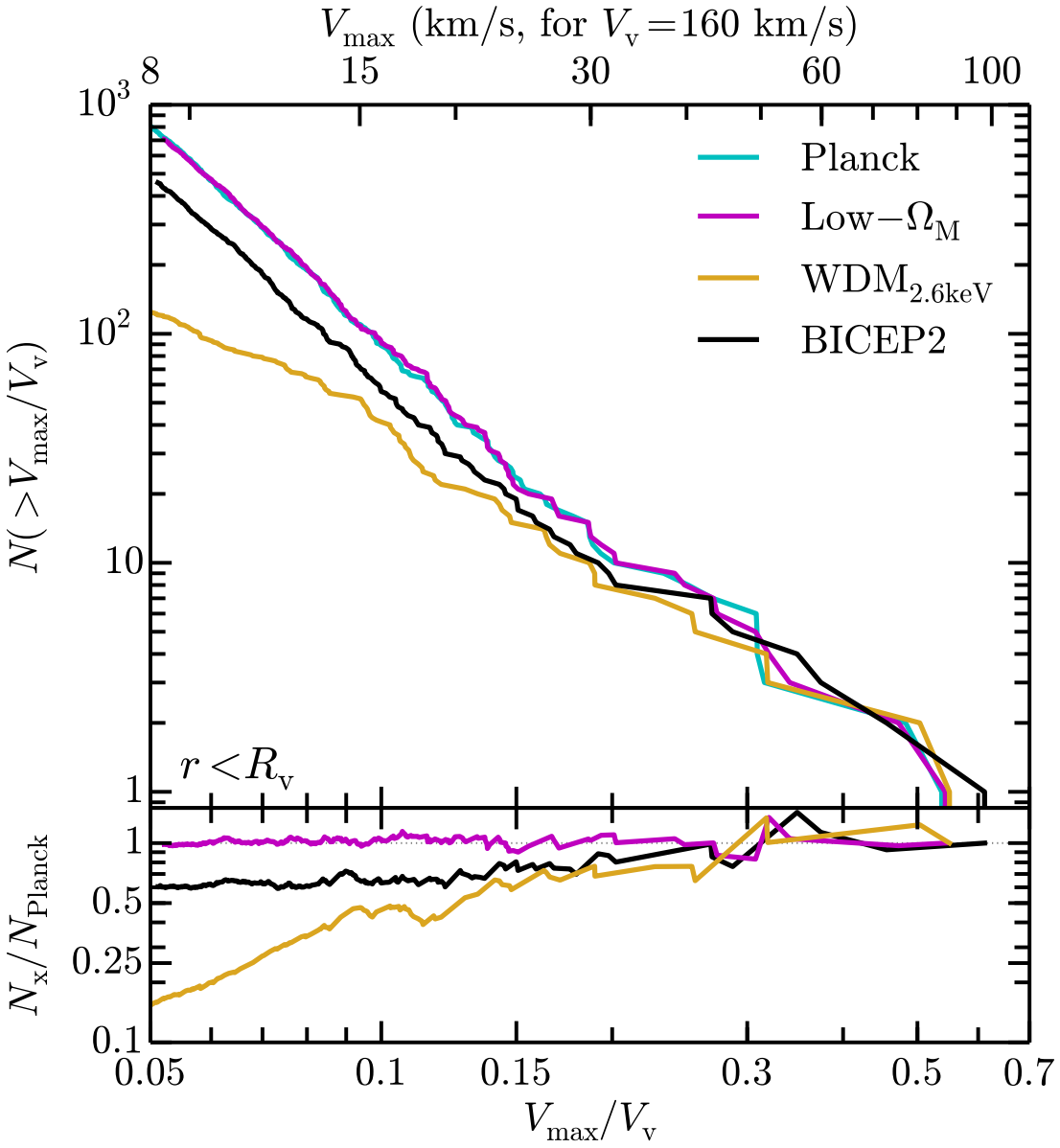


Figure 5.5: The anti-cumulative count of subhalos ($r < R_{\rm v}$) as a function of $V_{\rm max}$ normalized by the host virial velocity, $V_{\rm v}$ (upper panel) and the ratio of each cosmology to the *Planck* model (lower panel). Counts in the *Low*-$\Omega_{\rm M}$ cosmology (magenta line) match up nearly exactly with those in the standard *Planck* cosmology (cyan line), even though the host halo is $\sim 20\%$ less massive due to the modification in $\Omega_{\rm m}$. Counts in the *BICEP*2 cosmology (black line), however, are systematically low for $V_{\rm max}/V_{\rm v} \lesssim 0.25$ ($V_{\rm max} \lesssim 40$ km s$^{-1}$) and predict $\sim 50\%$ fewer halos at the resolution limit. The $WDM_{2.6{\rm keV}}$ model, meanwhile, drastically under-produces subhalos at low masses. Therefore, both the $WDM_{2.6{\rm keV}}$ and the *BICEP*2 model will alleviate the missing satellites problem, though $WDM_{2.6{\rm keV}}$ may eliminate too many subhalos to explain, e.g., the observed satellite mass function of M31 (Horiuchi et al., 2014). The top axis is scaled to $V_{\rm v} = 160$ km s$^{-1}$, the mean virial velocity of the host in the four simulations.

et al., 1996b) density profile

$$\rho(r) = \frac{\rho_{\rm s}}{(r/r_{\rm s})(1 + r/r_{\rm s})^2}, \tag{5.2}$$

where $r_{\rm s} = R_{\rm max}/2.1626$ is a characteristic scale radius and $\rho_{\rm s} = \rho_{\rm s}(R_{\rm max}, V_{\rm max})$ is four times the density at $r = r_{\rm s}$. We may therefore extrapolate a unique circular velocity curve into the inner regions of the halos to make predictions regarding the central densities and compare with observations at small radii. This extrapolation assumes that the inner structure of subhalos is not strongly dependent on cosmology (i.e. that subhalos still follow NFW profiles in *BICEP*2); for $WDM_{2.6{\rm keV}}$ at least, this extrapolation seems to be valid (Dunstan et al., 2011), but we note that varying the density profile can strongly impact the number of massive failures (Di Cintio et al., 2013; Garrison-Kimmel et al., 2014b). Similarly, we may predict the relative change in the annihilation signal from substructure by knowing only the relationship between $V_{\rm max}$ and $R_{\rm max}$, as the signal from a single halo or subhalo is proportional to $\rho_{\rm s}^2 r_{\rm s}^3$ (Strigari et al., 2008b).

We thus begin our investigation by presenting this relationship for subhalos of the main host (within 300 physical kpc, for comparison to the MW satellites) in the four cosmological models. Plotted in Figure 5.6 are the individual $R_{\rm max} - V_{\rm max}$ values for subhalos in each model, with the *BICEP*2 model plotted as black circles, the *Planck* model in cyan squares, the *Low*-$\Omega_{\rm M}$ model as magenta triangles, and the $WDM_{2.6{\rm keV}}$ model as yellow diamonds. The lines plot power-law fits to the subhalos:

$$\frac{R_{\rm max}}{1\ {\rm kpc}} = A \left( \frac{V_{\rm max}}{10\ {\rm km\,s^{-1}}} \right)^p. \tag{5.3}$$

The contribution to the least-squares fit from each halo is weighted by the $V_{\rm max}$ of that halo to account for the scarcity of high $V_{\rm max}$ halos, and the log-slope $p$ is held fixed at the value that best fits the data in the *Planck* cosmology, $p = 1.419$, allowing the normalization $A$ to

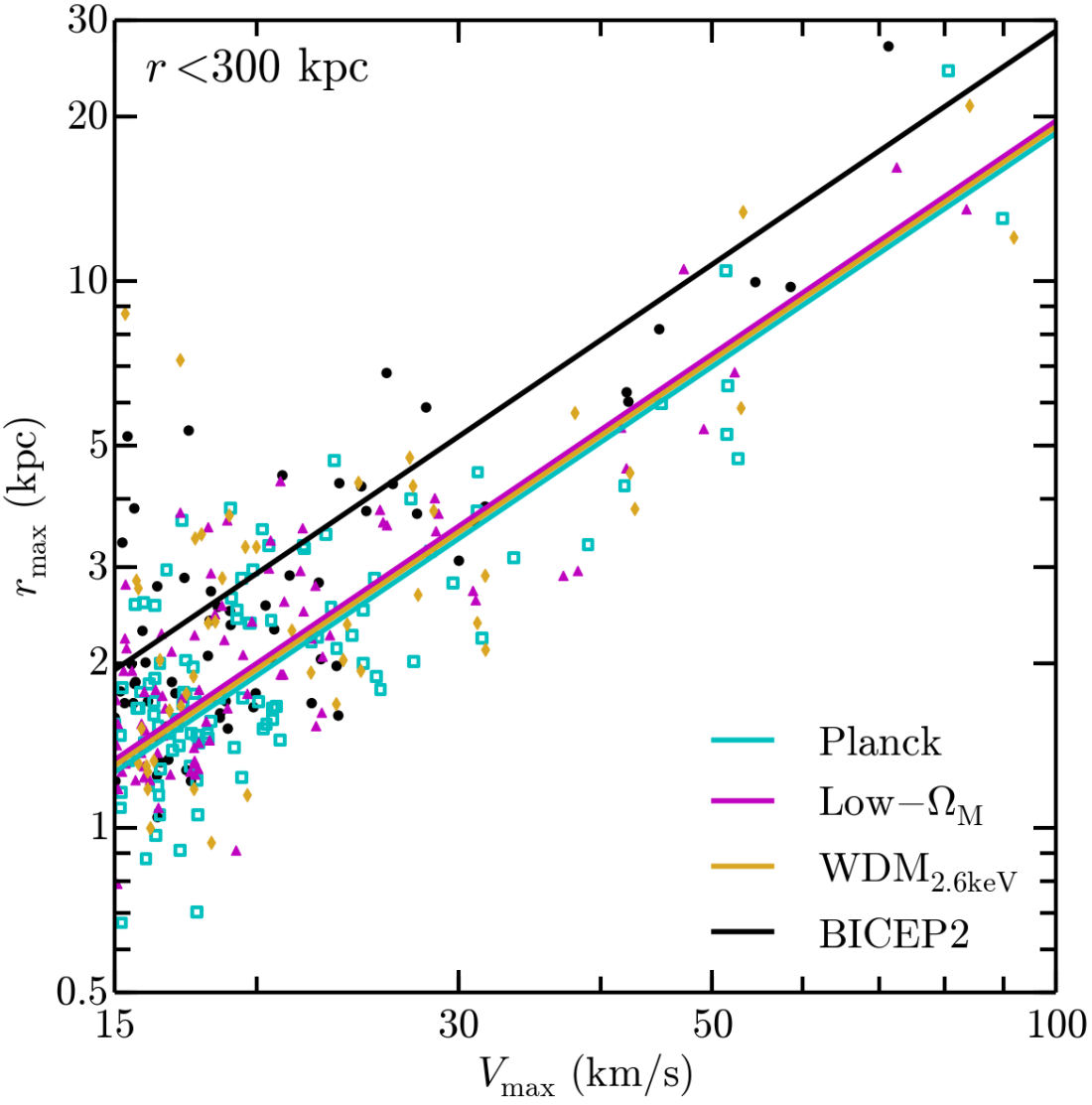


Figure 5.6: The relationship with $R_{\rm max}$ and $V_{\rm max}$ for subhalos in the *BICEP*2 (black circles), *Planck* (cyan squares), *Low*-$\Omega_{\rm M}$ (magenta triangles), and *WDM*$_{\rm 2.6keV}$ (yellow diamonds) cosmologies, along with power-law fits to the data (Equation 5.3). The fits are weighted by $V_{\rm max}$ with the log-slope held fixed at the best-fit value in the *Planck* model, $p = 1.419$ (though there are weak indications that the slope is steeper in the *BICEP*2 model). The best-fit normalization in the *BICEP*2 cosmology is 35% lower than in the *Planck* simulation. In addition to helping to alleviate TBTF (see Figure 5.7), this overall shift in $R_{\rm max}$ at fixed $V_{\rm max}$ also implies a $\sim$ 35% lower annihilation signal from each subhalo in *BICEP*2. The normalizations, $A$, are 0.71 (*Planck*), 0.75 (*Low*-$\Omega_{\rm M}$), 0.73 (*WDM*$_{\rm 2.6keV}$), and 1.09 (*BICEP*2).

vary. [10] The three *Planck*-like models agree nearly perfectly: the normalizations differ by only 5%. The *BICEP*2 model, however, is clearly offset from the remaining three cosmologies with a normalization 35% higher.

It is interesting to note that the $WDM_{2.6\mathrm{keV}}$ model yields similar subhalo structural parameters ($V_{\mathrm{max}}$ - $R_{\mathrm{max}}$) to those of the *Planck* models, at least for the velocity range plotted here. Below we show that this is *not* the case for field halos in $WDM_{2.6\mathrm{keV}}$, which are less concentrated than *Planck* halos in the field. We interpret this differences as an effect of enhanced subhalo stripping for the $WDM_{2.6\mathrm{keV}}$ subhalos. Host halos tend to strip matter from the outer parts of subhalos, making them more concentrated with time. The $WDM_{2.6\mathrm{keV}}$ host halo density and mass remain similar to that in *Planck* cosmology, and the relative stripping experienced by the low-concentration infalling subhalos is more significant than it is in any of the other models. This is also consistent with the fact that we see many fewer subhalos in the $WDM_{2.6\mathrm{keV}}$ case.

The differences seen in Figures 5.5 and 5.6 impact the counts of discrepant TBTF halos. We directly compare the circular velocity curves predicted for each of our runs to observations of the classical MW dwarf spheroidal (dSphs) galaxies in Figure 5.7 – each line represents a single subhalo within 300 kpc and each point indicates a MW satellite. The left panel plots the *Planck* model, the central panel indicates the results in $WDM_{2.6\mathrm{keV}}$, and the right panel plots subhalos in the adopted *BICEP*2 cosmology. As in Boylan-Kolchin et al. (2011, 2012), the observational sample is comprised of the galaxies within 300 kpc of the MW with $L > 10^5\ L_\odot$, excluding the Magellanic Clouds and the Sagittarius dwarf. The former is removed from the sample because satellites as large as the Clouds are rare around MW-size hosts (Boylan-Kolchin et al., 2010; Busha et al., 2011; Tollerud et al., 2011); we remove the latter because it is currently interacting with the MW disk and is therefore not in equilibrium. For the remaining dwarfs, we plot $V_{1/2}$ at $r_{1/2}$, the circular velocity at the half-light radius,

[10] We have also tested a quadratic fit in log-space and do not find evidence for a roll-off at small $V_{\mathrm{max}}$, though there are weak indications that the slope is steeper for the *BICEP*2 subhalos.

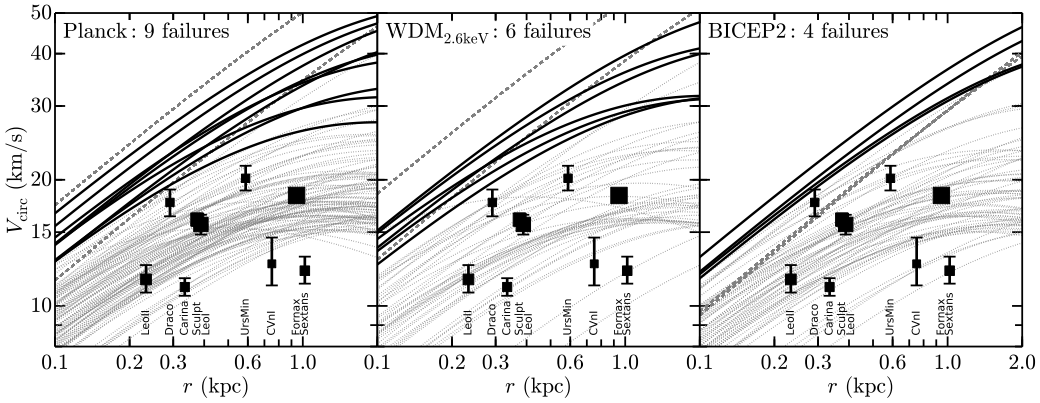


Figure 5.7: The rotation curves of all halos within 300 kpc of the host center with $V_{\rm max} > 15$ km s$^{-1}$, the smallest scale at which $R_{\rm max}$ can be reliably measured, in the *Planck* cosmology (left), the $WDM_{2.6\rm keV}$ model (center), and the adopted *BICEP*2 cosmology (right). The curves are extrapolated from $R_{\rm max}$ and $V_{\rm max}$ (Figure 5.6) by assuming an NFW profile. Also plotted are the constraints on the circular velocity at the half-light radius of the nine classical MW dwarfs used to define the TBTF problem in Boylan-Kolchin et al. (2011, 2012) from Wolf et al. (2010). Plotted as solid lines are those halos identified as massive failures – subhhalos that lie above the $1\sigma$ constraints on the MW dwarfs and thus cannot host any of the known bright satellites. As expected from Figure 5.6, which shows that subhalos in the *BICEP*2 cosmology are less dense at fixed $V_{\rm max}$ than in either the *Planck* or the $WDM_{2.6\rm keV}$ models, the problem is significantly alleviated (though not eliminated) by switching to the *BICEP*2 cosmology. For comparison, we note that the same halo contains eight massive failures in the *Low*-$\Omega_{\rm M}$ model.

with $1\sigma$ errors in Figure 5.7. The values are taken from Wolf et al. (2010), who used data from Walker et al. (2009), Muñoz et al. (2005), Koch et al. (2007), Simon & Geha (2007) and Mateo et al. (2008).

The lines in Figure 5.7 each indicate an NFW rotation curve for a single subhalo of the central host. The dashed lines indicate the simulated analogs to the Magellanic Clouds, defined here as subhalos with $V_{\rm max} > 60$ km s$^{-1}$, which we remove from our analysis and plot only for illustrative purposes. The dotted lines indicate circular velocity profiles that fall below the $1\sigma$ error on $V_{1/2}$ for at least one of the MW dSphs – these subhalos are nominally consistent with the observational data and can host a MW satellite. The solid lines, however, have circular velocities that lie above *all* the dSphs and therefore qualify as "massive failures" – subhalos without observational counterparts. Nearly all of these massive failures are large

enough, even today, to have formed stars in the presence of an ionizing background (Bullock et al., 2000; Somerville, 2002; Sawala et al., 2014).

Though the TBTF problem remains evident in all three models plotted here, [11] the number of massive failures is noticeably reduced in the *BICEP*2 cosmology relative to the *Planck* model. Perhaps surprisingly, the running power spectrum of *BICEP*2 eliminates more massive failures than the chosen WDM free-streaming cutoff.[12] Moreover, the remaining massive failures in the *BICEP*2 model lie well below the equivalent curves in the *Planck* cosmology, which acts to increase the efficacy of other processes (e.g. supernovae feedback) that may further reduce the central densities. Similarly, the *BICEP*2 cosmology significantly lowers the number of subhalos that are consistent with only Draco and Ursa Minor, the two highest density galaxies in the sample. Overall, the *BICEP*2 cosmology significantly reduces the magnitude of the TBTF problem, even without invoking baryonic processes that may further reduce the central densities (e.g. Zolotov et al., 2012), perhaps in a cosmology-dependent manner.

In addition to reducing the number of massive failures, the increase in $R_{\rm max}$ at fixed $V_{\rm max}$ in the *BICEP*2 cosmology implies a reduction in the substructure boost, i.e., the expected dark matter annihilation signal from subhalos. As noted above, the signal from a single halo scales as $\rho_{\rm s}^2 r_{\rm s}^3 \propto V_{\rm max}^4/R_{\rm max}$. Therefore, an increase of 35% in $R_{\rm max}$ at fixed $V_{\rm max}$ directly results in a 35% reduction in the annihilation signal. Furthermore, the overall boost is obtained by summing the signal from all the substructure by integrating the mass (or $V_{\rm max}$) function to masses well below $M_\odot$ (Martinez et al., 2009); assuming that the $\sim 50\%$ offset in the $V_{\rm max}$ function at the resolution limit ($V_{\rm max} = 8$ km s$^{-1}$) remains constant at lower masses, this implies that the substructure boost in the *BICEP*2 cosmology may be a factor of $\sim 5$ lower than in *Planck*. Moreover, the increasing roll-off of $P(k)$ at small scales implies that the

[11] Though we do not plot it, the central halo in the *Low*-$\Omega_{\rm M}$ cosmology hosts eight massive failures.

[12] Though a lighter WDM mass will be more effective (e.g., Schneider et al., 2014), it is constrained by the Ly-$\alpha$ forest (Viel et al., 2013) and subhalo counting (Polisensky & Ricotti, 2011); as discussed in Section 5.1, however, these constraints are subject to systematic uncertainties that are currently difficult to quantify.

relative offsets in both the $V_{\rm max}$ function and the $R_{\rm max} - V_{\rm max}$ relationship are even larger at small masses; the estimate will realistically be larger than 5.

For subhalos, the $R_{\rm max} - V_{\rm max}$ relation is due to a combination of the concentration-mass relationship at the time of formation and tidal stripping after infall onto the central host (Bullock et al., 2001; Ludlow et al., 2014). To more directly probe the former, Figure 5.8 plots $R_{\rm max}$ and $V_{\rm max}$ for halos in the field surrounding the central host, along with power-law fits (Equation 5.3) with $p$ again held fixed at best fit value in the *Planck* simulation, $p = 1.26$. We limit ourselves to objects at least 500 kpc from the central host to avoid the majority of "backsplash" galaxies that have interacted with the host in the past (Teyssier et al., 2012; Garrison-Kimmel et al., 2014a), which may have undergone significant tidal stripping, and we select halos within 1.5 Mpc to avoid high mass (low resolution) contaminating particles.

While the agreement between the *Planck* and *Low*-$\Omega_{\rm M}$ models remains in the field (as expected due to their similar power spectra), the effects of the modifications to $P(k)$ are apparent in both the $WDM_{\rm 2.6keV}$ and *BICEP*2 simulations. The latter two display significantly lower density halos, consistent with the suppression in power spectra at the time of formation; the fits to both are $\sim 50\%$ higher than the fit in the *Planck* cosmology. The most massive nearby field halo in the *BICEP*2 simulation is undergoing a major merger, resulting in an anomalously large $R_{\rm max}$ and we therefore perform the fit with and without that object. Including it results in the fit plotted as a black dashed line; the fit without that point is plotted as a solid black line.

## 5.4 Conclusions

We have tested the impact of the suppressed small-scale primordial power spectrum suggested by the recent *BICEP*2 results by simulating structure formation both with the "running"

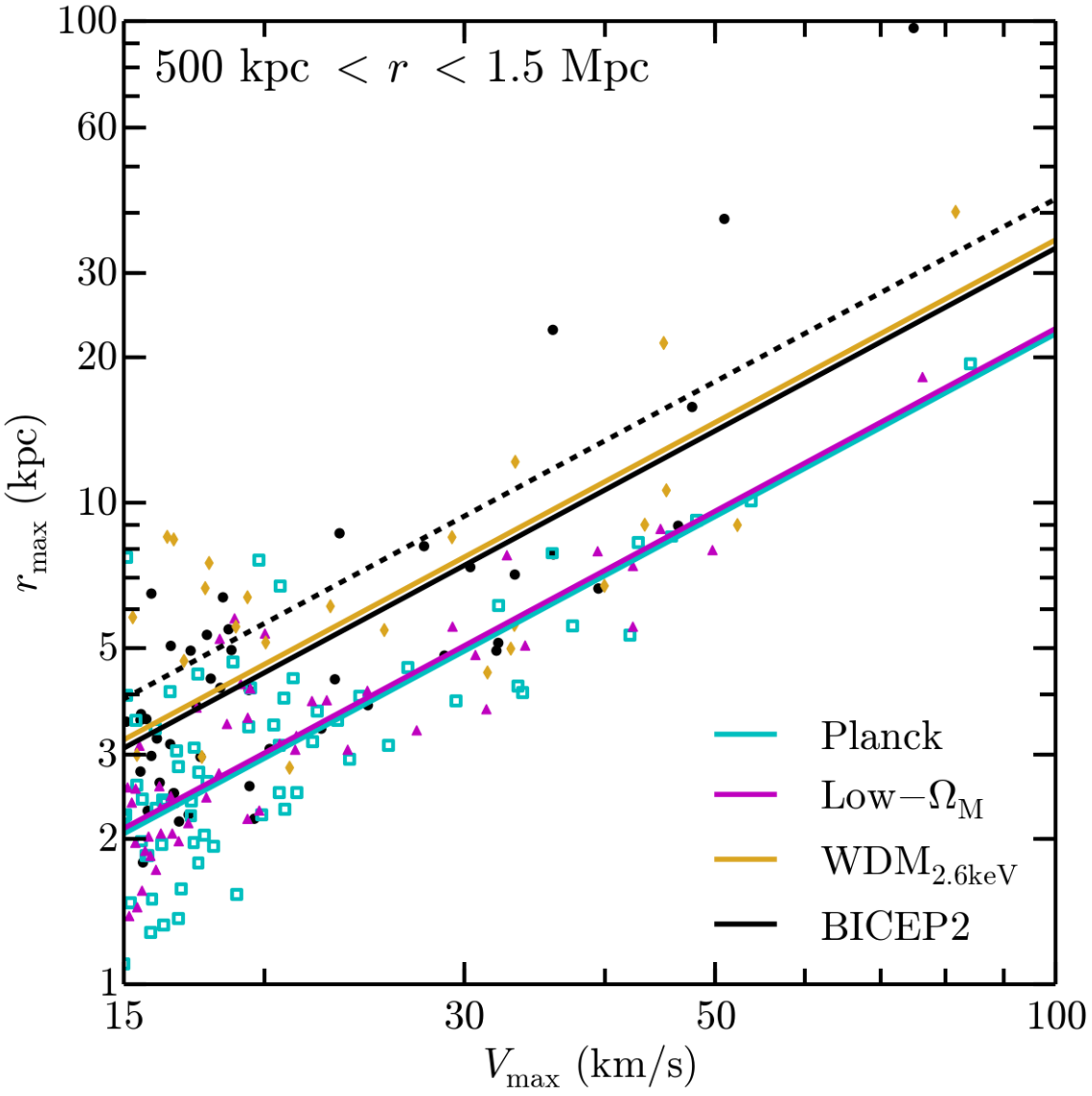


Figure 5.8: The $R_{\rm max}$-$V_{\rm max}$ relation for halos in the fields around the zoom-in target. Solid lines again plot fits (Equation 5.3) weighted by $V_{\rm max}$, with the log-slope again held fixed at the best-fit value for *Planck*, $p = 1.26$. The normalizations, $A$, are 1.23 (*Planck*), 1.26 (*Low*-$\Omega_{\rm M}$), 1.93 ($WDM_{2.6{\rm keV}}$), and 1.85 (*BICEP*2) – suppression in $P(k)$ at small scales in $WDM_{2.6{\rm keV}}$ and *BICEP*2 results in normalizations $\sim 50\%$ lower. The most massive halo in the *BICEP*2 field is excluded from the fit because the anomalously high $R_{\rm max}$ is due to an ongoing merger – including that halo results in a 20% larger normalization ($A = 2.35$), which is plotted as a black dashed line.

power spectrum suggested by these results and with the cosmology suggested by the *Planck* experiment, and using two control models – the *Planck* model with a free-streaming cut-off corresponding to a WDM particle mass of 2.6 keV (thermal) and the *Planck* power spectrum with an artificially lowered $\Omega_{\rm m}$. We have simulated the evolution of identical $(50\ h^{-1}\,{\rm Mpc})^3$ volumes from $z = 125$ until $z = 3$ and the formation of a MW-size host until $z = 0$ at high resolution. These simulations indicate that the suppression in the primordial power spectrum at small scales results in mild offsets in the large-scale halo mass function (consistent with expectations from linear theory) and non-trivial differences in the subhalo $V_{\rm max}$ function and the inner structure of both field and satellite halos. Specifically:

- The $V_{\rm max}$ function of subhalos around a MW-size host in the *BICEP*2 cosmology lies well below that of the same host in the *Planck* model for $V_{\rm max} \lesssim 40\ {\rm km\,s^{-1}}$, even after normalizing for the differing sizes of the hosts. There are twice as many resolved ($V_{\rm max} > 8\ {\rm km\,s^{-1}}$) subhalos within the virial radius of the central host in the *Planck* simulation as result in the *BICEP*2 cosmology. The *Planck* and *Low*-$\Omega_{\rm M}$ models agree after scaling for the host mass. Unsurprisingly, the $WDM_{\rm 2.6keV}$ simulation results in only $\sim 10\%$ as much substructure as our fiducial *Planck* run.

- Although masses of the largest subhalos around our selected host appear to be mostly unaffected by the changes in cosmology, the average concentrations (quantified here by the relationship between $R_{\rm max}$ and $V_{\rm max}$) of subhalos are significantly lower in the *BICEP*2 cosmology than any of the *Planck*-like models and our $WDM_{\rm 2.6keV}$ run. This increase in $R_{\rm max}$ at fixed $V_{\rm max}$ alleviates the too-big-to-fail problem, and may increase the efficacy of baryonic processes that could further reduce the central densities.

- Taken together, the above two results imply that the substructure "boost," the contribution to the dark matter annihilation signal due to subhalos, is at least a factor of $\sim 5$ times smaller in the *BICEP*2 cosmology. Although the absolute value of the boost

depends on many assumptions and is an uncertain quantity, this relative modification should be more robust and will work to lower previous upper limits to order unity.

While the above conclusions are drawn from simulations of only a single MW-size host halo, the overall trends demonstrated should hold for all such systems. Though there is significant scatter between MW-size systems (e.g. Boylan-Kolchin et al., 2010), the relative offset from the mean in the substructure population of a single host appears to remain largely static across cosmologies (Horiuchi et al., 2014). Therefore, the precise magnitude of the above changes may vary, but the general result that subhalos are less numerous and less dense in the *BICEP*2 model compared to *Planck* is robust. In order to accurately determine the range of substructure suppression and changes in concentration, one requires a large sample of simulations similar to those shown here; we elect to instead illustrate the general trends only.

Our results indicate that the level of spectral index running that reconciles the *BICEP*2 measurement with other constraints has interesting effects on dark matter structure over a range of scales. These changes are most evident at the smallest scales, where they help to alleviate small-scale issues with CDM. Though not addressed here, this type of reduction in small-scale power could have interesting implications for understanding cosmic reionization, which may require the early collapse of small halos and thus a fair amount of power on $\sim 10^8 M_\odot$ scales (e.g. Somerville et al., 2003; Robertson et al., 2013), and conversely studies of the early Universe may constrain the allowed running (similar to the constraints placed on WDM by Schultz et al., 2014). Signs of a non-trivial primordial power spectrum may also be explored in the Ly-$\alpha$ forest.

While it should be noted that inflationary models with precisely constant running at the level we have investigated have difficulty producing enough $e$-foldings (Easther & Peiris, 2006) and likely have higher order corrections to the power spectrum in this parameterization

(Abazajian et al., 2005), there are feasible models with scale-dependent running that produce similar suppression of power at dwarf scales to that considered here (e.g., Kobayashi & Takahashi, 2011; Wan et al., 2014). The broad point of this work is to highlight the salient role that a non-trivial primordial power spectrum has in affecting small-scale predictions in ΛCDM. In light of the exciting *BICEP*2 results interpreted as evidence for inflationary gravitational waves, the need to consider non-standard primordial power spectra in structure formation studies has grown all the more urgent.

## Chapter Acknowledgements

The authors thank Quinn Minor, Mike Boylan-Kolchin, Amjad Ashoorioon, Daniel Figueroa, and particularly the anonymous referee for helpful comments. SGK and JSB were partially supported by NSF grants AST-1009973 and AST-1009999. SH is supported by the JSPS fellowship for research abroad, KA is supported by NSF CAREER Grant No. PHY-11-59224, and MK is supported by NSF Grant Nos. PHY-1214648 and PHY-1316792.

We also acknowledge the computational support of the NASA Advanced Supercomputing Division and the NASA Center for Climate Simulation, upon whose *Pleiades* and *Discover* systems the simulations were run, and the *Greenplanet* cluster at UCI, upon which much of the secondary analysis was performed. This research has made use of NASA's Astrophysics Data System.

# Chapter 6

# Summary and Conclusion

This work has centered around using high-resolution simulations to better understand the distribution and dynamics of dark matter halos in and around the Milky Way and Andromeda galaxies, which together with $\sim 50$ dwarf galaxies, make up the Local Group. Here I summarize my key conclusions.

In Chapter 2, I introduced the ELVIS (Exploring the Local Volume in Simulations) suite, which follows the evolution and formation of thirty-six high resolution volumes, each of which is embedded within a cosmological-size box. Twelve of these volumes host LG-like pairs at $z = 0$; the other twenty-four host isolated halos mass-matched to those in the pairs for a total of forty-eight MW-size hosts. By comparing the isolated and paired samples, I showed that the fields around MW-size halos in LG-like configurations are filled with $\sim 50\%$ more structure (at fixed mass) than the fields around otherwise equivalent isolated hosts. Moreover, the kinematic distributions of field halos around paired MW-size hosts are significantly. Together, these imply that simulations of isolated MW-size hosts do not accurately model DM kinematics beyond the virial radius of those hosts. I also used the ELVIS simulations to show that the relation between stellar mass and halo mass must fall off more quickly with

decreasing halo mass than previously assumed in order to avoid overproducing the observed stellar mass function of the LG.

Chapter 3 leveraged the statistical power of the ELVIS suite to explore too-big-to-fail, an extant problem in the ΛCDM paradigm related to the central masses of dwarf halos. I demonstrated that TBTF is not only ubiquitous to MW-size hosts, but that it also exists outside the virial radii of those halos, where the environmental processes that are often invoked to solve it do not act. I also showed that TBTF cannot be solved by simply eliminating the most massive halos – one must also avoid overproducing Draco-like (i.e. relatively high density) dwarfs.

In Chapter 4, I explored a proposed non-environmental solution to TBTF: cyclic variations in the central potential driven by supernovae feedback. By manually varying the mass in an analytic potential, I show that galaxies with $M_\star \lesssim 10^6 M_\odot$ do not form enough supernovae to appreciably change their central potentials. Together with the results of Chapter 3, this suggests that the solution to too-big-to-fail may be non-baryonic.

Chapter 5 examined one such solution. Motivated by recent results concerning the matter power spectrum following inflation, I presented simulations of an identical halo, initialized in several cosmologies. I showed that a "rolling" spectral index, such that the matter power spectrum falls off slowly at small scales relative to the fiducial model, delays structure formation at small scales without violating constraints on the coldness of DM. This delay in dwarf structure formation significantly alleviates TBTF by lowering the central densities of dwarf halos. While it alone does not solve TBTF, a rolling spectral index may increase the efficacy of other proposed solutions.

The work presented here illustrates the power of dwarf galaxies to test physics including galaxy formation, the nature of dark matter, star formation and feedback, and even the cosmology of the Universe. However, there remain a number of unanswered questions involving

dwarfs both in the Local Group and throughout the Universe. For example, what impact does the presence of the many large satellites (the LMC-SMC pair and M33) imply about the accretion histories of the Milky Way and M31? How much scatter is there about the $M_\star - M_{\rm halo}$ relation on the dwarf end, and is it possible for that scatter to explain too-big-to-fail, at least in the Local Group? How much gas do dwarf galaxies deliver to their eventual hosts, and how quickly is that gas removed from the potential of the dwarf?

Upcoming advances in observational astronomy that will enable the study of dwarfs at much larger distances, combined with higher resolution simulations that can more accurately model the relevant physical processes, will begin to answer these questions, and many more, in the coming decades. Only by combining data and theory on dwarfs can the results from each be fully understood and contextualized, but taken together, they will inform our understanding not only of astronomy, but of particle physics and cosmology as well, in ways that were previously impossible.

# Bibliography


Abazajian K., Kadota K., Stewart E. D., 2005, JCAP, 0508, 008

Abazajian K. N., Aslanyan G., Easther R., Price L. C., 2014, arXiv:1403.5922 [astro-ph]

Adams E. A. K., Giovanelli R., Haynes M. P., 2013, arXiv:1303.6967 [astro-ph]

Ade P., et al., 2013, arXiv:1303.5082 [astro-ph]

Ade P. A. R. et al., 2014, Physical Review Letters, 112, 241101

Agnello A., Evans N. W., 2012, ApJ, 754, L39

Ahn C. P. et al., 2014, ApJS, 211, 17

Amorisco N. C., Agnello A., Evans N. W., 2013, MNRAS, 429, L89

Amorisco N. C., Evans N. W., 2012, MNRAS, 419, 184

Amorisco N. C., Zavala J., de Boer T. J. L., 2014, ApJ, 782, L39

Anderhalden D., Diemand J., Bertone G., Macciò A. V., Schneider A., 2012, JCAP, 10, 47

Anderhalden D., Schneider A., Macciò A. V., Diemand J., Bertone G., 2013, Journal of Cosmology and Astroparticle Physics, 3, 14

Anderson B., Kuhlen M., Diemand J., Johnson R. P., Madau P., 2010, ApJ, 718, 899

Arraki K. S., Klypin A., More S., Trujillo-Gomez S., 2013, MNRAS

Ashoorioon A., Dimopoulos K., Sheikh-Jabbari M. M., Shiu G., 2014, arXiv: 1403.6099 [hep-th]

Audren B., Figueroa D. G., Tram T., 2014, arXiv: 1405.1390 [astro-ph]

Babul A., Rees M. J., 1992, MNRAS, 255, 346

Baldry I. K. et al., 2012, MNRAS, 421, 621

Baldry I. K., Glazebrook K., Driver S. P., 2008, MNRAS, 388, 945

Behroozi P. S., Wechsler R. H., Conroy C., 2013c, ApJ, 770, 57

Behroozi P. S., Wechsler R. H., Wu H.-Y., 2013a, ApJ, 762, 109

Behroozi P. S., Wechsler R. H., Wu H.-Y., Busha M. T., Klypin A. A., Primack J. R., 2013b, ApJ, 763, 18

Belokurov V. et al., 2007, ApJ, 654, 897

Belokurov V. et al., 2006, ApJ, 647, L111

Benítez-Llambay A., Navarro J. F., Abadi M. G., Gottlöber S., Yepes G., Hoffman Y., Steinmetz M., 2013, ApJ, 763, L41

Bennett C. L. et al., 2003, ApJS, 148, 1

BICEP2 Collaboration et al., 2014, arXiv:1403.4302 [astro-ph]

Blitz L., Robishaw T., 2000, ApJ, 541, 675

Blitz L., Spergel D. N., Teuben P. J., Hartmann D., Burton W. B., 1999, ApJ, 514, 818

Boselli A., Boissier S., Cortese L., Gavazzi G., 2008, ApJ, 674, 742

Bovy J., Rix H.-W., 2013, arXiv:1309.0809 [astro-ph]

Boyarsky A., Ruchayskiy O., Iakubovskyi D., 2009, Journal of Cosmology and Astroparticle Physics, 0903, 005

Boylan-Kolchin M., Bullock J. S., Kaplinghat M., 2011, MNRAS, 415, L40

Boylan-Kolchin M., Bullock J. S., Kaplinghat M., 2012, MNRAS, 422, 1203

Boylan-Kolchin M., Bullock J. S., Sohn S. T., Besla G., van der Marel R. P., 2013, ApJ, 768, 140

Boylan-Kolchin M., Springel V., White S. D. M., Jenkins A., 2010, MNRAS, 406, 896

Boylan-Kolchin M., Springel V., White S. D. M., Jenkins A., Lemson G., 2009, MNRAS, 398, 1150

Breddels M. A., Helmi A., 2013, A&A, 558, A35

Breddels M. A., Helmi A., 2014, arXiv: 1404.5958 [astro-ph

Brook C. B., Di Cintio A., Knebe A., Gottlöber S., Hoffman Y., Yepes G., Garrison-Kimmel S., 2013, arXiv:1311.5492 [astro-ph]

Brooks A. M., Kuhlen M., Zolotov A., Hooper D., 2013, ApJ, 765, 22

Brooks A. M., Zolotov A., 2014, ApJ, 786, 87

Bryan G. L., Norman M. L., 1998, ApJ, 495, 80

Bullock J. S., 2010, arXiv:1009.4505 [astro-ph]

Bullock J. S., Johnston K. V., 2005, ApJ, 635, 931

Bullock J. S., Kolatt T. S., Sigad Y., Somerville R. S., Kravtsov A. V., Klypin A. A., Primack J. R., Dekel A., 2001, MNRAS, 321, 559

Bullock J. S., Kravtsov A. V., Weinberg D. H., 2000, ApJ, 539, 517

Busha M. T., Alvarez M. A., Wechsler R. H., Abel T., Strigari L. E., 2010, ApJ, 710, 408

Busha M. T., Wechsler R. H., Behroozi P. S., Gerke B. F., Klypin A. A., Primack J. R., 2011, ApJ, 743, 117

Cautun M., Frenk C. S., van de Weygaert R., Hellwing W. A., Jones B. J. T., 2014, arXiv: 1405.7697 [astro-ph]

Cen R., Gott, III J. R., Ostriker J. P., Turner E. L., 1994, ApJ, 423, 1

Collins M. L. M. et al., 2013, ApJ, 768, 172

Conroy C., Wechsler R. H., Kravtsov A. V., 2006, ApJ, 647, 201

Copernicus N., 1543, De revolutionibus orbium coelestium. Johannes Petreius

Corbelli E., 2003, MNRAS, 342, 199

Creasey P., Theuns T., Bower R. G., 2012, ArXiv e-prints

Das S. et al., 2014, Journal of Cosmology and Astroparticle Physics, 4, 14

Davis M., Efstathiou G., Frenk C. S., White S. D. M., 1985, ApJ, 292, 371

de Blok W. J. G., 2010, Advances in Astronomy, 2010

Del Popolo A., 2012a, MNRAS, 419, 971

Del Popolo A., Lima J. A. S., Fabris J. C., Rodrigues D. C., 2014, Journal of Cosmology and Astroparticle Physics, 4, 21

Di Cintio A., Knebe A., Libeskind N. I., Brook C., Yepes G., Gottlöber S., Hoffman Y., 2013, MNRAS, 431, 1220

di Cintio A., Knebe A., Libeskind N. I., Yepes G., Gottlöber S., Hoffman Y., 2011, MNRAS, 417, L74

Diemand J., Kuhlen M., Madau P., 2007a, ApJ, 657, 262

Diemand J., Kuhlen M., Madau P., 2007b, ApJ, 667, 859

Diemand J., Kuhlen M., Madau P., Zemp M., Moore B., Potter D., Stadel J., 2008, Nature, 454, 735

Donato F. et al., 2009, MNRAS, 397, 1169

Driver S. P. et al., 2011, MNRAS, 413, 971

Dunstan R. M., Abazajian K. N., Polisensky E., Ricotti M., 2011, arXiv: 1109.6291 [astro-ph]

Dyson F. W., Eddington A. S., Davidson C., 1920, Royal Society of London Philosophical Transactions Series A, 220, 291

Easther R., Peiris H. V., 2006, Journal of Cosmology and Astroparticle Physics, 9, 10

Efstathiou G., 1992, MNRAS, 256, 43P

Einasto J., 1965, Trudy Astrofizicheskogo Instituta Alma-Ata, 5, 87

Einstein A., 1916, Annalen der Physik, 354, 769

Elbert O. D., Bullock J. S., Garrison-Kimmel S., Rocha M., Oñorbe J., Peter A. H. G., 2014, ArXiv e-prints

Faerman Y., Sternberg A., McKee C. F., 2013, arXiv:1309.0815 [astro-ph]

Fardal M. A. et al., 2013, arXiv:1307.3219 [astro-ph]

Feng J. L., Kaplinghat M., Yu H.-B., 2010, Physical Review Letters, 104, 151301

Ferrero I., Abadi M. G., Navarro J. F., Sales L. V., Gurovich S., 2012, MNRAS, 425, 2817

Few C. G., Gibson B. K., Courty S., Michel-Dansac L., Brook C. B., Stinson G. S., 2012, A&A, 547, A63

Fillingham S. P., Cooper M. C., Wheeler C., Garrison-Kimmel S., Boylan-Kolchin M., Bullock J. S., 2015, ArXiv e-prints

Flores R. A., Primack J. R., 1994, ApJ, 427, L1

Font A. S. et al., 2011, MNRAS, 417, 1260

Forero-Romero J. E., Hoffman Y., Bustamante S., Gottlöber S., Yepes G., 2013, ApJ, 767, L5

Forero-Romero J. E., Hoffman Y., Yepes G., Gottlöber S., Piontek R., Klypin A., Steinmetz M., 2011, MNRAS, 417, 1434

Fraternali F., Tolstoy E., Irwin M. J., Cole A. A., 2009, A&A, 499, 121

Frenk C. S., White S. D. M., Davis M., Efstathiou G., 1988, ApJ, 327, 507

Gao L., Navarro J. F., Cole S., Frenk C. S., White S. D. M., Springel V., Jenkins A., Neto A. F., 2008, MNRAS, 387, 536

Garrison-Kimmel S., Boylan-Kolchin M., Bullock J. S., Kirby E. N., 2014b, MNRAS, 444, 222

Garrison-Kimmel S., Boylan-Kolchin M., Bullock J. S., Lee K., 2014a, MNRAS, 438, 2578

Garrison-Kimmel S., Horiuchi S., Abazajian K. N., Bullock J. S., Kaplinghat M., 2014c, MNRAS, 444, 961

Garrison-Kimmel S., Rocha M., Boylan-Kolchin M., Bullock J. S., Lally J., 2013, MNRAS, 433, 3539

Gelb J. M., Bertschinger E., 1994, ApJ, 436, 467

Gill S. P. D., Knebe A., Gibson B. K., 2005, MNRAS, 356, 1327

Giovanelli R. et al., 2013, AJ, 146, 15

Giovanelli R. et al., 2005, AJ, 130, 2598

Gnedin N. Y., 2000, ApJ, 542, 535

Gorbunov D., Khmelnitsky A., Rubakov V., 2008, Journal of Cosmology and Astroparticle Physics, 0810, 041

Gottloeber S., Hoffman Y., Yepes G., 2010, arXiv:1005.2687 [astro-ph]

Governato F. et al., 2012, MNRAS, 422, 1231

Grcevich J., Putman M. E., 2009, ApJ, 696, 385

Gritschneder M., Lin D. N. C., 2013, ApJ, 765, 38

Gross M. A. K., Somerville R. S., Primack J. R., Holtzman J., Klypin A., 1998, MNRAS, 301, 81

Guo Q., White S., Li C., Boylan-Kolchin M., 2010, MNRAS, 404, 1111

Hahn O., Abel T., 2011, MNRAS, 415, 2101

Haynes M. P. et al., 2011, AJ, 142, 170

Hazra D. K., Shafieloo A., Smoot G. F., Starobinsky A. A., 2014, Journal of Cosmology and Astroparticle Physics, 6, 61

Hernquist L., 1990, ApJ, 356, 359

Hernquist L., Katz N., Weinberg D. H., Miralda-Escudé J., 1996, ApJ, 457, L51

Hinshaw G. et al., 2013, ApJS, 208, 19

Ho S. et al., 2012, ApJ, 761, 14

Ho S., Cuesta A., Seo H.-J., de Putter R., Ross A. J., et al., 2012, ApJ, 761, 14

Holmberg E., 1958, Meddelanden fran Lunds Astronomiska Observatorium Serie II, 136, 1

Horiuchi S., Humphrey P. J., Oñorbe J., Abazajian K. N., Kaplinghat M., Garrison-Kimmel S., 2014, Phys. Rev. D, 89, 025017

Hou Z., Reichardt C., Story K., Follin B., Keisler R., et al., 2014, ApJ, 782, 74

Huang S., Haynes M. P., Giovanelli R., Brinchmann J., 2012b, ApJ, 756, 113

Huang S., Haynes M. P., Giovanelli R., Brinchmann J., Stierwalt S., Neff S. G., 2012a, AJ, 143, 133

Hubble E. P., 1926, ApJ, 64, 321

Ivezic Z. et al., 2008, arXiv:0805.2366 [astro-ph]

Jardel J. R., Gebhardt K., 2012, ApJ, 746, 89

Jardel J. R., Gebhardt K., 2013, ApJ, 775, L30

Jenkins A., Frenk C. S., White S. D. M., Colberg J. M., Cole S., Evrard A. E., Couchman H. M. P., Yoshida N., 2001, MNRAS, 321, 372

Johnston K. V., Bullock J. S., Sharma S., Font A., Robertson B. E., Leitner S. N., 2008, ApJ, 689, 936

Kahn F. D., Woltjer L., 1959, ApJ, 130, 705

Kamionkowski M., Koushiappas S. M., Kuhlen M., 2010, Phys. Rev. D, 81, 043532

Kamionkowski M., Liddle A. R., 2000, Phys. Rev. Lett., 84, 4525

Kannappan S. J., 2004, ApJ, 611, L89

Kannappan S. J. et al., 2013, arXiv:1308.3292 [astro-ph]

Kaplinghat M., 2005, Phys. Rev. D, 72, 063510

Karachentsev I. D., 2005, AJ, 129, 178

Karachentsev I. D., Kaisina E. I., 2013, AJ, 146, 46

Karachentsev I. D., Karachentseva V. E., Huchtmeier W. K., Makarov D. I., 2004, AJ, 127, 2031

Karachentsev I. D. et al., 2002, A&A, 389, 812

Katz N., White S. D. M., 1993, ApJ, 412, 455

Kauffmann G., White S. D. M., Guiderdoni B., 1993, MNRAS, 264, 201

Kawata D., Mulchaey J. S., 2008, ApJ, 672, L103

Kazantzidis S., Mayer L., Mastropietro C., Diemand J., Stadel J., Moore B., 2004, ApJ, 608, 663

Keeton C. R., Moustakas L. A., 2009, ApJ, 699, 1720

Kirby E. N., Bullock J. S., Boylan-Kolchin M., Kaplinghat M., Cohen J. G., 2014, arXiv:1401.1208 [astro-ph]

Klypin A., Kravtsov A. V., Valenzuela O., Prada F., 1999, ApJ, 522, 82

Klypin A. A., Trujillo-Gomez S., Primack J., 2011, ApJ, 740, 102

Knebe A., Libeskind N. I., Doumler T., Yepes G., Gottlöber S., Hoffman Y., 2011, MNRAS, 417, L56

Knollmann S. R., Knebe A., 2009, ApJS, 182, 608

Kobayashi T., Takahashi F., 2011, Journal of Cosmology and Astroparticle Physics, 1, 26

Koch A., Kleyna J. T., Wilkinson M. I., Grebel E. K., Gilmore G. F., Evans N. W., Wyse R. F. G., Harbeck D. R., 2007, AJ, 134, 566

Koposov S. et al., 2008, ApJ, 686, 279

Koposov S. E., Yoo J., Rix H., Weinberg D. H., Macciò A. V., Escudé J. M., 2009, ApJ, 696, 2179

Kowalczyk K., Łokas E. L., Kazantzidis S., Mayer L., 2013, MNRAS, 431, 2796

Kravtsov A., 2010, Advances in Astronomy, 2010

Kravtsov A. V., Berlind A. A., Wechsler R. H., Klypin A. A., Gottlöber S., Allgood B., Primack J. R., 2004, ApJ, 609, 35

Kroupa P., 2002, Science, 295, 82

Kuhlen M., Diemand J., Madau P., 2008, ApJ, 686, 262

Kuhlen M., Madau P., Silk J., 2009, Science, 325, 970

Kuzio de Naray R., Kaufmann T., 2011, MNRAS, 414, 3617

Kuzio de Naray R., McGaugh S. S., de Blok W. J. G., 2008, ApJ, 676, 920

Larson D. et al., 2011, ApJS, 192, 16

Leaman R. et al., 2012, ApJ, 750, 33

Lesgourgues J., Viel M., Haehnelt M., Massey R., 2007, Journal of Cosmology and Astroparticle Physics, 0711, 008

Letarte B. et al., 2009, MNRAS, 400, 1472

Li Y.-S., White S. D. M., 2008, MNRAS, 384, 1459

Libeskind N. I., Yepes G., Knebe A., Gottlöber S., Hoffman Y., Knollmann S. R., 2010, MNRAS, 401, 1889

Liu H., Mertsch P., Sarkar S., 2014, ApJ, 789, L29

Loeb A., Weiner N., 2011, Physical Review Letters, 106, 171302

Lovell M. R. et al., 2012, MNRAS, 420, 2318

Lovell M. R., Frenk C. S., Eke V. R., Jenkins A., Gao L., Theuns T., 2014, MNRAS, 439, 300

Ludlow A. D., Navarro J. F., Angulo R. E., Boylan-Kolchin M., Springel V., Frenk C., White S. D. M., 2014, MNRAS, 441, 378

Lunnan R., Vogelsberger M., Frebel A., Hernquist L., Lidz A., Boylan-Kolchin M., 2012, ApJ, 746, 109

Lux H., Read J. I., Lake G., 2010, MNRAS, 406, 2312

Madau P., Kuhlen M., Diemand J., Moore B., Zemp M., Potter D., Stadel J., 2008, ApJ, 689, L41

Makarov D., Karachentsev I., 2011, MNRAS, 412, 2498

Mamon G. A., Sanchis T., Salvador-Solé E., Solanes J. M., 2004, A&A, 414, 445

Martinez G. D., 2013, arXiv:1309.2641 [astro-ph]

Martinez G. D., Bullock J. S., Kaplinghat M., Strigari L. E., Trotta R., 2009, Journal of Cosmology and Astroparticle Physics, 6, 14

Mashchenko S., Couchman H. M. P., Wadsley J., 2006, Nature, 442, 539

Mateo M., Olszewski E. W., Walker M. G., 2008, ApJ, 675, 201

Mather J. C. et al., 1990, ApJ, 354, L37

McConnachie A. W., 2012, AJ, 144, 4

McConnachie A. W., Irwin M. J., Ferguson A. M. N., Ibata R. A., Lewis G. F., Tanvir N., 2005, MNRAS, 356, 979

McDonald J., 2014, arXiv:1403.6650 [astro-ph]

McGaugh S. S., 2005, ApJ, 632, 859

McQuinn K. B. W. et al., 2013, arXiv:1310.0044 [astro-ph]

Miller R. H., 1964, ApJ, 140, 250

Moore B., 1994, Nature, 370, 629

Moore B., Ghigna S., Governato F., Lake G., Quinn T., Stadel J., Tozzi P., 1999, ApJ, 524, L19

Moster B. P., Naab T., White S. D. M., 2013, MNRAS, 428, 3121

Muñoz R. R. et al., 2005, ApJ, 631, L137

Murray S. G., Power C., Robotham A. S. G., 2013, Astronomy and Computing, 3, 23

Navarro J. F., Eke V. R., Frenk C. S., 1996a, MNRAS, 283, L72

Navarro J. F., Frenk C. S., White S. D. M., 1996b, ApJ, 462, 563

Navarro J. F. et al., 2010, MNRAS, 402, 21

Newton I., 1687, Philosophiae Naturalis Principia Mathematica. Isaac Newton

Ng K. C. Y., Laha R., Campbell S., Horiuchi S., Dasgupta B., Murase K., Beacom J. F., 2014, Phys. Rev. D, 89, 083001

Ngan W. H. W., Carlberg R. G., 2014, ApJ, 788, 181

Oñorbe J., Garrison-Kimmel S., Maller A. H., Bullock J. S., Rocha M., Hahn O., 2014, MNRAS, 437, 1894

Ogiya G., Mori M., 2012, ArXiv e-prints

Oh S.-H., de Blok W., Brinks E., Walter F., Kennicutt, Robert C. J., 2011, AJ, 141, 193

Okamoto T., Gao L., Theuns T., 2008, MNRAS, 390, 920

Olsen K. A. G., Zaritsky D., Blum R. D., Boyer M. L., Gordon K. D., 2011, ApJ, 737, 29

Parry O. H., Eke V. R., Frenk C. S., Okamoto T., 2012, MNRAS, 419, 3304

Peñarrubia J., Pontzen A., Walker M. G., Koposov S. E., 2012, ApJ, 759, L42

Peirani S., de Freitas Pacheco J. A., 2006, New Astronomy, 11, 325

Penzias A. A., Wilson R. W., 1965, ApJ, 142, 419

Phillips J. I., Wheeler C., Boylan-Kolchin M., Bullock J. S., Cooper M. C., Tollerud E. J., 2014, MNRAS, 437, 1930

Piffl T. et al., 2013, arXiv:1309.4293 [astro-ph]

Planck Collaboration et al., 2013, arXiv:1303.5076 [astro-ph]

Polisensky E., Ricotti M., 2011, Phys. Rev. D, 83, 043506

Polisensky E., Ricotti M., 2014, MNRAS, 437, 2922

Pontzen A., Governato F., 2012, MNRAS, 421, 3464

Pontzen A., Governato F., 2014, Nature, 506, 171

Purcell C. W., Zentner A. R., 2012, Journal of Cosmology and Astroparticle Physics, 12, 7

Read J. I., Gilmore G., 2005, MNRAS, 356, 107

Read J. I., Wilkinson M. I., Evans N. W., Gilmore G., Kleyna J. T., 2006, MNRAS, 367, 387

Rhode K. L. et al., 2013, AJ, 145, 149

Richardson J. C. et al., 2011, ApJ, 732, 76

Ricotti M., Gnedin N. Y., 2005, ApJ, 629, 259

Robertson B. E. et al., 2013, ApJ, 768, 71

Robotham A. S. G. et al., 2012, MNRAS, 424, 1448

Rocha M., Peter A. H. G., Bullock J., 2012, MNRAS, 425, 231

Rocha M., Peter A. H. G., Bullock J. S., Kaplinghat M., Garrison-Kimmel S., Oñorbe J., Moustakas L. A., 2013, MNRAS, 430, 81

Rodríguez-Puebla A., Avila-Reese V., Drory N., 2013, ApJ, 773, 172

Rubin V. C., Ford, Jr. W. K., 1970, ApJ, 159, 379

Ryan-Weber E. V., Begum A., Oosterloo T., Pal S., Irwin M. J., Belokurov V., Evans N. W., Zucker D. B., 2008, MNRAS, 384, 535

Sales L. V., Navarro J. F., Abadi M. G., Steinmetz M., 2007, MNRAS, 379, 1475

Sánchez-Conde M. A., Prada F., 2014, MNRAS, 442, 2271

Sawala T. et al., 2014, arXiv:1404.3724 [astro-ph]

Schneider A., Anderhalden D., Macciò A. V., Diemand J., 2014, MNRAS, 441, L6

Schultz C., Oñorbe J., Abazajian K. N., Bullock J. S., 2014, MNRAS, 442, 1597

Simon J. D., Bolatto A. D., Leroy A., Blitz L., Gates E. L., 2005, ApJ, 621, 757

Simon J. D., Geha M., 2007, ApJ, 670, 313

Slater C. T., Bell E. F., Martin N. F., 2011, ApJ, 742, L14

Sohn S. T., Besla G., van der Marel R. P., Boylan-Kolchin M., Majewski S. R., Bullock J. S., 2012, ArXiv e-prints

Somerville R. S., 2002, ApJ, 572, L23

Somerville R. S., Bullock J. S., Livio M., 2003, ApJ, 593, 616

Springel V., 2005, MNRAS, 364, 1105

Springel V. et al., 2008, MNRAS, 391, 1685

Springel V. et al., 2005, Nature, 435, 629

Stanimirović S., Staveley-Smith L., Jones P. A., 2004, ApJ, 604, 176

Sternberg A., McKee C. F., Wolfire M. G., 2002, ApJS, 143, 419

Stewart K. R., Bullock J. S., Wechsler R. H., Maller A. H., 2009, ApJ, 702, 307

Strigari L. E., Bullock J. S., Kaplinghat M., Simon J. D., Geha M., Willman B., Walker M. G., 2008a, Nature, 454, 1096

Strigari L. E., Frenk C. S., White S. D. M., 2010, MNRAS, 408, 2364

Strigari L. E., Frenk C. S., White S. D. M., 2014, ArXiv e-prints

Strigari L. E., Koushiappas S. M., Bullock J. S., Kaplinghat M., Simon J. D., Geha M., Willman B., 2008b, ApJ, 678, 614

Strigari L. E., Wechsler R. H., 2012, ApJ, 749, 75

Teyssier M., Johnston K. V., Kuhlen M., 2012, MNRAS, 426, 1808

Teyssier R., Pontzen A., Dubois Y., Read J. I., 2013, MNRAS, 429, 3068

The Fermi-LAT Collaboration et al., 2013, ArXiv e-prints

Thoul A. A., Weinberg D. H., 1996, ApJ, 465, 608

Tikhonov A. V., Klypin A., 2009, MNRAS, 395, 1915

Tinker J., Kravtsov A. V., Klypin A., Abazajian K., Warren M., Yepes G., Gottlöber S., Holz D. E., 2008, ApJ, 688, 709

Tisserand P. et al., 2007, A&A, 469, 387

Tollerud E. J. et al., 2012, ApJ, 752, 45

Tollerud E. J., Boylan-Kolchin M., Barton E. J., Bullock J. S., Trinh C. Q., 2011, ApJ, 738, 102

Tollerud E. J., Boylan-Kolchin M., Bullock J. S., 2014, arXiv:1403.6469 [astro-ph]

Tollerud E. J., Bullock J. S., Strigari L. E., Willman B., 2008, ApJ, 688, 277

Trachternach C., de Blok W. J. G., Walter F., Brinks E., Kennicutt, Jr. R. C., 2008, AJ, 136, 2720

Tully R. B. et al., 2013, AJ, 146, 86

Vale A., Ostriker J. P., 2004, MNRAS, 353, 189

van der Marel R. P., Fardal M., Besla G., Beaton R. L., Sohn S. T., Anderson J., Brown T., Guhathakurta P., 2012, ApJ, 753, 8

Vera-Ciro C. A., Helmi A., Starkenburg E., Breddels M. A., 2013, MNRAS, 428, 1696

Viel M., Becker G. D., Bolton J. S., Haehnelt M. G., 2013, Phys. Rev. D, 88, 043502

Vogelsberger M., Zavala J., Loeb A., 2012, MNRAS, 423, 3740

Walker M. G., 2012, ArXiv e-prints

Walker M. G., Mateo M., Olszewski E. W., 2009, AJ, 137, 3100

Walker M. G., Peñarrubia J., 2011, ApJ, 742, 20

Wambsganss J., Bode P., Ostriker J. P., 2004, ApJ, 606, L93

Wan Y., Li S., Li M., Qiu T., Cai Y., Zhang X., 2014, Phys. Rev. D, 90, 023537

Wang J., Frenk C. S., Navarro J. F., Gao L., Sawala T., 2012, MNRAS, 424, 2715

Wang J., White S. D. M., 2007, MNRAS, 380, 93

Warren M. S., Quinn P. J., Salmon J. K., Zurek W. H., 1992, ApJ, 399, 405

Weiner B. J. et al., 2006, ApJ, 653, 1027

Weisz D. R. et al., 2011, ApJ, 743, 8

Weisz D. R., Dolphin A. E., Skillman E. D., Holtzman J., Gilbert K. M., Dalcanton J. J., Williams B. F., 2015, ArXiv e-prints

Wetzel A. R., Tollerud E. J., Weisz D. R., 2015, ArXiv e-prints

Wheeler C., Onorbe J., Bullock J. S., Boylan-Kolchin M., Elbert O., Garrison-Kimmel S., Hopkins P. F., Keres D., 2015, ArXiv e-prints

Willman B. et al., 2005, AJ, 129, 2692

Wolf J., Martinez G. D., Bullock J. S., Kaplinghat M., Geha M., Muñoz R. R., Simon J. D., Avedo F. F., 2010, MNRAS, 406, 1220

Woo J., Courteau S., Dekel A., 2008, MNRAS, 390, 1453

Woo J. et al., 2013, MNRAS, 428, 3306

Wu H.-Y., Hahn O., Wechsler R. H., Behroozi P. S., Mao Y.-Y., 2013, ApJ, 767, 23

Yniguez B., Garrison-Kimmel S., Boylan-Kolchin M., Bullock J. S., 2014, MNRAS, 439, 73

Zaggia S., Held E. V., Sommariva V., Momany Y., Saviane I., Rizzi L., 2011, in EAS Publications Series, Vol. 48, EAS Publications Series, Koleva M., Prugniel P., Vauglin I., eds., pp. 215–216

Zavala J., Vogelsberger M., Walker M. G., 2013, MNRAS, 431, L20

Zemp M., Moore B., Stadel J., Carollo C. M., Madau P., 2008, MNRAS, 386, 1543

Zentner A. R., Bullock J. S., 2002, Phys. Rev. D, 66, 043003

Zentner A. R., Bullock J. S., 2003, ApJ, 598, 49

Zolotov A. et al., 2012, ApJ, 761, 71

Zwicky F., 1937, ApJ, 86, 217